

NATIONAL AERONAUTICS AND SPACE ADMINISTRATION

Space Programs Summary No. 37-33, Volume III

for the period March 1, 1965 to April 30, 1965

The Deep Space Network

FACILITY FORM 802

N65-27826

(ACCESSION NUMBER)

(THRU)

112

(PAGES)

1

(CODE)

CR 63744

(NASA CR OR TRX OR AD NUMBER)

07

(CATEGORY)

GPO PRICE \$ _____

OTS PRICE(S) \$ _____

Hard copy (HC) 4.00

Microfiche (MF) .75



JET PROPULSION LABORATORY
CALIFORNIA INSTITUTE OF TECHNOLOGY
PASADENA, CALIFORNIA

May 31, 1965

NATIONAL AERONAUTICS AND SPACE ADMINISTRATION

Space Programs Summary No. 37-33, Volume III

for the period March 1, 1965 to April 30, 1965

The Deep Space Network

JET PROPULSION LABORATORY
CALIFORNIA INSTITUTE OF TECHNOLOGY
PASADENA, CALIFORNIA

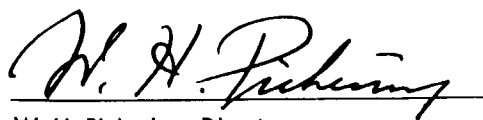
May 31, 1965

Preface

The *Space Programs Summary* is a six-volume, bimonthly publication that documents the current project activities and supporting research and advanced development efforts conducted or managed by JPL for the NASA space exploration programs. The titles of all volumes of the *Space Programs Summary* are:

- Vol. I. The Lunar Program (Confidential)
- Vol. II. The Planetary-Interplanetary Program (Confidential)
- Vol. III. The Deep Space Network (Unclassified)
- Vol. IV. Supporting Research and Advanced Development (Unclassified)
- Vol. V. Supporting Research and Advanced Development (Confidential)
- Vol. VI. Space Exploration Programs and Space Sciences (Unclassified)

The *Space Programs Summary*, Vol. VI consists of an unclassified digest of appropriate material from Vols. I, II, and III; an original presentation of technical supporting activities, including engineering development of environmental-test facilities, and quality assurance and reliability; and a reprint of the space science instrumentation studies of Vols. I and II.



W. H. Pickering, Director
Jet Propulsion Laboratory

Space Programs Summary No. 37-33, Volume III

Copyright © 1965, Jet Propulsion Laboratory, California Institute of Technology
Prepared under Contract No. NAS 7-100, National Aeronautics & Space Administration

Contents

I. Introduction	1
II. Tracking Stations Engineering and Operations	3
A. <i>Ranger IX</i> Tracking Data Analysis	3
B. Goldstone Operations	5
C. Advanced Antenna System	9
D. Performance of the DSIF Tracking Data Monitor Program During <i>Rangers VIII and IX</i>	19
E. Random Numbers and Their Generation	24
III. Communications Engineering Developments	26
A. S-Band Implementation for the DSIF	26
B. Ground Instrumentation for <i>Mariner IV</i> Occultation Experiment	32
C. Manned Space Flight Network S-Band Receiver/Exciter	39
D. S-Band Cassegrain Monopulse Feed Development	43
E. S-Band Test Antenna	48
F. Coherent Frequency Translation	50
G. Range Receiver	53
H. X8 Doppler Multiplier	54
I. Venus Station <i>Mariner IV</i> Support	56
J. Venus Station <i>Mariner IV</i> Encounter Receiver	58
References	62
IV. Communications Research and Development	65
A. Ground Antennas	65
B. Experimental Closed Cycle Refrigerator (CCR) for Masers	83
C. Venus Station Operations	84
D. High-Power 100-kw S-Band Transmitter	88
E. X-Band Lunar Radar Transmitter	89
F. Lunar-Planetary Radar	91
G. Communication Systems	96
H. Information Systems	107
References	110

I. Introduction

The Deep Space Network (DSN) is a precision communication system which is designed to communicate with, and permit control of, spacecraft designed for deep space exploration. The DSN consists of the Deep Space Instrumentation Facility (DSIF), the Space Flight Operations Facility (SFOF), and the DSN Ground Communication System (GCS).

The DSN is a NASA facility, managed by JPL through a contract between NASA and the California Institute of Technology. The Office of Tracking and Data Acquisition is the cognizant NASA office.

It is the policy of the DSN to continuously conduct research and development of new components and systems and to engineer them into the DSN to maintain a state-of-the-art capability.

The DSN has facilities for simultaneously controlling a newly launched spacecraft and a second one already in flight. Within a few months, it will be able to control simultaneously either two newly launched spacecraft plus two in flight or the operations of four spacecraft in flight at the same time. The DSIF is equipped with 85-ft antennas having gains of 53 db at 2300 Mc and a system temperature of 55°K, making it possible to receive sig-

nificant data rates at distances as far as the planet Mars. To improve the data rate and distance capability, a 210-ft antenna is under construction at the Goldstone Mars station and two additional antennas of this size are planned for installation at overseas stations.

The DSIF utilizes large antennas, low-noise phase-lock receiving systems, and high-power transmitters located at stations positioned around the Earth to track, command, and receive data from deep space probes. Overseas stations are generally operated by personnel of the respective countries. The DSIF stations are:

I.D. No.	Name	Location
11	Goldstone, Pioneer	Goldstone, California
12	Goldstone, Echo	Goldstone, California
13	Goldstone, Venus (R&D)	Goldstone, California
14	Goldstone, Mars (under construction)	Goldstone, California
41	Woomera	Island Lagoon, Australia
42	Tidbinbilla	Canberra, Australia
51	Johannesburg	Johannesburg, South Africa
61	Madrid (under construction)	Madrid, Spain
71	Spacecraft Monitoring	Cape Kennedy, Florida
72	Spacecraft Guidance and Command (under construction)	Ascension Island

The SFOF is located in a three-story building at the Jet Propulsion Laboratory in Pasadena, California, and utilizes operations control consoles, status and operations displays, computers, data processing equipment for analysis of spacecraft performance and space science experiments, and communication facilities to control space flight operations. This control is accomplished by generating trajectories and orbits, and command and control data, from tracking and telemetry data received from the DSIF in near real-time. The SFOF also reduces the telemetry, tracking, command and station performance data

recorded by the DSIF into engineering and scientific information for analysis and use by the scientific experimenters and spacecraft engineers.

The DSN Ground Communication System consists of voice, normal and high data rate teletype circuits provided by the NASA World-Wide Communications Network between each overseas station and the SFOF; teletype and voice circuits between the SFOF, Goldstone Stations, and Cape Kennedy; and a microwave link between the SFOF and Goldstone, provided by the DSN.

II. Tracking Stations Engineering and Operations

A. Ranger IX Tracking Data Analysis

1. Mission Description

The *Ranger IX* spacecraft was launched from Cape Kennedy on March 21, 1965 using the *Atlas/Agna B* booster for injection into a lunar transfer orbit. Liftoff occurred at 21:37:02.456 Greenwich Mean Time (GMT) on a 93.7-deg launch azimuth.¹ *Ranger IX* was injected

into parking orbit at 21:45:24, and into the lunar transfer orbit at 21:49:48. The DSIF tracked the spacecraft from shortly after transfer orbit injection until lunar impact at 14:08:21.325864 ± 0.000007 seconds on, March 24, 1965.² Actual tracking periods and nominal view periods for each DSIF station are shown in Table 1.

Prior to launch, preflight studies showed that an analysis of certain problems should be carried out in addition to the compilation of the preflight predictions. These included the problem of ETR predictions being late, the possibility of there being no DSIF-41 view period in

¹Liftoff and injection times are as reported by the Air Force Eastern Test Range (ETR). All times referred to in this Summary are in terms of GMT.

²See Part 4 for a further explanation of the actual impact time.

Table 1. *Ranger IX* view periods

DSIF station	Pass number	Nominal view period ^a		Actual view period ^b		Pass duration ^b	
		Start, day of year:hr:min	End, day of year:hr:min	Start, day of year:hr:min	End, day of year:hr:min	Nominal, hr:min:sec	Actual, hr:min:sec
71	Launch (L)	L	L + 7½ min	21:37:02 L	080:21:44:47	00:07:30	00:07:35
51	1	080:22:00:42	081:09:01	080:22:01	081:09:05	11:00:00	11:04:00
41	1	No view. Within 4 deg of main beam		080:23:00	082:01:42	00:00:00	02:42:00
12	1	081:08:33	081:17:14	081:08:24	081:17:17	08:41:00	08:54:00
41	2	082:14:22	082:02:22	081:13:35	082:03:22	12:00:00	13:53:00
51	2	081:21:40	082:09:45	081:21:37	082:10:04	12:05:00	12:27:00
12	2	082:08:56	082:17:43	082:08:57	082:17:44	08:47:00	08:47:00
41	3	082:14:36	083:02:37	082:14:08 ^c	083:03:20	12:01:00	13:12:00
51	3	082:21:55	083:09:55	082:21:45	083:10:16	12:00:00	12:31:00
12	3	083:09:00	083:14:08:21 Impact	083:09:13	083:14:08:21 Impact	05:08:00	04:55:00
41	4	No view. Within 8 deg of main beam	Impact	083:13:43 ^c	083:13:58	00:00:00	00:15:00

^aA nominal view period is calculated to include land masks and antenna limits such that the spacecraft remains in the main beam, i.e., within 0.5 deg or ≈3 db of the center of the main beam.

^bActual view period is the period between first solid receiver lock and last solid drop of receiver lock. Momentary drops are neglected.

^cWith squint-looking feed.

the first pass and the need for bias oscillators at the DSIF stations to obtain one-way data.

Preflight simulations indicated that tracking data analysis personnel could not depend upon getting parking or transfer orbit predictions from the ETR in time to use the information effectively for DSIF-51 acquisition. This necessitated more emphasis on preflight predictions. Due to the uprange injection, DSIF-41 had short or nonexistent view periods on the first pass, depending upon the launch day. For the *Ranger IX* trajectory (considering antenna angular constraints), the nearest DSIF-41 came to a view period was having the spacecraft 4 deg away from its main beam. Since DSIF-41 could not transmit on the acquisition aid, studies were made of the power in the transmitter side lobes to determine if two-way doppler could be obtained from DSIF-41 if necessary. These studies indicated that two-way lock at DSIF-41 on the first pass was possible but should be attempted only if DSIF-51 experienced doppler problems. It was necessary to determine the bias oscillator frequencies to be used by the DSIF, due to the nonstandard transponder beacon frequency. These determinations were turned over to the DSIF ground equipment analyst to implement at the stations.

2. Tracking Operations

The first DSIF station to track *Ranger IX* was DSIF-71 at Cape Kennedy. It acquired the spacecraft prior to launch and tracked it from launch to the horizon, taking telemetric data only. A trajectory seen by DSIF-71 is only a function of launch azimuth; therefore, new preflight predictions were not provided for *Ranger IX*. A new offset frequency was provided to compensate for the difference in frequencies between *Rangers VIII* and *IX*. DSIF-71 tracked *Ranger IX* for 7 min and 35 sec, several seconds below its horizon mask.

DSIF-51 acquired the spacecraft within 20 sec of its first view. The acquisition was made with the ground transmitter on; so that, when ground receiver lock was established, two-way lock was also established. The orbit determination process used at JPL is very sensitive to data near injection. By acquiring the spacecraft in a two-way mode, two-way doppler is obtained as near injection as possible. These data are of great value in obtaining a good orbit quickly without a vast amount of data. DSIF-51 was taking two-way doppler data within 20 sec from the start of the view period, which was a fast, efficient acquisition.

Approximately 13.5 min after first acquisition at 22:14:44, DSIF-51 switched the transmitter exciter chain from a voltage controlled oscillator (VCO) to a rubidium standard controlled frequency synthesizer. Tests on *Ranger VIII* had shown that the two-way doppler data taken while using the synthesizer had less noise than when a VCO was the frequency source. On *Ranger IX*, however, the data noise increased when the synthesizer replaced the oscillator. This increase in noise was observed at the Goldstone tracking data analysis area, using the tracking data monitor program. Following an analysis of the noise, it was decided to have the station return to the VCO. This was done at 22:36:06, and the noise decreased. The station then changed synthesizers and took data, using the new unit, between 22:55:15 and 23:12:10. When these data also proved to contain excess noise, a request was made for the station to change rubidium standards. Considerable discussion was involved since it was necessary for the station to interrupt the tracking momentarily to make this change. It was decided that DSIF-41 should go into a two-way mode and that DSIF-51 should change its rubidium standard during this period. When DSIF-51 reacquired two-way lock at 081:00:25:20,³ the data noise had been reduced, and it continued this way for the remainder of the pass. There was a time bias on the doppler data from 081:00:25:20 to 00:40:13 due to the changing of the rubidium standard. Although analysis is not yet complete, it appears that the rubidium standard was the cause of the noise.

DSIF-41 did not expect to go into a two-way mode on the first pass since the spacecraft trajectory was never within the main beam of the antenna. It did come within 4 deg of the main beam, and data were received on the acquisition aid due to the wider beamwidth. When the problem arose with the DSIF-51 doppler noise, it was decided to try to validate the data with some two-way data from DSIF-41. Since the spacecraft was 4 deg out of the transmitter beam, the possibility of lock was marginal. Two-way lock was obtained and was maintained for almost 20 min before the spacecraft moved too far from the main beam to maintain up-link lock.

Two-station noncoherent data taken at DSIF-41 when DSIF-51 was transmitting were nonconclusive in pointing out the possible frequency standard problem at DSIF-51. The two stations were on different sample rates, which caused problems in trying to correlate the data noise.

³Day of year:hr:min:sec.

3. Midcourse Maneuver

A midcourse maneuver was conducted at DSIF-12 on March 23, 1965. Motor ignition occurred at 12:30:10 and motor shutoff at 12:30:40. The total doppler shift was 88.5 cps, indicating a radial velocity shift of 13.8 m/sec. This compares with the nominal velocity input of 13.97 m/sec. The spacecraft was tracked throughout the burn period in a two-way doppler mode using a 1-sec non-destruct counter mode.

Premidcourse and postmidcourse tracking predictions were furnished during *Ranger IX* to two non-DSIF tracking stations: one operated by General Electric at Schenectady, New York and the other by Standard Oil of Ohio at Cleveland, Ohio.

4. Lunar Impact

Due to the trajectory of *Ranger IX* the possibility arose that DSIF-41 could see lunar impact. An extra set of predictions were generated, and they indicated that the spacecraft would impact before it would rise within the main beam of the DSIF-41 antenna, which was constrained by the 270 deg hour angle limits. A squint feed was installed at DSIF-41 to change the angle of the main lobe away from the central axis of the paraboloid. This was accomplished by moving the feed so that the angle of illumination was changed. DSIF-41 acquired the spacecraft 25 min before impact but dropped lock at 13:58 when the Goldstone transmitter failed. Because the voice net to DSIF-41 was tied in to the Blue (public information) Net which was giving TV system information, the station was not promptly notified of the transmitter failure. This resulted in not acquiring the spacecraft during the last 10 min before impact.

The DSIF-12 transmitter failed 10 min before lunar impact, causing the loss of receiver lock at DSIF-41 (mentioned earlier) and causing the DSIF-12 receiver to drop lock. Recovery was rapid at DSIF-12 with only 1 min of tracking data being lost. Due to the prime importance of the TV signal being recorded, the receiver operator swept the receiver frequency over to the beacon frequency without putting the doppler system in a one-way mode. To extract the doppler during this period, a new equation is necessary. Let

f_D = doppler frequency as recorded

\dot{r}/c = one-way doppler shift

F_T = frequency output by the transponder auxiliary oscillator

$$f_D = 960.1522714607 E6 = F_T \left(1 - \frac{\dot{r}}{c} \right)$$

The above equation takes into account the bias frequency, and the ground frequency is referenced to the station standard.

An experiment to measure the exact time of lunar impact was conducted at DSIF-12. This consisted of counting the station's 1-Mc reference frequency using the 1/min station time pulse as the start trigger and the decaying spin modulation output as the stop trigger. The spin modulation output (unfiltered coherent AGC voltage) is precalibrated and postcalibrated to measure the receiver delay. Receiver delay uncertainty has been the limiting factor in the impact time measurement. Analysis shows the 1- σ uncertainty to be 185 μ sec. Impact (loss of carrier) was recorded at 14:08:21.325916 \pm 185 μ sec. A second impact time was recorded by passing a 2-Mc spacecraft signal through a 300-kc filter along with the NASA 100 pps and a 1-Mc signal. This method showed the impact time to be 14:08:21.325864 \pm 7 μ sec.

Both times are uncorrected for wave-propagation time, which is estimated as 1.32704 sec. The second method is more accurate than the first but has the disadvantage in the reduction time of about two weeks compared to the instant readout and 1/2-hr calibration necessary for the first method. The two methods do agree, however, since the second time is nested within the stated uncertainty in the first.

An experiment was conducted to measure the difference in the settings of the DSIF-41 clocks and the DSIF-12 clocks. The mechanization was similar to the spin modulation output methods of measuring impact time. Calibration problems at DSIF-41 made the absolute time difference measurements invalid; however, it can be seen from the variance on the samples that the method is feasible and further investigation would be worthwhile.

B. Goldstone Operations

Ranger IX impacted in the lunar crater Alphonsus at 14:08:21, March 24, 1965, ending the series of *Ranger* missions. The spacecraft was tracked by the Echo station for all three view periods, and by the Pioneer station for the third view period only. Both stations recovered full video data transmitted from the *Ranger* cameras. At the Pioneer station Mars-bound *Mariner IV* tracking continued and construction began on the 30-ft antenna. Construction also began on the supply and storage building at Echo station.

1. Ranger IX

a. Echo station. The L-band equipment at Echo was maintained in an operational status between *Ranger VIII* and the launch of *Ranger IX*. Two operational readiness tests were conducted. The launch of *Ranger IX* occurred on March 21, 1965. During the first view period, the spacecraft was commanded to change from the low-gain to the high-gain antenna. The midcourse maneuver was performed during the second view period, and a terminal maneuver was performed during the third view period.

b. Pioneer station. Pioneer provided receiver backup and recovery of video from *Ranger IX*. In the interval between *Rangers VIII* and *IX*, the acquisition time of *Mariner IV* had advanced sufficiently so that Pioneer was able to transfer the *Mariner* track to DSIF-42 at Tidbinbilla, Australia, at the approximate acquisition time of *Ranger IX* by the Echo station. The change from the S-band configuration to the L-band was accomplished in less than 2 hr.

With the conclusion of the *Ranger* program, the L-band systems at both Echo and Pioneer are being dismantled and stored for subsequent disposition.

2. Mariner IV

a. Pioneer station. The tracking of the *Mariner IV* spacecraft is continuing on a routine basis. On March 5 the spacecraft central computer and sequencer switched the transmitter from the low-gain to the high-gain antenna.

In preparation for the occultation experiment to be performed during the Mars encounter, preliminary tests were conducted to establish compatibility of the occultation equipment with the S-band system. Additional tests are scheduled to ensure operational readiness.

b. Venus station. With the success of the *Mariner IV* track during the third view period of the *Ranger VIII* mission (SPS 37-32, Vol. III, p. 32), additional test tracking was performed. Two-way coherent and three-way non-coherent doppler between DSIF-11, -13, -42 and the spacecraft have been accomplished. Microwave interfaces between the Venus and Pioneer stations are still being optimized.

Final system testing of the *Mariner* exciter, including phase stability, was performed. The command loop between the Venus station and the spacecraft has been successfully locked and command modulation applied; however, no commands have been transmitted from the

Venus station. The *Mariner* system is operationally ready for Pioneer station backup.

c. Echo station. Completion of the *Ranger* program and the phase-out of the L-band system placed increased emphasis on the installation of the S-band system to provide additional backup to the Pioneer station during the forthcoming *Mariner IV* Mars encounter. In preparation for the installation, an S-band wing (Fig. 1) was added to the existing control building (SPS 37-31, Vol. III, p. 5; SPS 37-32, Vol. III, p. 6). Occupancy of the building began soon after the completion of the *Ranger IX* mission when portions of the new S-band receiver were moved from temporary storage into the new wing. Equipment installation is progressing rapidly (Figs. 2 and 3).

Portions of the L-band equipment that could be used in the S-band system have been removed for quality control inspection and for modifications if needed. The L-band servo equipment was moved intact and reinstalled in less than 24 hr to provide antenna drive control for the cable and equipment work being performed thereon. The receiver has been assembled and interrack cabling is in process. Testing of digital instrumentation equipment is in progress with the use of representative tests provided by Scientific Data Systems. Other equipments are being installed as they arrive and are released by quality control.

Structural modifications to the transmitter and receiver cages are in progress on the antenna. Relocation of the receiver cage to the east side of the reflector is being effected to provide easier access to the equipment from

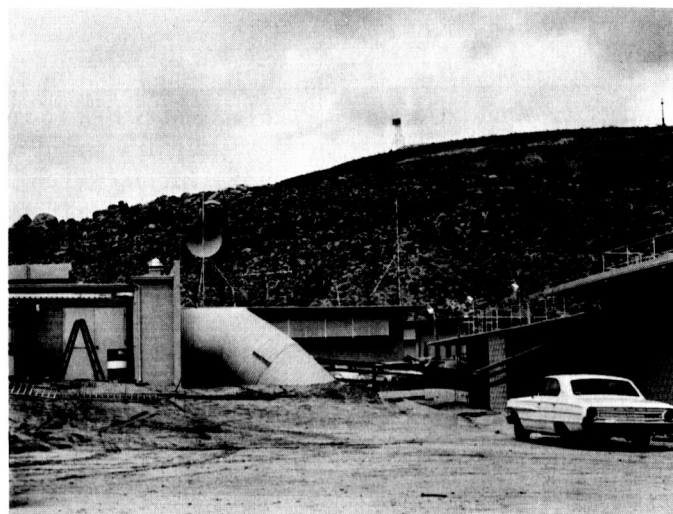


Fig. 1. Antenna side of the new wing showing the cable tunnel termination



Fig. 2. Antenna servo and receiver installation



Fig. 3. Digital instrumentation and analog instrumentation installation

the ground. No major structural changes are being made to the antenna because of the limited time remaining before Mars encounter.

3. Pioneer Project

a. Echo station. A room in the Echo station control building formerly used as a maintenance and office area, has been equipped with a raised floor for installation of the Pioneer project mission dependent equipment (Fig. 4). Personnel from Ames/NASA and Space Technology Laboratory have installed and conducted preliminary tests on three racks of equipment containing the telemetry data

extractor, the command controller, and the test data generator. The display and recording equipments are scheduled for installation in May.

The current equipment provides for the reception and processing of both engineering and scientific telemetric data from the spacecraft into the Echo computer and then to the SFOF at Pasadena. In addition, the command encoder, using the Echo computer for verification, will be interfaced with the Echo station transmitter for command transmission to the spacecraft. Two operations personnel from the Echo station attended a one-week school at Space Technology Laboratory and will operate and test

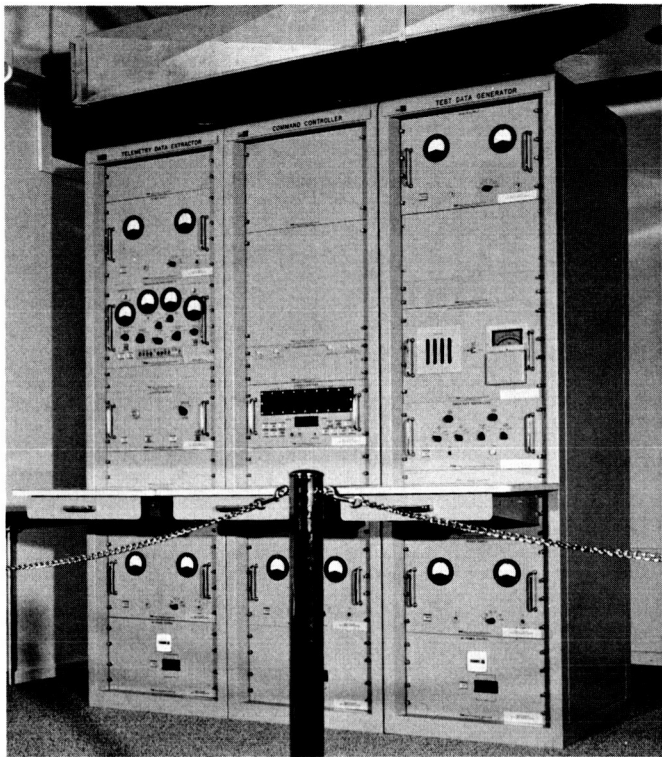


Fig. 4. Pioneer project mission dependent equipment installation

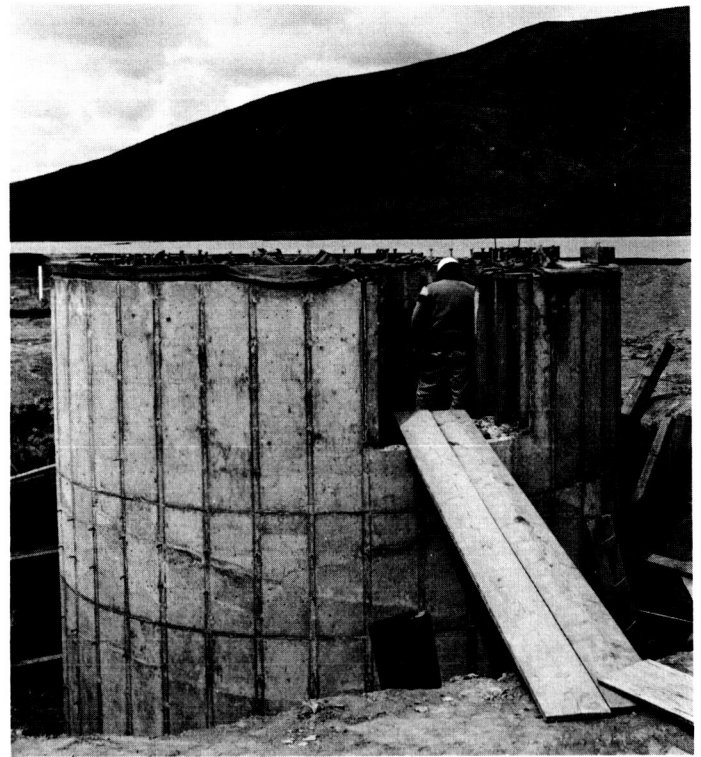


Fig. 6. View of 30-ft antenna base pedestal under construction

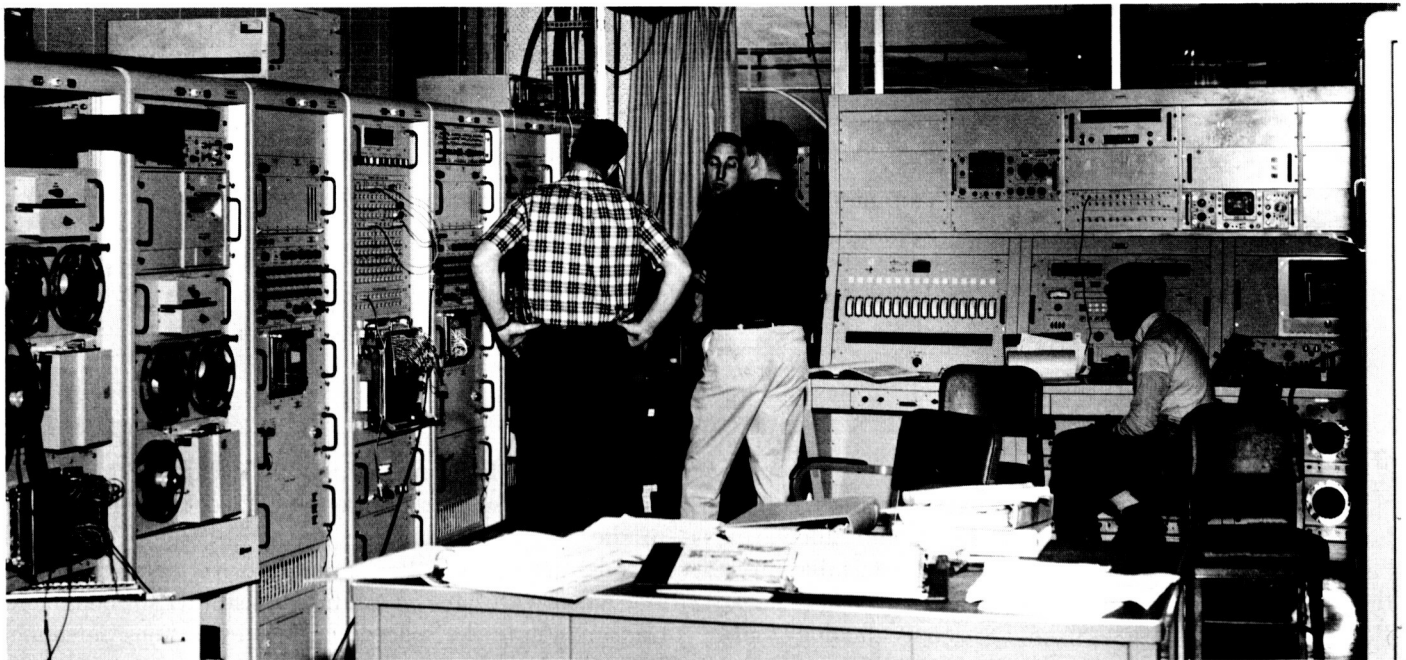


Fig. 5. Surveyor project ground control equipment installation

the equipment during the Pioneer missions. Full interface testing will be accomplished when the Echo S-band system is operational.

4. Surveyor Project

a. Pioneer station. The DSIF/Surveyor project compatibility tests were performed between Mariner tracking periods. These tests included (1) the initial testing of the FR-1400 recorder's capability of recording Surveyor low-level subcarrier oscillators, (2) leakage of the Surveyor transponder, and (3) command word error testing. Testing of the on-station data processing equipment interface is in



Fig. 7. Floor slab of the bulk stores building

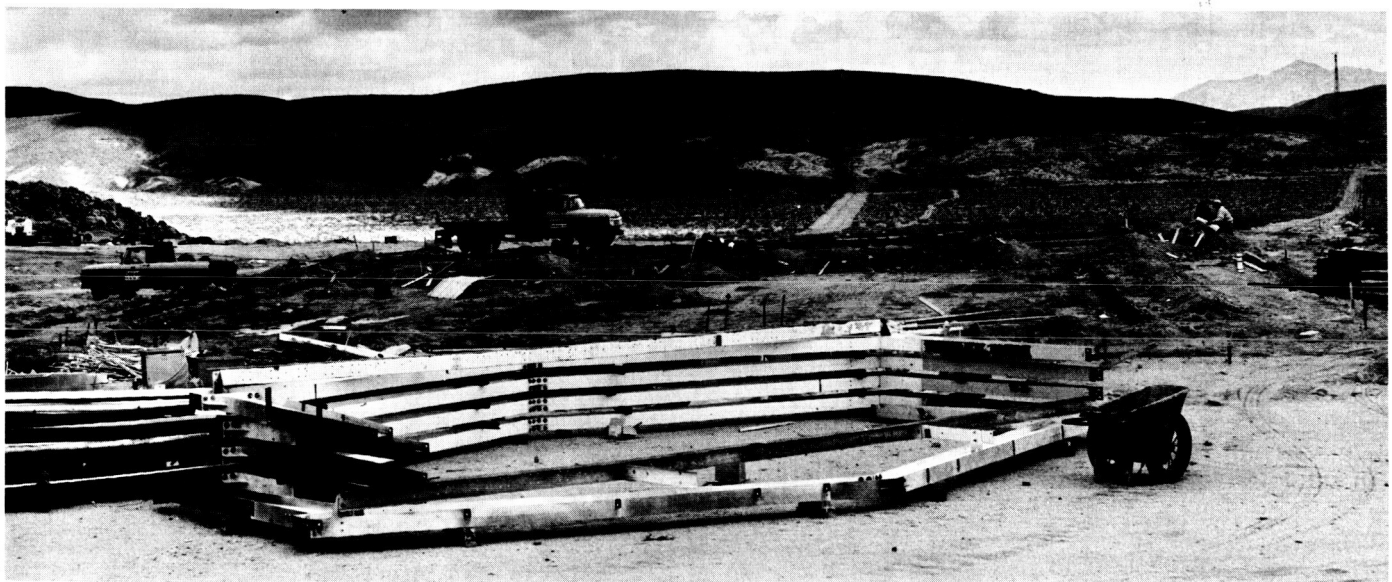


Fig. 8. Beginning construction of the warehouse building

progress. Fig. 5 illustrates equipment rack arrangement in the Surveyor control room.

5. Construction

a. Pioneer station. Fig. 6 illustrates the construction of the concrete pedestal for the 30-ft antenna to be installed at the Pioneer station. Work is progressing satisfactorily.

b. Echo station. Two prefabricated buildings of steel are being erected east of the transportation building and the generator building. The smaller building, 33 x 80 ft, will be used for bulk stores. The larger building, 94 ft on the front with 74- and 82-ft long sides, will be used as a warehouse. Figs. 7 and 8 illustrate the construction progress in mid-April.

C. Advanced Antenna System

1. Synopsis

A 210-ft D advanced antenna system (AAS) is being designed and constructed for the Mars site of the Goldstone space communications station. The operating frequency of the AAS will be at the S-band frequencies of 2.1 to 2.3 Gc.

The AAS is designed specifically for deep space communications and will be integrated with related systems and equipment of the Deep Space Instrumentation Facility (DSIF). Completion of the AAS, as an operational receiving station, is scheduled for June 1966.

Work progress has been reported regularly in the SPS, along with a series of discussions concerning major components of the system. The project continues to progress satisfactorily and indications are that the scheduled project completion date will be met. Figs. 9 and 10 are a comparison of the antenna construction as of April 6, 1965 and the model of the completed 210-ft AAS.

Component fabrication for the AAS structure and drives is nearing completion. Fabrication of the major structural components is complete except for the primary reflector surface panels and the feed cone. These two components are scheduled for completion in May 1965. Fig. 11 is a photograph of one of the elevation wheel trusses being fabricated at Rohr Corporation, Chula Vista, California.

The quadripod and subreflector of the AAS are being test assembled at Rohr Corporation, prior to shipment to the Mars site. All other fabricated components are on-site awaiting erection.

The antenna servo electronics have been fabricated, tested in plant, and shipped to the Mars site by Dalmo Victor Company, Belmont, California. All hydraulic equipment for the servo system has been installed on the AAS except brakes and drive motors. Installation of the servo electronics has begun. A discussion of the AAS servo and control subsystem follows.

The architectural and engineering work for the AAS structure is complete except for a number of minor items, the rotating stair, and cable wrapup. Fig. 12 shows the Mars site on March 29, 1965.

On-site erection of the elevation wheel assemblies is now complete and erection of the 210-ft D primary reflector structure has begun.

Procurement and fabrication activities are in progress for the DSIF electronic equipment, a precision angle data system (master equatorial), ancillary equipment, and inter/intrasite communications.

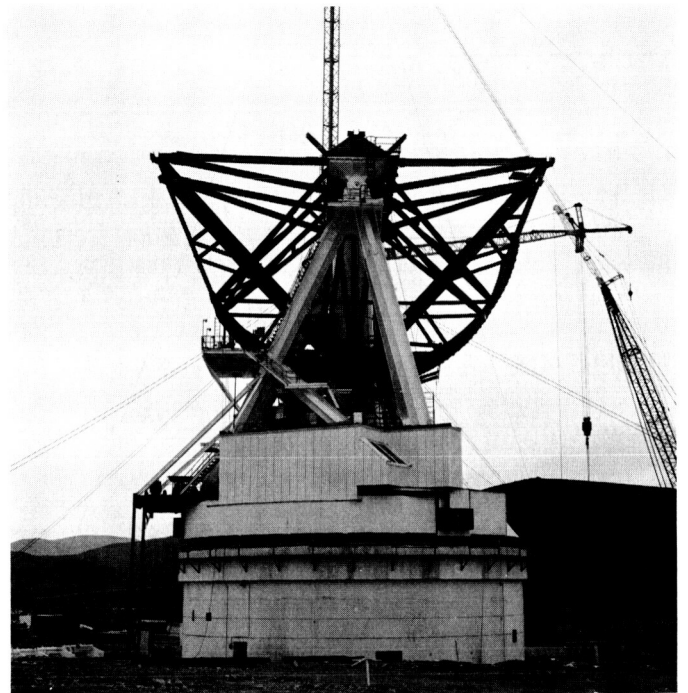


Fig. 9. Construction progress, April 6, 1965

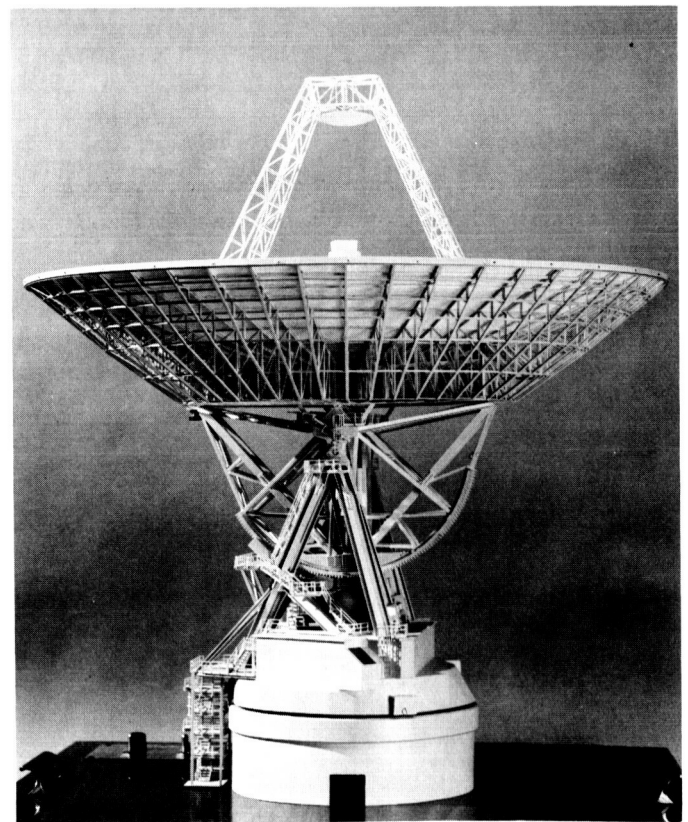


Fig. 10. AAS model



Fig. 11. Elevation wheel truss fabrication

2. Servo and Control Subsystem

The servo and control subsystem controls the motion of each axis of the antenna in all modes of operation. The design and fabrication of all of the assemblies is complete and the subsystem is being installed and tested at the Mars site. The Dalmo Victor Company has the responsibility for this component under a subcontract to Rohr Corporation.

There are four principal areas of design within this subsystem: the hydraulics, which supplies the power to drive the antenna; the electronics, which controls the use of the hydraulics; the analog data portion, which controls

the antenna beam position in certain modes of operation and provides a display of axis position; and the servo loop design, which is concerned with the stability of the antenna in all modes of operation.

The primary mission for the AAS is to track sidereal targets which are within 10 deg of the ecliptic plane. This requirement is the basis for the functional requirements of the servo and control subsystem. The controlling functional requirements are as follows: tracking accuracy of 0.01-deg 3σ in Precision I environment conditions; tracking rates of 0.2 deg/sec in both Precision I and II conditions; and acceleration of 0.1 deg/sec under Precision II conditions.

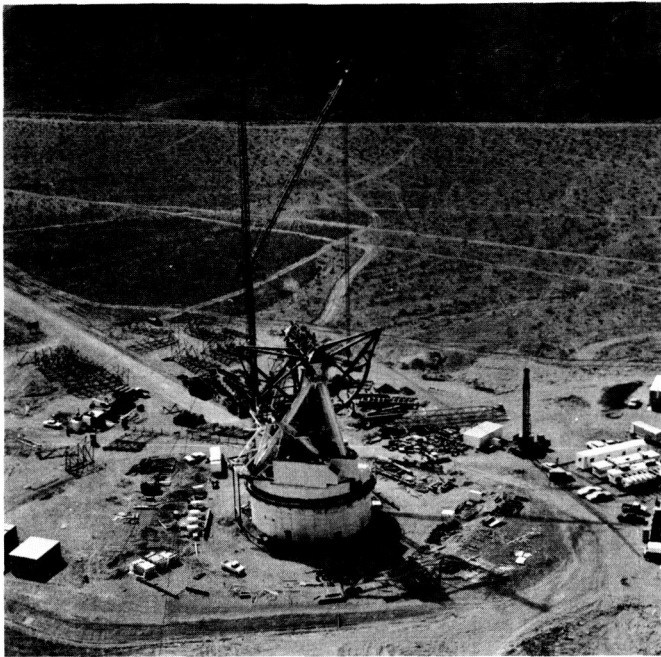


Fig. 12. Mars site, March 29, 1965

The velocity and torque requirements for the antenna drives are summarized in Table 2. The choice of the antenna drive system for the AAS was based on an extensive review of the available equipment and a predicted performance in this application. The particulars of the application include: a four-point drive to minimize gear

loads; wide bandwidth rate loop to increase stiffness to gusty wind loads; commercially available components with a known history of reliable operation; and low radio noise. These factors, plus the successful use of similar drives on the DSIF antennas, led to selection of a servo valve controlled hydraulic drive.

Hydraulic drive motors are used at each of the four drive points on each axis to control the antenna. Each motor will develop 30 hp at maximum load and maximum velocity. Under stall conditions, four motors acting together will develop 11×10^6 ft-lbs of torque, referred to the axis, which is more than is required to drive the antenna through any position in a 50-mph wind. These motors are especially selected for their low friction characteristics.

To control the 100-gal/min load flow required for each axis, two flow-control type servo valves will be used in parallel. These valves will be two stage with a flapper nozzle configuration for the first stage and a power spool for the second stage. They will have less than 90 deg of phase shift at 45 cps, and less than 2% null shift. The pressure gain of the valves will be approximately 10,000 psi/ma to reduce the deadband. The null pressure will be approximately 500 psi to improve the no load breakaway friction of the motors. The servo valves will be controlled by a valve driver using a current feedback loop to eliminate the phase shift due to the valve preamp coil.

Table 2. Torque summary

Item	Precision I	Precision II	Limit	Survival (any position)	Survival (zenith)
Wind velocity, mph	30	45	50	70	120
Axis velocity, deg/sec	0.5	0.2	0.1	—	—
Axis acceleration, deg/sec ²	0.2	0.1	0.05	—	—
Drive countertorque	Yes	Yes	No	No	No
Wind torque, ft-lb					
{ Az	1.85×10^6	4.16×10^6	5.16×10^6	10.1×10^6	3.4×10^6
{ El	2.12×10^6	4.77×10^6	5.9×10^6	11.6×10^6	22.7×10^6
Wind gust torque, ft-lb					
{ Az	0.595×10^6	1.33×10^6	1.65×10^6	2.24×10^6	—
{ El	0.68×10^6	1.53×10^6	1.89×10^6	3.76×10^6	—
Acceleration torque, ft-lb					
{ Az	0.356×10^6	0.178×10^6	0.089×10^6	—	—
{ El	0.314×10^6	0.157×10^6	0.079×10^6	—	—
Parasitic torque, ft-lb					
{ Az	0.20×10^6	0.20×10^6	0.20×10^6	—	—
{ El	≈ 0	≈ 0	≈ 0	—	—
Net on-axis torque, ft-lb					
{ Az	3.00×10^6	5.86×10^6	7.80×10^6	12.34×10^6	3.4×10^6
{ El	3.11×10^6	6.46×10^6	7.87×10^6	15.32×10^6	22.7×10^6

Two hydraulic power supplies are included; each is capable of developing 120 gal/min at 3000 psi. Each supply is powered by a 2300-v, 200-hp electric motor. A 300-gal/min precharge system is provided to prevent pump cavitation and to provide continuous full-flow filtration and fluid temperature control. Either power supply is capable of supplying the drive system for all normal mission requirements.

Stainless steel pipe and tubing are used throughout to insure the cleanest possible oil system. The servo valves and motors have extremely tight tolerances and 10μ filters are provided to prevent oil contamination.

A second motor is mounted at each drive point to provide torque to wind up the backlash in the gear trains. These motors are plumbed in opposing pairs with a fixed pressure across them so that the torque developed at one gear box input is resisted by an equal and opposite torque at the input of the second gear box. This torque level is set so that the antenna is never operated in the backlash region of the gear box until the wind velocity is above 30 mph.

The design of the servo electronics is based on the same modular concept that has been used on the antennas at Goldstone. This concept allows operational amplifiers, compensation networks, and relays to be interchanged or replaced easily in troubleshooting and routine maintenance.

The servo amplifier operates on the axis electrical error signals and develops the current signal to control the servo valve. Chopper stabilized, transistorized, operational amplifiers are used to insure low noise and minimum drift operation regardless of the operating mode.

The antenna servo control panel is the interface between the servo system and the human operator. This panel contains all the system stop-start controls, the operating mode selection pushbuttons, the tracking error meters, the secondary axis position readout displays, and the command controls for the secondary modes.

An interlock circuit is designed into the servo system so that the system is fail safe and cannot be operated when it is not safe to do so. The system will automatically shut down if a failure occurs in the hydrostatic bearing or servo hydraulic pumping systems, in the axis brake or gear

box lubrication system, or if there is any loss of power supply voltages.

The interlock system is complex for this antenna, and therefore, a system condition monitor or fault panel is provided to indicate to the operator the condition of the particular subsystem or components. This monitor is designed on a green board concept—if all indicators are green, the system is in a go condition, and if there is a red indicator the system is in a no go condition.

Data gear boxes are geared to each axis of the antenna. Pairs of synchro data pickoffs are geared to each of the data gear boxes and are cam compensated to correct for systematic errors in angular position. These synchros operate back to back with synchro pairs located in the antenna control panel. The position error signals from these synchros are used to command the antenna servo in the manual mode of operation and to provide an axis position display in all other modes of operation.

The purpose of the servo loop design is to insure that the antenna will have minimum tracking error in all modes of operation. The prime factors which effect the tracking error are the friction or deadband errors and the wind gust errors. The starting point of the servo loop design is the static and dynamic characteristics of the antenna mechanical and structural elements. The servo design is required to integrate the antenna characteristics with the servo electronics and the drives to meet the mission and functional requirements of the antenna system.

The position loop design has become standardized for the large antenna structures. A modified Type II servo system is used on all DSIF and Venus station antennas. A Type II servo system is characterized by the following: it has an extremely high dc gain which reduces the velocity lag error to zero and provides some attenuation of the acceleration lag error; it is inherently unstable and must be modified with lead-lag networks at the frequency band which is selected for closing the position loop. The selection of the frequency or bandwidth at which the loop is to be closed is based on the mode of operation. For low-noise error signals, such as those from a D to A converter or for high-level RF tracking signals, a high bandwidth such as 0.5 cps is used. For error signals containing a large amount of noise, such as RF tracking signals near the receiver threshold, a low bandwidth such

as 0.01 cps is used. The maximum bandwidth at which the loop can be closed is limited by the structural resonance and residual phase shift from the rate loop and the error signal detectors. Under ideal conditions when there is minimum residual phase shift, the loop can be closed at as high as one-half the structural resonance frequency.

To meet the functional requirement in the slave modes, the position loop bandwidth must be at least 0.2 cps, and it probably will be set at approximately 0.5 cps, which is a factor of 3 below the predicted 1.5 cps structural resonance frequency.

Since the design of the position loop is largely predetermined, the characteristics of the rate loop become very important for matching the antenna characteristics to the requirements. The goal of this design is a wide bandwidth loop, with no deadband and a high output impedance over the frequency range predicted for the wind spectrum.

The design bandwidth of the rate loop for the AAS is 15 cps. This is required even though the hydraulic resonance is approximately 1 cps. Since the hydraulic resonance contributes 180 deg of phase shift and would normally drive the loop unstable, lead-lag compensation is used to reduce the system phase at 15 cps so that the loop can be closed. Differential pressure feedback is presently used on some antennas to accomplish the same end; however, this technique has detrimental side effects which tend to increase the deadband and increase the tracking error.

To increase the torque stiffness, the drive point inertia will be increased from 1 times the reflected antenna inertia to 5 times the reflected antenna inertia. This will improve the characteristics of the rate loop by increasing the dc loop gain and by decreasing the pole-zero frequency spread of the reflected structural resonances. The only side effect will be that the frequency of the hydraulic resonance will be reduced; but, as noted above, the loop can be compensated for this effect.

In order to use a lead-lag network in the rate loop compensation, high performance dc tachometers are required. These tachometers are characterized by a high sensitivity and a low ripple content so that the output

signal can be differentiated over a frequency range of 5 to 50 cps regardless of the antenna velocity. One tachometer will be used at each drive point and the average taken for the feedback signal.

The loop design has been studied using both linear analysis techniques and a nonlinear analog computer study. In addition, the same techniques have been applied on the 30-ft D antenna at the Venus site. In all cases, the design has been verified and the tracking error has been less than $\frac{1}{2}$ the 0.01 deg specified for the AAS.

3. Feed for the AAS

Scale model tests of the feeds for the AAS consisted of examinations of results obtained with the feedhorns alone, the feedhorns and Cassegrain reflector combinations, and the secondary radiation patterns and gains of the Goldstone Venus 30-ft reflector.

Secondary radiation patterns of the 30-ft reflector were previously reported (SPS 37-30, Vol. III, pp. 110-115); in this summary recently available data on the reflector surface deflections are presented, and the correlation of predicted and measured patterns is discussed.

Recent work. The Goldstone Venus 30-ft reflector has, throughout 1964 and early 1965, provided a nominally true paraboloid at zenith attitude; this was accomplished by adjusting panel attach points on the backup structure while observing, with a centrally located theodolite, 160 datum targets located at 5 radial stations, one pair per station on each of the 16 inner and outer reflector panels. Fig. 13 is a photograph of the antenna, showing the mechanical characteristics of the reflector surface. During the adjusting period, February 1964, inclement weather precluded an exact setting of the panels. An exact setting is defined to be better than 0.005 in. RMS, for the targets, caused by measurement uncertainty. A second survey conducted during August 1964 proved the zenith attitude surface to be approximately 0.012 in. RMS for the targets, hence the term nominally true paraboloid at zenith.

During January 1965, using an all-attitude theodolite centrally located as before, the 160 datum targets were read with the reflector oriented to the horizon attitude, important inasmuch as collimation tower data are obtained in this position. In addition, a completely inde-

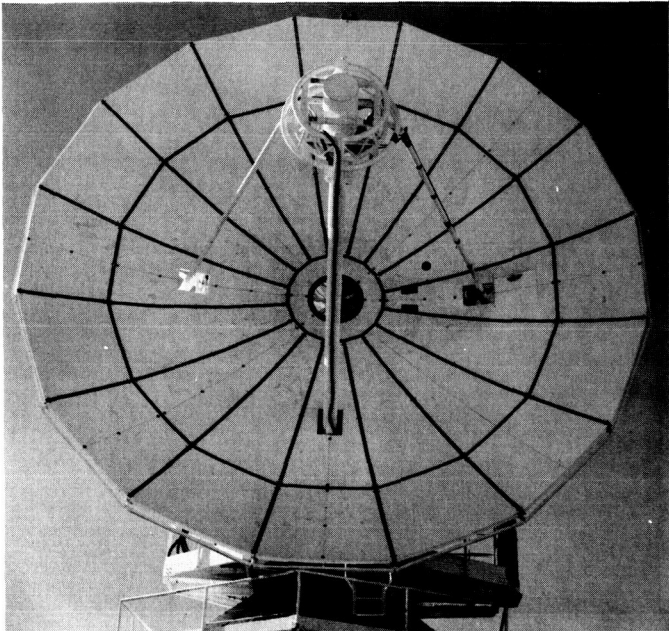


Fig. 13. Panel layout, 30-ft reflector

pendent survey utilizing two theodolite triangulation from the ground was conducted (*SPS 37-31*, Vol. IV, A. Ludwig, p. 285); the results of the two methods were found to be generally in agreement.

Fig. 14 shows the complete map of horizon-look deflections from the best-fit paraboloid as determined from the IBM 7094 RMS program, based on the 160 target locations. Because Fig. 14 is somewhat complex by including, for example, the inexact settings at zenith mentioned above and the one damaged panel attach point, Fig. 15 was prepared and is considered suggestive of optimum horizon-look deflections from a best-fit paraboloid assuming a perfect surface at zenith. Figs. 14 and 15 are calibrated in terms of one-half RF pathlength, a parameter useful for pattern analysis and results from electromagnetic reflection at the surface; the actual mechanical deformations parallel to the axis are somewhat larger and are a function of angle subtended from the focus

$$dZ = 2 \frac{\text{One-half RF pathlength}}{1 + \cos \psi}$$

The most divergent half pathlengths ± 0.045 in. at the rim, therefore, represent ± 0.06 in. mechanically, from best-fit. The symmetry of mechanical deflections, particu-

larly the zero contours in Fig. 15, is good. The horizontal symmetry is better than the vertical symmetry, a result of the fact that gravity is acting symmetrically on the structure for a plane through the horizontal but asymmetrically for a plane through the vertical.

Figs. 14 and 15 were prepared as an intermediate step to arrange deflection data as input to the IBM 7094 Radiation Pattern Program. Consequently, the aperture was divided in an (r, β) coordinate system consisting of a 27×112 matrix. A value of 27 radial subapertures was selected on the basis of maximum machine capacity; 112 azimuthal divisions were selected to yield approximately square subapertures sufficiently small to include quadripod shadowing accurately and at the same time providing an integral number of subapertures per panel. Deflection data from the 160 targets were linearly interpolated, on a panel-by-panel basis, for each of the 32 panels. Because each panel is represented by only 4 to 6 targets, the linear interpolation is strictly accurate for only perfectly manufactured panels; thus, the maps and linearized deflection data do not include either the panel manufacturing error or the deflection within individual panels. The best-fit RMS of one-half the full RF pathlength of the 160 target locations is 0.023 in. Assuming perfect environmental conditions and the manufacturer's stated panel accuracy of 0.019 in. RMS, the overall horizon look surface is about 0.031 in. RMS. Indications are that the manufacturer is conservative, i.e., the actual panel accuracy is expected to be 0.010–0.019 in. RMS, effecting 0.026–0.031 in. RMS overall, for perfect conditions.

Figs. 16 and 17 compare computed and measured far field radiation patterns using an optical blocking model of the quadripod shown in Fig. 13. These measured patterns were presented in *SPS 37-30*, Vol. III and are repeated for comparison. Computed patterns utilize experimentally determined feed amplitude and phase data as presented in *SPS 37-32*, Vol III, p. 74, and the surface irregularities in Fig. 14. It is clear in both Figs. 16 and 17 that the general features of near-in null-filling and overall shape agree; however, the measured levels are generally higher in amplitude, indicating the experimental surface is either generally like Fig. 14 but with greater pathlength deviations or that the experimental surface has imposed on the deviations shown in Fig. 14, additional deviations of either a random or ordered nature or a combination of both. Because Fig. 14 assumes perfectly manufactured panels as mentioned above, it is evident that additional information is required on the panel accuracy if gain and pattern predictions are to be improved.



Fig. 14. Complete map, 30-ft reflector

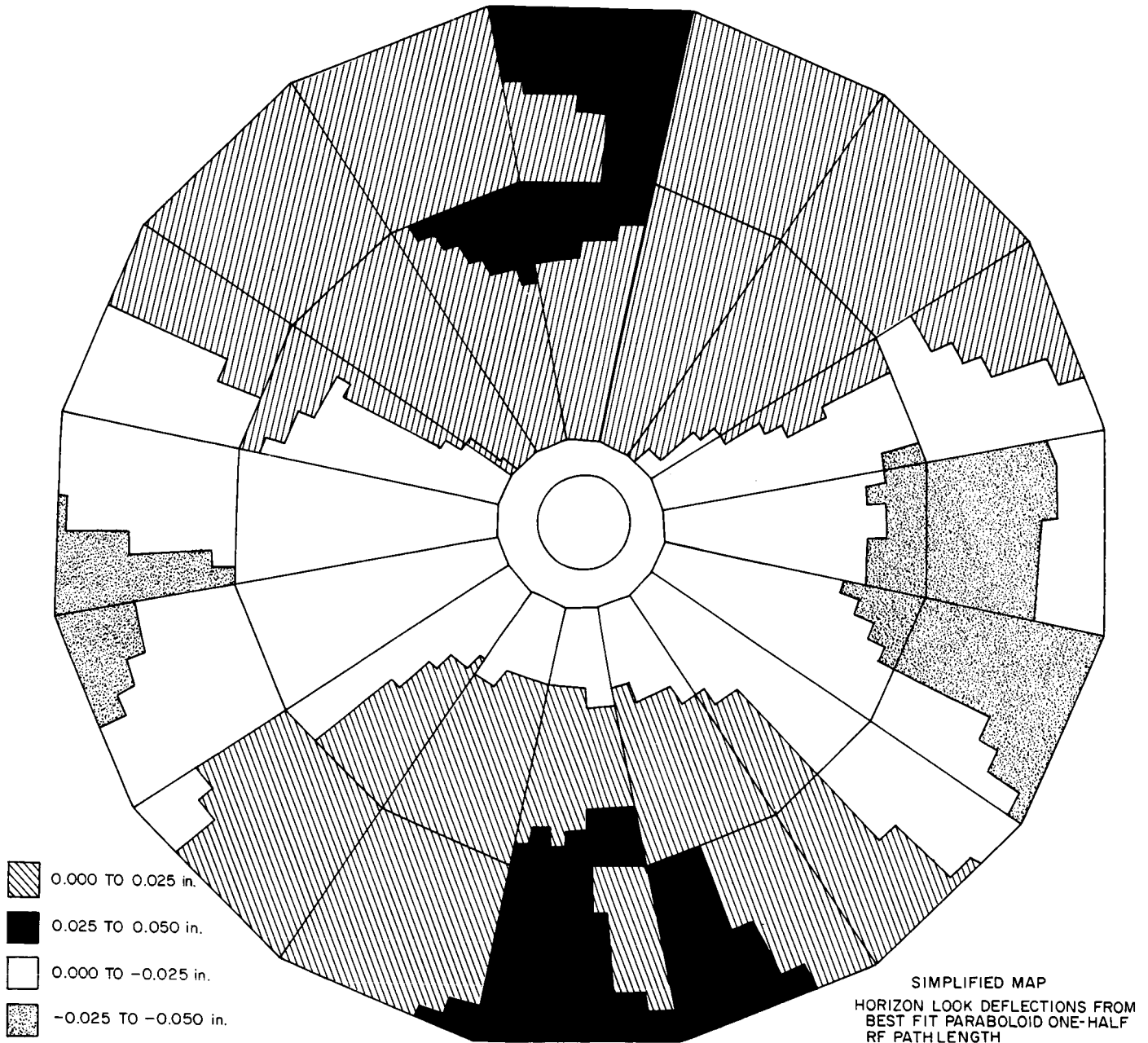


Fig. 15. Simplified map, 30-ft reflector

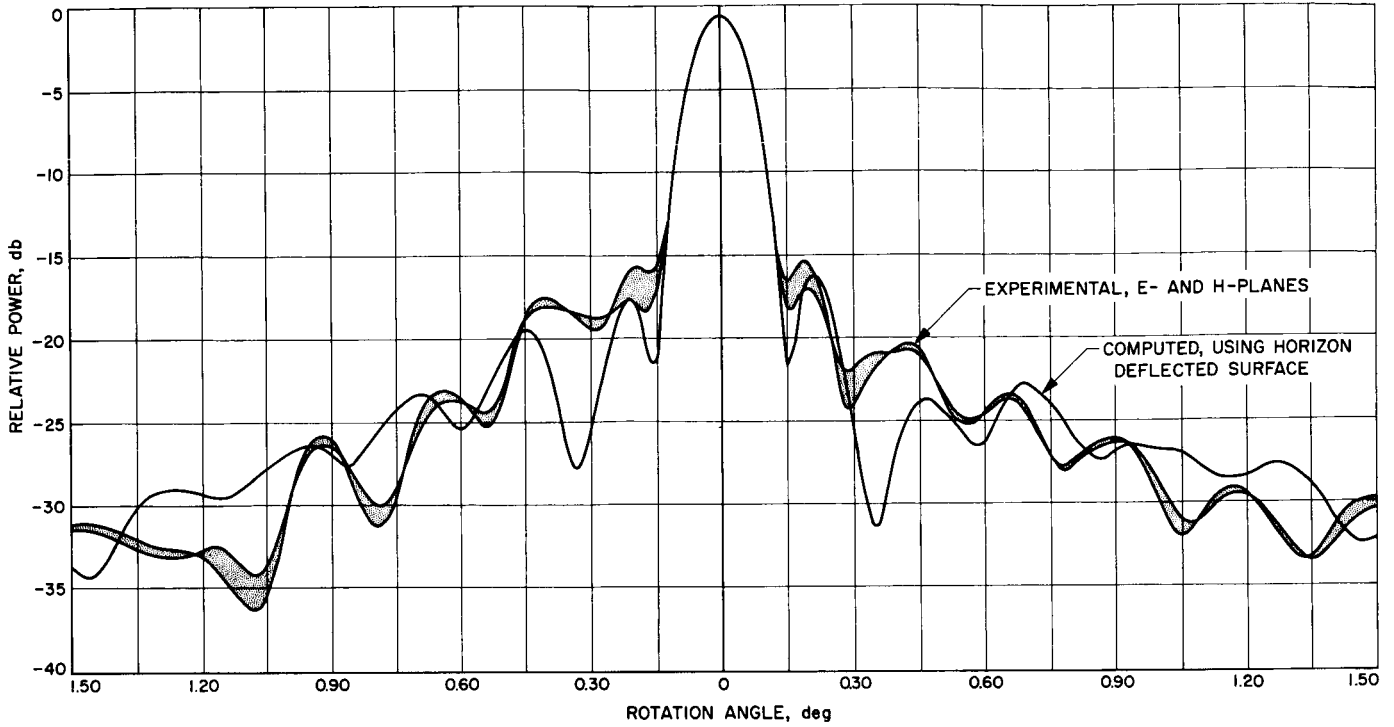


Fig. 16. Azimuth patterns, 30-ft reflector, 16330 Mc, dual mode feed

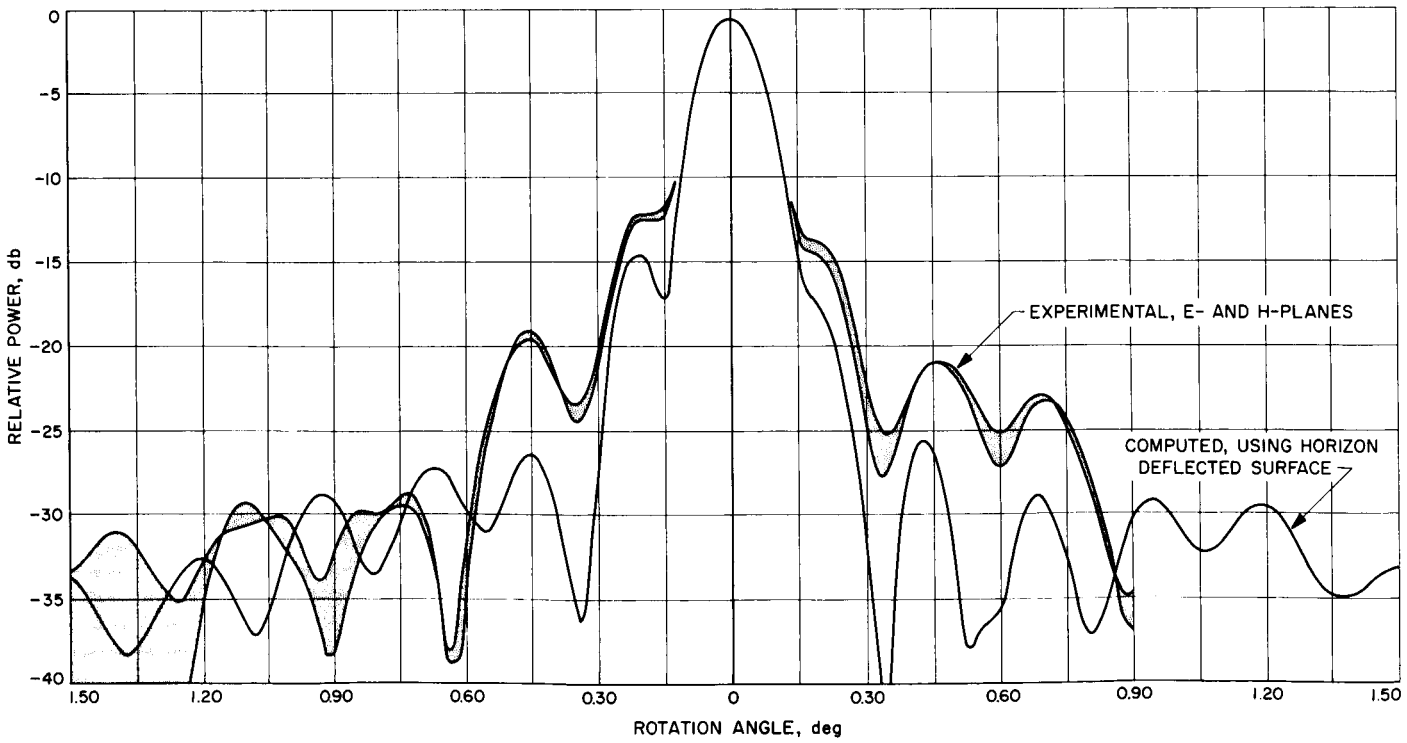


Fig. 17. Elevation patterns, 30-ft reflector, 16330 Mc, dual mode feed

D. Performance of the DSIF Tracking Data Monitor Program During *Rangers VIII* and *IX*

The tracking data monitor (TDM) at Goldstone has two primary objectives: (1) monitoring of Deep Space Instrumentation Facility (DSIF) tracking performance during a mission; and (2) developing new techniques for monitoring future DSIF missions. The program is written

in symbolically coded machine language for the 8192 word (24 bit) Scientific Data Systems 920 computer. Its principal inputs are (1) real time teletype or near real time punched cards of the standard DSIF format which includes station number, time, data code, and doppler data; and (2) magnetic tape with predicted doppler shift. The program extracts the noise from the doppler input, computes statistics on the noise, then outputs a plot (Figs. 18 and 19) and a printout (Figs. 20 and 21) of noise residuals and computed statistics.

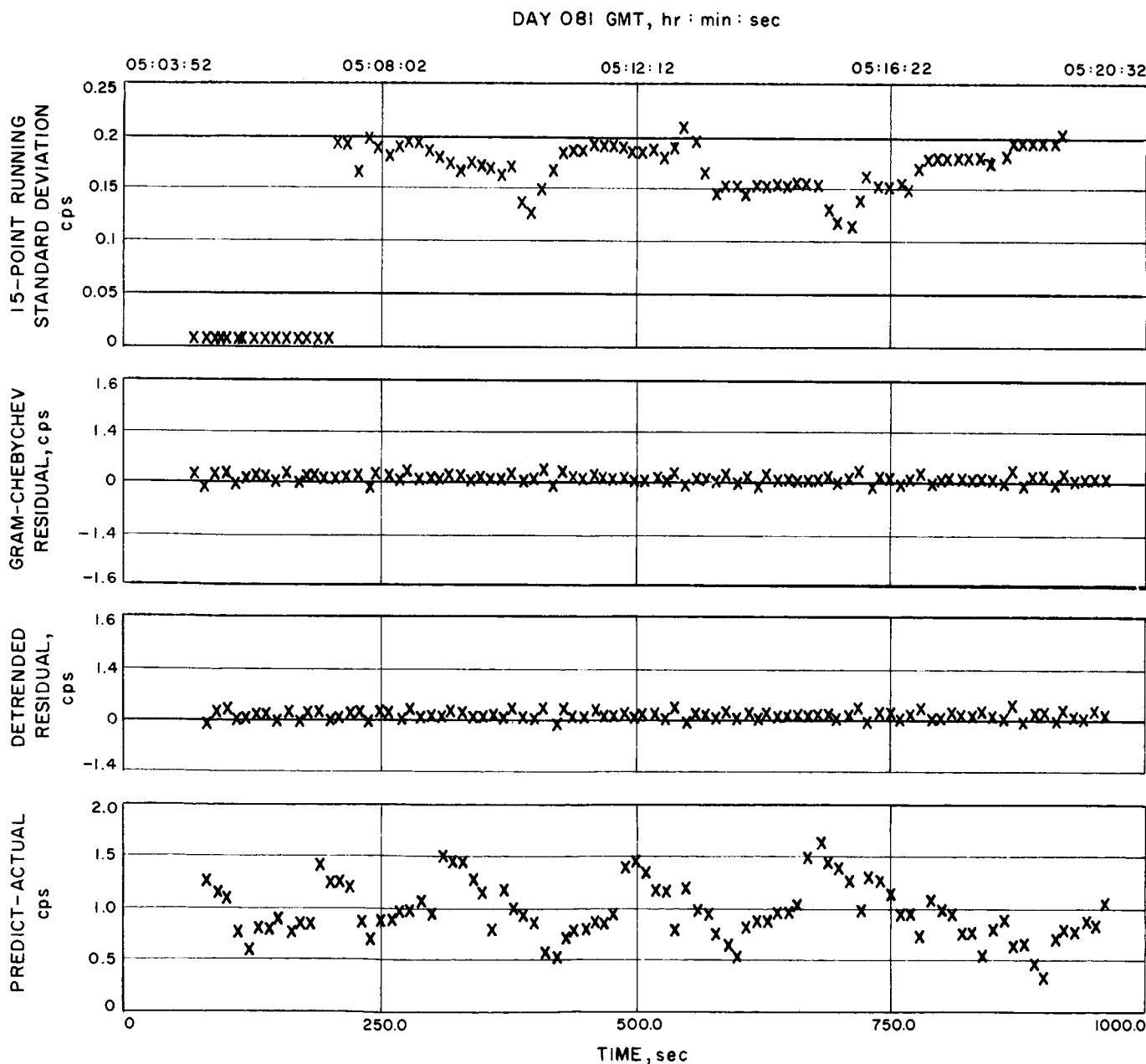


Fig. 18. Typical *Ranger IX* output plot

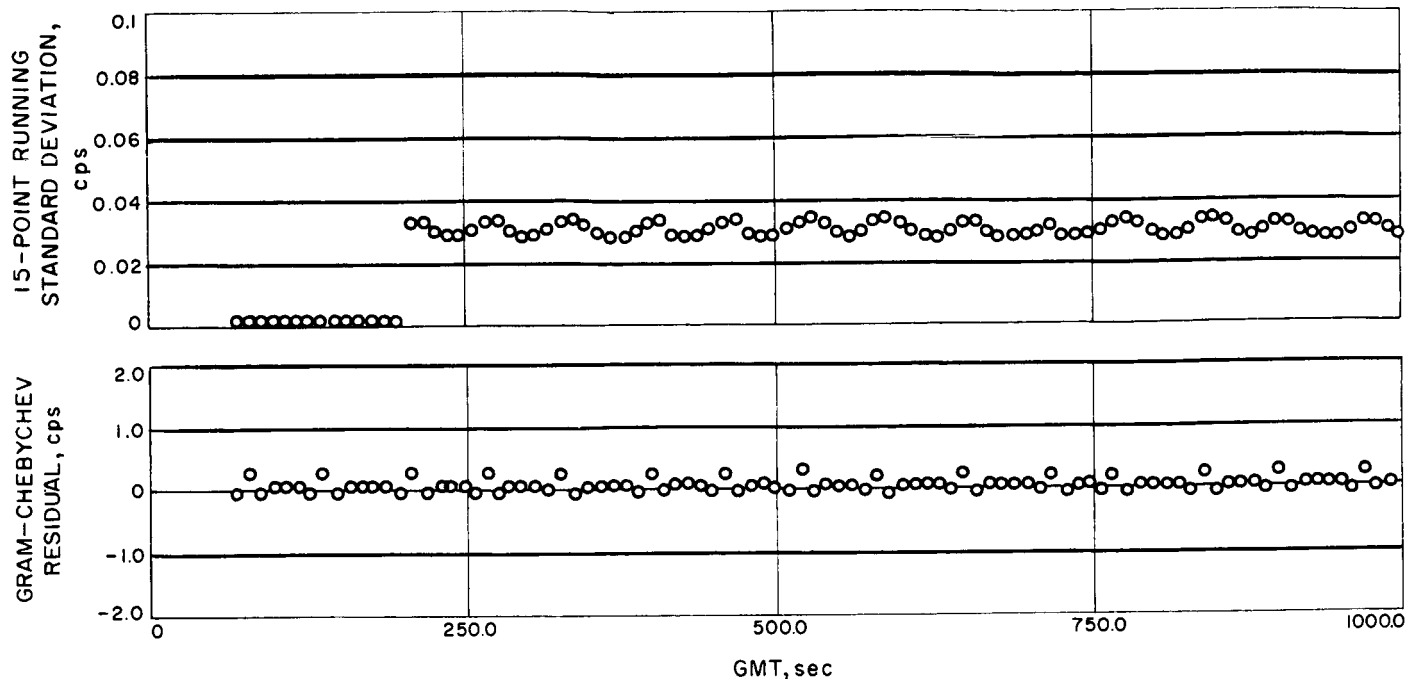


Fig. 19. Typical Chebychev roundoff domes

Current TDM usage checks: (1) the doppler input signal for bias to see if frequency and time are correct; and (2) the noise residuals for station performance. A voice link with the space flight operations facility (SFOF) at JPL gives information on possible problems and allows the complete SFOF facilities to be used for guidance and assistance.

The inclusion of a Gram-Chebychev technique for noise extraction was a significant improvement made between *Rangers VIII* and *IX*. It is typical of the development advancements made to the TDM in the past. The eventual goal is to develop a real time, automatically operated program, which performs as complete an analysis as can be programmed into the machine. The program must be readily revisable and as nearly self-explanatory as possible.

The primary input data are generated at the DSIF station and converted to Baudot code, then teletype transmitted to the computer facility and punched on paper tape in Baudot code. The paper tape is then converted to decimal punch cards which are input to the computer. The program has the capability of using either continuous count or destructive count doppler input data.

The predicted doppler shift is written on a magnetic tape in a binary format by a geocentric trajectory program. Generation of this tape is done between launch minus 10 min and launch plus 20 min when DSIF teletype data begin arriving.

There are also 21 input parameters which include start time, sample time, magnetic tape prediction information, plot scaling parameters, and several parameters to change the statistical method and a number of points in the statistics. These parameters are input one per card and control the usage of the program. They allow great flexibility in data type, calculation procedures, and output.

Before discussing the noise extraction methods, several terms should be defined. Running standard deviation is defined to be the standard deviation of the last N (normally 15) points. Bias is defined to be the deviation of the mean from zero. Doppler noise estimation in the program is accomplished by four numeric methods. In order to establish common parameters, the nondestructive (continuous) count is differenced and converted to cycles per second (doppler shift plus 100,000 cps bias) before the noise estimate takes place.

The first and simplest of the four detrending or noise extraction methods is to difference the 1-sec doppler with a predicted value (from a geocentric trajectory program).

RANGER TRACKING DATA MONITOR

PARAMETERS

! TS ...+10.0000
 ! EPOK ..+18232.0
 ! T1ST ..+18232.0
 ! ALPHA +1.00000
 ! NPIK ..+0.00000
 ! KMAX ..+10.0000
 ! NK+0.00000
 ! TRESIG.+1000.00
 ! STATNR+15.0000

51	081	050402	8040		GBC NOT READY					117628.699	
51	081	050412	8040		GBC NOT READY					117627.799	
51	081	050422	8040		GBC NOT READY					117626.599	
51	081	050432	8040		GBC NOT READY					117625.500	
51	081	050442	8040		GBC NOT READY					117624.399	
51	081	050452	8040		GBC NOT READY					117623.500	
51	081	050502	8040	.000000	.000000						
1.00000	OVERFLOW	OVERFLOW	OVERFLOW	OVERFLOW	OVERFLOW	OVERFLOW	OVERFLOW	OVERFLOW	OVERFLOW	OVERFLOW	
1.00000	.000000	.000000	.000000	.000000	.000000	.000000	.000000	.000000	.000000	.000000	
.100002288	.100000858	-.000000476			.099609	.099853	.130950	117622.199		1.160517454147	
51	081	050512	8040	.000000	.000000						
1.00000	-.384384	OVERFLOW	OVERFLOW	OVERFLOW	OVERFLOW	OVERFLOW	OVERFLOW	OVERFLOW	OVERFLOW	OVERFLOW	
2.00000	1.00000	.000000	.000000	.000000	.000000	.000000	.000000	.000000	.000000	.000000	
-.400000095	-.400000095	.200000762			-.199462	-.499755	.455200	117621.199		1.208929061889	
51	081	050522	8040	.000000	.000000						
51	081	050732	8040	-.013473	.188659						
1.00000	-.418853	-.421127	.316482	.177627	-.277389	.124176	.062896	-.455352	.738586		
16.0000	15.0000	14.0000	13.0000	12.0000	11.0000	10.0000	9.00000	8.00000	7.00000		
.100000858	.099999427	-.199999809			.000244	.107177	.304443	117606.199		1.136928558349	
51	081	050742	8040	.026538	.162872						
1.00000	-.367324	-.425201	.263397	.198287	-.217376	.031890	.148620	-.510040	.705688		
17.0000	16.0000	15.0000	14.0000	13.0000	12.0000	11.0000	10.0000	9.00000	8.00000		
.200001239	.199999809	.199999809			.011230	.199707	.303222	117605.000		.8165140151977	
51	081	050752	8040	-.006801	.194580						
1.00000	-.392211	-.399383	.265762	.219894	-.233947	-.044738	.265472	-.564514	.729064		
18.0000	17.0000	16.0000	15.0000	14.0000	13.0000	12.0000	11.0000	10.0000	9.00000		
-.399999618	-.399999618	.000000000			-.011474	-.411376	.321807	117604.000		.6398248672485	
51	081	050802	8040	-.013442	.184844						
1.00000	-.465164	-.331893	.278106	.180099	-.249786	-.010986	.281860	-.594116	.747024		
19.0000	18.0000	17.0000	16.0000	15.0000	14.0000	13.0000	12.0000	11.0000	10.0000		
.200001239	.199999809	-.199999809			.000244	.211425	.323516	117602.899		.8616278171539	
51	081	050812	8040	.006557	.179290						
1.00000	-.437484	-.371810	.295867	.189208	-.256103	-.025619	.286224	-.549575	.670074		
20.0000	19.0000	18.0000	17.0000	16.0000	15.0000	14.0000	13.0000	12.0000	11.0000		
.100000858	.099999427	.199999809			.004394	.099609	.316955	117601.799		.8489298820495	
51	081	050822	8040	-.000114	.185180						
1.00000	-.439392	-.400497	.374954	.131866	-.269531	.002731	.299285	-.542694	.582489		
21.0000	20.0000	19.0000	18.0000	17.0000	16.0000	15.0000	14.0000	13.0000	12.0000		
-.199997901	-.199999332	-.100000381			-.004638	-.204589	.313171	117600.799		.9355115890502	

Fig. 20. Actual tracking data monitor printout

Station #	Day #	Time	Data Code	Running Mean	Running Standard Deviation
51	081	050852	8040	.006572	.183227

Ten Correlation Coefficients (in order normalized).

1.00000	-.455474	-.321395	.367660	.006332	-.145172	.003279	.218368	-.475128	.529632
23.0000	23.0000	22.0000	21.0000	20.0000	19.0000	18.0000	17.0000	16.0000	15.0000

Number of Lagged Products in the Correlation Coefficient Above.

.000001430	.000000000	-.099999904	.000244	-.000244	.306945	117597.500	.8909351825714
First Detrended (Gram-Chebyshev) Residual	Second Detrended (Modified Gram- Cheby) Residual	Third Detrended (Method 2) Residual	Mean of All Data	Residual Less Mean	SD of All Data	CPS Doppler Count From Raw Data	Predicted Doppler Less Actual Counted Doppler

Fig. 21. Tracking data monitor printout key

If the predictions are of good quality, the bias on the residuals will obviously be quite small.

The second detrending method assumes the data can be approximated over short intervals by a second order polynomial of the form

$$\text{Doppler} = A + B \cdot t + C \cdot t^2$$

The coefficients are not computed, instead the residual is computed directly. When operating on five residuals at a time, it computes a residual as follows:

$$r(t) = y(t + 2\alpha) - y(t - 2\alpha) - 2[y(t + \alpha) - y(t - \alpha)]$$

In practice, the difference period α is taken as the tracking data or counter sampling rate (i.e., 5 consecutive points are used to make the residual) to

$$r(t) = y(t + 2) - 2[y(t + 1) - y(t - 1)] - y(t - 2)$$

In practice, we find that, although this method has several faults, it detrends very well. It was used to calculate the running standard deviation and autocorrelation coefficients during the *Ranger VIII* mission.

The third detrending method is that of simple forward differencing. The same assumption made previously, i.e., the second derivative (difference), a constant, is used so that our residual is given by

$$r(t) = y(t) - 2[y(t + \alpha)] + y(t + 2\alpha)$$

and, again α is set to the sampling rate for normal practice. The simplicity of this technique makes this the standard of comparison as well as the easiest to hand calculate when a check is desired.

The fourth detrending method, a Gram-Chebyshev five-point polynomial fit, was developed just prior to the *Ranger IX* mission and was used for the mission. This technique is still in the developmental stage and will be extended to include prediction of the next point. It passes a second order polynomial through the last five-points and computes the residual directly by

$$R(t - 2) = \bar{y} - \frac{2}{7}[y(t - 4) + y(t)] + \frac{1}{7}y(t - 3) + Y(t - 1) - \frac{5}{7}y(t - 2)$$

Where

$$\bar{y} = \text{arithmetic mean of } y(t), Y(t-1), \dots, y(t-4)$$

This technique produces excellent results and consequently the running standard deviation and autocorrelation calculations were modified for *Ranger IX* to use the noise residuals computed by this method. One very nice feature of this method is that roundoff can be recognized on the noise and running standard deviation plots by the characteristic dome shown in Fig. 19, thereby allowing better data interpretation.

Present program operation does not use data which are in any way abnormal. Generation of statistics is stopped when the receiving mode is altered, a time skip is encountered, an undecipherable card is found, an error is found, or when any other abnormality occurs. A complete restart is required except for a time skip, an error discovery, or undecipherable cards. The autocorrelation table is kept when a time skip, an error discovery, or an undecipherable card is found, but complete detrender and running standard deviation tables must be filled before the autocorrelation table begins filling again. Many of the teletype errors are recognizable, so some programming has now been done on better usage of all the data.

The statistics calculated by the previously listed methods are output on a 30- \times 30-in. Benson Lehner point plotter, accurate to four digits. Although the autocorrelation graph is not shown, Fig. 18 is a typical TDM plot. Interpretation of the running standard deviation plot can determine periodic noise fluctuation and give excellent trends for noise increase or decrease. Interpretation of the Gram-Chebyshev and differential residuals is difficult because a particular residual is influenced by several others (in the detrending process). The lower plot, or predicted minus actual, gives excellent information on noise levels and complex roundoff patterns.

The printout (Fig. 20) corresponding to the plot in Fig. 18 gives many additional parameters for interpretation in special cases, such as very early or late in the trajectory when the assumption that doppler can be approximated by a polynomial $Y = A + B \cdot t + C \cdot t^2$ does not hold. Note that time in Fig. 20 is not continuous; there is a 13-point skip between 05:05:22 and 05:07:32. This was done to show initialization and later calculation. The key in Fig. 21 can be used for interpretation of Fig. 20.

When the TDM is used for data analysis in real time, the principal output of the program is a plot of residuals

(three types), the standard deviation of the last N (normally 15) points, and the first 10 autocorrelation coefficients. Fig. 18 is a typical plot from *Ranger IX* which, although lacking the autocorrelation coefficients, shows very nice numerical truncation effects in the observed minus predicted doppler plot. Interpretation of autocorrelation and standard deviation reveals periodicities. Interpretation of residuals and standard deviation give noise levels, change in noise levels, and residual pattern (i.e., if due to single bad points, etc.). When combined with direct voice line communication, analysis of the data reveals midcourse motor event time, magnitude and direction of midcourse change, abnormal spacecraft position and velocity performance, and abnormal DSIF station performance.

The best way to illustrate the operation of the TDM during the *Ranger VIII* and *Ranger IX* missions is to give examples. During the *Ranger VIII* midcourse maneuver DSIF tracking data were monitored as near real time as teletype operation allowed. This included confirmation of timing for pitch and roll, confirmation of midcourse event time, and evaluation of magnitude and direction of velocity change. During the first pass of *Ranger IX*, the Johannesburg station experienced very high noise data. Immediate evaluation led to a change of the rubidium standard, which seemed to fix the problem.

The *Ranger VIII* and *IX* missions gave an opportunity to learn a great deal more about what necessary and desirable changes could be made to the TDM program. The biggest problem has been the resolution of bad data caused by bad teletype transmission, counter skip, data formatting, etc. Two approaches to the problem are being developed for inclusion.

The first approach is simply to interpolate over the missing interval. Interpolation works in many cases, but long intervals are impossible to handle. In the practical case, interpolation over more than one skip destroys data integrity. In addition, if an interpolation has been made recently (last 5 points) and another must be made, proper interpolation is impossible.

The second approach is a search and recovery of essential information from the data card and inclusion of recovered data into the statistics. The principal problem with this method is that automatic operation without operator decisional interruptions is difficult to achieve for irrecoverable errors.

In practice, a combination of these two techniques has proven highly effective in exploratory programs. The newly developed data recovery procedures, including a direct Baudot alphabetic to numeric substitution, are being included in a Fortran tracking data monitor program, as well as interpolation and extrapolation with Gram-Chebyshev, least squares polynomial, and a sequential estimation (Kalman filtering) polynomial. A combination of these methods gives an accurate prediction of missing or unresolvable doppler.

Since its inception, the TDM has become more flexible and more complex. Its present configuration allows many options but still allows addition or modification of new statistical methods. Although a good deal of operator training is required to run the TDM at present, it does a good job of near real time tracking data evaluation. Future development will make the TDM easier to run and faster as well as capable of more complete analysis.

E. Random Numbers and Their Generation

Most noise and error input signals occurring in practical electrical systems vary in a random manner with respect to time; sequences of random numbers, therefore, can be used to simulate the random nature and consequences of noise and errors in a system. There exist some simple and efficient techniques suitable for generating these sequences.

Although a computer such as the Scientific Data System's (SDS) 920 displays in all its operations a systematic nature, there exists a concise and convenient method for generating a sequence of random numbers. Thus, for every random variable x_n , let $F(X)$, the cumulative distribution function, exist such that $F(X) = P(x_n \leq X)$ where P is the probability of occurrence. Then by definition

$$F(-\infty) = 0$$

$$F(\infty) = 1$$

$$X_1 \leq X_2 \rightarrow F(X_1) \leq F(X_2)$$

Now if x_n is a continuous random variable, then the continuous probability density function is $f(X) = dF(X)/dX$ having the following properties.

$$f(X) \geq 0$$

$$\sum f(X) = 1 \quad \text{If } x_n \text{ is a discrete random variable}$$

$$\int_{-\infty}^{\infty} f(X) = 1 \quad \text{If } x_n \text{ is a continuous random variable}$$

Therefore, let N belong to the integers such that N is greater than one. If x_n belongs to the real positive numbers between zero and one; and if $Nx_n = x_{n+1}$, then x_{n+1} is a sequence and it is uniformly distributed between zero and one. The validity can be shown by

- (1) A frequency histogram to show the sample distribution to be uniform.
- (2) That x_n , belonging to the sequence x_{n+1} , is statistically independent—let R equal the correlation coefficients.
 - (a) If R is large, associativity is high.
 - (b) If R is small, associativity is low.
 - (c) And R should be independent of the unit in which the variable is measured.
 - (d) Therefore, to achieve the properties of a , b , and c , let

$$R_x(j) = \frac{1}{(N-j)} \sum_{i=1}^N x_i x_{i+j} \quad \text{where } j = 0, 1, 2, \dots$$

which is the autocorrelation function and the normalized form is

$$\Psi(j) = \frac{R_x(j)}{R_x(0)}$$

These sequences are generated by the SDS 920 computer as follows: The A register is filled with "N," the largest possible odd power of three or five; then multiplying this number in the A register by 2^{-23} or the smallest possible number "XO" scaled at bit 23. Now the fractional result is found in the B register. This value in the B register is the new fraction which will multiply

N next time and is the first random number. The command sequence is

```
LDA N
MUL XO
CLA
RSH 1
XAB
STA XO
```

To show the aforementioned characteristics of a random sequence, one thousand numbers were generated and shifted to lie between ± 0.5 . Fig. 22 shows the autocorrelation function, and it is readily seen that the numbers are uncorrelated. Fig. 23 gives the results of the distribution function which reveals uniform distribution.

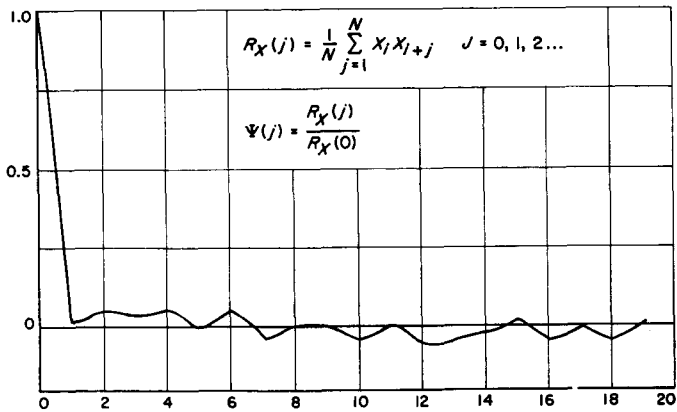


Fig. 22. Normalized autocorrelation of 1000 numbers

Thus, the members of the supposed time series are statistically independent and uniformly distributed over the interval.

Other rectangular distributions can easily be found by multiplying by a scale factor and adding a bias. From the central limit theorem of statistics if a population has a finite variance σ^2 and mean μ , then the distribution of the sample mean approaches the normal distribution with the variance σ^2/n and μ , as a sample size n increases. In short, the average of x_n from any distribution approaches the Gaussian distribution as N becomes large. Thus, we see a Gaussian sequence that can readily be formed from one of the above rectangular sequences.

The type of output desired, fixed point, floating point, single precision, or double precision, can readily be made available by the user. The author worked in floating point double precision and single precision fixed point with excellent results.

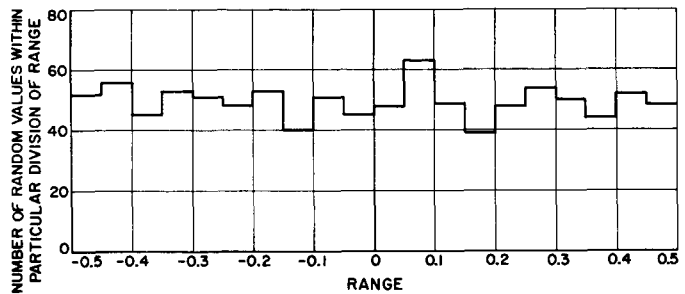


Fig. 23. Sample distribution of 1000 random numbers

III. Communications Engineering Developments

A. S-Band Implementation for the DSIF

1. *Traveling Wave Maser for the DSIF*

A maintenance schedule has been prepared for the closed-cycle refrigerators (CCR) in the DSIF. The objective of the schedule was to optimize the *Mariner IV* tracking mission. Final servicing of equipment will occur in June and allow uninterrupted tracking through July and August.

A detailed study of the flow-diagram in the compressor assembly of the CCR has been made to explain some of the anomalous behavior often observed in the field. A delicately balanced flow of oil which is essential in preventing overheating in the compressor has been isolated as a crucial factor in the system performance. This problem was particularly aggravating since there appeared to be no convenient way of anticipating malfunction. However, the recent investigation has shown that by monitoring certain pressures and temperatures in the assembly it is possible to maintain proper surveillance of the compressor.

A kit of parts and instructions will be provided all stations in the near future for adequately monitoring the critical parameters.

2. *Acquisition Aid for Ascension Island*

a. Summary. An S-band acquisition antenna system is required for DSIF-72 (Ascension Island). Specifically, this system will facilitate acquisition of *Surveyor* spacecraft immediately after their appearance above the local horizon.

The design concept for the DSIF-72 acquisition antenna system was described in *SPS 37-31*, p. 29. The system will consist of a small amplitude comparison monopulse, receiving antenna mounted at the 30-ft antenna apex, a high power transmitting horn mounted on the 30-ft antenna surface, a collimation tower horn, receiving bandpass filters, and interconnecting cabling.

The small tracking antenna and high power horn are being designed in-house. Both paraboloidal reflector and horn configurations have been experimentally investigated for the tracking antenna; the horn configuration

has been chosen as superior. The transmitter horn and polarizer have been designed and are in fabrication; pattern tests of a scale model are also complete.

b. Recent work on receiving antennas. As discussed in the previous report summary two possible approaches were considered for the tracking antenna: a paraboloid for beamwidths less than 15 deg and a horn for beamwidths greater than 15 deg. To settle the question of desired beamwidth, a detailed study was performed by the systems analysis section to determine the look angle dispersions at DSIF-72 which would result from guidance anomalies in the *Atlas Centaur* system to be used for *Surveyor*. The largest anomalies considered are those which would require maximum use of the *Surveyor* mid-course correction capability. For these extreme conditions, all trajectories pass through an angular uncertainty region roughly 15 deg in diameter, as shown in Fig. 1. A coverage circle roughly 20 deg in diameter is required to provide sufficient time for acquisition.

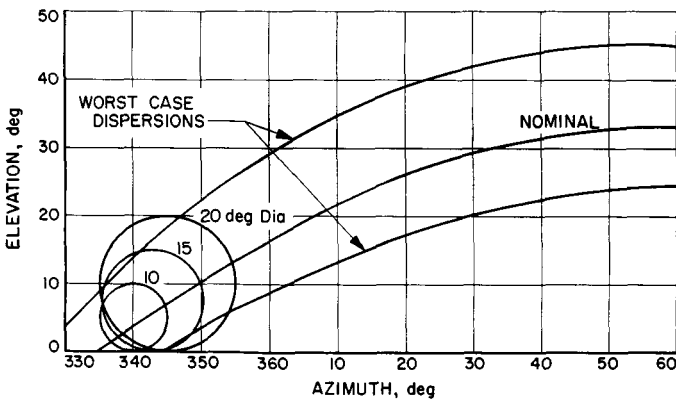


Fig. 1. Trajectory dispersions at DSIF-72

Fig. 1 does not necessarily imply that a 15-deg beamwidth would be an ideal choice; a narrower beamwidth might be desirable to increase performance for the case of near-nominal trajectories. Fig. 2 shows the reference channel gain to be expected as a function of the beamwidth chosen, for the case of a paraboloidal antenna design. It can be seen that a reference channel half power beamwidth of 12-14 deg is ideal for ± 10 deg coverage in that both coverage and axial gain are maximized. Also it can be seen that the antenna gain at ± 10 deg is almost independent of beamwidth for the beamwidth range of 14-20 deg. On the other hand, for beamwidths less than 12 deg, the gain at ± 10 deg decreases rapidly with decreasing beamwidth. The curves in Fig. 2 are terminated at the 10-db points since the pattern phase characteristic deteriorates beyond this level to the point

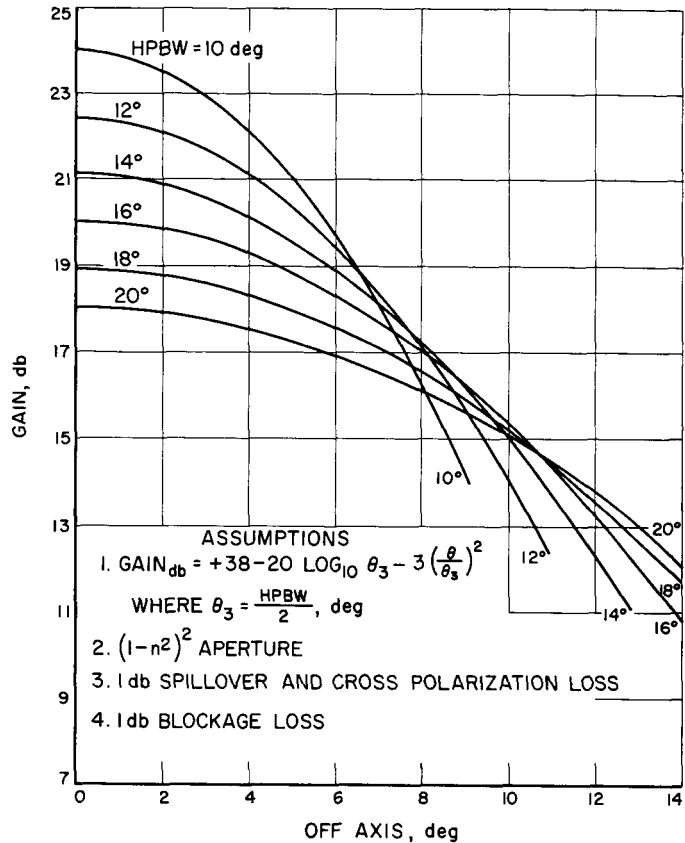


Fig. 2. Off-axis gain as a function of antenna bandwidth

that the monopulse phasing becomes grossly incorrect. The general conclusions, therefore, are that (1) a reference channel beamwidth of 12-14 deg is ideal, (2) a beamwidth less than 12 deg is unacceptable and (3) a beamwidth of 14-20 deg is acceptable but involves some degradation of axial gain. The tradeoff is further complicated by the fact that because of the aperture blockage problem the paraboloid approach becomes impractical for beamwidths greater than 10-15 deg, requiring use of the horn approach. For a given beamwidth in this range, the horn will have a superior axial gain by 2-3 db. Thus, depending on engineering details, a 16-deg beamwidth horn may be the performance equivalent of a 12-deg paraboloid.

Because of the complex tradeoff between paraboloid and horn approaches, it has been necessary to perform a parallel investigation of both approaches. A preliminary computer investigation of the paraboloid case was described in SPS 37-31. This study defined the best paraboloid geometry and also indicated marginal feasibility of a 12-14-deg beamwidth. For this reason, a feed design was chosen which could be used as either a focal point

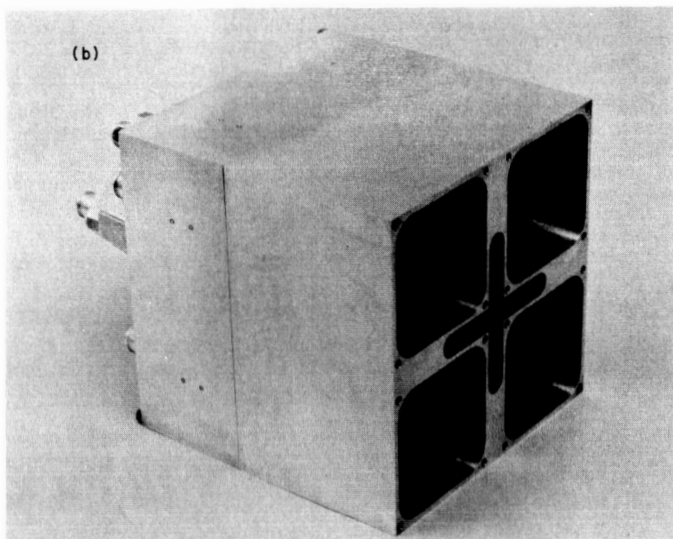
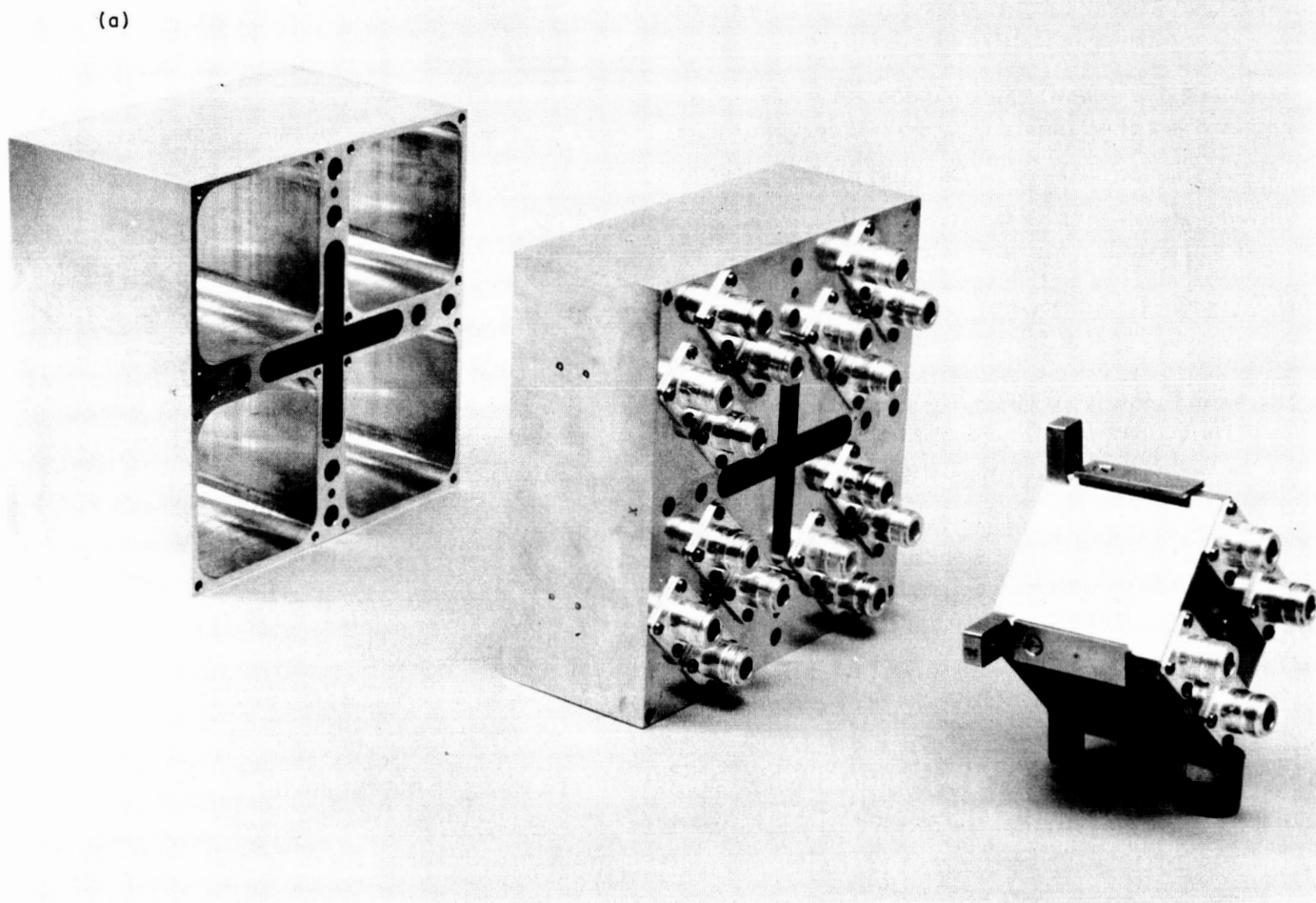


Fig. 3. Prototype feed, (a) exploded view (b) assembled view

feed in the paraboloid approach or for the excitation device in the horn design.

The prototype feed is shown in Fig. 3 (a) and (b). Each of the five feed elements is excited by a miniaturized coaxial turnstile junction to provide nominal righthand circular polarization (RCP). The basic design of the polarizers is shown in Fig. 4; this type of device has the same four-plane symmetry properties as the more familiar waveguide turnstile junction (Ref. 1) and hence provides two matched outputs, RCP and LCP; for this application the LCP output will be terminated. The junctions have been matched to a VSWR of 1.03 with an LCP to RCP isolation of 35 db; element ellipticity is approximately 0.5 db.

Secondary error channel patterns taken with the prototype feed, a prototype coaxial bridge and a 42-in. paraboloid are shown in Fig. 5. These patterns were made with the "diamond" error channel configuration and indicate satisfactory performance. The center element reference channel pattern, shown in Fig. 6, indicates, however, an unacceptably narrow beamwidth. Use of an effectively smaller reference channel aperture is shown in Fig. 7. The aperture blockage effect (not accurately predictable in the computer study) is seen to produce unacceptable pattern degradation. Based on this result, the paraboloid

approach has been discontinued because of the limited time for solving the aperture blockage.

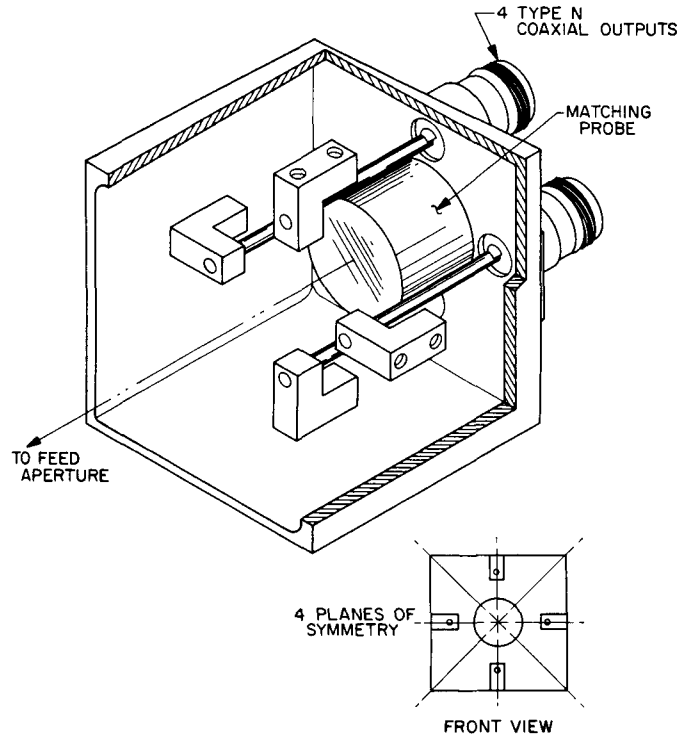


Fig. 4. Coaxial turnstile junction

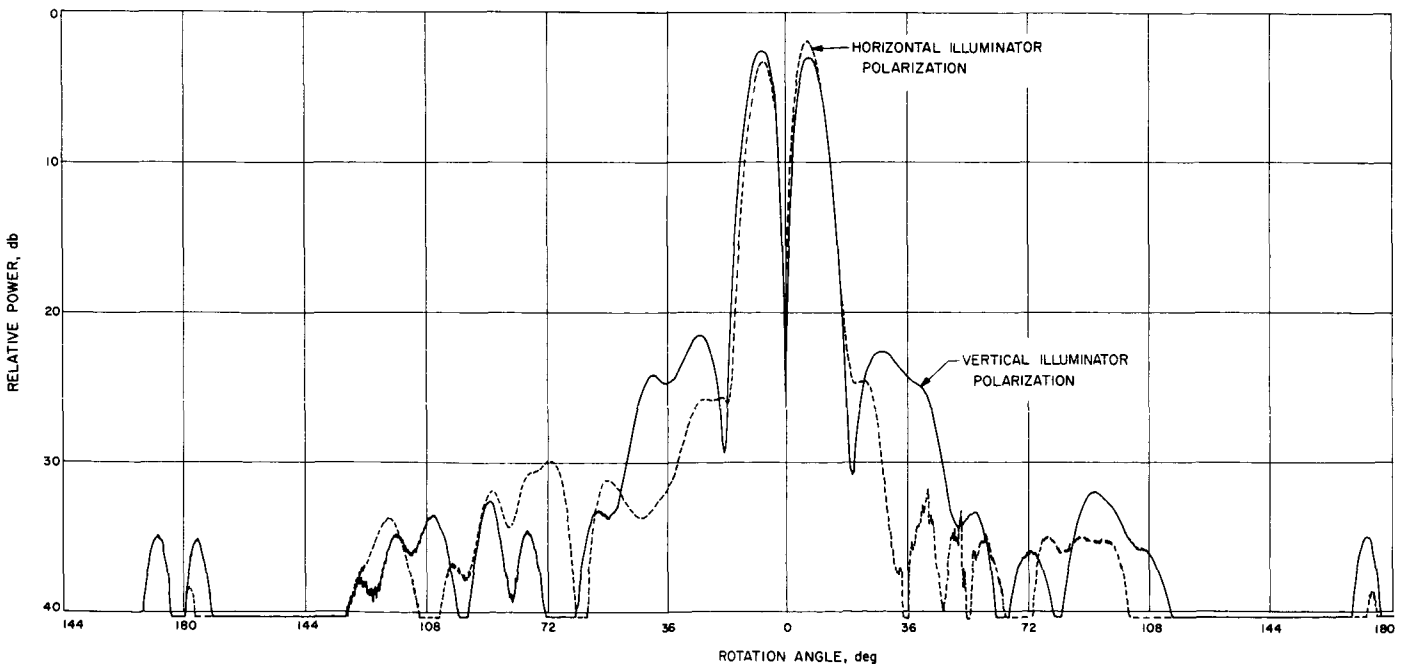


Fig. 5. Paraboloid secondary two-element error patterns

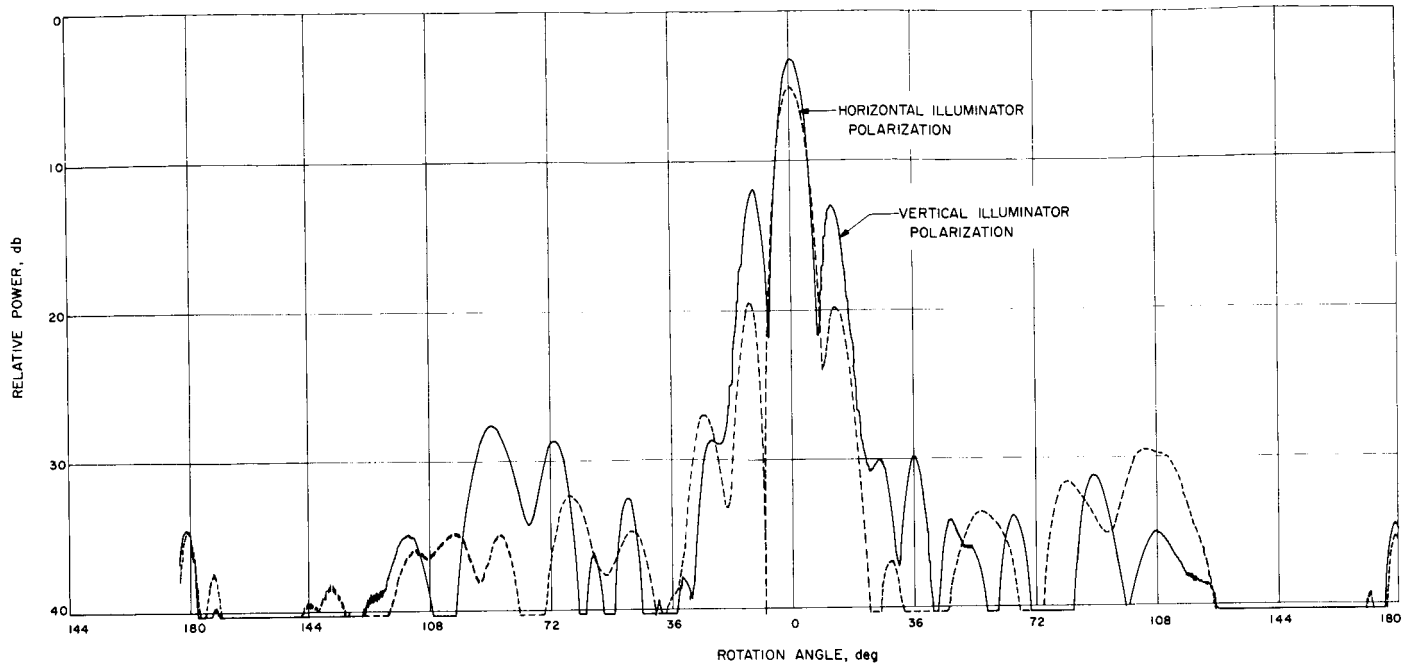


Fig. 6. Paraboloid secondary center element reference patterns

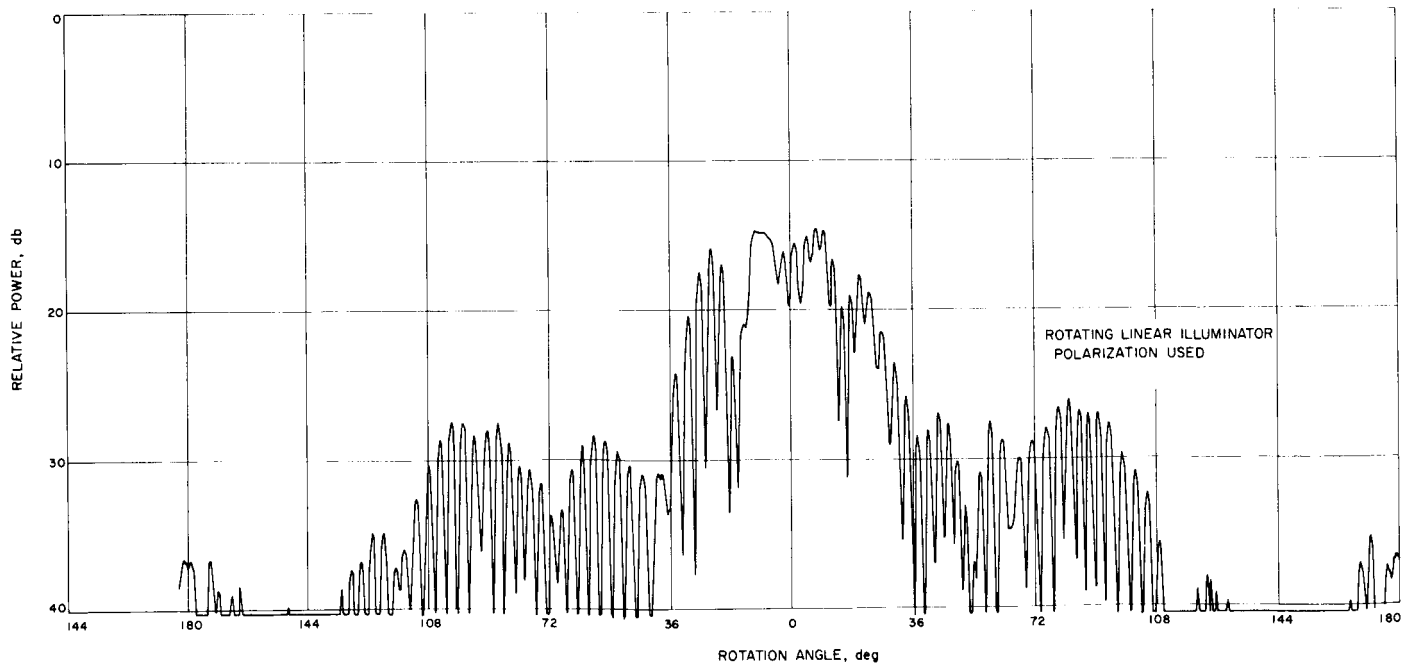


Fig. 7. Paraboloid secondary four-element reference patterns

Fig. 8 shows the prototype multimode horn. This horn uses the same conceptual design as the Hughes Aircraft Company (HAC) horn utilized in the existing DSIF acquisition antennas. For this application, however, phys-

ical size considerations dictated the use of a larger horn flare angle; 15-deg half angle as opposed to the HAC 6-deg design. Preliminary measured error channel patterns are shown in Fig. 9. A preliminary reference channel

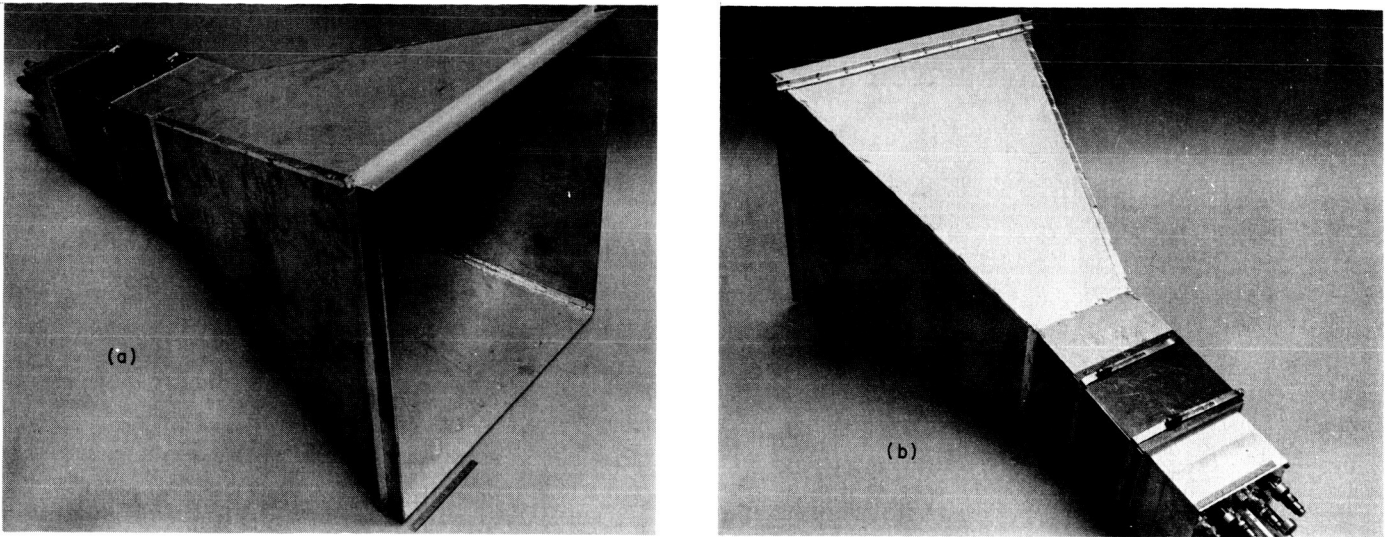


Fig. 8. Prototype multimode feedhorn, (a) three-quarter angle view (b) rear view

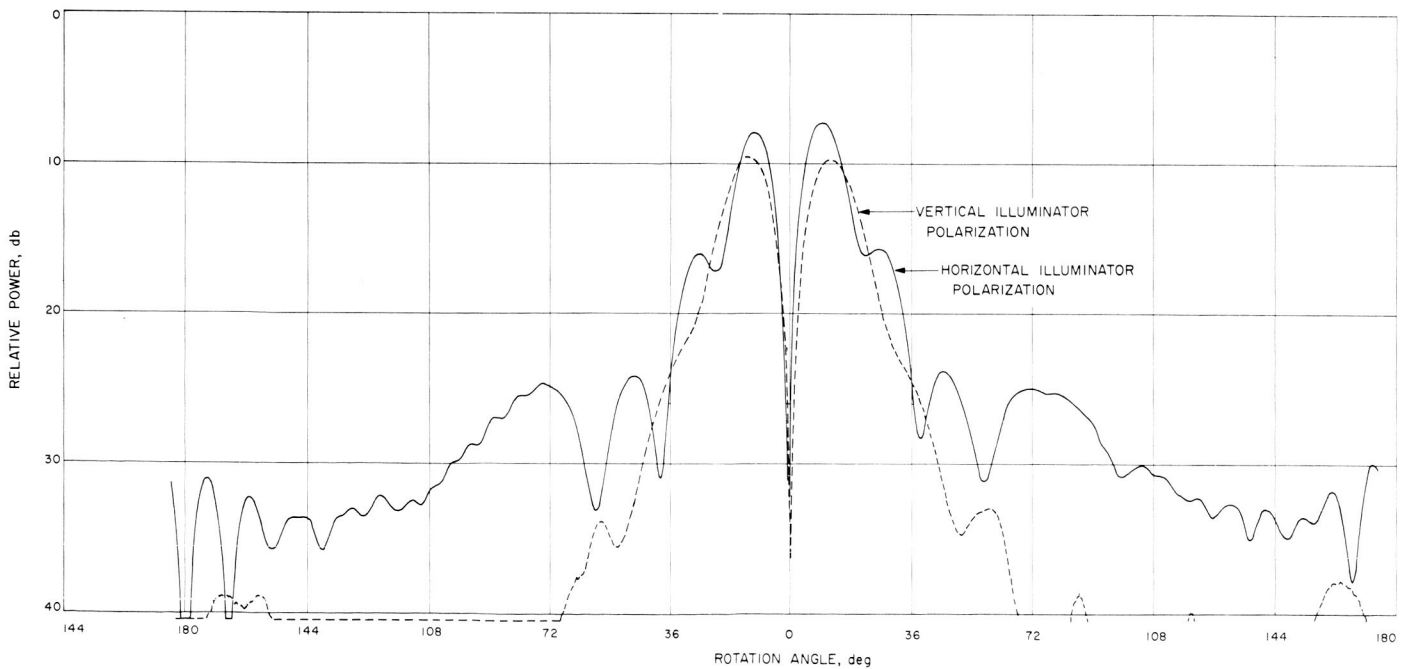


Fig. 9. Multimode horn error channel patterns

pattern using the sum of the error channel elements is shown in Fig. 10. At present, further tests are in progress to improve ellipticity, sidelobe level, and to determine gain and phase characteristics.

c. Transmitting antenna. Modelwork conducted at 9600 Mc in support of the advanced antenna system feed studies indicated a transmitter horn flare half angle of 15 deg would provide the shortest horn with minimum

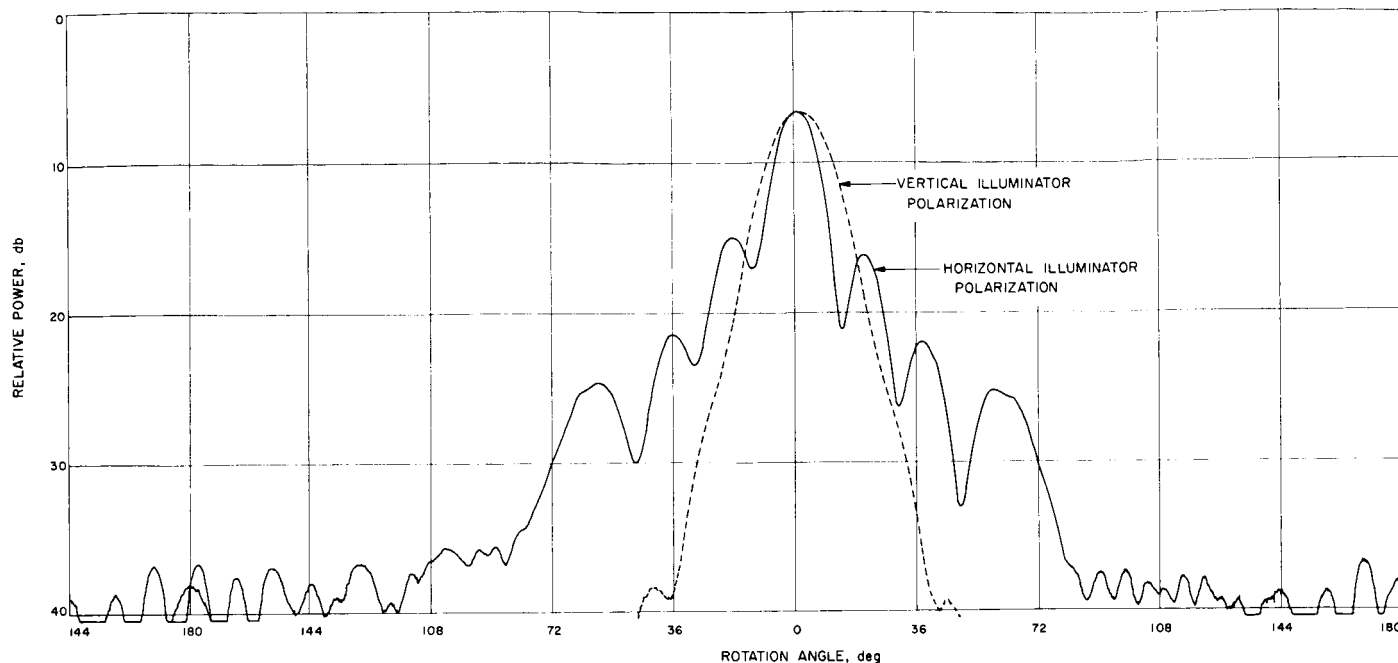


Fig. 10. Multimode horn reference channel patterns

phase errors and good sidelobe performance. As described in the previous reporting, an approach has been chosen which will allow field modification of the beamwidth and gain. Additional 15-deg model horns were constructed to allow exact measurement of horn aperture size for selected beamwidths.

A 26-deg half-power beamwidth horn would be the widest beamwidth required and model patterns show it would not significantly illuminate the apex mounted tracking feed or 30-ft main antenna feed. Horn sections of 20 and 16 deg will be provided to increase the station capability. A nominal 13-deg horn will be used for normal station operation, providing maximum gain and horizon coverage.

The transmitter horn assembly will consist of a waveguide turnstile junction for RCP transmission, a higher order mode suppressor section, the basic 26-deg horn section with a protective window; and additional horn sections as required.

Work to date includes construction of the turnstile and mode suppression sections, design of the full scale horn, and a contract for construction of the full scale horn. Design work is continuing on the integration of the horn into the 30-ft antenna structure.

B. Ground Instrumentation for Mariner IV Occultation Experiment

1. Summary

The *Mariner IV* occultation measurements will differ from those ordinarily made by the DSIF in that the duration of the phenomena involved will be short. The integration techniques normally used to obtain precise data cannot be applied in this experiment. To measure the occultation phenomena, two separate implementations will be employed. The first is the normal S-band configuration on receiver channel No. 1. From this configuration the received power as a function of time will be determined from the static and dynamic AGC voltages. The doppler frequency will be obtained from the doppler extractor. To increase the resolution and decrease the quantization error, the normal doppler output will be multiplied by eight and will have its constant frequency bias removed.

The second channel will operate as an open loop triple conversion superheterodyne. All three local oscillator signals will be derived from the rubidium standard and synthesized to the required frequency. The output of the second channel will then be a frequency translated,

amplified version of the S-band received signal which will be in the 1 to 3 kc range at the output so that it can be recorded on magnetic tape before detection.

When the spacecraft reappears from behind Mars, either the auxiliary crystal oscillator aboard the spacecraft will be used as a frequency standard or the spacecraft will be locked to an uplink signal. Measurements to aid in deciding which of the alternatives to select have been made.

2. Recent Work

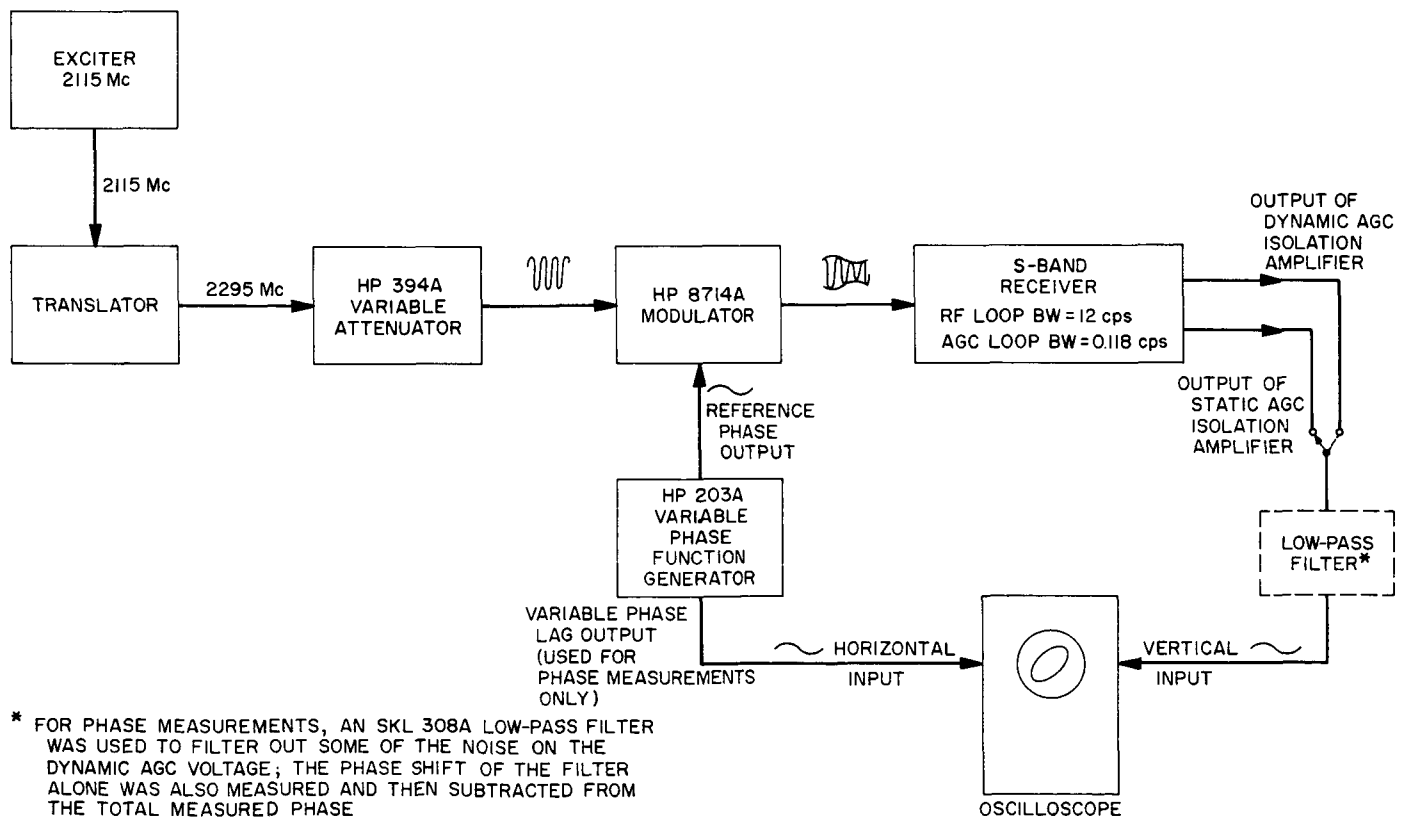
a. Closed loop AGC tests. A testing program has been started to determine the required procedures for obtaining received power, as a function of time, from the dynamic and static AGC. As a result of these tests, a preflight and postflight calibration procedure will be evolved to insure that the data will be taken in a readily reducible manner.

One of the preliminary tests made was to measure the AGC closed loop frequency response. A sinusoidally am-

plitude modulated RF carrier was used as the receiver input signal and the AGC loop amplitude and phase responses were measured at dynamic and static AGC outputs. These preliminary tests were made at a strong RF signal level (approximately 70 db above threshold) and with modulation frequencies from 0.01 to 100 cps.

The engineering lab RF and telemetry receiver (presently located at JPL) was used to make the preliminary AGC tests. This work was done in conjunction with the RF Systems Development Section. Fig. 11 shows the block diagram of the test setup used for measurements of the AGC loop amplitude and phase response of the receiver at the dynamic (unfiltered) and static (filtered) AGC outputs. The results are shown in Fig. 12 and 13.

Derivation of the theoretical equation for the AGC closed loop transfer function is discussed in a paper by Victor and Brockman (Ref. 2). The equation and parameters for specific signal levels may also be found in JPL Specification DOR-1076-DSN.



* FOR PHASE MEASUREMENTS, AN SKL 308A LOW-PASS FILTER WAS USED TO FILTER OUT SOME OF THE NOISE ON THE DYNAMIC AGC VOLTAGE; THE PHASE SHIFT OF THE FILTER ALONE WAS ALSO MEASURED AND THEN SUBTRACTED FROM THE TOTAL MEASURED PHASE

Fig. 11. Test setup for measurement of AGC loop frequency response

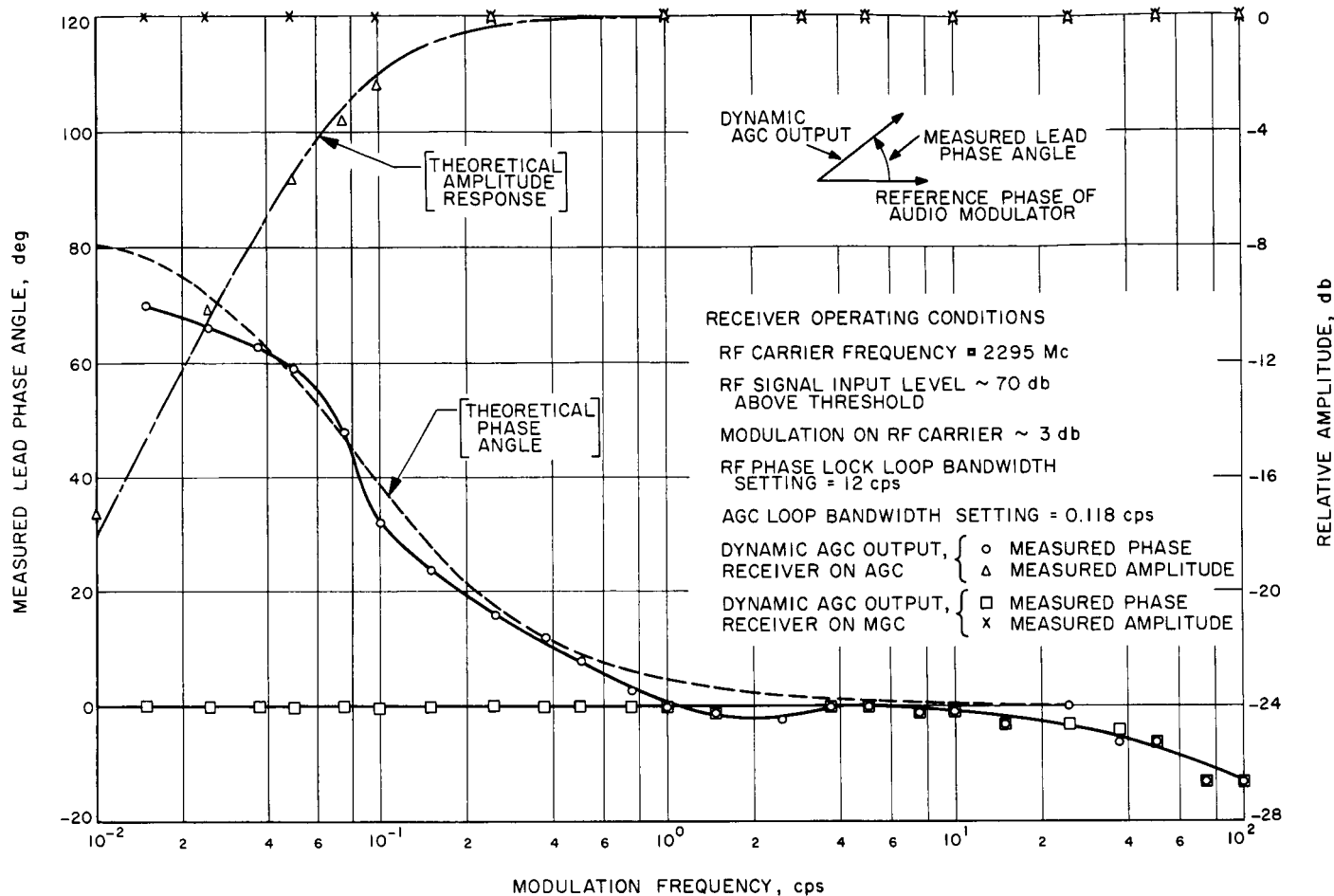


Fig. 12. Dynamic AGC frequency response

Using the equivalent AGC loop model given in Ref. 2, we obtain the following AGC closed loop transfer function

$$H(s) = \left[\frac{K_{CAD}K_{VCA}F(s)}{1 + K_{CAD}K_{VCA}F(s)} \right] \quad (1)$$

where

K_{CAD} = coherent amplitude detector gain parameter, v/db (approximately 0.115 v/db for the strong signal cases)

K_{VCA} = receiver IF gain parameter, db/v

$F(s)$ = AGC loop filter transfer function

s = complex frequency

If the AGC loop filter is an operational amplifier phase lag inverting circuit, then the AGC loop filter transfer function is given by

$$F(s) = \left[\frac{-G_F}{1 + G_F\tau_F s} \right] \quad (2)$$

where

G_F = ratio of the feedback and input resistors

τ_F = filter time constant, sec

Substitution of the expression of $F(s)$ into Eq. (1) and letting $s = j\omega$ for the steady state case of a sinusoidally modulated input, the closed loop AGC response becomes

$$H(j\omega) = \left[\frac{1}{\left(1 - \frac{1}{G_L}\right) - j\left(\frac{\tau_L\omega}{G_L}\right)} \right] \quad (3)$$

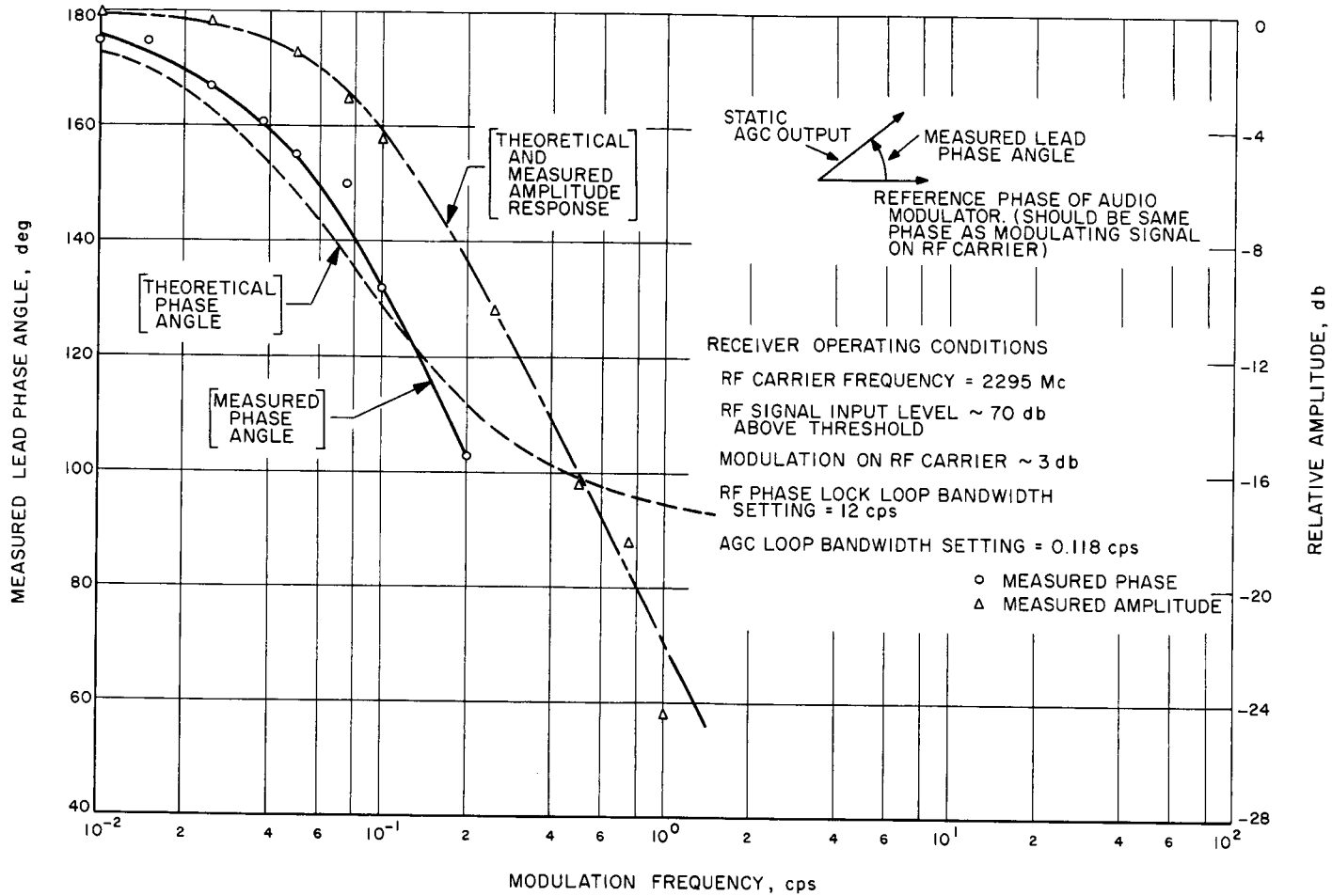


Fig. 13. Static AGC frequency response

where

$$\begin{aligned} \tau_L &= \text{AGC loop time constant} \\ &= G_{FTF} \approx (100 \times 3.8) = 380 \text{ sec} \end{aligned}$$

and

$$\begin{aligned} G_L &= K_{CAD} K_{VCA} G_F \\ \omega &= \text{angular frequency} = 2\pi f \\ f &= \text{modulation frequency, cps} \end{aligned}$$

The dynamic AGC transfer function is given as

$$K_{CAD} [1 - H(j\omega)] = -\frac{K_{CAD}}{G_L} \left[\frac{1 + j\omega\tau_L}{\left(1 - \frac{1}{G_L}\right) - j\left(\frac{\omega\tau_L}{G_L}\right)} \right] \quad (4)$$

and the static AGC transfer function is

$$\frac{1}{K_{VCA}} [H(j\omega)] = \frac{1}{K_{VCA}} \left[\frac{1}{\left(1 - \frac{1}{G_L}\right) - j\left(\frac{\omega\tau_L}{G_L}\right)} \right] \quad (5)$$

Using

$$\begin{aligned} \tau_L &= 380 \text{ sec} \\ K_{CAD} &= +0.115 \text{ db/v} \\ K_{VCA} &= -16.7 \text{ v/db (determined experimentally)} \\ G_F &= +100 \\ G_L &= K_{CAD} K_{VCA} G_F \approx -190 \end{aligned}$$

as the values for the theoretical parameters in Eq. (4) and (5), the theoretical phase and normalized amplitude

responses were calculated and are shown plotted in Fig. 12 and 13 for dynamic and static AGC, respectively. As may be seen in Fig. 12 and 13, the theoretical and measured amplitude and phase responses are in reasonably good agreement. The normalized amplitude and phase response at the output of the dynamic AGC for manual gain control (MGC) operation (open loop) is also shown in Fig. 12. For MGC operation, the MGC voltage was adjusted to give the same IF receiver gain as obtained during AGC operation. The estimated accuracy of the measured phase angles is ± 5 deg for the pass band frequencies.

The preceding measurements were obtained at signal levels of about 70 db above receiver threshold. During the *Mariner*-Mars encounter, the signal level is expected to be about 6 to 15 db above threshold. Due to the high noise to dynamic AGC signal ratio near threshold, it becomes increasingly difficult to make measurements of the dynamic AGC frequency response. Plans are being made to measure the amplitude response of the AGC system near threshold levels by tape recording the AGC outputs and postfiltering the data using narrow band filtering techniques.

b. Doppler extraction tests. A module has been developed to take the 1-Mc offset doppler frequency from the doppler extractor, add an additional bias frequency, multiply it by eight and subtract all the multiplied bias so that the output signal of the module is the doppler frequency multiplied by eight. This multiplied signal is then counted by the tracking data system. This module is described elsewhere in this summary.

In the DSIF, doppler data are normally acquired over long periods of time. To minimize the quantization error, a cumulative count is taken in which the total number of positive going zero crossings are counted. The error for any one interrogation interval is ± 1 count; however, the cumulative error is also ± 1 count for any number of interrogation intervals. In the occultation case the highest frequency resolution possible is wanted. By multiplying the doppler frequency by eight the quantization error is reduced and the resolution is increased.

The doppler multiplier was installed and tested at the Pioneer station. Two Hewlett-Packard synthesizers were driven by the station rubidium standard. One synthesizer was used in the transmitter synthesizer assembly, and

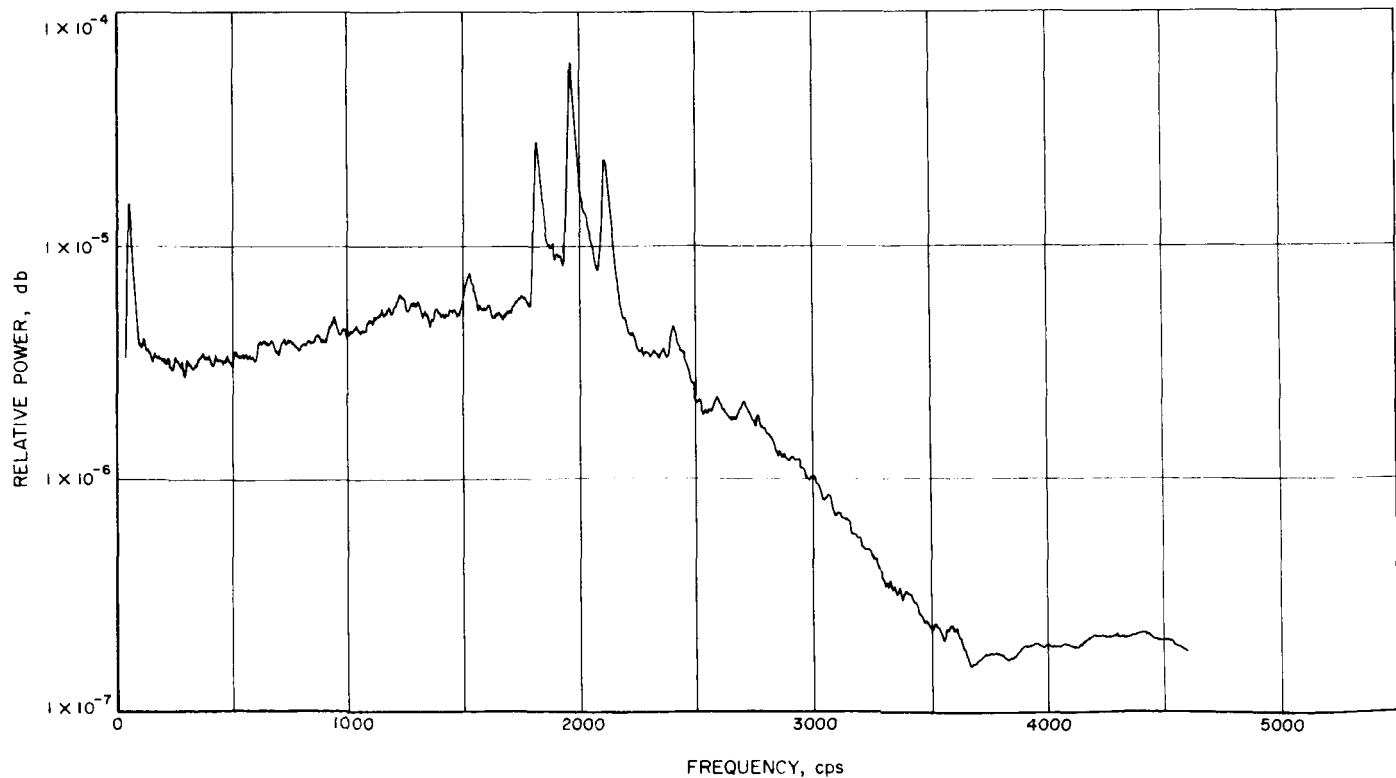


Fig. 14. Power spectral density of *Mariner IV* signal using 24.6-cps window

the other was used to drive the test transmitter. By using two synthesizers it was possible to simulate a very stable offset. The data handling system then made 10-sec cumulative doppler counts. The standard deviation of the counts was reduced to cycles per second of doppler at S-band. The threshold was -163 dbm. At -145 dbm the RMS was 0.00738, at -155 dbm the RMS was 0.00892 and at -161 dbm it was 0.18382 cps. After these measurements were made, a series of 1-sec cumulative count measurements were made using the $\times 8$, $\times 1$, and $\times 2$ doppler. The $\times 2$ doppler uses the same input as the $\times 1$ but counts both positive and negative going zero crossings. The data are now being reduced.

c. Open loop occultation receiver. The open loop receiver, described in SPS 37-20, Vol. III, pp. 34-35, was installed at the Pioneer station. It was found that this system produces no measurable deterioration on the nor-

mal receiver channel No. 1 when it is in operation on channel No. 2. When it is not being used on channel 2, channel 2 can also operate in a completely nondegraded closed loop fashion. On the night of April 1, 1965 the open loop receiver channel was used to receive the *Mariner* signal. The parametric amplifier was employed so that the signal in the phase-lock loop was approximately 14 db above threshold (roughly the level expected at encounter). The output of the open loop receiver was recorded on magnetic tape. A spectral analysis was made later at JPL using an analog technique. Fig. 14 shows a power spectral density plot in which a 24.6-cps window was employed; power is plotted on a logarithmic scale. In Fig. 15 a 6.2-cps window was used to obtain a plot that is linear in power. The higher order harmonics of the phase modulated signal are clearly discernible. The above data were recorded using a direct magnetic recording technique at a tape speed of $3\frac{3}{4}$ in./sec.

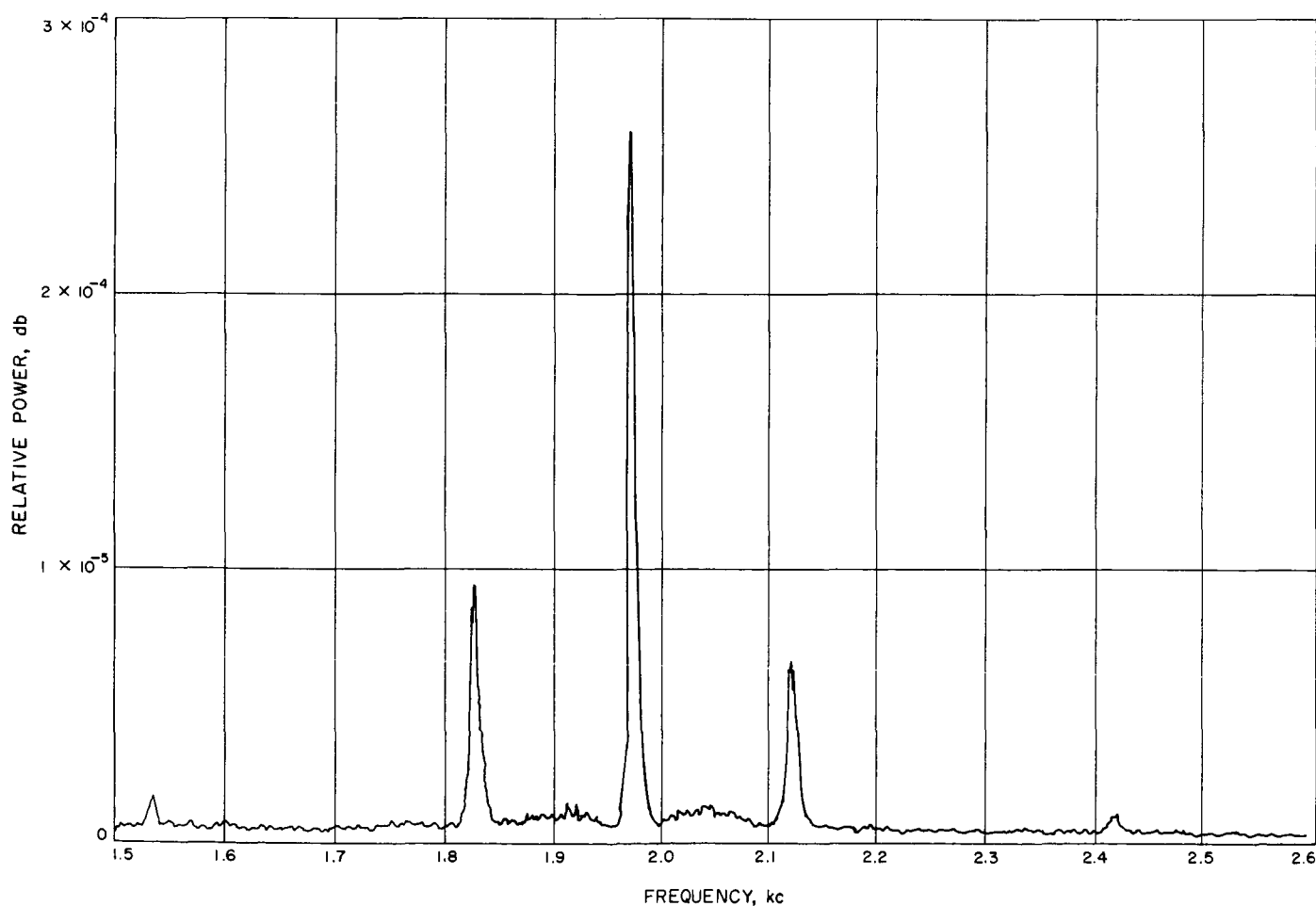


Fig. 15. Power spectral density of *Mariner IV* signal using 6.2-cps window

Tests have been started to determine the optimum recording technique. FM tape recordings will probably be made at 30 in./sec. It is necessary to record the data so that neither the doppler frequency data nor the amplitude modulation data will be degraded.

While operating this equipment, it was decided that a real time indication of received signal is necessary and that an audio loop tracking filter can accomplish this function.

The audio frequency tapes will be digitized at JPL, and the resultant digital tape will be processed in a computer; a digital program is now being prepared to accomplish this. The digital program will in essence act like an audio frequency superheterodyne. It will use the ephemeris to subtract out all free space doppler shift. If there were no doppler shift due to the atmosphere or amplitude modulation due to Fresnel diffraction, the output of the computer program would simply be a CW note. The atmospheric doppler shift will cause a frequency perturbation in the CW note, and the Fresnel diffraction will amplitude modulate it.

An alternate data processing technique is to use an audio loop tracking filter on the analog data.

d. Spacecraft transponder acquisition time tests. As the spacecraft reemerges from behind the planet, there may be an attempt to lock the vehicle transponder to the uplink. It is desirable to lock the transponder to the uplink because the frequency stability will be several orders of magnitude greater in the locked condition than when it is being driven by the auxiliary oscillator. However, the drawbacks of attempting transponder lockup are due to the uncertainties of lockup time and the attendant frequency and power transients which will occur when the vehicle switches from the auxiliary oscillator to the uplink signal.

To determine the lockon times to be expected, a series of tests was performed in an environmental vacuum test tank on the type approval vehicle radio system. A synthesizer was driven by a rubidium standard. The output of the synthesizer was multiplied up in the test transmitter, attenuated and sent into the transponder in the environmental test chamber. The output of the transponder was monitored for frequency and power level. The AGC voltage and the auxiliary oscillator VCO switch voltage were also monitored. They were found to give an excellent indication of the time of switching. A digital

data logging system was used to record the transponder output data as well as the transmitter on-off status on magnetic tape.

Fig. 16 is a plot of mean lock-on times as a function of offset from best lock frequency. There are three curves: -120, -130 and -140 dbm. If the low gain vehicle receiver is used in conjunction with the 10-kw transmitter, the signal level will be approximately -134 dbm without command modulation or -137 dbm with command modulation. It should be emphasized that these measure-

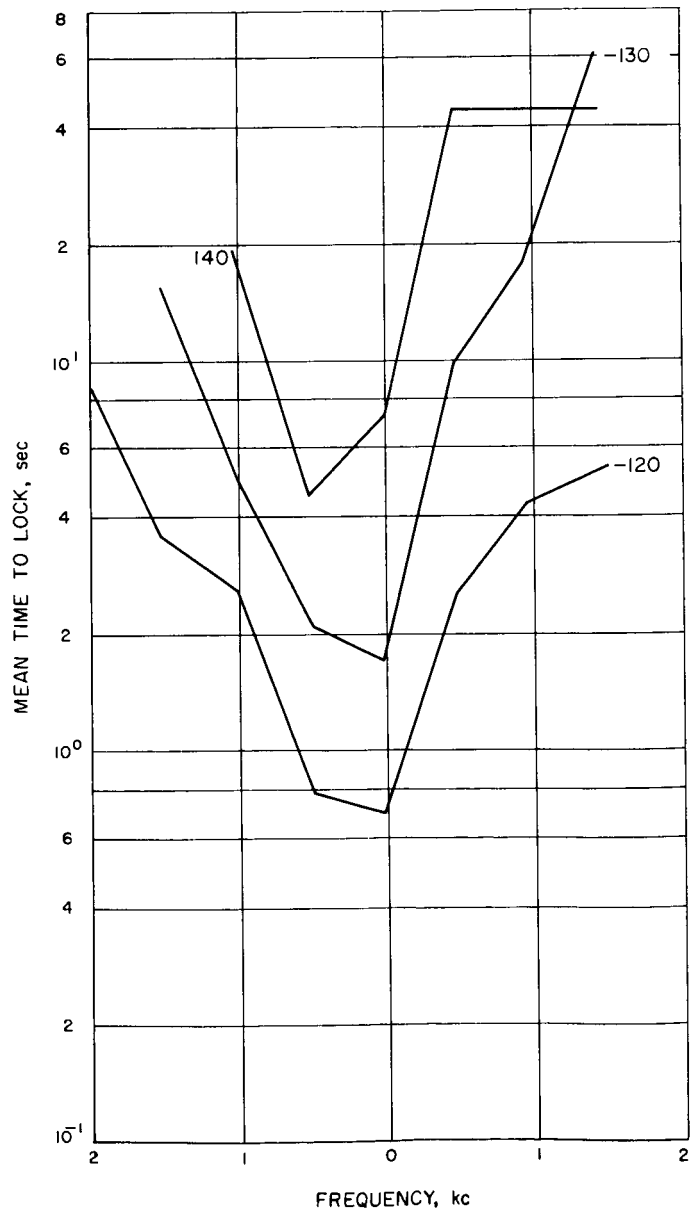


Fig. 16. Transponder lock-on time vs. frequency offset

ments have a very large statistical spread, and the averages for each point on the graph were taken from only 3 to 16 measurements. For example, the mean lock-on time for -130 dbm at no frequency effect is 1.7 sec; however, the minimum value was 0.6 sec, and the maximum was 2.7 sec out of a total of 16 measurements. According to Viterbi's analysis (Ref. 3) (for a noise free case), at best-lock frequency the acquisition time goes to zero. However, in the receiver there is not really a best-lock frequency because of noise but there is, rather, a best-lock frequency probability distribution function.

The VCO output has been measured when the receiver was out of lock. This was done on the serial 7 transponder system by Section 336. It can be seen in Fig. 17 that the histogram has the shape of a noisy normal distribution.

The frequency was measured before multiplication by 120 so that standard deviation of the receiver out of lock is 1.32 kc at S-band. It must be remembered, however, that these measurements have not been made on the spacecraft itself but, rather, on similar equipment in a space simulation. At present, lock-on time data are being monitored from the spacecraft. A further complication at encounter arises from the temperature transients induced by turning on the encounter mode experiments which will cause an additional perturbation on the VCO frequency.

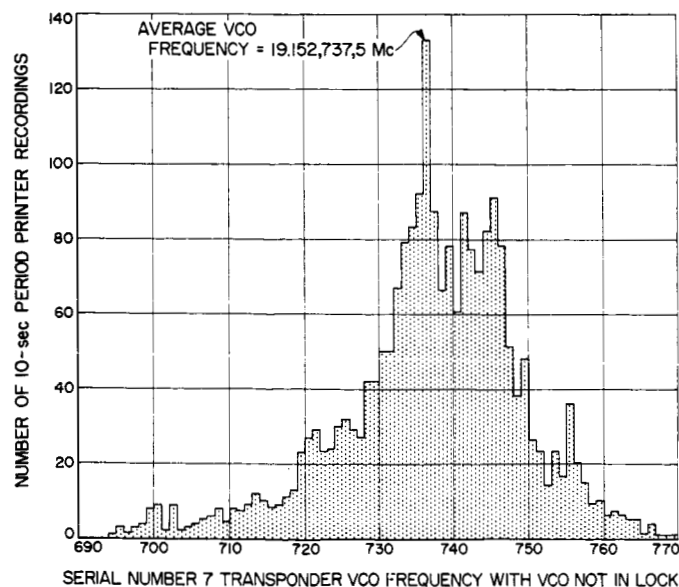


Fig. 17. Number of 10-sec counts vs. VCO frequency when not in lock

C. Manned Space Flight Network S-Band Receiver/Exciter

1. Introduction

The Manned Space Flight Network (MSFN) S-band receiver/exciter is designed for use in the MSFN. The MSFN is the Earth-based portion of a two-way, phase coherent, precision tracking and communications system capable of providing command, telemetry, and position tracking for manned space vehicles. It will measure two angles (X and Y), radial velocity, and range to the space vehicle as well as provide an efficient and reliable two-way communications capability.

The MSFN S-band receiver/exciter is similar in design to the DSIF S-band equipment and employs a modular building block philosophy suitable for use in permanent or semipermanent ground-based installations. The DSIF S-band receiver/exciter [Goldstone duplicate standard (GSDS) 1964 model] is described in *SPS 37-28*, Vol. III, pp. 30-39 and *SPS 37-32*, Vol. III, pp. 10-19. This summary presents the RF design characteristics for the MSFN equipment and a description which outlines the basic differences between the MSFN and GSDS 1964 DSIF receiver/exciter. A block diagram of the MSFN receiver/exciter is shown in Fig. 18.

2. Receiver

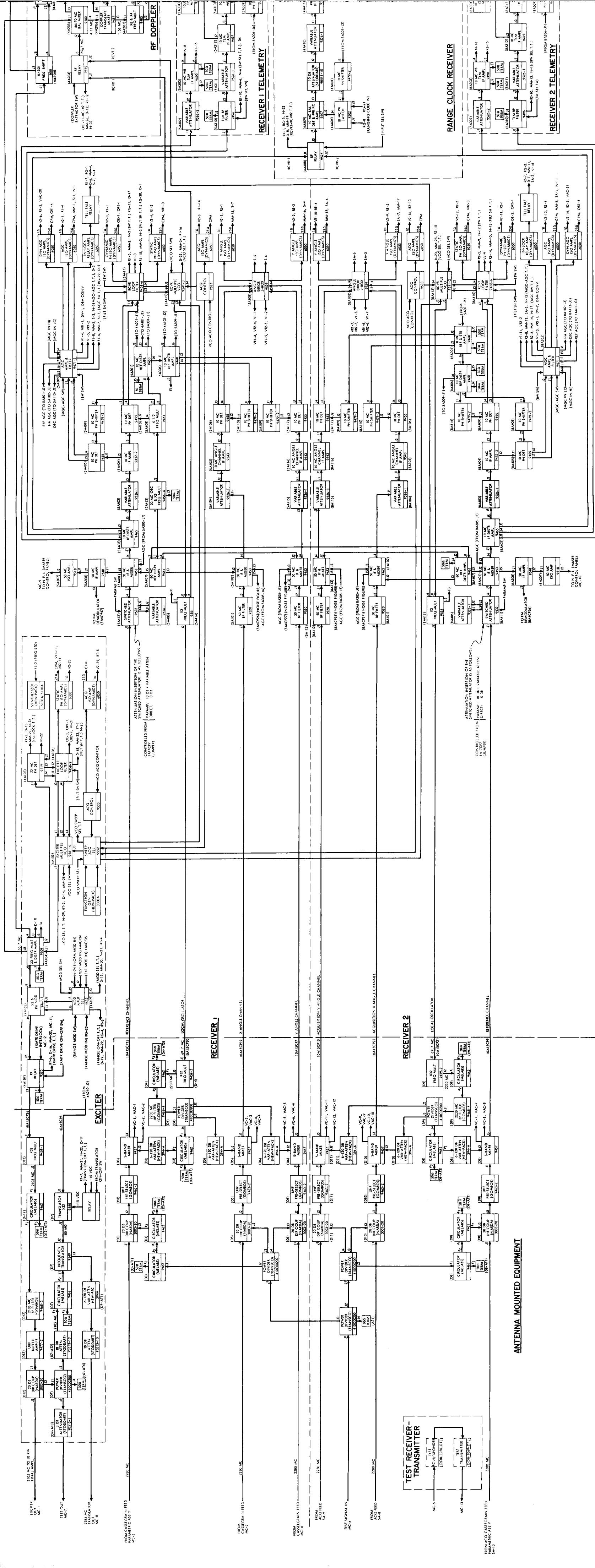
The receiver contains eight major functional elements whose functional capabilities are outlined in *SPS 37-28*, Vol. III, pp. 30-39. The RF design characteristics for the receiver are summarized in Table 1. Design of the MSFN receiver differs from the GSDS 1964 DSIF receiver as follows:

a. Reference receivers. Each reference receiver provides capability for reception at any one of four selectable frequencies with a multiple voltage controlled oscillator (VCO) which provides a rapid receive-frequency switch-over capability. Two of these frequencies provide phase-coherent reception capability in the 2280- to 2290-Mc range, while the other two frequencies normally provide FM (noncoherent) reception capability in the 2270- to 2280-Mc range (Table 1). An exception to this occurs during operation with the lunar excursion module (LEM) at 2282.5 Mc (presently assigned frequency) where reception may be either phase-coherent with phase modulation or noncoherent with frequency modulation.

The VCO in reference receiver 1 normally operates at either of the two phase-coherent frequencies in conjunc-

Table 1. RF design characteristics, preliminary

Item	Characteristics	Item	Characteristics
Receiver		Receiver (Cont'd)	
a. Type	Phase-coherent double conversion superheterodyne	j. Precision doppler	
b. Effective noise temperature	2700 ± 300°	(1) Accuracy	0.01 cps RMS at carrier frequency for 1-min sample spacing
c. Input signal level	-60 dbm to threshold	k. Angle error detection	
d. Frequency		(1) Gain tracking	Differential ± 2 db max
(1) Range	Noncoherent (FM) reception, 2270 to 2285 Mc Coherent reception, 2280 to 2290 Mc	(2) Phase tracking	Differential ± 15 deg max
(2) Assignment	RF Range clock	(3) Error detection peak Receiver only	± 1.0 v ± 2 db
Phase-coherent reception		Parametric amplifier operation	± 0.5 v ± 2 db
LEM or S-IVB	2282.5 Mc 495.334 kc		
CSM	2287.5 Mc 496.419 kc	Transmitter-exciter	
FM reception		a. Frequency control	Phase stable crystal controlled oscillator—frequency synthesized from an atomic frequency standard during precision frequency operation.
CSM	2272.5 Mc		
S-IVB	2277.5 Mc	b. Stability	Precision operation
LEM	2282.5 Mc	(1) Frequency	1:10 ¹¹ for 20 min 5:10 ¹¹ for 10 hr Manual operation 1:10 ⁷ for 20 min 2:10 ⁶ for 10 hr (ΔT ± 3°C)
(3) Tracking capability	± 11.5/10 ³	(2) Phase	7° RMS—noise error with noise BW of 50 cps—exciter and receiver combined error
(4) Acquisition sweep range	Zero to ± 6.0/10 ³	c. Frequency	
(5) Selection	Rapid switchover capability	(1) Range	2100 to 2110 Mc
e. Noise bandwidth	Threshold BW	(2) Assignment	LEM or S-IVB CSM
(1) RF	50 cps +0/-20% 200 cps +0/-20% 700 cps +20/-0%	(3) Tuning capability	± 9.0/10 ⁵ (precision operation)
(2) Range receiver		(4) Acquisition sweep range	Zero to ± 6.0/10 ³
Range clock loop	4 cps +0/-20% 16 cps +0/-20% 40 cps +0/-20%	(5) Selection	Rapid switchover capability
Code clock transfer loop	120 cps ± 10%	d. Power output	
(3) AGC (at RF threshold)	0.35 cps 3.5 cps 13.1 cps	(1) Exciter	+ (35 ± 1.5) dbm
f. RF threshold signal levels		(2) Test signal	+ (7 ± 3) dbm
50 cps +0/-20% 200 cps +0/-20% 200 cps +20/-0%		(3) Frequency translator (attenuator set at minimum)	- (27 ± 5) dbm
Reference receiver		e. Modulation	
-(147 ± 1) dbm -(141 ± 1) dbm -(135 ± 1) dbm		(1) Type	Phase
g. Detected telemetry		(2) Command	
(1) Modulation	Phase modulation	Bandwidth	Direct coupled (DC) to 100 kc
(2) Bandwidth (1 db)	Selectable 2.2 kc, 10 kc, 210 kc, and 1.25 Mc	Sensitivity	3 (+0.3, -0.0) rad peak/v peak to 3.0 rad peak
(3) Output level	0 ± 2 dbm (1 rad RMS modulation index under strong signal conditions)	Input impedance	50 Ω
(4) Output impedance	50 Ω	(3) Range	DC to 2 Mc
h. 10 Mc IF output for telemetry (nondetected)		Bandwidth	5 (+0.5, -0.0) rad peak/v peak to 2.1 rad peak
(1) Modulation	AM, FM, or φM	Sensitivity	
(2) Bandwidth		Input impedance	50 Ω
Fixed (3 db)	6.0 ± 0.8 Mc		
Selectable (1 db)	4.5 kc, 20 kc, 420 kc, and 2.8 Mc		
(3) Output impedance	50 Ω		
i. 50 Mc IF output for FM			
(1) Bandwidth (3 db)	9.0 ± 1.0 Mc		
(2) Output level	-10 to -20 dbm		
(3) Output impedance	50 Ω		



ANTENNA MOUNTED EQUIPMENT

SUBSYSTEM INTERFACES

Table with columns for DATA SUBSYSTEM, ANTENNA MICROWAVE, STATION CONTROL & MONITOR, TELEMETRY & COMMAND DATA HANDLING, TRACKING DATA HANDLING, RANGING, and FREQUENCY & TIMING INPUTS. Each column lists various components and their associated part numbers.

SUBSYSTEM MONITORING

Table listing monitoring components and their locations. Columns include OSCILLOSCOPE, VTVM (CONTINUED), COUNTER, WAVE ANALYZER, and DIGITAL VM (CONTROL PANEL SELECT - CABINET 3).

SUBSYSTEM SUBASSEMBLIES

Table mapping SPEC NO. to SUBASSEMBLY NO.'S and SCHEMATIC ASSEMBLY NO.'S. It lists various subassembly types such as AMPLIFIERS, FILTERS, and RELAYS.

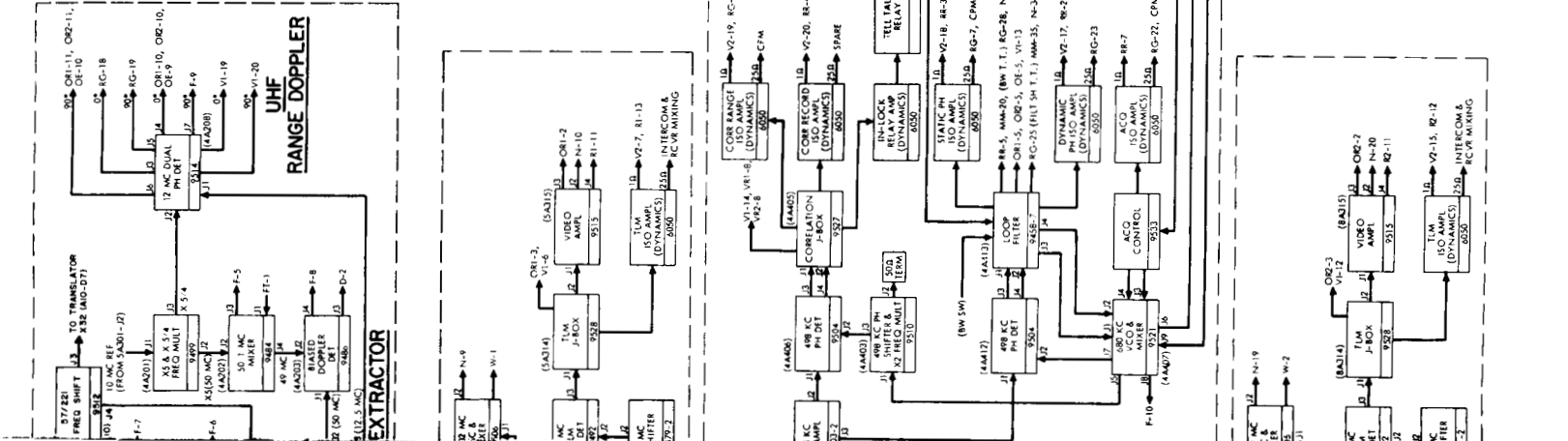


Fig. 18. MSFN unified S-band RF receiver/exciter subsystem block diagram

tion with the corresponding transmitter-exciter frequency to provide capability for two-way phase-coherent operation at either of the two S-band transponder frequencies (CSM or LEM). The VCO in reference receiver 2 operates at any one of the four frequencies to provide either a phase-coherent reception capability, which would normally be required during spacecraft acquisition, or a noncoherent reception capability at one of the S-band FM frequencies.

The RF loop noise bandwidths have been increased, as shown in Table 1. In particular, the widest loop noise bandwidth (700 cps) has been selected so as to accommodate the frequency sweep rates which will be required for rapid two-way RF acquisition during the Earth-orbital phase of the Apollo mission. As shown in Fig. 18, the acquisition sweep waveform can be selected for the VCO in either reference receiver 1 or 2 to accomplish RF acquisition for either one-way, down-link coherent reception or pseudo two-way coherent reception during multistation reception.

b. Telemetry and FM. Both receivers provide a 50-Mc output (Table 1) in addition to the detected telemetry and 10-Mc outputs. During FM reception, the 50-Mc output from reference receiver 2 normally provides the signal for FM demodulation. It should be noted that the detected telemetry (maximum selectable bandwidth) provides a 1-db bandwidth of 1.25 Mc to accommodate the down-link voice subcarrier.

c. Range clock receiver. The VCO's for the range clock phase-locked loop and the code clock transfer loop operate in conjunction with a 680-kc oscillator-mixer (Fig. 18) to accommodate, with a single VCO crystal, the change in clock frequency resulting from a change in S-band operating frequency. The range clock and code clock loop noise bandwidths are shown in Table 1. The code clock transfer loop noise bandwidth has been increased to 120 cps to minimize the delay associated with the settling time of this loop during range acquisition.

3. Transmitter-exciter

The transmitter-exciter contains two major functional elements whose functional capabilities are outlined in SPS 37-28, Vol. III, pp. 30-39. RF design characteristics of the exciter are summarized in Table 1. Design of the MSFN exciter differs from the GSDS 1964 exciter as follows:

- (1) The exciter provides capability for transmission at one of two selectable frequencies. A multiple VCO

provides a rapid transmit-frequency switchover capability in the 2100- to 2110-Mc range (Table 1). The MSFN receive and transmit frequencies are related by the ratio 240/221 during two-way coherent operation. The acquisition sweep is selected for the exciter VCO to accomplish automatic RF acquisition during the normal two-way coherent mode of operation.

- (2) The S-band receive-frequency test signal is coherently derived from the transmit-frequency (Fig. 18). This test signal is used for closed signal path testing and performance evaluation during coherent mode operation.

D. S-Band Cassegrain Monopulse Feed Development

1. Summary

Integration of the S-band Cassegrain monopulse (SCM) feed into the Cassegrain cone assembly has been completed, and seven SCM cone assemblies have been manufactured and tested. Four of the SCM cones are presently in operation for *Mariner IV*; two more SCM cones will be installed and operational prior to encounter. The seventh cone is assigned to the Pioneer Station for Apollo support. Development of the suppressed-sidelobe SCM feed was reported in SPS 37-32, Vol. III and previous summaries.

2. SCM Cone Assembly

After development and fabrication of the suppressed-sidelobe version of the SCM feed, as reported in SPS 37-32, Vol. III, a one-quarter size scale model of a complete SCM cone assembly using this advanced feed was constructed. This model demonstrated that use of the feed within the confines of established antenna geometry was feasible and that there was adequate room inside the existing DSIF cone housing design for all the necessary microwave equipment, without unduly restricting the movement of personnel for operation and maintenance.

Using this scale model as a basis for design, a contract was awarded to Hughes Aircraft Company, Fullerton, California, in August 1963, to complete the detail design of the SCM cone assembly except for the traveling wave maser (TWM) and to fabricate and partially test five cone assemblies. In August 1964, after delivery of the first five

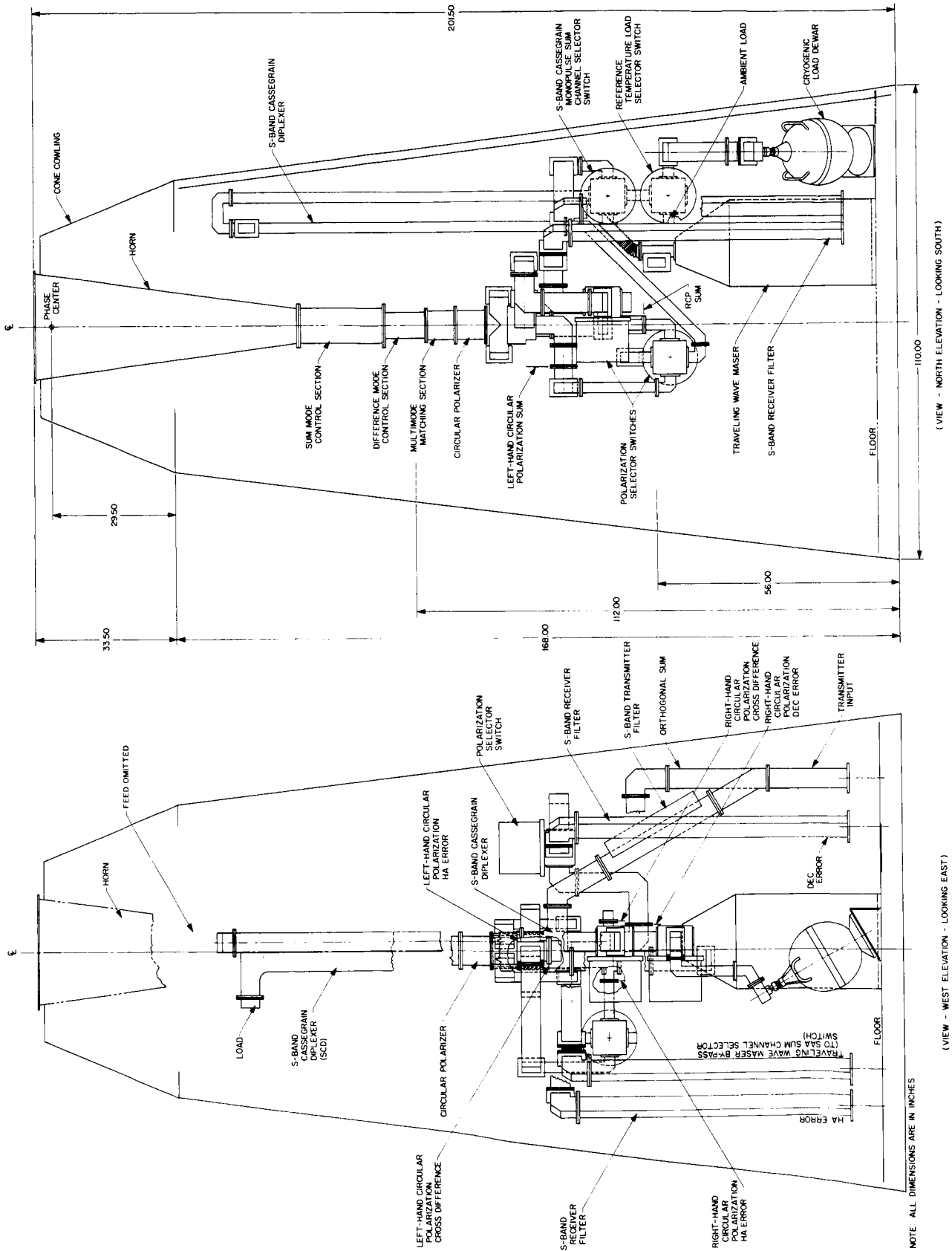


Fig. 19. S-band Cassegrain monopulse cone assembly

SCM cone assemblies, a follow-on contract for two additional cones was awarded to Hughes Aircraft Company, bringing the total to seven. Under separate contract, four additional SCM feeds were fabricated for use as S-band acquisition antennas (SAA), as reported in *SPS 37-28*, Vol. III. Thus, a total of eleven suppressed-sidelobe SCM feeds have been delivered.

The resulting SCM cone assembly is shown in Fig. 19. The cone assembly on its handling trailer at Goldstone is shown in Fig. 20. The SCM cone assembly contains the following major components (Fig. 19):

- (1) SCM feed
- (2) TWM (installed by JPL after cone delivery)
- (3) One diplexer
- (4) One transmitter filter
- (5) Two receiver filters
- (6) Five waveguide switches

Items 3 through 5 were described in *SPS 37-30*, Vol. III; item (6) was described in *SPS 37-31*, Vol. III. The system

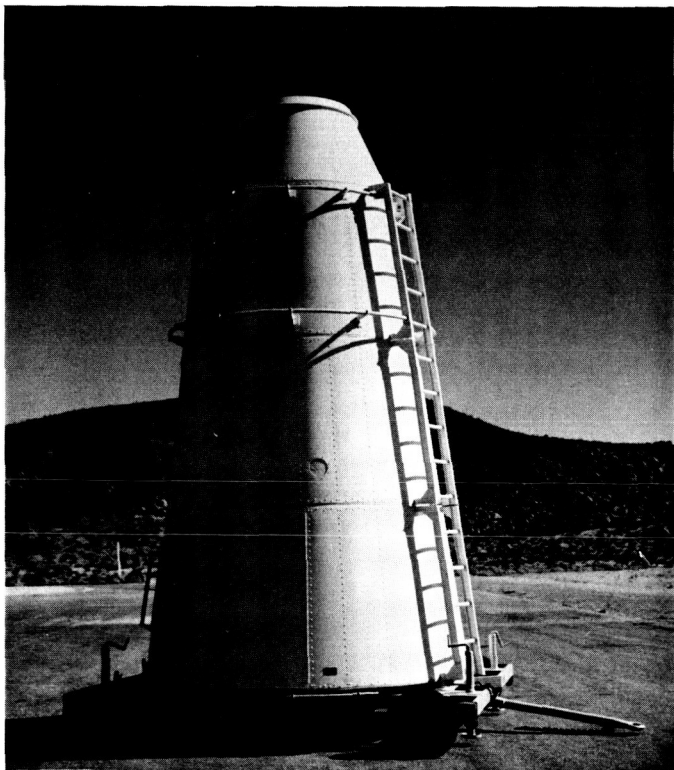


Fig. 20. SCM cone assembly on cone handling trailer

operation of the SCM cone assembly, and its interface with the rest of the S-band system, was discussed in detail in *SPS 37-28*, Vol. III; a block diagram of the GSDS 1964 S-band RF system appears on p. 30 of *SPS 37-28*.

Not shown in Fig. 19 are the many brackets required to locate precisely and rigidly support the microwave components within the cone under normal operation and during handling and overseas shipping. All support brackets have been designed to withstand up to 5 g, 0 to 10 cps, handling vibrations with adequate safety margins.

Most complex of these bracket assemblies is that for the SCM feed itself. Fig. 21 shows a portion of this mounting structure. Its design is such that, together with the mounting adapters on the feed, precision alignment of the complete feed assembly in six dimensions is possible during assembly of the cone. The open space between the feed support trusses has been intentionally left unobstructed on this side of the cone in order to provide personnel with access to the complete SCM feed for inspection purposes. As illustrated in Fig. 19, most of the microwave hardware has been grouped into the western half of the cone, and several persons can work in the cone at one time without crowding.

3. SCM Cone Assembly Tests

When the SCM cones are assembled at the contractor's facility, a mockup is used in place of the TWM in order to locate precisely the waveguide interface and TWM mounting holes. The completed cone assembly is shipped to Goldstone, where the mockup is replaced with a working TWM assembly.

Each SCM cone assembly is fully ground tested at the Goldstone antenna range, using a 10-kw test transmitter and a trailer-mounted test receiver. Following completion of ground tests, the cone is mounted on one of the Goldstone 85-ft antennas (when available) and thoroughly antenna-tested.

These antenna tests include, but are not limited to, the following:

- (1) Complete voltage standing wave ratio (VSWR) measurements of all ports
- (2) Measurement of the cone assembly isolation matrix
- (3) System temperature determinations

- (4) Secondary antenna pattern measurements, including ellipticities, error channel null depths, and null plane orthogonality
- (5) Aperture efficiency and antenna gain by radio source observations

Complete tests on one SCM cone assembly result in over one hundred pages of test data; certain results are discussed below.

Table 2. SCM feed isolation matrix

$f = 2295 \text{ Mc}$

OUTPUT	Right-hand circular polarization (RCP)				Left-hand circular polarization (LCP)			
	Sum	HA	Dec	Cross	Sum	HA	Dec	Cross
RCP sum	0	46	33	34	40	43	38	43
RCP HA	R	0	16	44	37	18	16	46
RCP Dec	R	R	0	44	44	17	18	36
LCP Sum	R	R	R	40	0	33	33	37
LCP HA	R	R	R	46	R	0	16	41
LCP Dec	R	R	R	35	R	R	0	35
$f = 2113 \text{ Mc}$								
RCP Sum	0	38	38	32	32	42	33	41
LCP Sum	R	40	37	35	0	45	38	33

R denotes reciprocal isolation; value appears elsewhere in table.

Prior to installation by the contractor of an SCM feed in the cone, complete test data are taken on the feed itself. Table 2 gives the isolation matrix for one of the feeds. This may be compared with Table 3, which presents the same isolation matrix as measured by JPL on the installed cone assembly. These latter measurements are performed on the cone with the hyperboloid properly

Table 3. SCM cone assembly isolation matrix with cone installed on DSIF-12 antenna

$f = 2295 \text{ Mc}$

OUTPUT	RCP				LCP			
	Sum	HA	Dec	Cross	Sum	HA	Dec	Cross
RCP Sum	0	46	34	NA	43	47	41	NA
RCP HA	R	0	17	NA	40	NA	17	NA
RCP Dec	R	R	0	NA	46	18	NA	NA
LCP Sum	R	R	R	NA	0	36	35	NA
LCP HA	R	R	R	NA	R	0	17	NA
LCP Dec	R	R	R	NA	R	R	0	NA
$f = 2113 \text{ Mc}$								
RCP Sum	0	NM	NM	NA	30	NM	NM	NA
LCP Sum	R	NM	NM	NA	0	NM	NM	NA

*R denotes reciprocal isolation; value appears elsewhere in table.
 NA denotes value not available because of interconnecting waveguides (see text).
 NM denotes value not measurable because of waveguide filters installed (see text).*

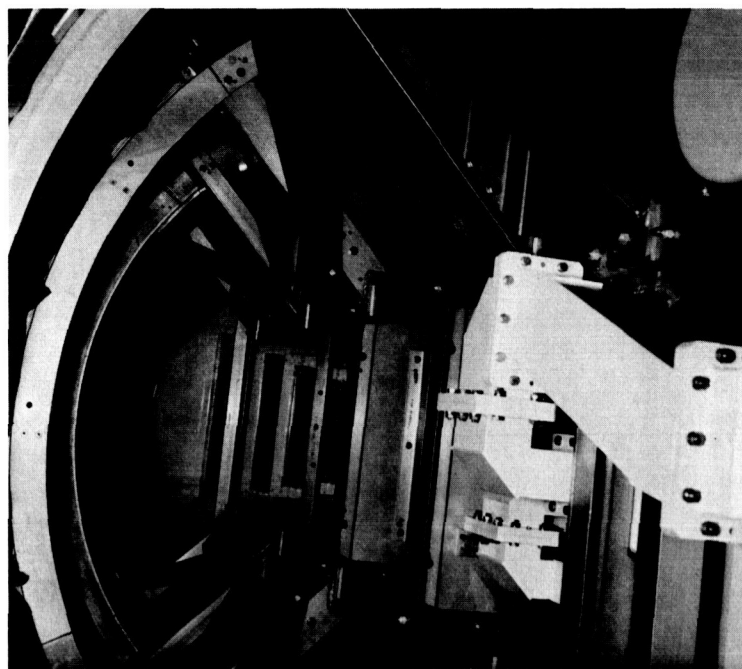


Fig. 21. SCM feed mounting structure

focused and the vertex plate adjusted for good sum-to-sum isolations at both frequencies. Some of the isolations that are measurable on the SCM feed by itself cannot be repeated on the cone assembly without disconnecting waveguides; this is not considered necessary since other measurements on the cone assembly would reveal any serious degradation of performance in these isolations. Also, because of the diplexer and filters installed in the cone, it is not practical to measure certain isolations directly. The isolations of the diplexer and filters are measured prior to their installation in the cone.

It is somewhat anomalous that certain isolations in Table 3 are higher than in Table 2. This is apparently due to the fact that the 85-ft antenna presents a more reflection-free environment, despite the presence of the hyperboloid, than the antenna range at the contractor's facility.

The critical isolations affecting system temperature are quite satisfactory and represent a considerable improvement over those obtained with the prototype feed (SPS 37-16, Vol. III, p. 17). For example, the total contribution to system temperature due to finite feed isolation is only 0.39° K when the TWM is connected to the right-hand circular polarization (RCP) sum port, using Table 2. Table 3 indicates that the contribution is actually even less.

Fig. 22 shows representative secondary patterns measured on the Pioneer antenna, using the near-field collimation tower. The patterns are in good agreement with theory and are not substantially different from those measured on the prototype feed (SPS 37-18, Vol. III). Uniform aperture illumination over the paraboloid would produce 17.5-db first sidelobes; allowing for aperture blockage and near-field focus degradation, the observed 15- to

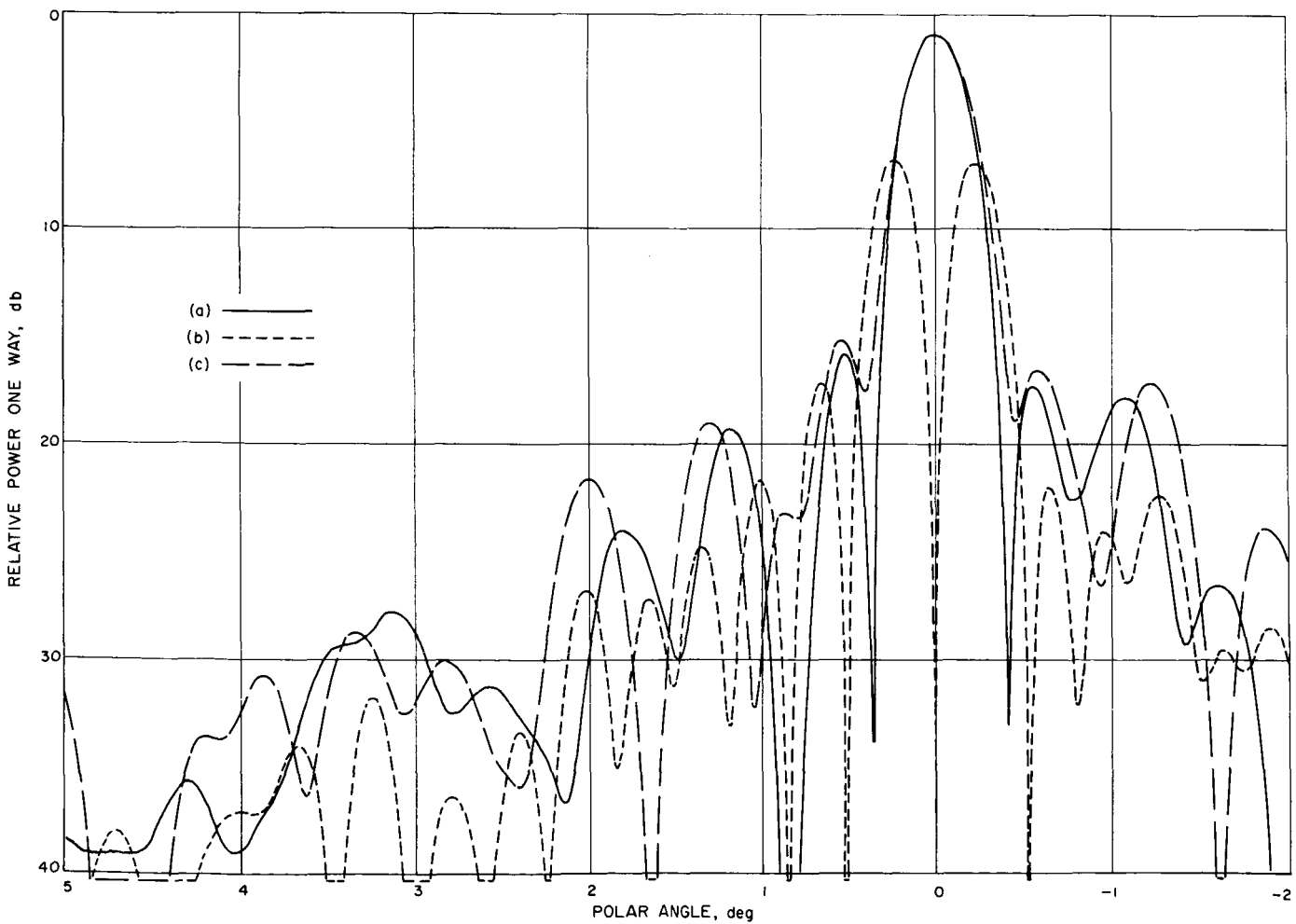


Fig. 22. SCM secondary radiation patterns (a) RCP Sum, Dec plane, 2295 Mc; (b) RCP Dec error, 2295 Mc; (c) RCP Sum, Dec plane, 2113 Mc (Amplitude scale for sum and error patterns is arbitrary; true relative level of sum to error peaks is approximately 3 db)

16-db sidelobes are quite reasonable. Some of the observed asymmetry is due to antenna distortion and ground reflections resulting from the very low elevation angle of the collimation tower test antenna. Radio source drift curve data indicate almost perfect symmetry of first and second sidelobes.

Table 4 presents preliminary aperture efficiency and antenna gain data at 2295 Mc for four different antennas on three continents. The Pioneer antenna, DSIF-11, is the oldest antenna in the DSN and is known to have the poorest surface. The Tidbinbilla antenna, DSIF-42, has the first precision surface to be used by the DSN (*SPS 37-31*, Vol. III, p. 18). Thus the apparent variation in aperture efficiency between antennas has some correlation with known antenna characteristics and does not necessarily reflect a difference in the four SCM cone assemblies involved.

Table 4. Antenna aperture efficiency and gain at 2295 Mc, SCM feed system

Parameter	DSIF Station			
	11	41	42	51
Aperture efficiency, %	51	55	58	52
Aperture efficiency, db	-2.92	-2.59	-2.37	-2.84
Antenna gain, db	53.0	53.3	53.5	53.0

The efficiencies and gains given in Table 4 are direct measurements and refer to the efficiency and gain at the SCM sum channel selector switch. With a very slight correction, this is the antenna efficiency or gain at the input to the TWM; and thus it includes all losses in the SCM cone due to the feed, diplexer, two waveguide switches, and several interconnecting waveguides. The approximate total of the losses between the feed and the maser is 0.18 db. Therefore, the actual antenna gain at the feed output is about 53.4 ± 0.3 db or an aperture efficiency of about $57 \pm 4\%$. As reported in earlier summaries, the aperture efficiency of the prototype (nonsuppressed-sidelobe) SCM feed was approximately 47%.

In future summaries measured system noise temperature data will be presented in detail along with further discussions of antenna gains and efficiencies as determined by radio sources. Briefly, the complete system temperature, using the SCM cone assembly with the TWM, has been determined to be $42 \pm 3^\circ$ K with the antenna at zenith. The antenna temperature, measured at the SCM feed output, has been determined to be approximately 13° K, or about one half that of the prototype feed. Thus,

the suppressed-sidelobe technique has substantially reduced the system temperature while increasing the antenna gain by about 0.9 db.

For comparison, the dual-mode listening feed in use on the Venus radar antenna (DSIF-13) produces an antenna temperature of approximately 10° K, and provides an aperture efficiency of about 62% with a comparable antenna surface.

E. S-Band Test Antenna

1. Summary

Development of the S-band test antenna (STA) used to make gain, pattern, and ellipticity measurements on the DSIF antennas has been completed. Prototype and production models have been tested and meet the specified requirements. The STA's are installed and operating at the DSIF stations.

2. Background

Prior to 1962 there existed at JPL a requirement for an S-band collimation antenna having a low ellipticity and voltage standing wave ratio (VSWR) and capable of operating in either of three polarized modes, right circular, left circular and rotatable linear. This polarization diversity allows the determination of the gain, antenna pattern, ellipticity, and cross polarization characteristics of the 85-ft antenna which operates in a circularly polarized mode.

A survey of the market at that time indicated that there were no antennas available that would satisfy the requirement. Therefore, JPL initiated a two-phase contractor supported development program for the fabrication and testing of two prototype STA's and four production STA's which would meet the required performance characteristics. The prototype STA's are being updated to reflect the production configuration.

3. General Description

The STA system consists of the following equipment (Fig. 23):

- (1) Eight-foot paraboloidal reflector assembly
- (2) Circular aperture feed assembly
- (3) Control panel

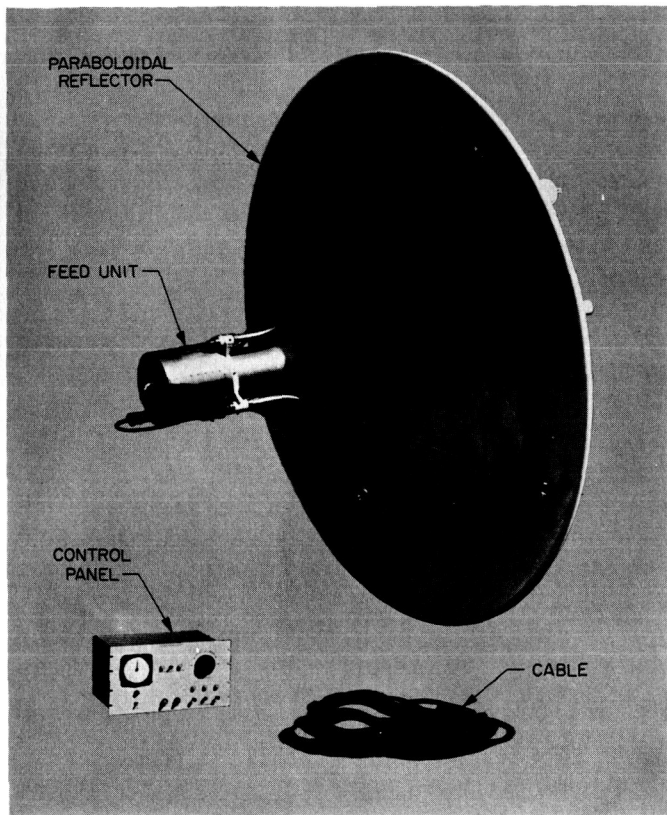


Fig. 23. S-band test antenna

The reflector assembly consists of a paraboloidal reflector measuring 8 ft in diameter with focal length to diameter ratio of 0.375, a mounting structure which provides a plus and minus 5-deg adjustment in both azimuth and elevation, an optical boresight telescope with protective housing, and a spar and horn ring structure for feed support.

The feed assembly consists of a dipole and coaxial rotary joint with a 7/8-in. coax output, an iris section which acts as a polarization transducer, a drive motor for changing and orienting polarizations, two synchro-transformers (one has a 1 to 1 gear ratio and the other a 36 to 1 ratio), and logic switches for control and read-out of polarization changes. The feed system also includes a weatherproof housing and radome.

The control panel consists of a 19- × 10.5-in. panel with operating controls and a dial indicator for polarization orientation read-out, a power supply, motor speed control, and 150 ft of connecting control cable.

Table 5 lists the system performance characteristics.

Table 5. System performance characteristics

Frequency	2110 ± 10 and 2290 ± 10 Mc.
VSWR	Less than 1.2 to 1 over the specified frequency bands.
Polarization	Rotatable linear and both right and left circular.
Ellipticity	No greater than 1 db over the specified frequency bands for right or left circular polarization.
Gain	31.25 ± 0.25 db over the specified frequency bands, relative to an isotropic radiator.
Gain variation	Less than ± 0.1 db as a function of feed rotation at either of the specified frequencies.
Cross polarization	Cross-polarized component at least 20 db down within 1 deg of the peak of the main beam.
Sidelobe level	20 db down for any polarization over the specified frequency bands.
Beamwidth	Less than 4.5 deg at the half power points.
Power capacity	100 w CW power for any polarization and any frequency within the specified bands.

4. Theory of Operation

RF energy is fed into the 7/8-in. coaxial input and is converted into a TE₁₁ mode inside the circular waveguide by means of the dipole transition. The linear TE₁₁ mode is then fed into the polarization transducer to produce either rotatable linear, right circular, or left circular polarization.

To obtain linear polarization, the dipole input is aligned parallel to the irises of the polarization transducer, as indicated in Fig. 24. By locking the dipole

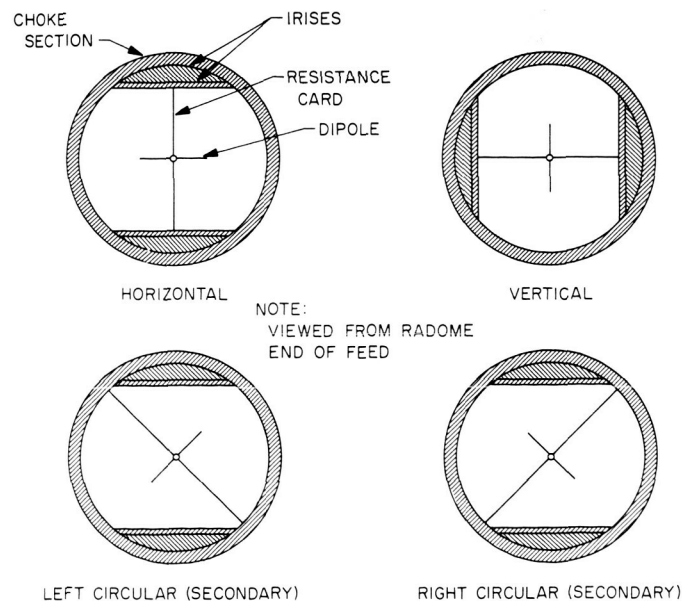


Fig. 24. Linear and circular polarization viewed from radome end of feed

input in this position relative to the irises and rotating the entire feed, the linear polarization may be rotated continuously.

For circular polarization, the irises are set at 45 deg to the dipole (Fig. 24). This allows the incident vector to be converted into two equal magnitude, orthogonal vectors, one of which is advanced in time while the other is delayed. The total time phase difference between these two vectors is made 90 deg by the geometry of the polarization transducer over the frequency range 2100 to 2300 Mc. Hence, the radiated energy is circularly polarized.

Either right circular or left circular polarization (Fig. 24) may be obtained depending on the orientation of the irises with respect to the dipole.

5. DSIF Operation

The STA's are installed near the top of the standard DSIF collimation tower while the polarization control panel is located in the collimation microwave cabinet at the base of the tower. The STA's have been operating since July 1963 and have experienced only one failure, a defective microswitch in the feed unit of one of the overseas STA's. Replacement corrected the fault.

F. Coherent Frequency Translation

1. Introduction

The capability of self-checking exists in the receiver-exciter system. This is accomplished by translating a sample of the exciter signal to the receiver frequency. The exciter characteristics can then be examined with the receiver and the receiver calibrated with the exciter. In the 1964 S-band receiver-exciter system (SPS 37-28 and 37-32, Vol. III, pp. 30-39 and 10, respectively), this was accomplished by combining a sample of the exciter signal with a signal generated from a crystal oscillator. The primary drawbacks of this mechanization are

- (1) The necessity of changing the oscillator crystal each time the exciter is moved from one channel frequency to another.
- (2) Since the derived receiver frequency is not coherent with the exciter, there is no capability of performing coherent tests.

To remove these limitations, a coherent translator was developed for use in the Manned Space Flight Network (MSFN) system and subsequent Deep Space Net (DSN) systems. The coherent relationship between the receiver frequency and the transmitter frequency is 240/221. A coherent reference signal related to the exciter by the factor 19/221 is derived and combined with a sample of the exciter signal to obtain the coherent receiver frequency (Fig. 25).

In addition to obtaining the capability of coherent translation, the performance of the translator was extended in other areas; namely, an increase in the dynamic range, an increase in the bandwidth to cover the coherent portion of the MSFN band and the DSN band, the addition of a high level power monitoring output, and improved shielding to permit calibrations down to threshold levels.

The improved design consists primarily of two new subassemblies, the translator module combining the two frequencies and a $\times 32$ frequency multiplier module generating the coherent reference signal.

2. Translator Module

The block diagram of the translator module is shown in Fig. 26. The design goals for the translator were as follows:

- (1) Power output of -10 dbm minimum
- (2) Bandwidth of 20 Mc at the 1-db points
- (3) Minimum cross-coupling between the output and input ports
- (4) Linear power conversion of the exciter signal
- (5) Minimum RF leakage out of the module

The translator mixer module is a passive high level mixer which uses a silicon varactor diode as the mixing element. The diode is mounted in a common wall iris between two pair of quarter wave coaxial cavities. The reference signal is injected into the diode through a coaxial low-pass filter. A lumped element matching section transforms the diode VHF impedance to 50 Ω for optimum reference signal coupling. Iris coupling is used between each adjacent section of cavities and loop coupling for the S-band input and output terminals.

The input pair of cavities is tuned to a nominal center frequency of 2110 Mc, and the output pair is tuned to a nominal center frequency of 2290 Mc. The bandwidth at

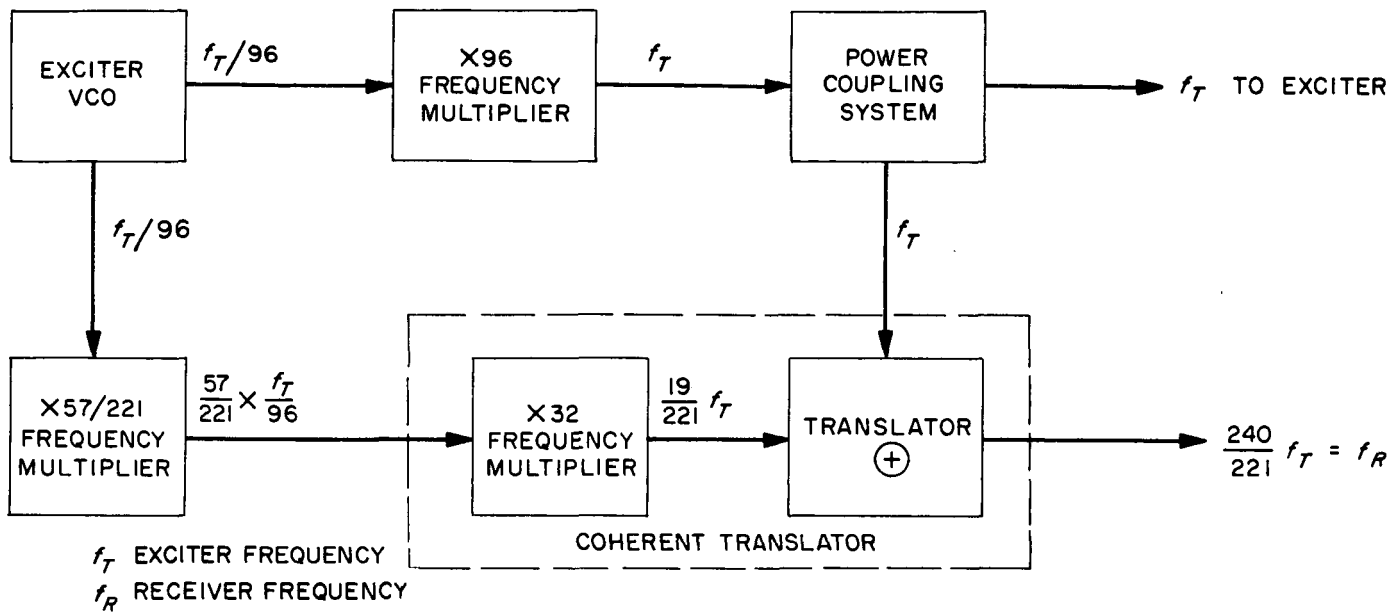


Fig. 25. Coherent translator block diagram

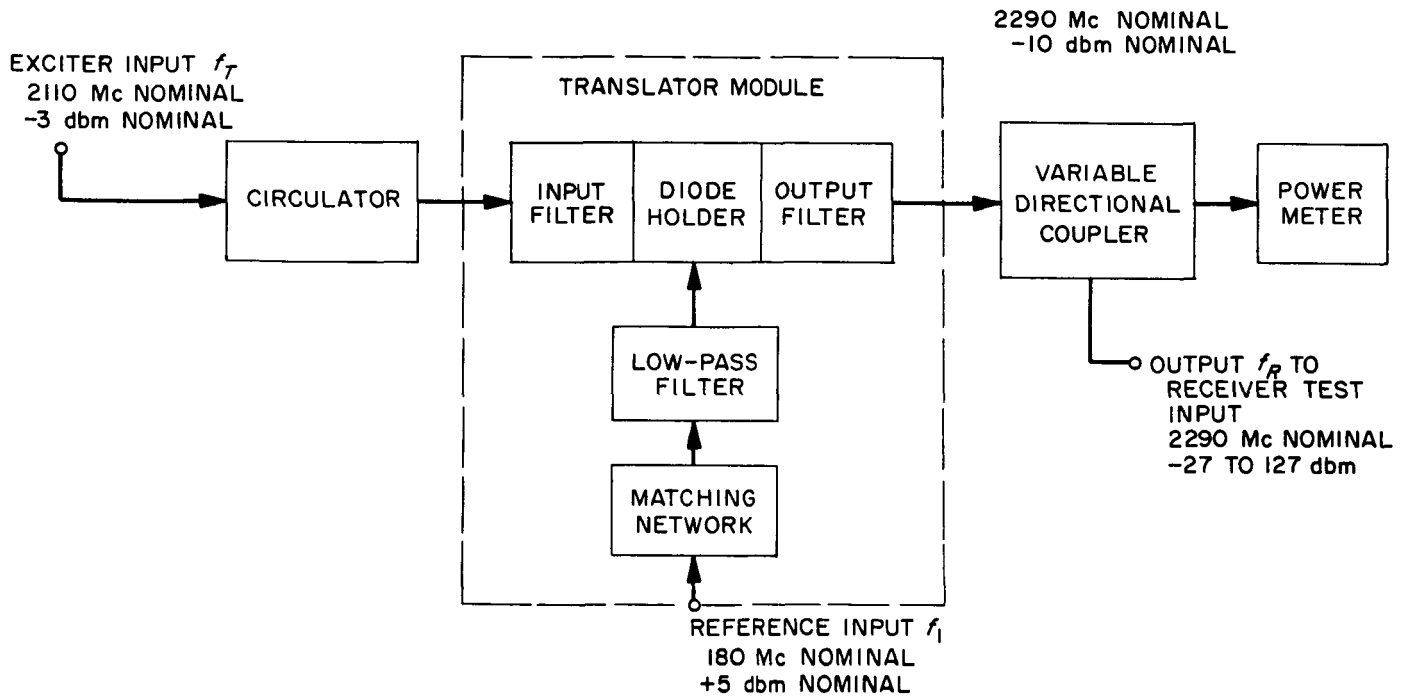


Fig. 26. Translator block diagram

the 1-db points is 20 Mc. This is sufficient to translate the combined DSN and MSFN transmit bands of 2100 to 2120 Mc to the corresponding receive frequencies in the band from 2280 to 2300 Mc without retuning and allows the use of the same module either the DSN or the coherent portion of the MSFN S-band systems.

The isolation between the exciter input jack and the translator output jack is at least 40 db. The addition of a circulator in the exciter input line further reduces the level of the output signal that gets back into the exciter line by at least another 26 db. This minimizes the possibility of a stray signal getting into the receiver input by

way of the various switches and directional couplers in the test signal instrumentation.

Output levels in excess of 0.1 mw were easily attained with most diodes. This allows convenient output power monitoring with a power bridge. The yield of usable diodes from a batch of 24 ran about 80%. To improve the output level stability of the module, the diode is driven at least 2 db beyond the point where the output begins to limit to the reference signal. This limiting has no effect on the conversion linearity of the exciter signal. The conversion linearity of the exciter signal is shown in Fig. 27. A photograph of the translator module is shown in Fig. 28.

Leakage out of the connector flanges and other joints in the module was undetectable with a -90 dbm sensitivity receiver. The module was also tested in a representative DSIF receiver system. An AGC curve was plotted to receiver threshold with no evidence of leakage problems.

All of the design goals for the translator have been achieved. Its relatively high output and low leakage level permit its use as a test transmitter for AGC calibrations by including a precision calibrated variable attenuator in the output line. Several production models have been assembled with reproducible characteristics from unit to unit. Its implementation in the DSIF S-band system

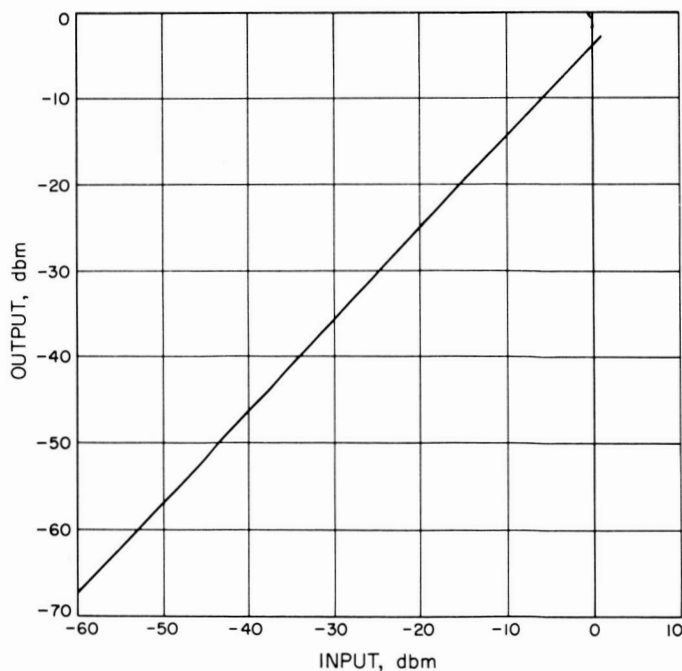


Fig. 27. Conversion linearity

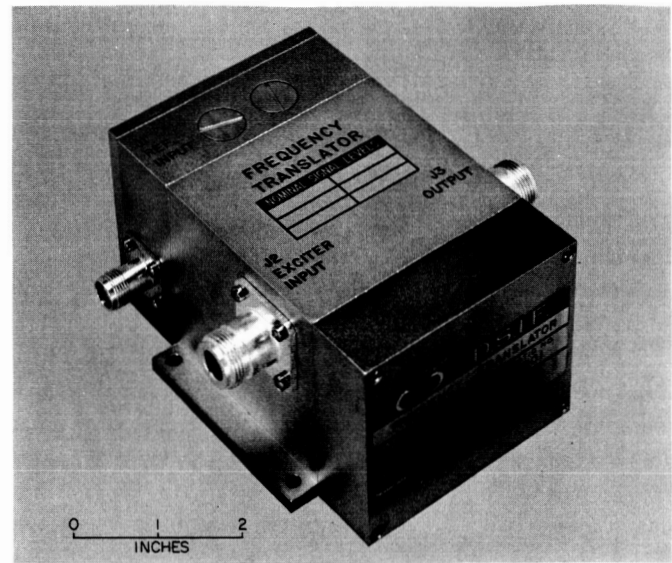


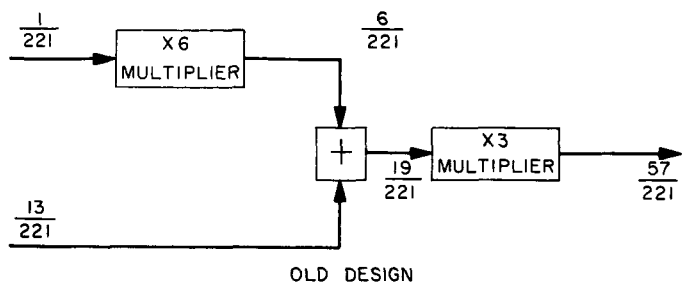
Fig. 28. Translator module

affords an additional capability for accurate calibration and greater flexibility for accommodating the various channels allocated to the DSN and MSFN frequency bands.

3. $\times 32$ Frequency Multiplier Module

To derive the coherent reference signal for the translator module, a $\times 32$ frequency multiplier is used to multiply the nominal 5.65 Mc signal at the output of the existing 57/221 frequency shifter to a nominal 180 Mc. The multiplier utilizes transistor circuitry exclusively. The input frequency is multiplied $\times 4$, $\times 4$, and $\times 2$ consecutively. Intermediate tuned amplifiers are used following each $\times 4$ multiplier to assure that all sidebands generated in the multiplication process are a minimum of 40 db below the desired output frequency.

The control of the levels of unwanted sidebands at the output of the $\times 32$ frequency multiplier is a function of the spectrum of the incoming signal. In order to obtain a satisfactory reference signal spectrum at the input of the $\times 32$ frequency multiplier, it was necessary to improve the design of the $\times 57/221$ frequency multiplier. This consisted of a change in the method of generation and the frequencies of the signals combined in the mixer (Fig. 29). These frequencies were selected to produce the minimum level of sidebands in the spectrum at the mixer output. These sidebands are the result of the combination of frequencies generated in the nonlinear mixing process as well as the introduction of undesirable phase modulation. Tests indicate that the level of these sidebands at



the 57/221 output in the modified design are low enough to remain more than 40 db below the desired signal after being multiplied in the $\times 32$ frequency multiplier.

G. Range Receiver

In the Deep Space Net (DSN) 1964 receiver-exciter system (SPS 37-28, Vol. III, pp. 30-39) the voltage controlled oscillators (VCO's) in the range receiver and code clock transfer loops have crystals at the clock frequency. Since the clock frequency is related to the S-band exciter frequency (f_t) by the factor $(5/221)(f_t/96)$, it is necessary to replace the crystal in the range receiver and transfer loop VCO's each time the exciter channel is changed. The necessity for changing VCO crystals is being eliminated in the Manned Space Flight Net (MSFN) and future DSN systems by the injection of a reference signal into these loop VCO's (Fig. 30). The VCO output frequency (clock) is the difference between the reference signal and the 680-kc VCO signal.

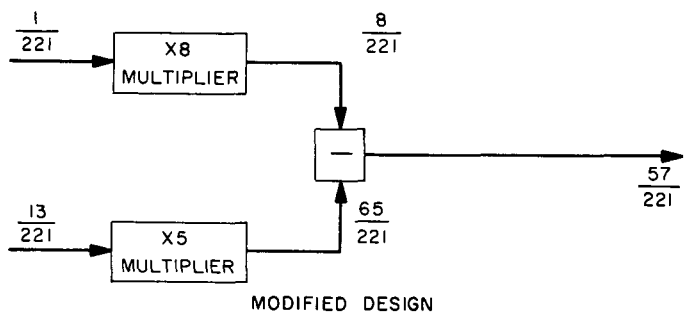


Fig. 29. Block diagram 57/221 frequency multiplier subassembly

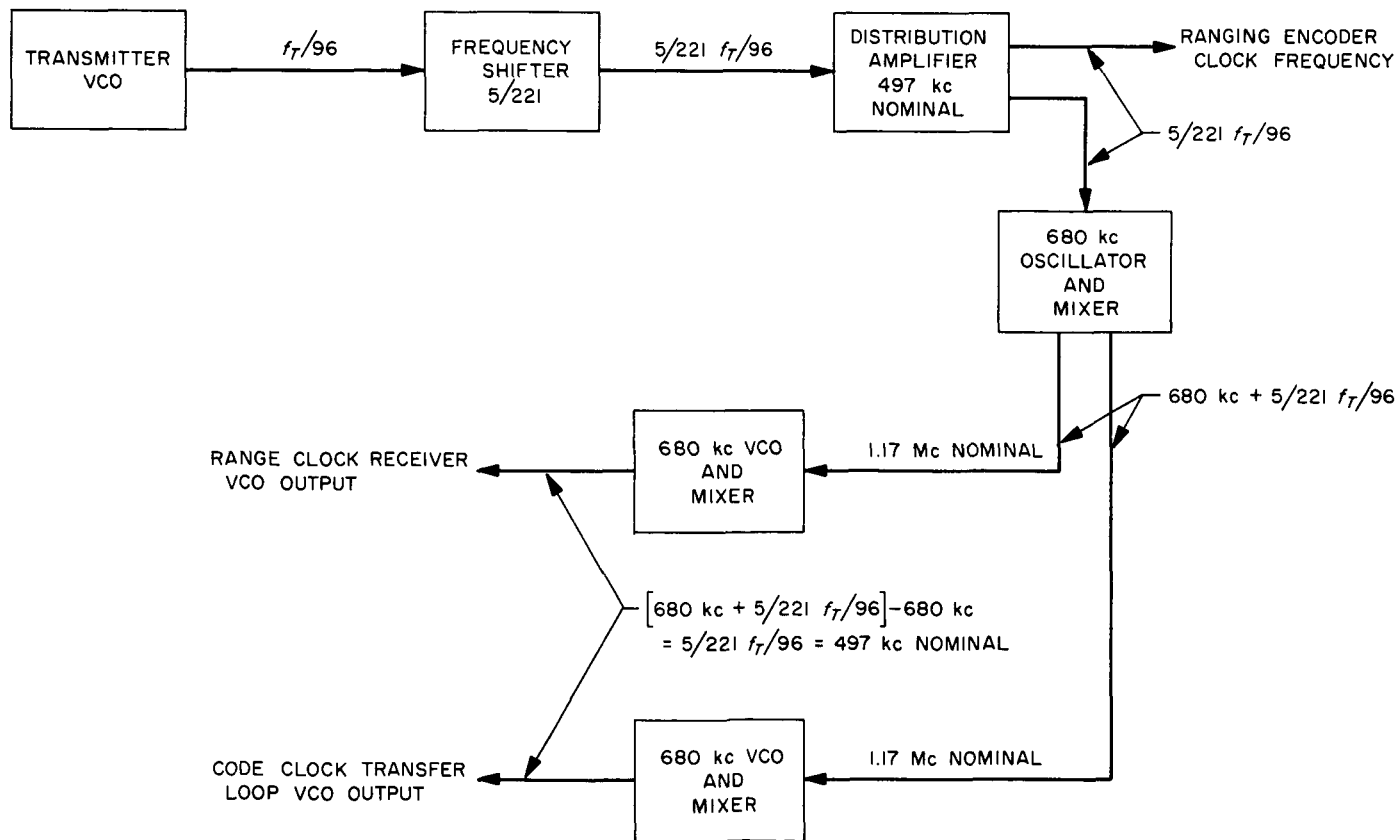


Fig. 30. Block diagram—range and code clock loop

The reference frequency for the VCO units is generated within a new module design, a 680-kc oscillator/mixer. This unit contains an internal 680-kc crystal controlled oscillator and a balanced mixer. The 680-kc signal is summed with the clock signal generated from the exciter VCO. Since the clock signal is changed as the exciter VCO is transferred from one channel to another, the reference signal frequency will also follow the exciter frequency changes. The range receiver VCO output frequency will, therefore, maintain its coherent relationship with the exciter VCO without the necessity of a crystal change.

Fig. 31 is a graph of the VCO characteristics within a typical 680-kc VCO/mixer unit. Fig. 32 shows the conversion bandpass characteristics between the 1.17-Mc reference input terminal and the 497-kc output terminals

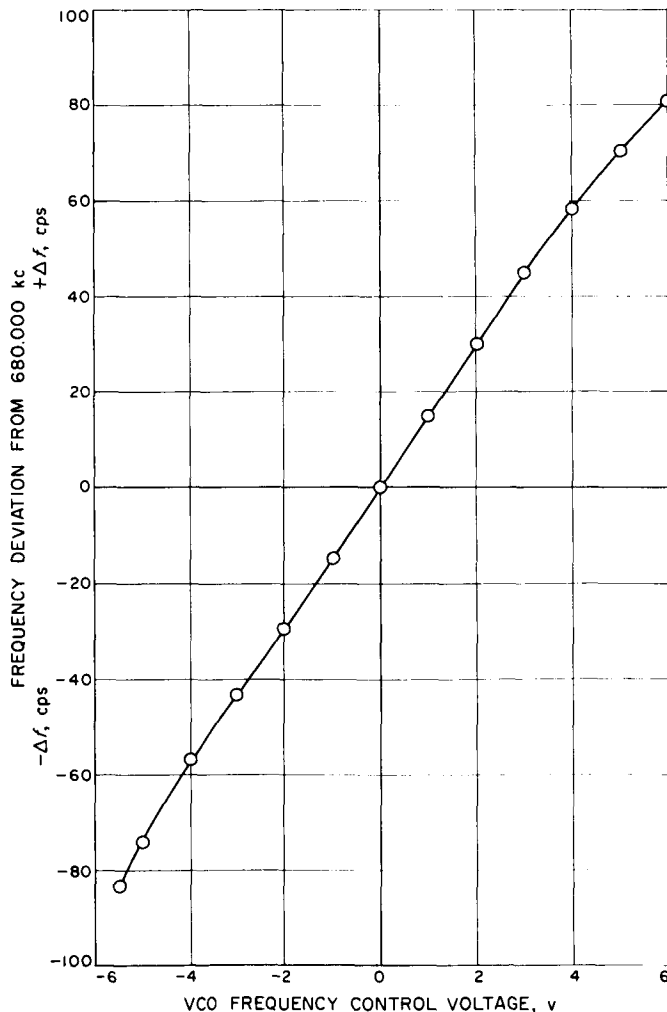


Fig. 31. 680-kc VCO frequency vs control voltage

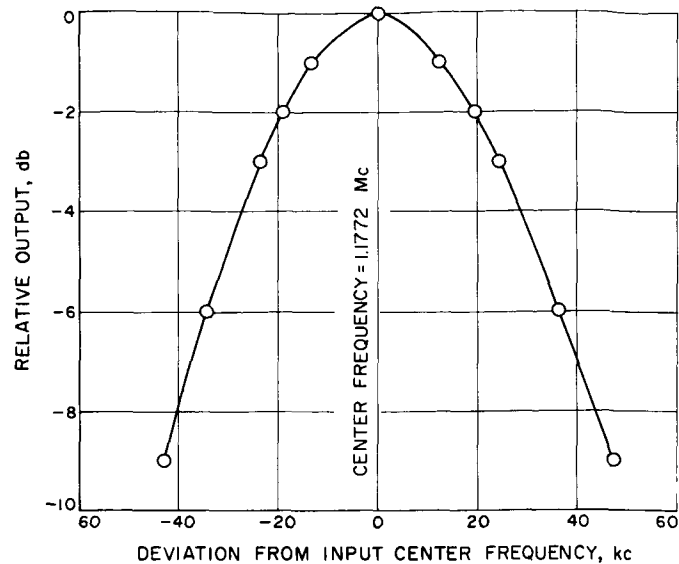


Fig. 32. Conversion bandpass characteristics 680-kc VCO/mixer

on a typical VCO/mixer unit. The reference input frequency range, for an equivalent deviation of ± 10 Mc at the exciter S-band frequency (which covers the coherent MSFN and the DSN bands), is approximately ± 2.5 kc. Measurements of the VCO stability of the oscillator/mixer configuration indicate comparable performance with the 1964 DSN receiver-exciter system (SPS 37-28 and 37-32, Vol. III, pp. 30-39, 10, respectively). There is no measurable degradation in phase stability resulting from the use of the oscillator/mixer technique. In addition, evaluation of this technique indicates that there is no measurable leakage of the reference clock signal from the exciter into the receiver range and code clock transfer loops.

H. $\times 8$ Doppler Multiplier

The existing doppler measurements are related to the receiver frequency in the S-band communications system (Fig. 33). However, there is an increasing need for more resolution in doppler measurements in both the MSFN and DSN. There are practical hardware limitations to the improvement that can be obtained from doppler multiplication, such as oscillator stability, receiver noise at low signal levels and the ability of the data reduction equipment to handle the higher doppler frequencies.

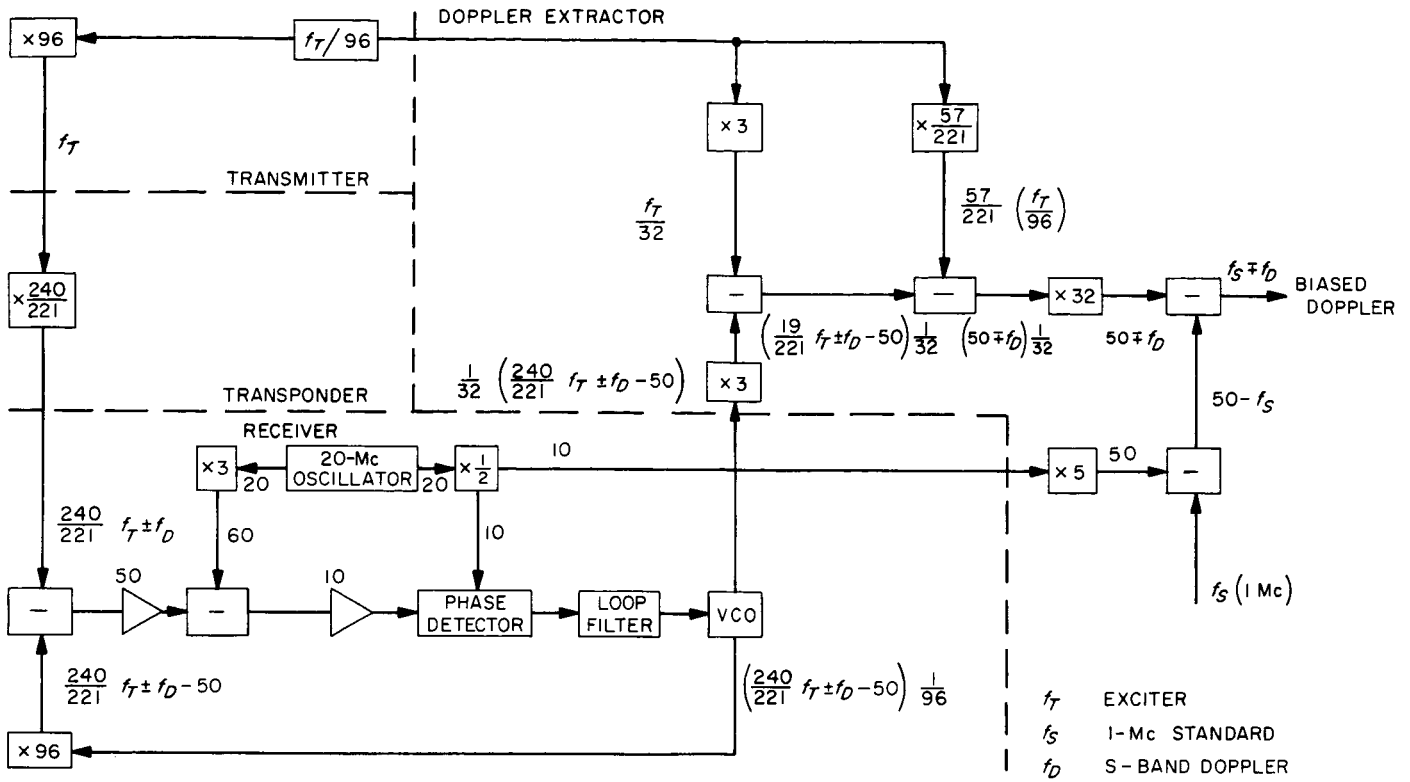


Fig. 33. S-band doppler block diagram

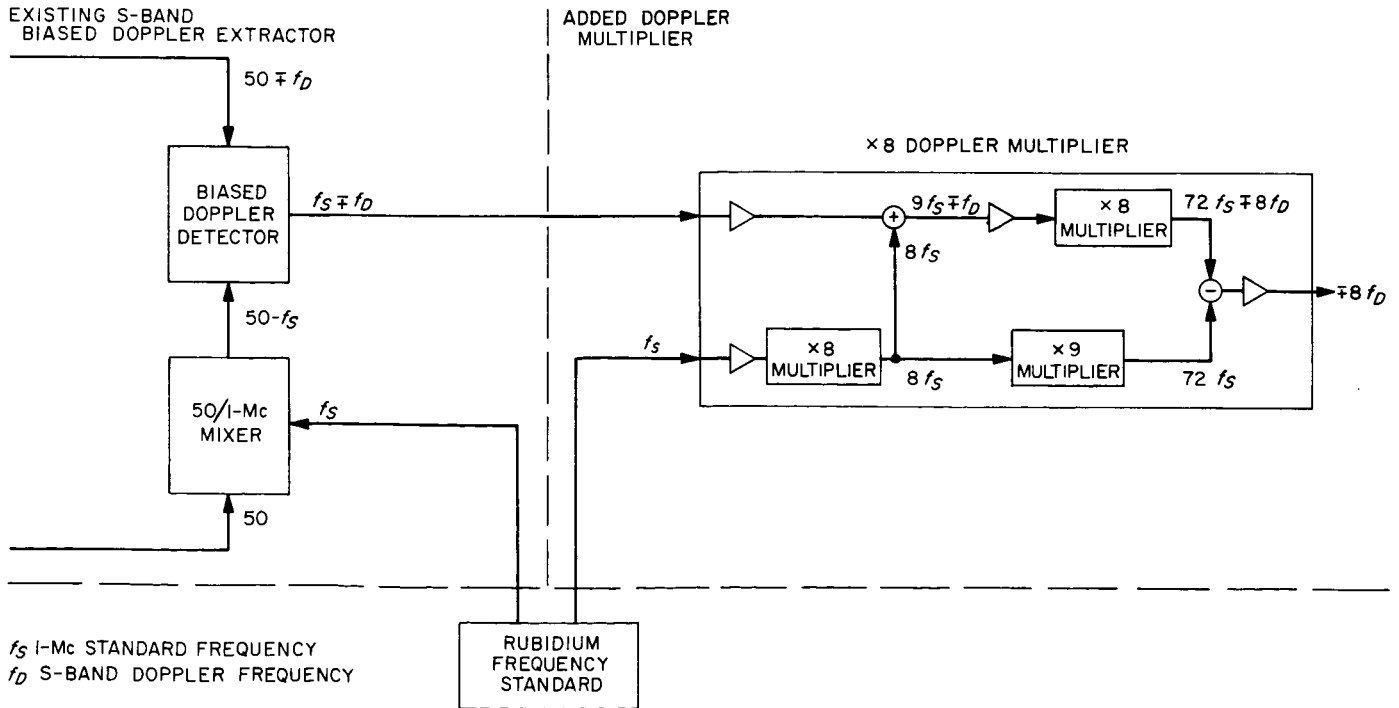


Fig. 34. $\times 8$ doppler multiplier block diagram

Evaluation of the usefulness of increased doppler resolution is now in progress at the Goldstone Pioneer Station in a feasibility study of a prototype doppler multiplier.

Fig. 34 is a functional block diagram of this $\times 8$ doppler multiplier showing its connection to the present doppler extractor system. This particular mechanization was selected so that it could be added to the present doppler extractor without any change in the existing design. To maintain the doppler frequency within the capability of the data handling equipment, it was decided not to provide a frequency bias. The criteria for the final configuration of a doppler extractor with increased resolution would be determined primarily by what is considered a practical multiplication factor.

Preliminary results of the analysis of of doppler data, recorded during several *Mariner IV* tracking periods through the $\times 8$ multiplier, indicate some increase in the resolution attainable. If the evaluation of the prototype doppler multiplier indicates a significant improvement, this particular multiplier will be used during the *Mariner IV* occultation experiment. Further evaluation will continue to determine the optimum multiplication factor and mechanization of increased doppler resolution for use in the MSFN and DSN.

I. Venus Station *Mariner IV* Support

1. Introduction

A ground transmitting power of 100 kw (CW) will be required for the *Mariner IV* program under certain operating conditions. The 100-kw amplifier portion of this high power facility has been discussed in SPS 37-25 through 37-32, Vol. III. In addition to the klystron amplifier portion, the high power facility includes the amplifier exciter, RWV equipment microwave link to the Pioneer Station (DSIF-11), and a $\times 6$ loop at the Pioneer Station to obtain the necessary reference for doppler measurements.

2. Incidental Phase Modulation

In SPS 37-32, Vol. III, p. 32, the incidental phase modulation on the transmitter signal, due to power supply ripple, was discussed. The source of the power supply ripple was determined to be the series limiter tube. This was replaced with a series resistor in the high voltage line to the klystron. A test was then performed to establish the incidental phase modulation first from the exciter alone and second from the exciter-klystron amplifier combination (Fig. 35). The two synthesizers were required

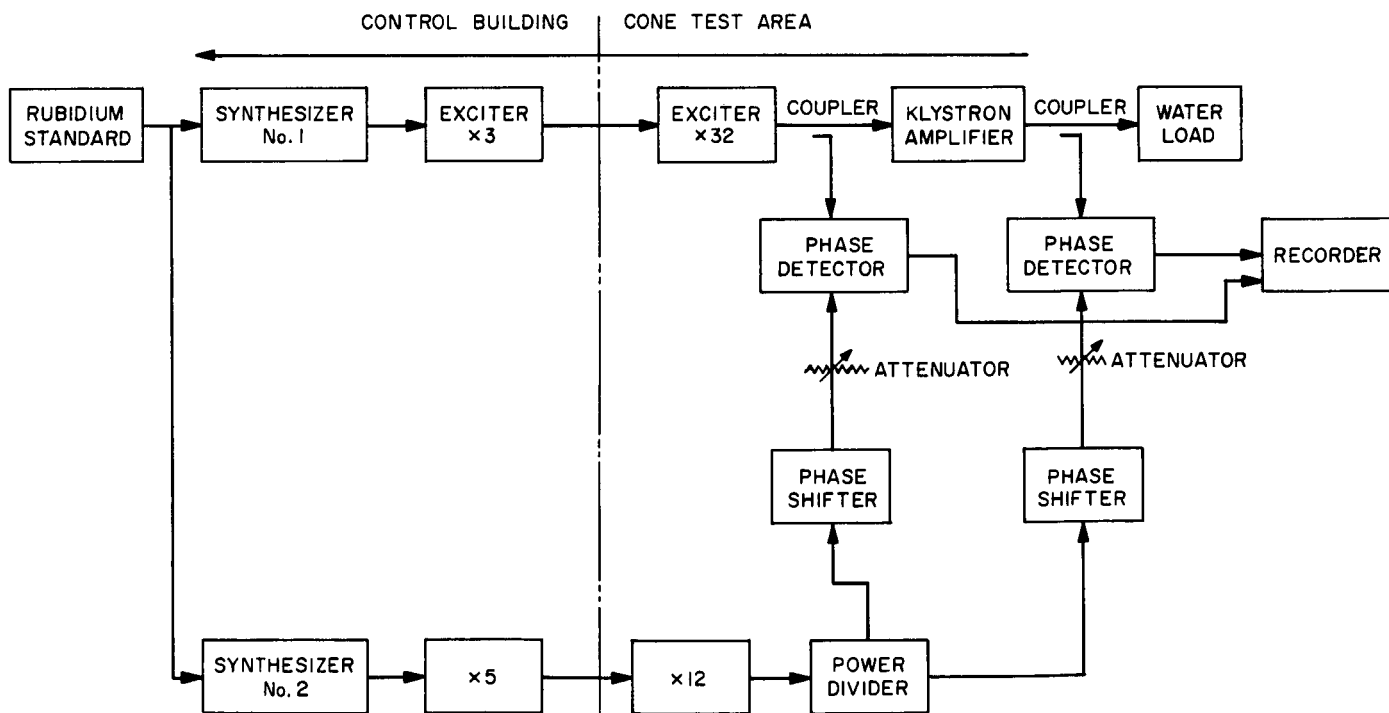


Fig. 35. Exciter-amplifier incidental phase modulation test setup

since the only channel, other than the exciter, available in this frequency range had a multiplication factor of 60. Synthesizer No. 1 was set at 22.038540 Mc, and synthesizer No. 2 was set at 35.261665 Mc. The resultant frequency into the phase detectors was then 2115.699840 Mc, and the phase detector output was the instability between the two systems. To incorporate frequency into the calibration curve for ± 90 deg, synthesizer No. 1 was changed by 0.2 cps, which produced a low frequency beat at the output. Results of the instability measurement are shown in Fig. 36. The RMS incidental phase modulation from the exciter was 6.4 deg and from the exciter-klystron amplifier combination 6.8 deg. This incidental phase modulation of 6.8 deg from the 100-kw transmitting subsystem at the Venus Station established the basic minimum phase error prior to making the additional incidental phase modulation measurements described below.

During this reporting period, three operational tests have been conducted with *Mariner IV*, using the 100 kw transmitter system at the Venus Station (DSIF-13) and the Pioneer Station receiver. These tests have been satisfactory, locking the up-link with the high power transmitter was done without difficulty. These operational tests have also included satisfactorily locking the spacecraft command link. However, when the data were reduced, the doppler residuals were found to be greater

than those obtained when the Pioneer Station was both transmitting and receiving.

When the Venus Station's 100-kw transmitter is used, the Venus exciter VCO frequency is divided by six to approximately 3.7 Mc and sent to the Pioneer Station over the microwave link. At the Pioneer Station the 3.7 Mc is multiplied by six to regain the exciter VCO frequency for use in extracting the spacecraft doppler. A series of tests was run to determine the cause of the increase in the doppler residuals, and they are described below.

The equipment arrangement for the tests is shown in Fig. 37. Using this setup, the incidental phase modulation for the basic Venus exciter loop was measured to be 0.06-deg RMS (Fig. 38).

To determine the incidental phase modulation due to the 1/6 and $\times 6$ modules, these modules were inserted in the exciter loop at Point A of Fig. 37. The results of this measurement are shown in Fig. 39. The RMS incidental phase modulation increased to approximately 0.068 deg, demonstrating that the contribution of the division and multiplication equipment was not significant.

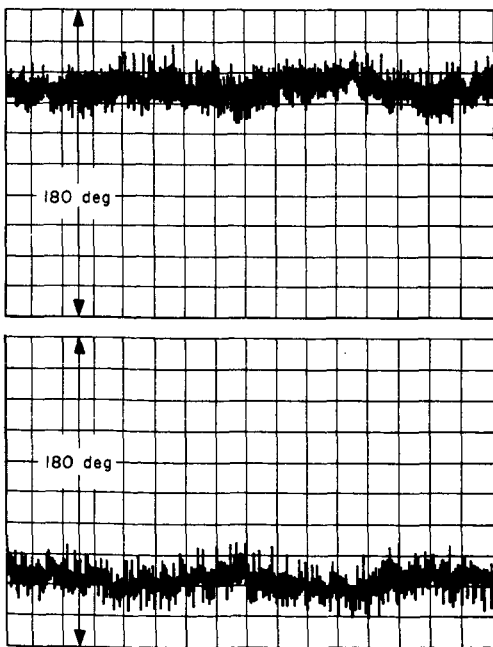


Fig. 36. Incidental phase modulation from 2116-Mc exciter and klystron amplifier

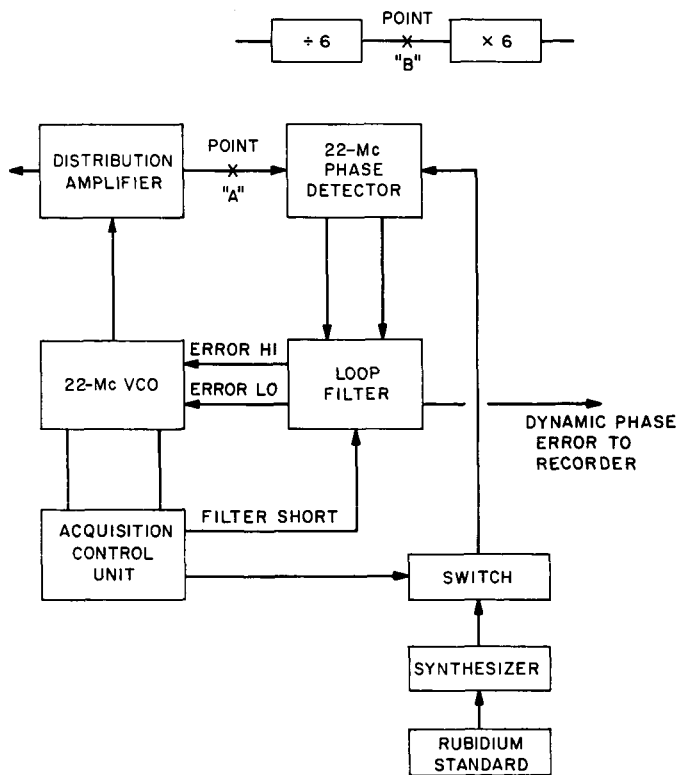


Fig. 37. Microwave link incidental phase modulation test setup

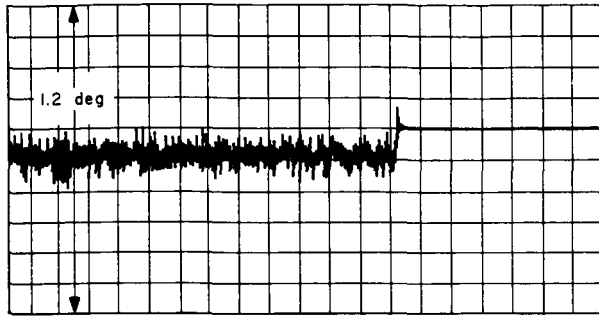


Fig. 38. Incidental phase modulation for Venus exciter loop

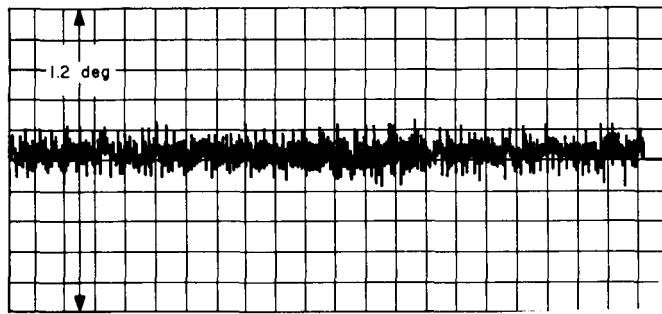


Fig. 39. Incidental phase modulation with 1/6 and $\times 6$ modules inserted at point "A" of Fig. 37

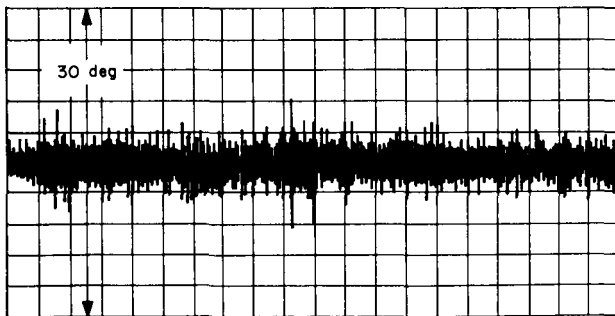


Fig. 40. Incidental phase modulation with microwave link inserted at point "B" of Fig. 37

The 3.67-Mc signal was then sent via the microwave link from the Venus Station to the Pioneer Station and back and inserted at Point B in Fig. 37 with the 1/6 and $\times 6$ modules inserted at Point A, as above. The incidental phase modulation measured 2.6 deg RMS (Fig. 40). To determine the incidental phase modulation that can be attributed to a one-way path over the microwave link, this value should be divided by $(2)^{1/2}$ to obtain a one-way value of 1.8 deg RMS.

To compare this incidental phase modulation, resulting from the microwave link, with the 6.8-deg RMS from the exciter-klystron amplifier combination, the 1.8-deg RMS must be multiplied by 96 to be at the same frequency.

It is evident from the above tests that the increase in the doppler residuals, when the Venus Station is used as the transmitting station, is attributable to the incidental phase modulation introduced by the microwave link. During the next reporting period further tests will be made to determine the best method of removing this source of error.

J. Venus Station Mariner IV Encounter Receiver

1. Introduction

The *Mariner IV* support project (SPS 37-32, Vol. III, and earlier) at the Venus Station includes, in addition to the 100-kw transmitting capability and the suitcase telemetry reception for *Mariner* during the flights of *Rangers VIII* and *IX*, a low-noise, narrow- and broad-band, flexible receiving capability for use during the encounter phase. This capability will be achieved by the use of planetary radar techniques and hardware, adapted to the operational frequency and telemetry requirements. In addition to telemetry reception just prior to encounter and for some weeks after, it is planned to record the received spectrum during the period of occultation for later analysis in conjunction with a similar experiment to be conducted simultaneously at the Pioneer Station.

2. Implementation

As shown in Fig. 41, the present Mod IV lunar and planetary radar receiver will be used extensively in this application. Except for the programmed local oscillator (PLO), which is to be slightly modified, the balance of the equipment will be specially installed. The latter consists of an antenna-mounted S-band to 30-Mc converter and a one-bay rack containing the local oscillator components and a commercial frequency synthesizer. Two open loop modes for occultation and three basic telemetry modes (Fig. 41) offer a high degree of reliability, both from the equipment standpoint and the ability to optimize local oscillator purity with respect to signal strength

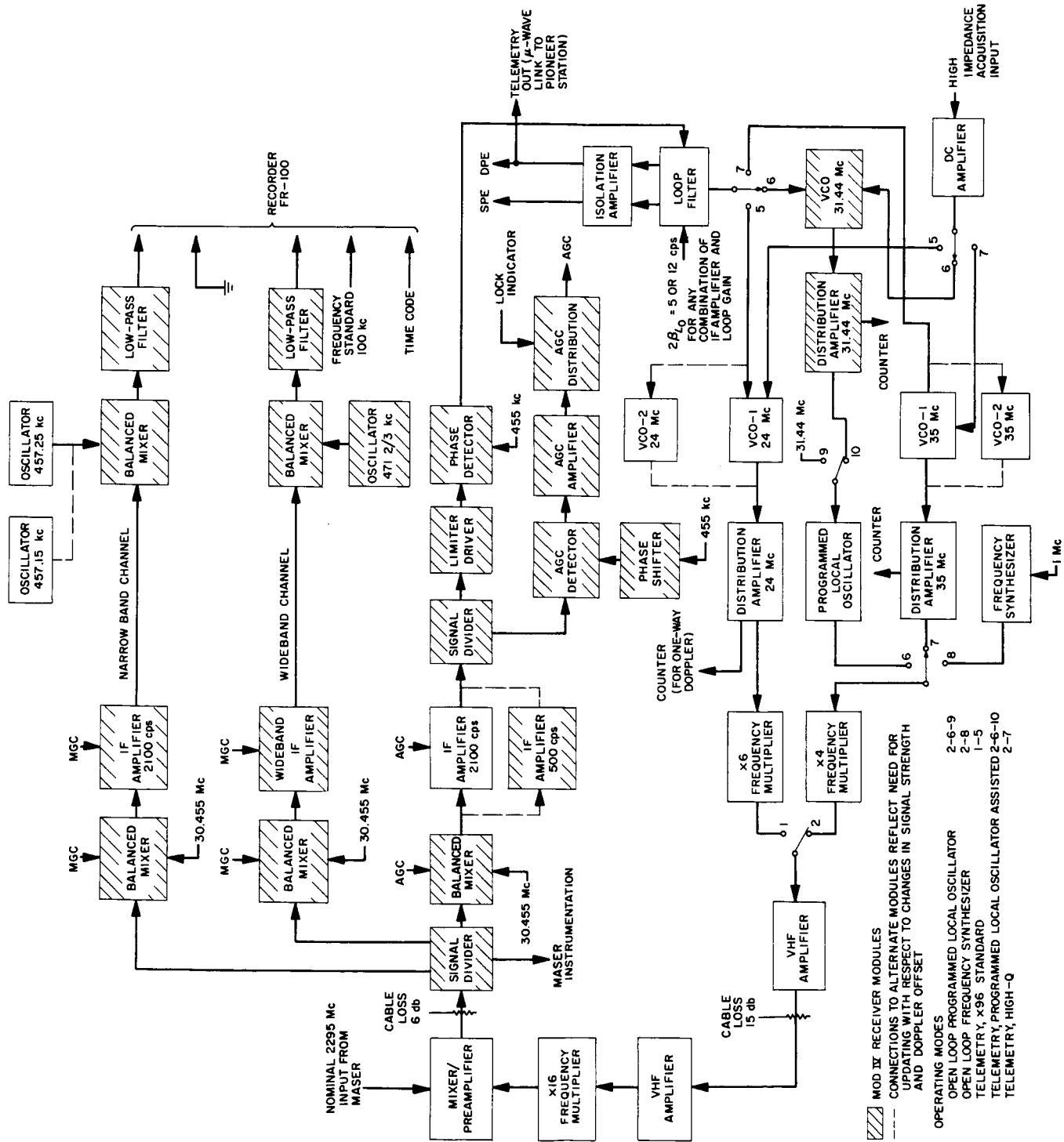


Fig. 41. Venus Station/Mariner encounter receiver

and *a priori* doppler data. To minimize operating difficulties, the various controls have been interlocked to provide panel selection of any one of the five basic modes tabulated in Fig. 41 and the independent selection of two loop bandwidths for telemetry. Standard loop bandwidth is provided, with oscillator tracking ranges and

stabilities comparable to those of the DSIF. In addition, it is expected that postcounter tracking with one-way doppler will be extended to the limit of the capability of

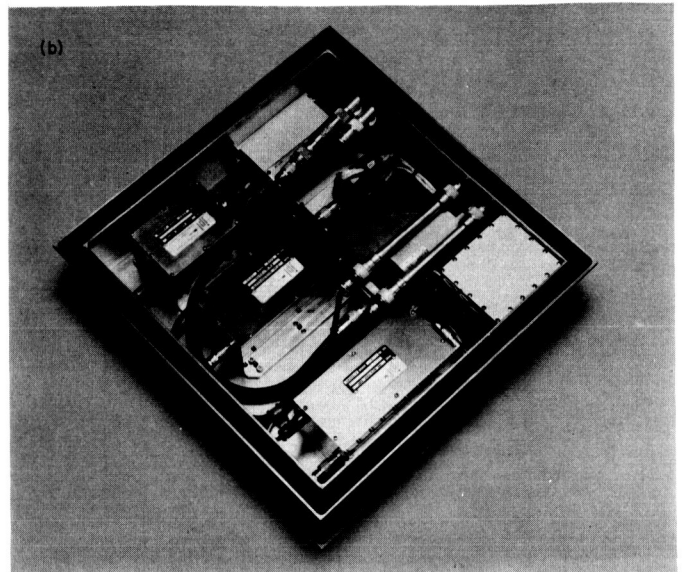
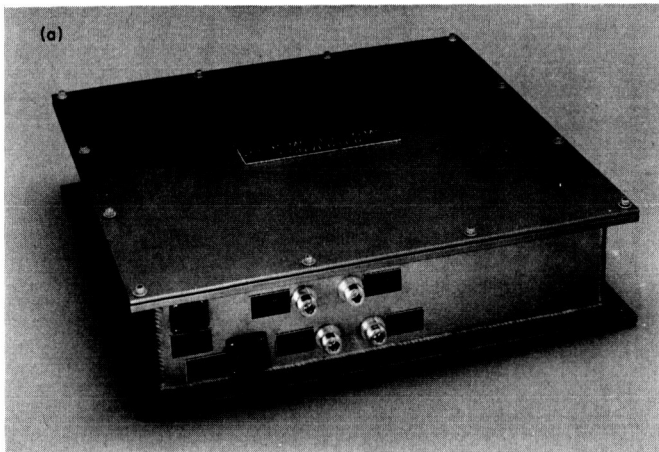


Fig. 42. S-band converter (a) front view, (b) cover removed

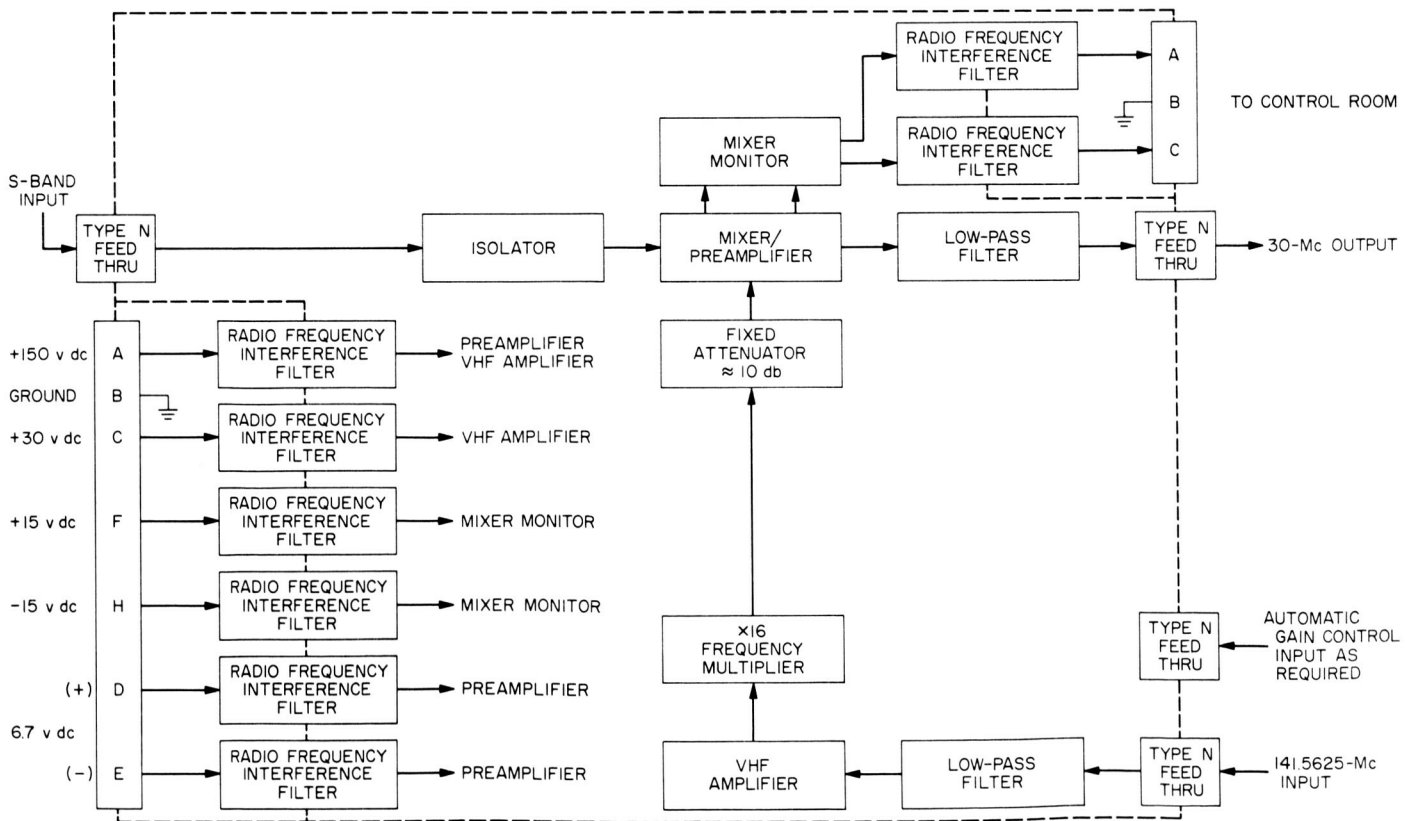


Fig. 43. 2295- to 30-Mc converter

a 5 cps ($2B_{L_0}$) threshold. This is being implemented in two ways: (1) by using the "high-Q" low phase noise voltage controlled oscillator (VCO) of the lunar and planetary radar with doppler offset accomplished by the PLO; and (2), as an alternate, three similar high-Q VCO's will be available on center frequencies selected by means of the trajectory data presently available; each of them will track unassisted over a comparatively narrow range.

Preliminary system testing has been completed on all new equipment except high-Q VCO's, using the S-band transponder ranging station at JPL (SPS 37-32, Vol. III, p. 62) in lieu of the required portions of the Venus Station Mod IV receiver. Final assembly of the special bay, utilizing the prechecked subsystem described above, is presently being done, with the Goldstone installation anticipated during the month of May, 1965. The antenna cone equipment (power supply, cabling, and converter mock-up) were installed during January while the maser and waveguide modifications were being made.

Figs. 42 and 43 show the configuration of the S-band converter which was originally designed for a laboratory

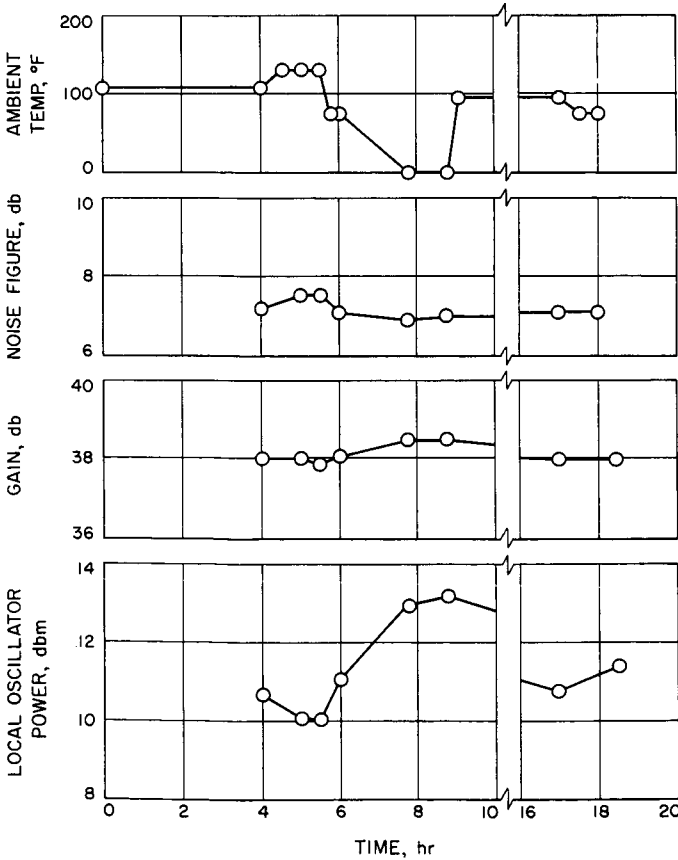


Fig. 44. Converter temperature data

test system. The mixer/preamplifier is of a type previously evaluated and reported in SPS 37-26, Vol. III, pp. 45-47.

3. Test Data

The over-all converter performance at room temperature is as follows:

Conversion gain	39.0 db
Noise figure, double sideband	7.0 db
Bandwidth (3 db)	8.5 Mc
Mixer balance	23.0 db

A temperature test (Fig. 44) was performed simulating the extremes to be expected in operation. Not plotted are IF bandwidth data which revealed no measurable change. The changes in gain and noise figure, while tolerable due to periodic system calibrations, reveal excessive variation in local oscillator drive power to the mixer. The instability probably resulted from redesign of the purchased $\times 16$ frequency multiplier, since originally the supplier's test data indicated approximately 1-db variation over a comparable temperature range. The redesign referred to was necessitated by "break-up" and excessive broadband noise, including the 30-Mc removed signal band, both as a critical function of multiplier input level. These effects have been eliminated from this unit by means of varactor bias and coupling changes. The problem is currently under investigation on a second unit and is closely related to the problems encountered at X-band (SPS 37-31, Vol. III, p. 53). Closed loop, strong signal oscillator phase jitter has been evaluated on several oscillators, as shown in Table 5. The oscillators labeled

Table 5. Strong signal phase jitter, simulated threshold

Receiver Oscillator (identified by expected doppler)	$2B_{L_0}$ cps	Goldstone duplicate standard test transmitter source, deg rms	Commercial synthesizer source, deg rms
5.5 km/sec (interim)	12	5.5	4
12.5 km/sec (interim)	12	7	7
12.5 km/sec (specification)	12	3.5	2
18.9 km/sec (specification)	12	3	2.5
Hi-Q (projected)	12	—	1.1
Hi-Q (projected)	5	—	2.5

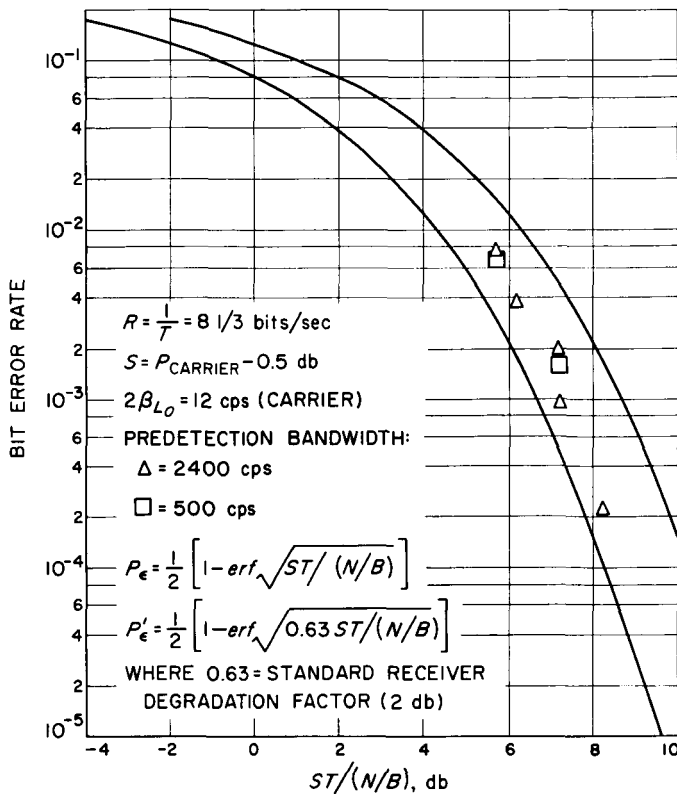


Fig. 45. Telemetry threshold performance

“interim” utilize crystals urgently procured shortly after the first of the year to be available in the event this system would have been required in March. The improved performance of the “spec” (procured to specifications for low noise use) crystals in the same two oscillators meets expectations. Comparison of the figures for test transmitter versus synthesizer source is difficult to interpret due to the fact that the spectrum of noise exhibited by the test transmitter and receiver oscillators is much narrower (tens of cycles per second) than that of the synthesizer (hundreds or thousands of cycles per second). Spectral

properties of this type of synthesizer are presently under independent study.

The final test conducted to date was concerned with telemetry compatibility. In addition to routine checking of a specially adapted research and development receiver, it was considered advisable to determine what, if any, degradation would be experienced due to predetection filtering to 500-cps bandwidth. For simplicity this receiver uses the same signal channel and phase detector for both carrier tracking and telemetry detection. The intended use of 5-cps threshold bandwidth requires a relatively narrow predetection bandwidth. The point of concern is that at the present *Mariner IV* telemetry bit rate of $8\frac{1}{3}$ cps, there is significant sync power over a 600-cps band. As shown in Fig. 45, no detectable degradation in bit error rate was evident. The data of Fig. 45 show the results of a total of seven tests using different signal levels and predetection bandwidths. The basic probability curve (Ref. 4) describes average ideal performance. The adjusted curve to the right in Fig. 45 is considered nominal performance. The fit of the data to this curve is reasonable, considering that the absolute tolerance of the signal power was estimated to be $\pm \frac{1}{2}$ db and the noise spectral density to be $+0, -1$ db.

4. Conclusion

It appears that the receiver objectives will be met. Given the adaptation to the operational frequency, the existing radar largely provides the capability of occultation reception, the success of which will be largely dependent upon real time frequency prediction and post-encounter data processing. However, the overall Venus Station *Mariner* operation involves the likelihood of transmitter operation during the encounter phase (during which reception will be interrupted) and scheduling considerations with respect to the lunar and planetary radar experiments.

References

1. C. G. Montgomery, et al., "Principles of Microwave Circuits," MIT Radiation Laboratory Series, Vol. 8, McGraw-Hill Book Company, New York, 1948, pp. 459-466.
2. Victor, W. K., and Brockman, M. H., "The Application of Linear Servo Theory to the Design of AGC Loops," Proceedings of the IRE, Vol. 48, February 1960, pp. 234-238.

References (Cont'd)

3. Viterbi, A. J., "Acquisition and Tracking Behavior of Phase-Locked Loops," External Publication 673, Jet Propulsion Laboratory, Pasadena, July 14, 1959.
4. Springett, J. C., *Telemetry and Command Techniques for Planetary Spacecraft*, Technical Report No. 32-495, Jet Propulsion Laboratory, Pasadena, January 15, 1965.

IV. Communications Research and Development

A. Ground Antennas

1. Calibration of 2388-Mc Planetary Radar Feedcone

a. Insertion loss. For determination of low-noise antenna temperature, the effective antenna temperature usually is compared to the effective noise temperature of one or two cryogenic noise standards on a radiometric system. For defining effective noise temperature of these noise sources at a common reference point (usually maser input), VSWR's and insertion losses of interconnecting transmission lines must be known accurately.

VSWR and insertion loss measurements recently were made for the noise source-to-maser interconnecting transmission lines on the new 2388-Mc R&D cone at the Venus Station. The redesigned cone layout was described in *SPS 37-31*, Vol. III, p. 56. Fig. 1 is a block diagram showing the transmission lines which were measured.

These insertion loss and VSWR measurements were made at 2388-Mc using an AC ratio transformer insertion loss measuring system and a waveguide reflectometer system, respectively. Results of these measurements are summarized in Table 1.

b. Microwave thermal noise termination. The traveling wave maser (TWM) for the 2388-Mc radar system used on the 85-ft antenna at the Venus Station was rebuilt and repackaged in the closed cycle refrigerator (*SPS 37-31*, Vol. III, p. 56). The waveguide instrumentation is shown in Fig. 1. A liquid helium cooled termination was included in the maser closed cycle refrigerator for calibration purposes, to replace the open cycle Dewar cooled load used previously. A liquid helium cooled waveguide termination in an open glass Dewar which can be connected periodically to the calibrate waveguide switch for precise, absolute calibrations has been completed (Fig. 2) and installed in an open Dewar in the cone at a 30-deg bias to the vertical. The intake and exhaust tubes are connected to

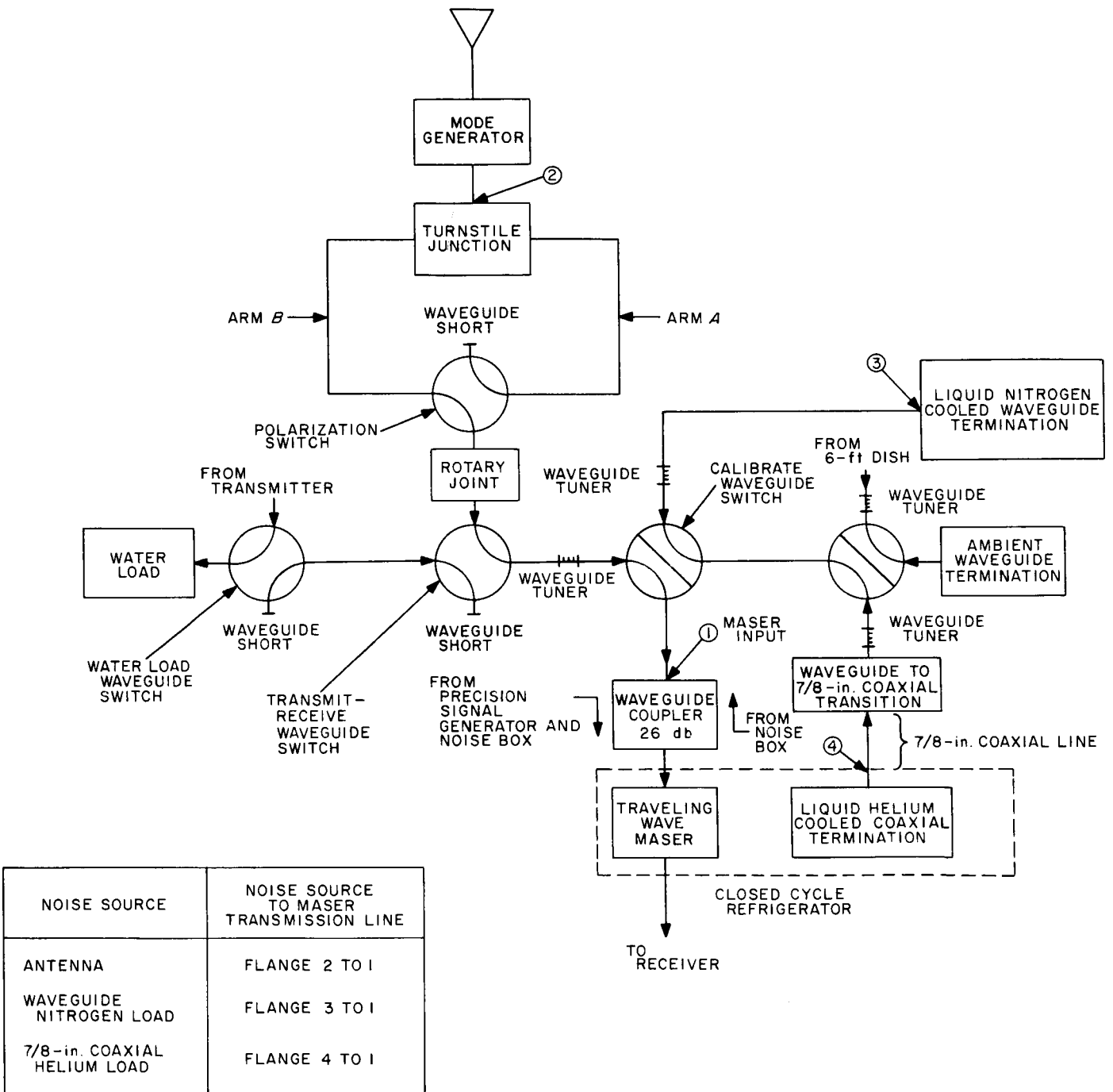


Fig. 1. 2388-Mc R&D cone diplexer-calibrate system

Table 1. Measured transmission line parameters of the 2388-Mc R&D cone diplexer—calibrate system

Antenna receive line	
VSWR looking into Flange 1 with matched circular waveguide load on Flange 2; (turnstile assembly rotated)	
Via Arm A	1.051 minimum 1.054 maximum
Via Arm B	1.038 minimum 1.047 maximum
Dissipative insertion loss between Flange 1 and 2 for case of matched source and matched load ^a	
Via Arm A	0.068 ± 0.005 db, probable error
Via Arm B	0.067 ± 0.005 db, probable error
Waveguide nitrogen load line	
VSWR looking into Flange 1 with matched waveguide load on Flange 3	1.01 ± 0.01
Dissipative insertion loss between Flange 1 and 3 for the case of matched source and matched load	0.038 ± 0.003 db, probable error
7/8-in. coaxial helium load line	
VSWR looking into Flange 1 with matched load on Flange 4	1.40 ± 0.18
Dissipative insertion loss between Flange 1 and 4 for the case of matched source and matched load	0.16 ± 0.13 db, ^b total uncertainty
^a The term, dissipative insertion loss for the matched source and matched load case, as used in this table, corresponds to Beatty's definition of the dissipative component of attenuation (Ref. 1)	
$A_{il} = 10 \log_{10} \left[\frac{1 - S_{11} ^2}{ S_{21} ^2} \right]$	
^b This particular insertion loss measurement was a nonprecision measurement due to the use of an unmatched single-channel bolometer system and a standing wave indicator. The VSWR of the bolometer load assembly was 1.11 ± 0.01 and the 7/8-in. helium load line was not tuned out for this measurement.	

projections on the outside of the cone (Fig. 3) to facilitate filling with liquid nitrogen. The liquid nitrogen life is approximately 24 hr in the laboratory and 20 hr mounted in the cone, under normal moving antenna operation. The documentation of the termination and Dewar is given in JPL prints No. 128349 to 128368, inclusive. Accurate thermal temperature measurements are provided for the ambient waveguide termination with a thermistor thermometer with remote readout.

c. Calibration. Results of the recent waveguide insertion loss recalibration measurements in the cone, described

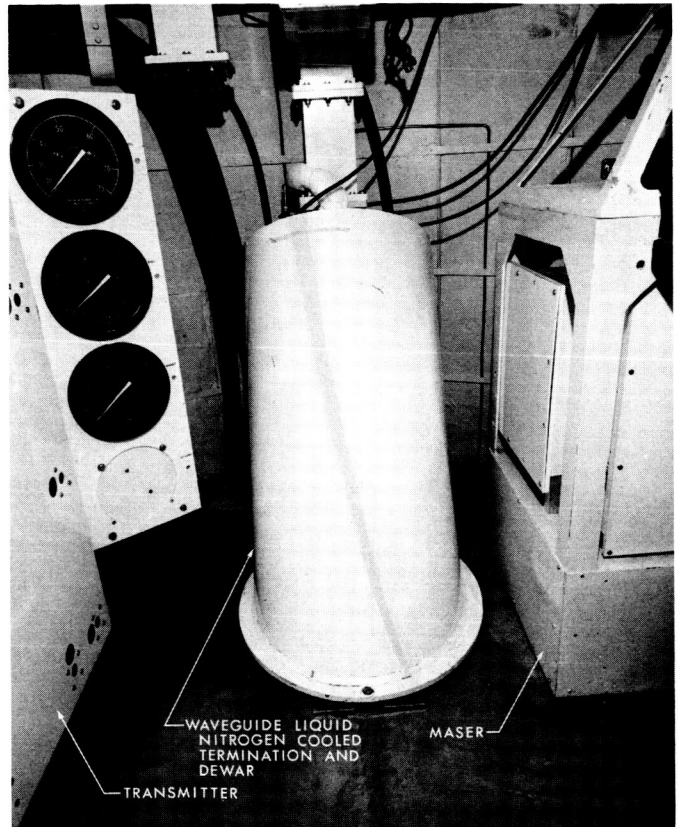


Fig. 2. WR-430 waveguide liquid nitrogen cooled termination installed in 2388-Mc cone on the 85-ft antenna at the Venus Station

previously, require the recalibration of the nitrogen cooled thermal termination. The insertion loss between this point and the maser input (defined at the input to the 26-db waveguide directional coupler) is 0.038 db. The original measurement at JPL on November 6, 1964 (immediately after the waveguide installation), indicated 0.029 db. It is anticipated that the waveguide insertion loss measurements will be repeated at some future date to indicate the long-term stability of these calibrations. The recalibration also accounts for changes in atmospheric pressure for the liquid nitrogen cooled termination. A convenient approximation for the equivalent noise temperature T' of a microwave thermal noise source accounting for first-order effects of transmission line losses, external temperature, and cryogenic temperature pressure dependence is given by (SPS 37-32, Vol. IV, p. 247)

$$T' = T(760) + a\Delta P + 0.23026 [T_0 - T(760)] \times \left[\frac{L_1}{2} (\text{db}) + L_2 (\text{db}) \right] \quad (1)$$

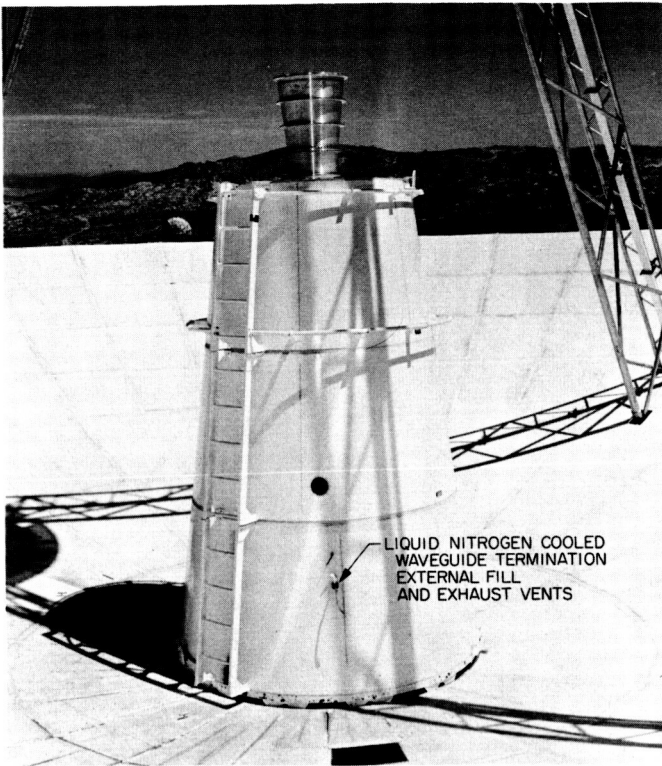


Fig. 3. 2388-Mc cone on 85-ft antenna of the Venus Station, showing intake and exhaust tubes on the liquid nitrogen cooled waveguide termination

where

$T(760)$ = liquid temperature at a pressure of 760 mm Hg

ΔP = pressure deviation in mm Hg

a = proportionality constant of the cryogenic liquid ($^{\circ}\text{K}/\text{mm Hg}$)

T_0 = ambient temperature

L_1 = transmission line losses occurring over that portion of the line which has a temperature distribution between ambient temperature and the cryogenic temperature.

L_2 = transmission line losses at ambient temperature

For the waveguide liquid nitrogen cooled termination with the equivalent noise temperature defined at the maser input

$$a = 0.011^{\circ}\text{K}/\text{mm Hg}$$

$$L_1 = 0.0067 \text{ db}$$

$$L_2 = 0.0479 \text{ db}$$

resulting in

$$T_N (\text{waveguide termination}) \simeq 76.45 + 0.011\Delta P + 0.0118 T_0 \quad (2)$$

The liquid helium cooled waveguide termination installed in a 10-liter glass Dewar is used on a periodic basis to calibrate the gas tube. The equivalent noise temperature of this termination defined at the output flange is 6.2°K . Accounting for the preceding 0.038-db waveguide losses to the maser input (Ref. 2)

$$T_H (\text{waveguide termination}) \simeq 6.15 + 0.0087 T_0 \quad (3)$$

The temperature pressure dependent term has been dropped since it is small ($\approx 0.0014^{\circ}\text{K}/\text{mm Hg}$; Ref. 3).

The coaxial transmission line liquid helium cooled termination is calibrated radiometrically with the ambient temperature waveguide termination for most accuracy and is typically $\approx 35^{\circ}\text{K}$, defined at the maser input. An estimate can be made of the equivalent noise temperature of this termination from the insertion loss measurements.

For this termination

$$L_1 = 0.0974 \text{ db} \pm 0.002 \text{ (Maury Microwave Corp., manufacturer)}$$

$$L_2 = 0.1802 \text{ db} \pm 0.13 \text{ db (Part Ia of this article)}$$

Then with $L_2 = 0.1802$, and using the second-order terms in the equivalent noise temperature expansion necessary with the high insertion loss (Ref. 2)

$$T_H (\text{coaxial termination}) \simeq 0.953 T + 0.0466 T_0 \quad (4)$$

With $T = 4.3^{\circ}\text{K}$, and $T_0 = 294^{\circ}\text{K}$, this reduces to

$$T_H (\text{coaxial termination}) \simeq 17.8^{\circ}\text{K}.$$

For the upper temperature limit the insertion loss of L_2 is 0.3102 db and

$$T_H (\text{coaxial termination}) \simeq 0.933 T + 0.0669 T_0.$$

And again, if $T = 4.3^{\circ}\text{K}$ and $T_0 = 294^{\circ}\text{K}$, this reduces to

$$T_H (\text{coaxial termination}) \simeq 23.7^{\circ}\text{K}.$$

These temperatures are considerably below the radiometrically measured temperature of the termination. The possible sources for the discrepancy are high coaxial transmission line connector losses or a poor heat sink of the termination to the final stage heat station of the

maser. A possible technique for checking the latter is to test a similarly constructed unit in the laboratory in a wet and dry liquid helium container.

2. Gain Calibration of 30-ft Antenna at 22 Gc

Sweep frequency radiometric observations of Venus centered at the water vapor line (13.5 mm) have been conducted jointly with personnel from the following JPL Sections: Lunar and Planetary Sciences, Communications Elements Research, Communications Engineering and Operations, and the Radioscience Group of Space Instruments. Observations consisted of precalibrations, operations during the near-conjunction period (June 18, 1964), and postcalibrations.

The Goldstone 30-ft reflector was utilized as a focal-point fed large aperture; D/λ ranged 630 to 730, and resulting half-power beamwidths in the order of 7 min of arc were measured.

Considerable attention was given to the problem of accurately determining the aperture efficiency. Three distinct approaches were taken: calculations of expected performance were made, calibrations using a far-field collimation station were performed, and radio-astronomical observations were conducted using the near bodies (Moon, Sun) and Taurus A.

Antenna pattern measurements, as well as the Dicke radiometer, have been reported previously (SPS 37-29, Vol. IV, pp. 122-131). This article will discuss the aperture efficiency calculations and collimation station calibrations; radio-astronomical results will be reported separately in a future JPL Technical Report.

a. Predictions. The feedhorn used for the 22-Gc work and the 30-ft aperture were examined carefully in order to calculate over-all efficiency. Table 2 lists contributions considered.

Table 2. 22-Gc gain prediction parameters

Item	Description
1	Amplitude efficiency, spillover loss (includes cross-polarization)
2	Phasefront efficiency (includes movement with frequency)
3	Insertion loss feedhorn output to reference point
4	Aperture blockage due to apex
5	Aperture blockage due to quadripod
6	Aperture shape, 16-sided polygon
7	Aperture surface loss

Amplitude and phasefront patterns of the feedhorn were measured at the JPL Mesa Antenna Range in the E-, H- and 45-deg planes at 20.79, 22.11 and 24.09 Gc; these frequencies were used in order to utilize existing high-stability signal availability.

The 18 amplitude patterns (normal and cross-polarized) were reduced using a JPL-developed computer program which numerically integrates the patterns to determine Items 1, 4, 5, and 6 (Table 2 and SPS 37-26, Vol. IV, p. 200).

The nine phasefront patterns and associated feedhorn phase center determinations showed no significant phase error for any given pattern (less than 10 deg) and furthermore, no significant (less than 0.05 in.) movement of phase center with pattern plane and/or frequency. The uncertainty in the efficiency calculations caused by phase error and antenna defocussing with frequency is expected to be ± 0.1 db for Items 1, 2, 4, 5, and 6 in Table 2.

The insertion loss and VSWR of the RG-53/U waveguide twist and 7.2-in. waveguide section combination (Item 3, Table 2) were measured with the DC potentiometer insertion loss test set (Ref. 4) at discrete frequencies between 20.6 and 24.0 Gc. The test set was matched at each frequency to a VSWR less than 1.02 in each direction. A circulator was needed between the unknown and the first directional coupler to reduce the error caused by the reflecting power due to the high VSWR of the twist at some frequencies. The insertion loss error is felt to be less than 0.01 db in Table 3.

Table 4 shows Items 1 through 6, inclusive, as functions of frequency. All were assumed to vary slowly and smoothly over the band, with the exception of Item 3.

Item 7 in Table 2, aperture surface loss caused by deviations of the paraboloid from a true figure, is not

Table 3. Feedhorn output to reference point characteristics

Frequency, Gc	VSWR	Insertion loss, db
20.6	1.60	0.344
21.0	1.15	0.337
21.5	1.25	0.373
21.9	1.24	0.365
22.5	1.17	0.443
23.0	1.16	0.472
23.5	1.08	0.440
24.0	1.09	0.405

Table 4. Gain factors as a function of frequency

Frequency, Gc	Loss relative to perfect surface 30-ft-diameter aperture, db						
	1	2	3	4	5	6	Total ^c
20.6	1.79	0.10 ^a	0.344 ^b	0.56	0.62	0.14	3.55
21.0	1.81	0.10	0.337	0.58	0.62	0.14	3.59
21.5	1.85	0.10	0.373	0.59	0.62	0.13	3.67
21.9	1.90	0.10	0.365	0.60	0.62	0.12	3.71
22.5	1.97	0.10	0.443	0.62	0.62	0.12	3.87
23.0	2.03	0.10	0.472	0.64	0.62	0.11	3.97
23.5	2.10	0.10	0.440	0.65	0.62	0.10	4.01
24.0	2.17	0.10	0.405	0.67	0.62	0.10	4.06

^aTolerance ±0.10 db, estimated
^bTolerance ±0.01 db
^cTolerance ±0.11 db, estimated

well known; however, it is felt that reliable bounds can be placed on the predictions.

As discussed on p. 14 of this report, several optical surveys of the 30-ft reflector have been conducted with the paraboloid pointing at the zenith and at the horizon; all data presented are applicable to the 22-Gc work.

Table 5 shows the allocations of surface accuracy components assumed for this study, as a function of elevation angle.

The general characteristics of the reflector are seen to degrade with look-angles near the horizon because of gravity-induced distortions. Best viewing is obtained at zenith. Mechanical uncertainties due to the exact shape of 32 individual surface panels being unknown (0.010–0.019 in.) for reflector panels, manufacture, and environmental uncertainties due to thermal gradients across the aperture being unknown (0.000–0.007 in.) for reflector structure, thermals, are shown in Table 5. Near-ideal environment is assumed to be satisfied, i.e., winds less than 5 mph. Predictions for higher winds further degrade

Table 5. Assumed surface accuracy of 30-ft reflector (true parabola set at zenith, ideal environment)

1 σ, in. × 10 ³	90-deg elevation		45-deg elevation		0-deg elevation	
	Minimum	Maximum	Minimum	Maximum	Minimum	Maximum
1. Reflector panels						
Manufacture	10	19 ^b	10	19 ^b	10	19 ^b
Deadload	7	7	7	7	7	7
Windload	0	Negligible	0	Negligible	0	Negligible
Field erection	9	12	9"	12"	9"	12"
Thermals						
Transient	0	2	0	2	0	2
Steady	0	1	0	1	0	1
2. Reflector structure						
Deadload	0	0	9.2"	9.2"	14"	14"
Windload	0	Negligible	0	Negligible	0	Negligible
Thermals						
Transient	0	7	0	7	0	7
Steady	0	7	0	7	0	7
(Σσ ²) ^{1/2} in. × 10 ³	15.2	25.6	21.9	31.0	26.0	34.5
Center value	20.4		26.5		30.3	

^a Assumed coherently additive, based on field surveys
^b Manufacturer's data

Table 6. Surface loss, db (30-ft reflector)

Frequency, Gc	Zenith		45-deg elevation		Horizon	
	Minimum	Maximum	Minimum	Maximum	Minimum	Maximum
20.6	0.48	1.36	1.00	2.02	1.42	2.49
21.0	0.50	1.42	1.04	2.09	1.44	2.58
21.5	0.52	1.49	1.09	2.20	1.54	2.70
21.9	0.54	1.55	1.13	2.27	1.60	2.81
22.5	0.58	1.64	1.20	2.39	1.69	2.96
23.0	0.60	1.72	1.26	2.51	1.76	3.10
23.5	0.63	1.79	1.31	2.61	1.84	3.24
24.0	0.66	1.87	1.36	2.72	1.92	3.38

the surface rather seriously at 22 Gc, restricting observations to periods of low winds.

Surface loss (Table 6) is computed from relations derived by J. Ruze (Ref. 5) for large correlation interval.

Large correlation interval undoubtedly is satisfied for this large structure, distorted slowly by gravity operating at such a short wavelength. The loss is seen to be a strong function of elevation angle and a weaker function of frequency. A total spread of 3.38-0.48 \approx 3.0 db is indicated. Typical operating conditions for one viewing,

based on total surface tolerance limits, indicate a center frequency (21.9 Gc) gain increase of $+1.16 \pm 0.10$ db for horizon-to-zenith observations in addition to atmospheric; 20.6 and 24.0 Gc increases of $+1.03 \pm 0.10$ and $+1.39 \pm 0.13$ db, respectively, are indicated.

Figs. 4, 5, and 6 show the predicted over-all efficiency, relative to a perfect surface, uniformly illuminated, circular aperture of 30-ft diameter, as a function of frequency and elevation angle (the sum of Tables 4 and 6). These figures also include all tolerances mentioned above. Fig. 7 shows the predicted gain change with elevation angle, caused by structural deformations. It will be noted that relative wide estimates of surface deformations allow rather tight bounds to be placed on the gain change. The estimates presented in Figs. 4, 5, and 6, however, cannot be tightened without additional information.

b. Calibration. Antenna gain measurements were made on the 30-ft antenna at the Venus Station on July 22-23, 1964. The gain was measured with a gain standard horn at 21.9 Gc, and also with a broad band FXR horn at 20.6, 21.0, 21.5, 21.9, 22.5, 23.0, 23.5, and 24.0 Gc.

The criterion for the minimum range R , for antenna gain measurements with an antenna diameter D , at a

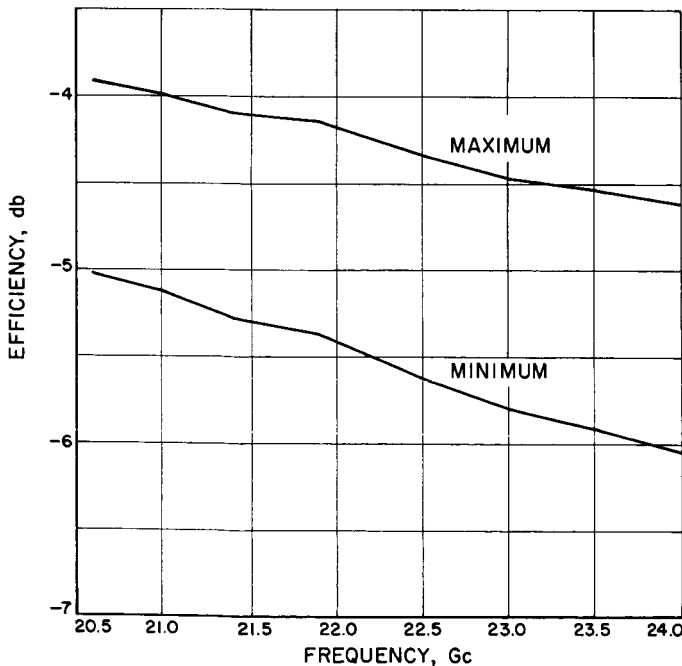


Fig. 4. Predicted over-all efficiency, zenith, 30-ft reflector

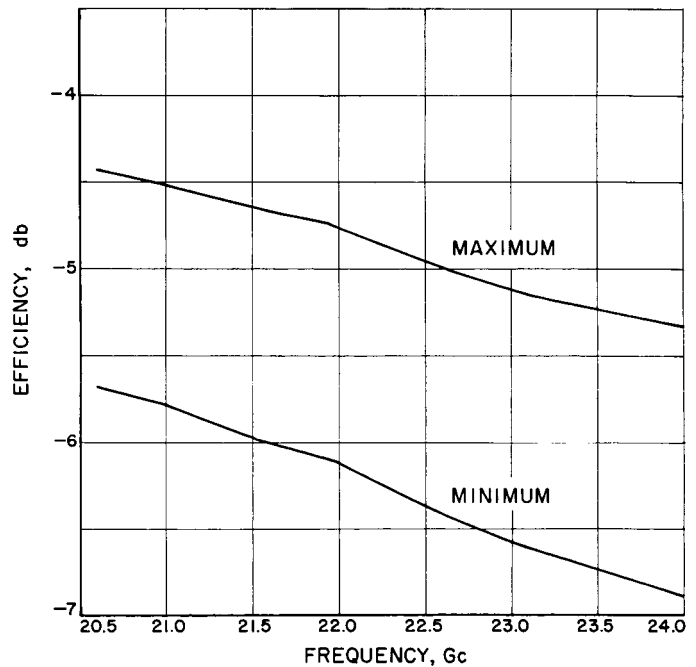


Fig. 5. Predicted over-all efficiency, 45-deg elevation, 30-ft reflector

wavelength λ , is usually given (for less than 1% maximum antenna gain measurement error) by (Ref. 6)

$$R = \frac{2D^2}{\lambda}$$

For the 30-ft antenna at 13.5 mm, we should have

$$R > \frac{2(30)^2}{13.5} \left[\frac{10 \times 2.54 \times 12}{5.280} \right] = 7.7 \text{ mi.}$$

The collimation tower for the 30-ft Venus Station antenna is located on Mt. Tiefert, with a range of 66,331 ft or 12.56 mi. Fig. 8 shows the 30-ft antenna pointed toward Mt. Tiefert; the 13.5-mm feed and radiometer are mounted at the apex. Fig. 9 shows a horizon mask view from the 30-ft antenna to Mt. Tiefert.

One of the most accurate methods for antenna gain measurements is the substitution method. In this technique a comparison is made of the signal level received from the transmitter between the antenna under evaluation, and a gain standard horn at the receiver location.

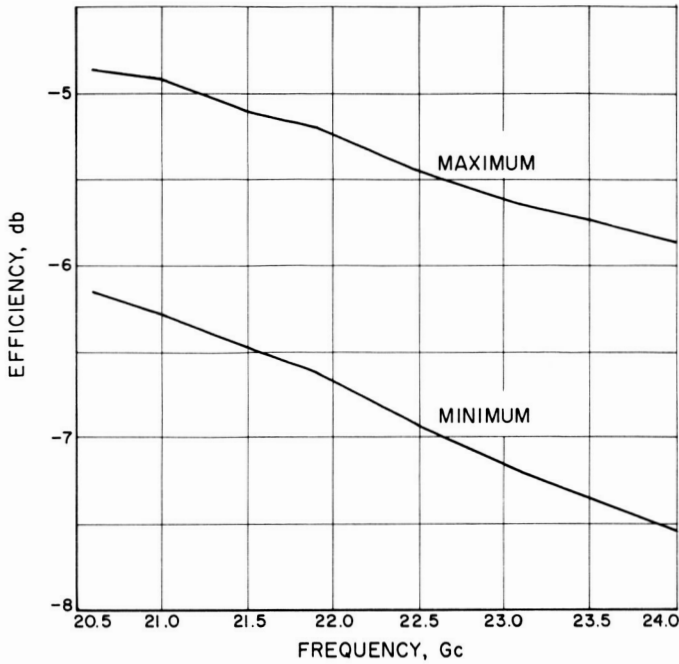


Fig. 6. Predicted over-all efficiency, horizon, 30-ft reflector

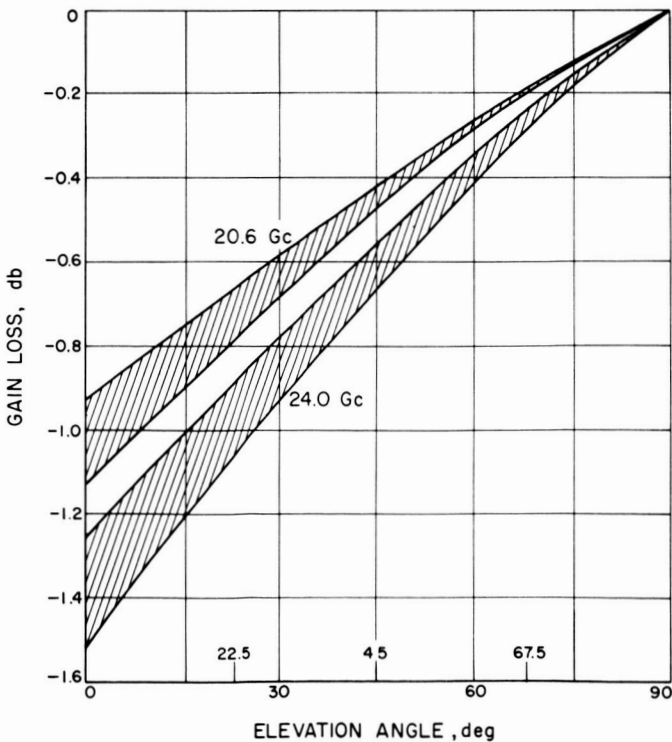


Fig. 7. Predicted gain change with elevation angle

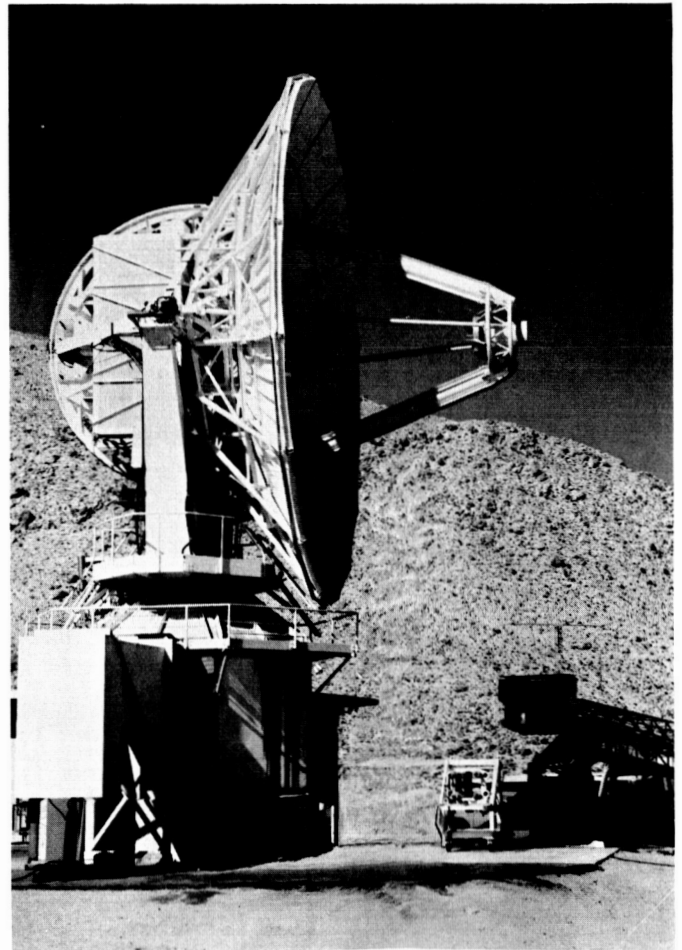


Fig. 8. Venus Station 30-ft antenna pointed in direction of Mt. Tiefert

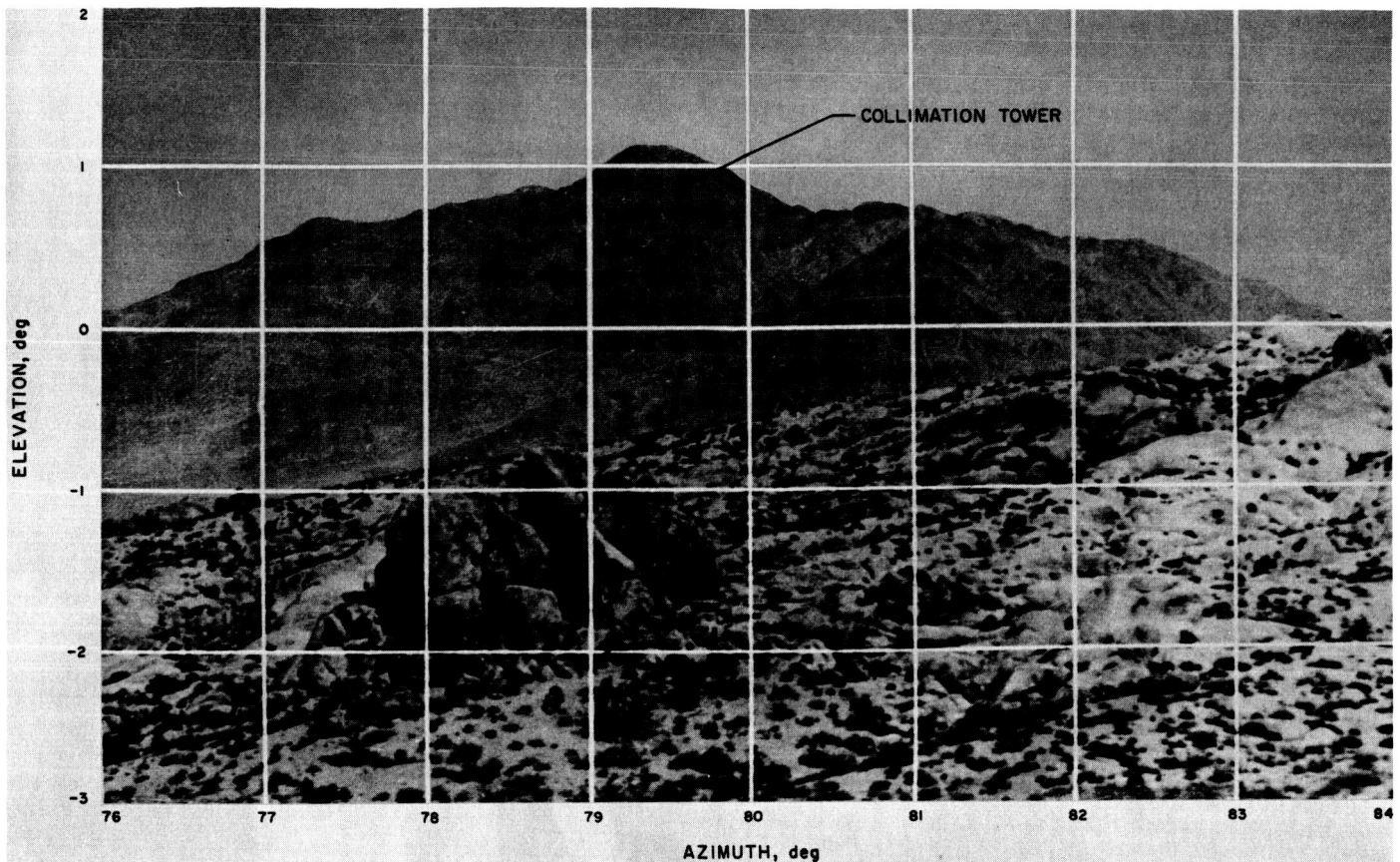


Fig. 9. Horizon mask from Venus 30-ft antenna

The principal advantage of this method is that the atmospheric loss need not be accounted for. However, the wide beam of a gain standard horn located on the 30-ft antenna would intercept the ground rise shown in Fig. 9, thus eliminating this method.

The measurement technique utilized compared the power transmitted from a 13.5-mm continuous wave (CW) signal source to that received at the 30-ft antenna with a thermistor power meter calibrated by a DC substitution method. A power comparison was made at the antenna for each of the radiometer calibration frequencies. With this technique, an absolute error in the power measurement scheme is common to both measurements and will cancel in the gain calculation.

c. Calibration measurements. The antenna gain was measured at each calibration frequency at the calibration reference point after the waveguide twist shown in the block diagram of the 13.5-mm radiometer shown on p. 76.

A block diagram of the 13.5-mm transmitter used to transmit the antenna gain calibrating signal from Mt.

Tiefert is shown in Fig. 10. The transmitter is capable of transmitting approximately 1 w. The gain standard horn shown in Fig. 11 was specially fabricated for use at 21.9 Gc. The design has been used and tested extensively at S-band (*SPS 37-22*, Vol. III, p. 11). The gain of this horn is 22.02 ± 0.09 db, probable error, at 21.9 Gc. This number was obtained by transferring the results from the S-band gain standard horn; the 21.1 Gc is a true scale model of the latter.

The gain standard horn was matched with a waveguide tuning section to a VSWR less than 1.02 at 21.9 Gc, having a VSWR under 1.05 over a 50-Mc frequency band. The insertion loss of the tuner was determined by matching with an identical waveguide section to a matched termination. The insertion of the two sections was measured with the microwave insertion loss test set (Ref. 4) and found to be 0.1056 db. Assuming symmetry, the loss of each section is therefore 0.053 db. The FXR Model K-638AF, Serial No. 148 (Ref. 7) horn was matched with a slide screw tuner at each of the calibration frequencies. It was possible to reset the match to better than 1.02 with the slide screw tuner at each frequency, using the

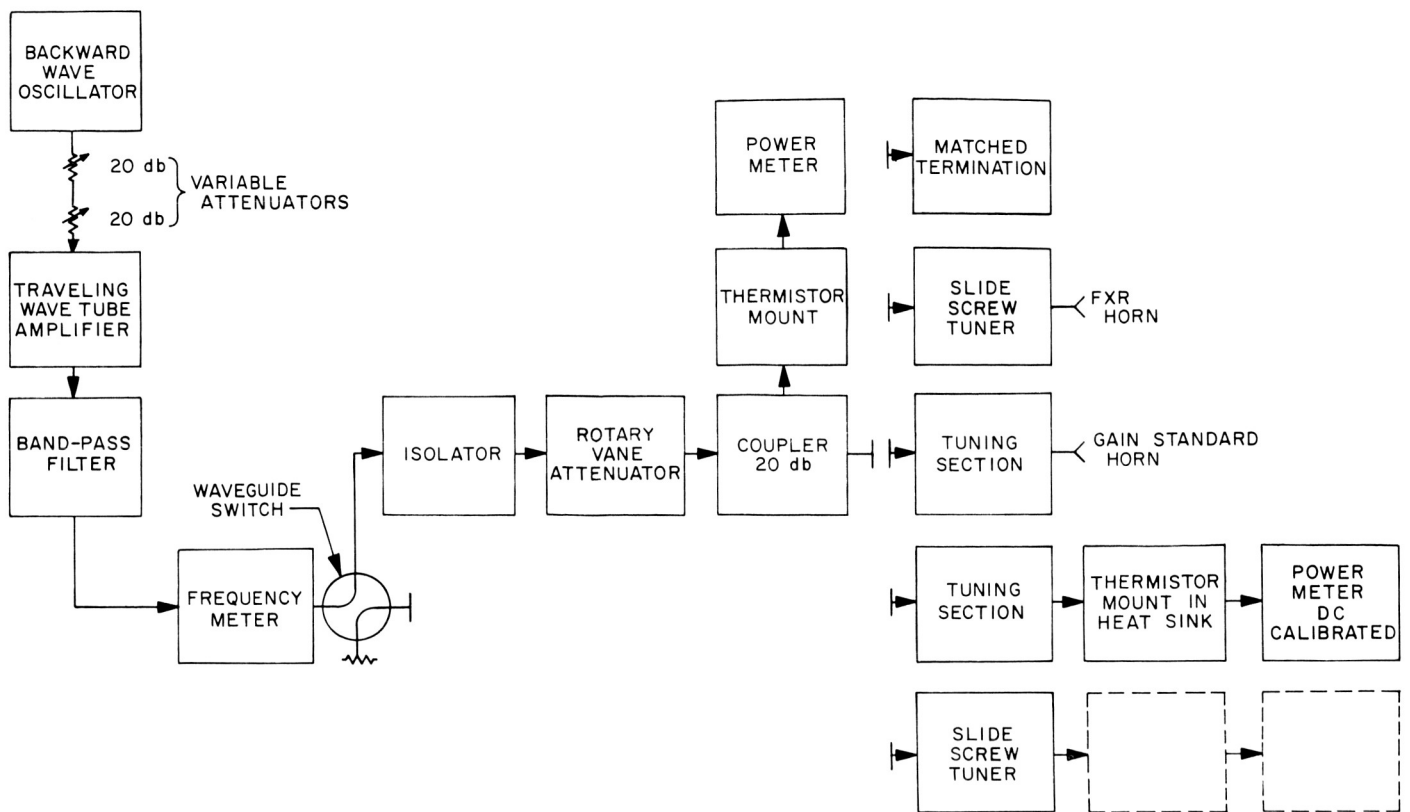


Fig. 10. Block diagram of transmitter used for 13.5-mm band antenna



Fig. 11. 21.9-Gc JPL-fabricated gain standard horn

micrometer and scale readout. The thermistor mount¹ in the heat sink (Figs. 12 and 13) was matched with a fixed tuned section at 21.9 Gc and a slide screw tuner at each of the calibration frequencies. It was necessary to use a thermal heat sink with the thermistor mount and to record the power meter output on a sensitive recorder in order to obtain the required power resolution (0.01 w) when used at the antenna, due to the high space loss. The power meter was calibrated with a DC power substitution using a mercury battery and a precision potentiometer.

A transfer technique is required to calibrate the transmitted power of approximately 1 w since the power meter thermistor mount cannot tolerate more than 15 mw. It would be possible to calibrate the transmitted power in a straightforward manner if the power were sampled through a directional coupler, but it was felt that the coupler insertion loss measurements of approximately 20 db would introduce additional errors. The

¹Hewlett-Packard Co. Model K-486A used with power meter model H-P 431B.

transmitted power measurement was performed with the setup shown in Fig. 10 employing these steps:

- (1) The matched termination is connected to the transmitter output and the rotary vane precision attenuator is set to a 1-db reading.
- (2) The variable attenuators are set for a desirable indication (P_0) on the level set power meter, located on the side arm of the coupler. This is the level set that is used later during the antenna gain measurements.

- (3) The tuning section and power meter thermistor mount are connected to the transmitter output and the rotary vane precision attenuation is set for 10 mw on the DC calibrated power meter.
- (4) The rotary vane precision attenuator is adjusted back to the 1-db setting and the variable attenuators are set for 10 mw on the DC calibrated power meter.
- (5) The rotary vane precision attenuator is set to the same setting as Step 3 and the power P'_T is measured with the DC calibrated power meter.

If the change in the precision rotary vane attenuator readings between Steps 1 and 3 is represented by the ratio L , the transmitted power in Step 2 is

$$P_T = \frac{10 \text{ mw}}{L} \quad (1)$$

The change in the precision rotary vane attenuator between Steps 4 and 5 also is represented by the ratio L and,

$$P'_T = (10 \text{ mw})L \quad (2)$$

Eliminating L in Eqs. (1) and (2),

$$P_T = \frac{(10 \text{ mw})^2}{P'_T} \quad (3)$$

This is the transmitted power indicated by the DC calibrated power meter when the level set reading is adjusted to P_0 . The calibration accuracy of the rotary vane attenuator is not critical with this technique since it is being

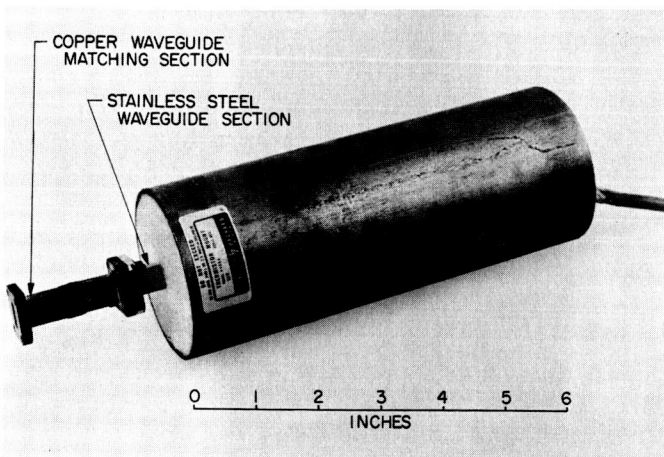


Fig. 12. Thermally isolated power meter thermistor mount

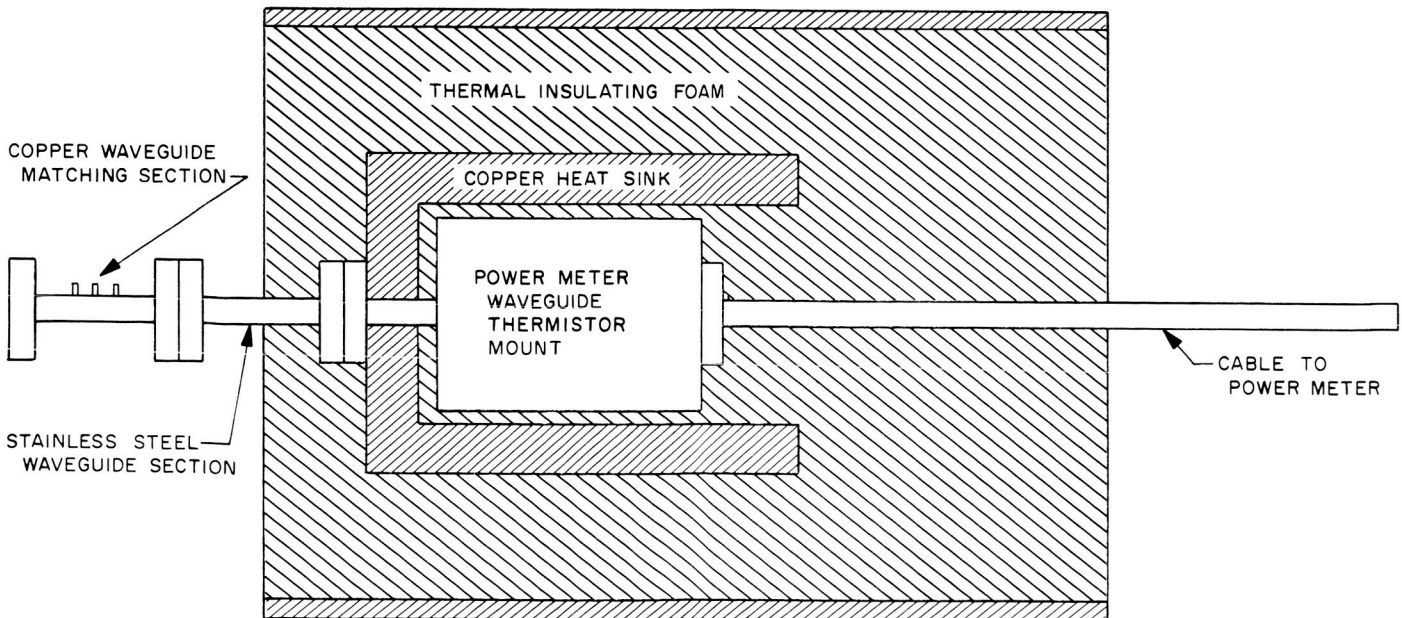


Fig. 13. Schematic of thermally isolated power meter thermistor mount

Table 7. Transmitted power and level set power meter reading as a function of calibration frequency

Frequency, Gc	Level set power meter reading P ₀ ,mw	Transmitted power, dbm	
		Fixed tuned section	Slide screw tuner
20.6	8.0	+29.88	+28.39
21.0	8.0		+28.51
21.5	8.0		+28.92
21.9	8.0		+29.49
22.5	4.0		+26.73
23.0	4.0		+26.79
23.5	0.80		+19.81
24.0	2.0		+23.71

used only as a transfer standard. The observed level set power meter reading and transmitted power is tabulated in Table 7 as a function of calibration frequency. The level was set with the variable attenuator slightly below the maximum attainable so that the level always could be repeated.

A block diagram of the received power measurement scheme used on the 30-ft Venus antenna is shown in Fig. 14. The matched, thermally isolated thermistor mount was connected directly to the calibration reference point behind the waveguide twist. Due to the high space loss, the received power was very low so that the power meter

was battery-operated for best amplitude stability and minimum 60-cycle power interference. The low level power was measured by calibrating the analog recorder with the DC substituted power. To minimize the thermoelectric effects in the thermistor mount, which occur at low power levels (Ref. 8), it was necessary to reverse the polarity of the DC substituted power and average the calibration on the analog recorder. The DC power applied to the thermistor mount was determined by reading the voltage across a precision calibrated resistor with a potentiometer.

Fig. 15 shows DC power calibration samples at various low power levels used to determine the linearity of this technique. The voltage magnitude and polarity across a series 100-Ω resistor to the thermistor and the consequent calculated DC applied powers are indicated on the recording. Three deflections are averaged for each polarity and results of the linearity test are shown in Fig. 16.

The transmitter was boresighted and properly polarized, with respect to the 30-ft antenna, by maximizing the received signal level. This is not a very critical operation due to the wide beamwidth of the transmitter horns (3-db bandwidth approximately ±10 deg for the FXR horn and ±13 deg for the gain standard horn). The 30-ft antenna was boresighted by moving it at a constant angular rate in each axis with the antenna drive computer, and recording the power meter output.

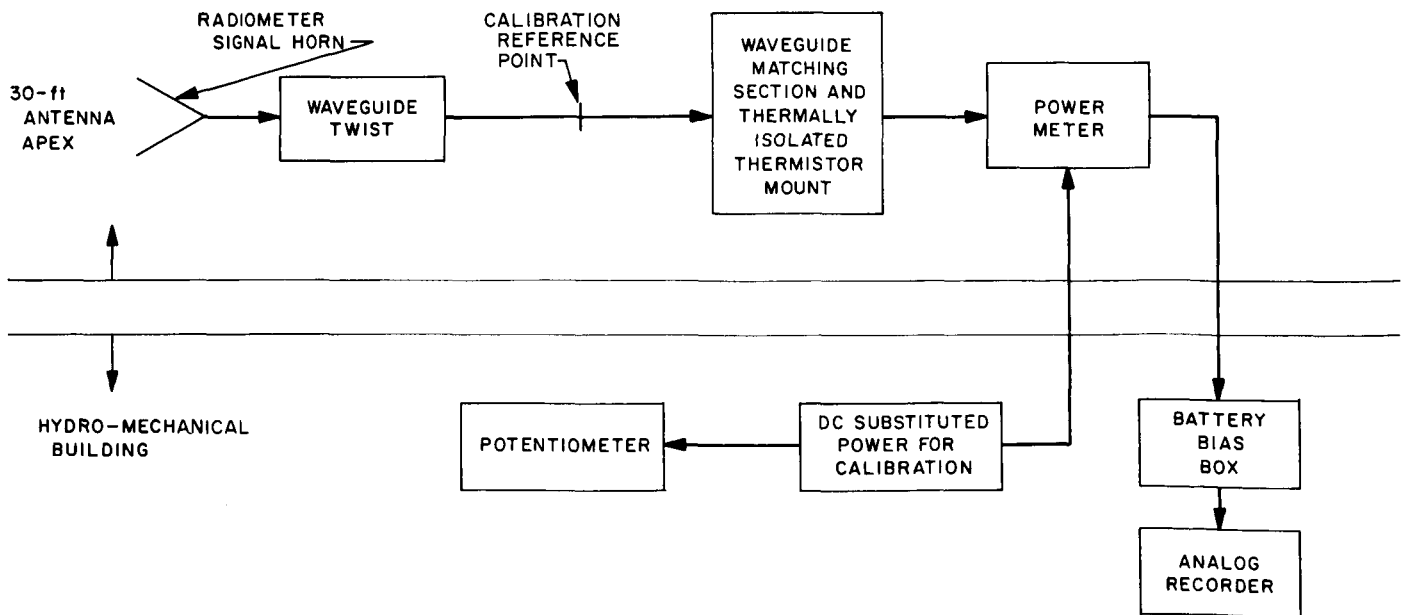


Fig. 14. Block diagram of received power measurement scheme used on 30-ft Venus antenna at 13.5 mm

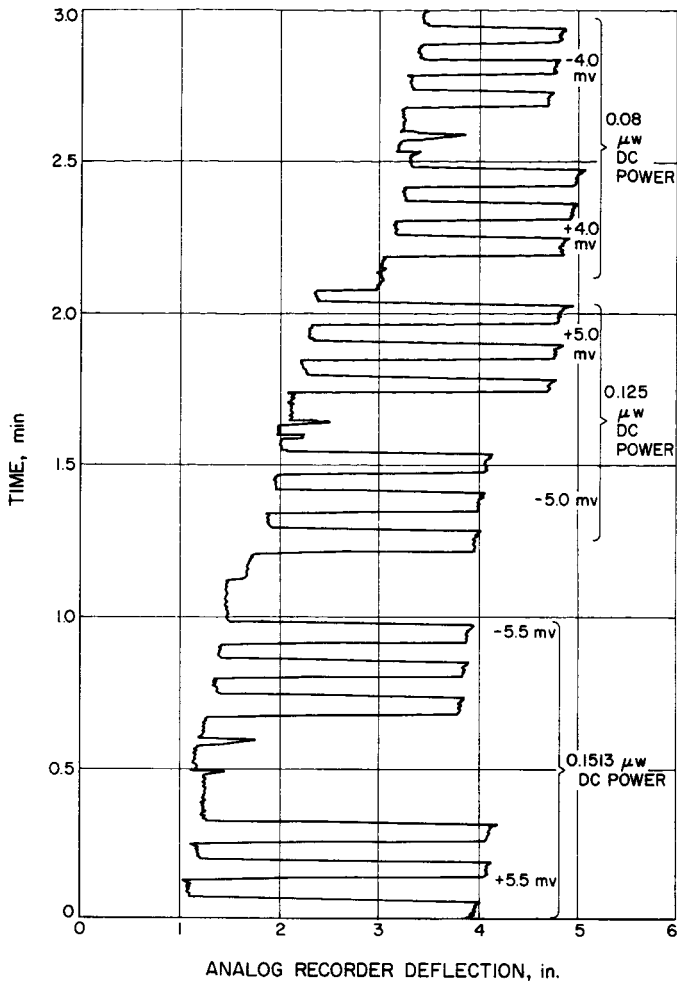


Fig. 15. Sample DC calibration measurements made with analog recorder at low power levels with the thermally insulated thermistor power meter mount

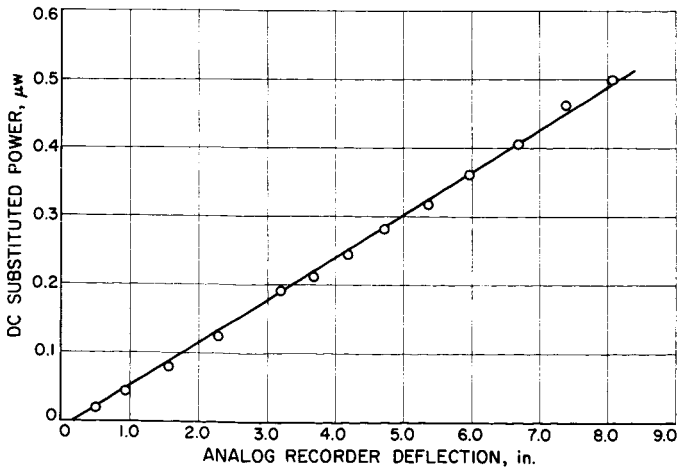


Fig. 16. DC power calibration versus analog recorder output

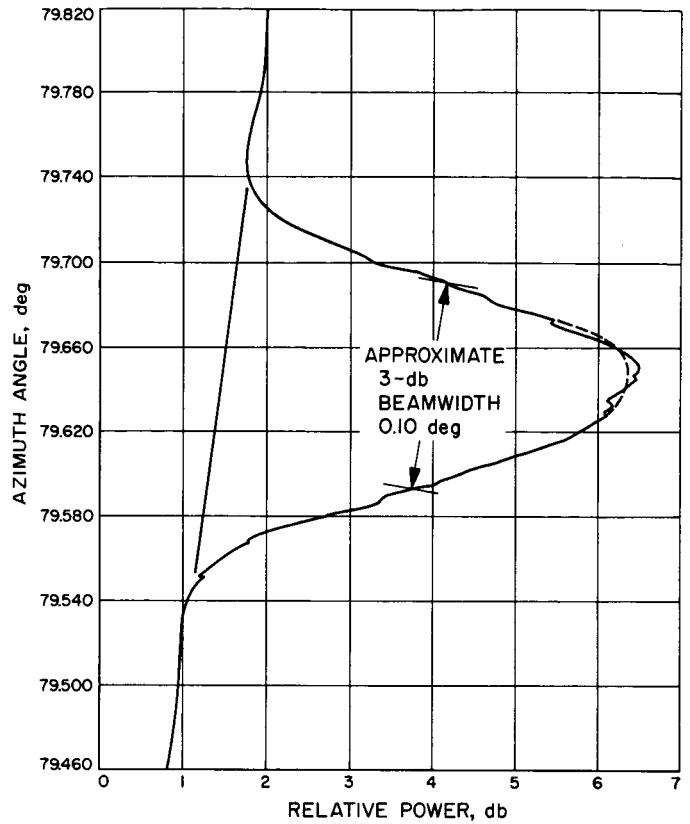


Fig. 17. Sample analog recording of power meter output versus 30-ft antenna, azimuth angle used to boresight to Mt. Tiefert 21.9-Gc transmitter

In the sample 30-ft antenna boresighting recording of Fig. 17, the FXR horn was used at the transmitter with approximately 975 mw. The slide screw tuner was used with the thermistor power meter mount at the 30-ft antenna. The maximum received power at the azimuth angle of 79.640 deg was approximately 0.275 μ w. The rms resolution of the power measurement over a short time period is better than 0.01 mw. The 3-db azimuth beamwidth from this recording is approximately 0.10 deg, which agrees with the RF pattern data (SPS 37-29, Vol. IV, p. 122).

Fig. 18 shows a sample recording of the received power measurement No. 3 at 21.9 Gc, with the standard gain horn slide screw tuner assembly at the transmitter and the thermistor power meter mount slide screw tuner assembly at the 30-ft antenna. With this measurement technique, the transmitter is turned on and off repeatedly. The recording is calibrated with the transmitter off and the DC calibration (both positive and negative polarity) repeatedly turned on and off. The DC power of 0.2278

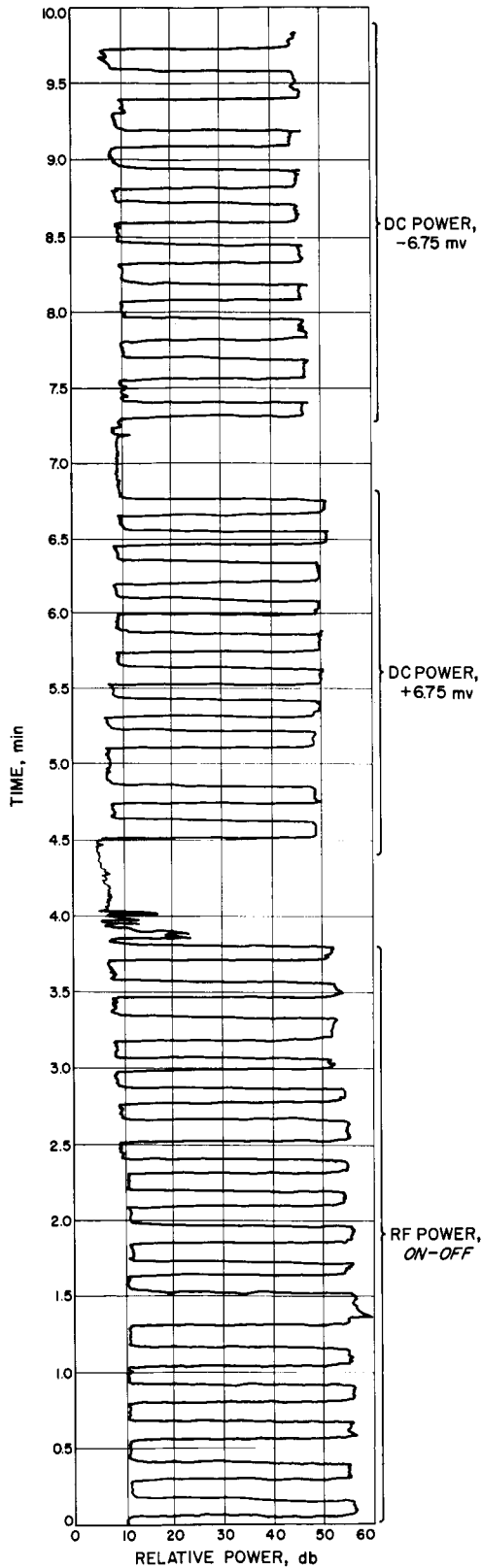


Fig. 18. 30-ft antenna received power measurement No. 3

μw , applied to the thermistor mount for this recording, is set by adjusting the voltage across a $100\text{-}\Omega$ precision resistor to 6.75 mv , as indicated on a precision potentiometer. For this measurement, the average recorder deflections for the DC and RF powers are 38.35 and 43.11 divisions, respectively, so that the received RF power P_R is

$$\left(\frac{43.11}{38.35}\right) 0.2278 = 0.256 \mu\text{w}.$$

Since the same technique was used to calibrate both the transmitted and received power, absolute errors cancel. Seventeen complete gain measurement sequences were made between $23:00\text{ hr}$ on July 22 and $00:30\text{ hr}$ on July 23, 1964. Various combinations of horns and tuners were used in Tests 1 through 4, 8 and 13 through 17, at 21.9 Gc . The gain was measured at each calibration frequency in Tests 5 through 12 with the FXR horn and slide screw tuner (Table 8). Gain measurements were made in Tests 15 and 16, with and without a band-pass filter (tuned to 21.9 Gc), to determine if errors were being introduced from signal harmonics. A low-pass filter was not available when this series of gain measurement tests was performed. Within the resolution of the instrumentation, the test results indicate that harmonics were not a serious problem. A gain measurement was made with a 90-deg twist in the transmitter (causing cross-polarization) to verify that the correct polarization was used on the transmitter.

The calculated path loss between the Mt. Tiefert transmitter and the Venus Station receiver included the atmospheric attenuation due to both oxygen and uncondensed water vapor (this calculation contributed by D. Jones will be given in greater detail in a JPL Technical Report "13.5-mm Band Radiometric Measurements of Venus," to be published). An attenuation of 0.19 db due to oxygen was assumed to be essentially constant over the frequency interval of interest (Ref. 9). The absorption coefficient for water was obtained from Barratt and Chung (Ref. 10), using measurements of the wet and dry bulb temperatures taken at both Mt. Tiefert and the Venus Station. Tabulations of the experimental conditions at the Venus and Tiefert locations are given in Table 8.

Antenna efficiency is calculated from (Ref. 11)

$$\eta = \frac{(P_R/L)}{P_T G_T \left(\frac{D}{4d}\right)^2} \quad (4)$$

Table 8. Experimental conditions at the Venus Station and Mt. Tiefert for the antenna 13.5-mm band gain measurements

Test identification No.	Time	Frequency	Venus Station				Mt. Tiefert					
			Experimental conditions	Dry temperature, °F	Wet temperature, °F	Temperature difference, °F	Barometric pressure, in. Hg	Experimental conditions	Dry temperature, °F	Wet temperature, °F	Temperature difference, °F	Barometric pressure, in. Hg
1	2300	21.9	Slide screw tuner on thermistor mount	82.0	57.0	25.0	29.95	Slide screw tuner with gain standard horn	78.0	55.0	23.0	29.93
2	0400	21.9	Fixed tuner	77.0	54.0	23.0	29.95	Fixed tuner with gain standard horn	76.0	53.0	23.0	29.93
3	0545	21.9	Slide screw tuner	76.0	53.0	23.0	29.95	Same as 1	76.0	53.0	23.0	29.93
4	0640	21.9	Slide screw tuner	80.0	57.0	23.0	29.95	Slide screw tuner with FXR horn	77.5	53.0	24.5	29.93
5	0715	20.6	Slide screw tuner	83.0	56.0	—	29.95	Slide screw tuner with FXR horn	78.2	53.2	25.0	29.93
6	0730	21.0	Slide screw tuner	78.0	55.0	23.0	29.95	Slide screw tuner with FXR horn	78.5	53.6	24.9	29.93
7	0745	21.5	Slide screw tuner	80.0	56.0	24.0	29.96	Slide screw tuner with FXR horn	78.5	54.2	24.3	29.94
8	0807	21.9	Slide screw tuner	82.0	56.2	25.8	29.96	Slide screw tuner with FXR horn	78.5	54.5	24.0	29.94
9	0820	22.5	Slide screw tuner	82.0	56.0	26.0	29.96	Slide screw tuner with FXR horn	79.0	53.5	25.5	29.94
10	0835	23.0	Slide screw tuner	81.0	56.0	25.0	29.96	Slide screw tuner with FXR horn	79.0	53.5	25.5	29.94
11	0847	23.5	Slide screw tuner	82.0	56.2	25.6	29.97	Slide screw tuner with FXR horn	79.0	54.8	24.2	29.95
12	0857	24.0	Slide screw tuner	82.5	56.5	26.0	29.98	Slide screw tuner with FXR horn	79.3	54.5	24.8	29.96
13	0915	21.9	Slide screw tuner	85.0	57.2	27.8	29.98	Slide screw tuner with FXR horn	79.5	54.5	25.0	29.96
14	1107	21.9	Slide screw tuner, Antenna rebore sighted	95.0	60.0	35.0	29.98	Slide screw tuner with FXR horn	88.0	59.0	27.0	29.96
15	1150	21.9	Slide screw tuner	95.0	60.0	35.0	29.98	Standard gain horn, no filter	94.0	58.0	36.0	29.96
16	1205	21.9	Slide screw tuner	95.0	62.0	33.0	29.98	Standard gain horn with filter	94.0	58.0	36.0	29.96
17	1230	21.9	Slide screw tuner	—	—	—	29.98	FXR horn with 90-deg twist	—	—	—	29.96

Table 9. 30-ft antenna gain data reduction

Test identification No.	Frequency, Gc	Received power P_{Rr} , mw	Received power P_{Rr} , dbm	Transmitted power P_{Tr} , dbm	Horn gain G_T , db	Atmosphere loss L , db	Antenna efficiency η , db
1	21.9	0.260	-35.855	+29.490	+21.967	-3.31	-5.07
2	21.9	0.275	-35.611	+29.880	+21.967	-2.97	-5.56
3	21.9	0.256	-35.922	+29.490	+21.967	-2.84	-5.61
4	21.9	0.466	-33.324	+29.490	+23.890	-2.83	-4.94
5	20.6	0.431	-33.655	+28.390	+23.610	-1.88	-4.84
6	21.0	0.413	-33.838	+28.510	+23.690	-2.22	-4.89
7	21.5	0.419	-33.784	+28.920	+23.800	-2.69	-4.88
8	21.9	0.425	-33.711	+29.490	+23.890	-2.90	-5.26
9	22.5	0.203	-36.920	+26.730	+24.010	-3.05	-5.68
10	23.0	0.193	-37.143	+26.790	+24.100	-2.95	-6.15
11	23.5	0.0356	-44.487	+19.810	+24.180	-2.58	-6.96
12	24.0	0.0910	-40.410	+23.710	+24.250	-2.35	-7.09
13	21.9	-	-	-	-	-3.03	-
14	21.9	0.470	-33.284	+29.490	+23.890	-3.13	-4.60
15	21.9	0.269	-35.705	+29.490	+21.967	-2.92	-5.31
16	21.9	0.273	-35.635	+29.490	+21.967	-2.97	-5.19
17	21.9	-	-	-	-	-	-

where

P_R = received power

P_T = transmitted power

G_T = gain of transmitter antenna

D = diameter of receiving antenna

d = distance between the transmitter and receiver

L = atmospheric loss (power ratio)

Table 9 gives the antenna gain measurements and data reduction.

The individual terms of Eq. (4) and the efficiency are tabulated in Table 9 using -78.932 db for $(D)/(4d)^2$. Run 13 is deleted because of a calibration error during the measurement. A plot of the resulting measured efficiency as a function of frequency is shown in Fig. 19. Also shown is a best least-squares fit straight line obtained from all the measured data points.

The equation of the least-squares fit straight line in Fig. 19 can be represented by

$$\eta(f) = \eta(21.9 \text{ Gc}) + b\Delta f \quad (5)$$

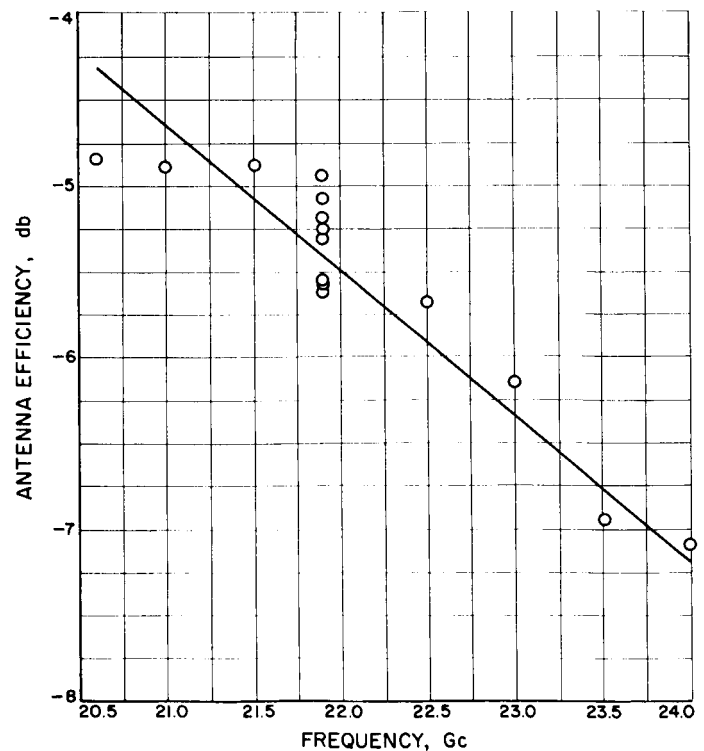


Fig. 19. Plot of measured efficiency of 30-ft antenna as a function of frequency

where

$$\eta(f) = \text{antenna efficiency, db}$$

$$\eta(21.9 \text{ Gc}) = \text{antenna efficiency at 21.9 Gc, } -5.32 \text{ db}$$

$$f = \text{frequency, } = 21.9 \text{ Gc} + \Delta f$$

$$b = \text{slope, } -0.772 \text{ db/Gc}$$

The probable errors associated with the random measurement errors are

$$p_e \eta_o \text{ (probable error of an observation point)} = 0.22 \text{ db}$$

$$p_e \eta(21.9 \text{ Gc}) \text{ [probable error of the constant in Eq. (5)]} = 0.06 \text{ db}$$

$$p_e b \text{ [probable error of the slope in Eq. (5)]} = 0.07 \text{ db/Gc}$$

These errors do not include bias errors such as those due to equipment nonlinearities or theoretical errors such as those involved in the atmospheric attenuation calculations.

A summary, providing a consolidation of predicted and measured efficiencies, will be reported separately upon completion of the radiometric measurements.

3. Continuous Wave (CW) Signal Power Calibration with Thermal Noise Standards

a. Introduction. A convenient measure of a spacecraft received power level in a typical tracking station is the receiver AGC voltage which is calibrated for absolute received power, defined at the receiver input with a calibrated test transmitter. The relative accuracy of the test transmitter is dependent primarily on the test transmitter precision attenuator. Absolute calibration accuracy is dependent on the power level set and the insertion loss calibration between the test transmitter and the receiver input. Insertion loss calibration is difficult and typically includes a waveguide directional coupler, waveguide to coaxial transition and coaxial transmission lines.

The receiving system equivalent noise temperature can be determined accurately with the use of calibrated microwave thermal terminations. The test transmitter CW signal power can be calibrated directly at the receiver input by comparison to the known receiver input equivalent noise power. A CW signal power calibration by the Y-factor method normally used in noise temperature calibrations has been used to calibrate the test transmitter. This technique determines the absolute power directly at the receiver input and does not require

insertion loss measurements between the receiver input and test transmitter.

The calibration method consists of accurately measuring the ratio between the CW signal power P_s , plus the system noise power P_n , and the system noise power. A precision attenuator is adjusted for equal power levels with the CW signal on and off.

The power ratio at the receiver output is

$$Y = \frac{P_n + P_s}{P_n} \quad (1)$$

The input signal power P_{si} has been shown to be [SPS 37-32, Vol. IV, p. 246, Eq. (9)]

$$P_{si} = (Y - 1) \frac{kT_s B}{g(f_s)} \quad (2)$$

where

$$k = \text{Boltzmann's constant } (1.38 \times 10^{-23} \text{ j/}^\circ\text{K})$$

$$T_s = \text{equivalent input noise temperature of the receiving system } (^\circ\text{K})$$

$$B = \text{system bandwidth} = \int_0^\infty g(f) df, \text{ (cps)}$$

$$g(f) = \frac{G(f)}{G(f_o)} = \text{normalized gain response (usually } f_o \text{ is the frequency of the maximum response)}$$

$$g(f_s) = \frac{G(f_s)}{G(f_o)} = \text{normalized gain at the signal frequency } f_s$$

The Y-factor method of CW signal power measurement was used to calibrate the test transmitter used with the 2295-Mc maser and suitcase telemetry receiver in the *Mariner C* cone at the Venus Station February 19, 1965. Fig. 20 is a block diagram of the instrumentation.

The normalized gain response $g(f)$ of the filter is shown in Fig. 21; physically, it is a temperature-controlled narrow-band crystal filter. Since this bandwidth is very narrow, compared to the IF bandwidth, it adequately describes the system bandwidth. The bandwidth B , was evaluated by numerical integration on a computer to be 9555 cps (+39.80 db). The CW signal frequency f_s , was measured to be 49,999,970 cps, where $g(f_s) = -0.75$ db. The system temperature was measured to be 27.7°K (14.43 db). Then, with $k = -198.60$ dbm, for this system, from Eq. (2),

$$P_{si} = -143.62 \text{ dbm} + (Y - 1) \text{ db} \quad (3)$$

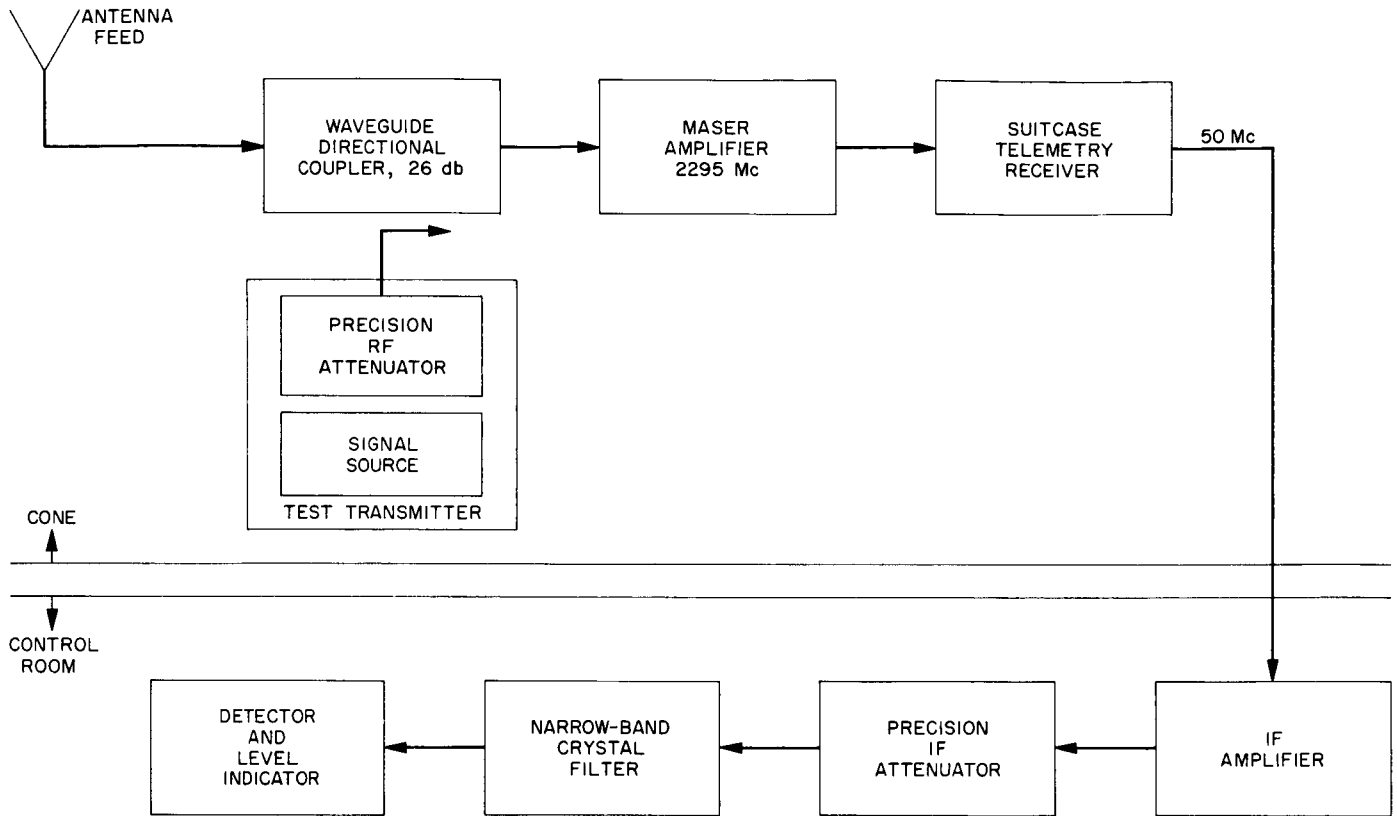


Fig. 20. 2295-Mc low-noise receiving system and CW power level measurement instrumentation

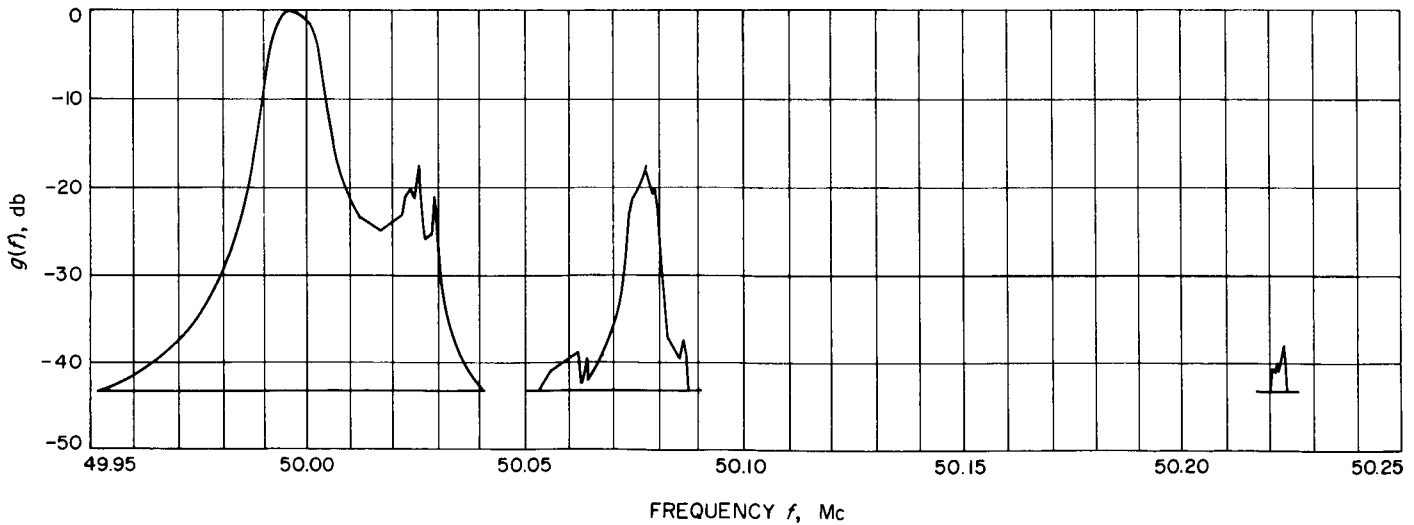


Fig. 21. Response of 50-Mc band-pass crystal filter

The test procedure consists of adjusting the precision IF attenuator for the same output level with no RF signal, and then with an RF signal, and recording the difference. Table 10 shows these Y-factor readings for

two sets of readings taken on February 19, 1965, at the Venus Station with the *Mariner C* cone, maser and suitcase telemetry receiver as a function of the nominal signal level.

Table 10. Nominal and calibrated CW test signal levels

Nominal test signal level, dbm	AGC voltage, v	Y-factor			Y-1, db	Calibrated test signal level, dbm
		First run, db	Second run, db	Average, db		
-100	11.50	43.36	43.24	43.29	43.29	100.3
-104	10.75	39.50	39.35	39.42	39.42	104.2
-108	10.50	35.76	35.66	35.71	35.71	107.9
-112	10.00	31.36	31.30	31.33	31.33	112.3
-116	9.40	27.57	27.52	27.54	27.53	116.1
-120	9.15	24.07	23.94	24.00	23.98	119.6
-125	8.75	19.25	19.26	19.25	19.20	124.4
-130	8.20	14.04	13.87	13.95	13.71	129.9

Also shown are the receiver AGC voltage and the calibrated test signal levels. Fig. 22 is a plot of the nominal and calibrated test signal levels. The calibration range is limited at the higher signal levels by the dynamic range or linearity of the instrumentation and at the lower range by the bandwidth of the filter and resolution of the instrumentation.

The calibration accuracy for this technique was calculated using the parameters of this system [SPS 37-32, Vol. IV, p. 246, Eq. (11)]. With a bandwidth of 9555 cps

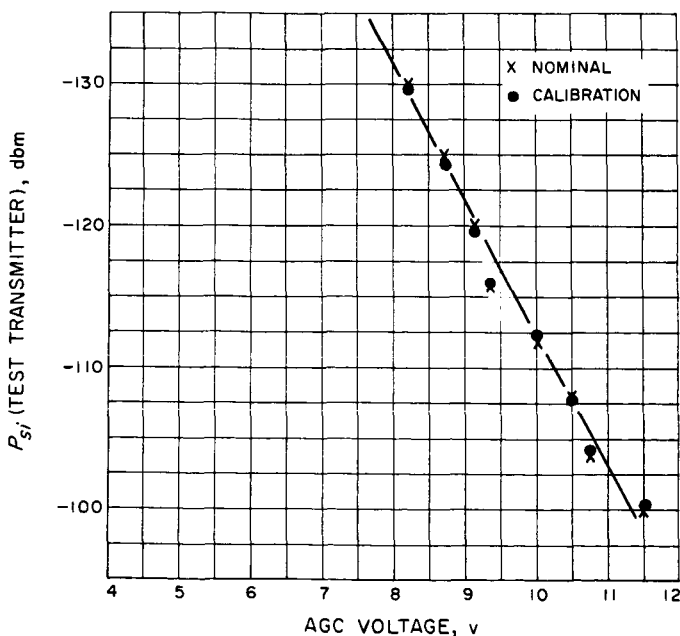


Fig. 22. Test transmitter signal strength versus AGC voltage

and post detector time constant of 0.1 sec used for the above measurements, the accuracy is about 4% at high signal power levels. At CW signal power levels below approximately -135 dbm, the accuracy falls off rapidly. If the bandwidth and time constant are changed to 1000 cps and 10 sec, respectively, the signal level can be measured to -160 dbm with high accuracy.

B. Experimental Closed Cycle Refrigerator (CCR) for Masers

The prototype CCR (based on the JPL-Syracuse University design described in SPS 37-31, Vol. III, p. 38) was completed recently and tested with a traveling wave maser (TWM) installed. A cool-down time of 5½ hr, approximately one-half the time required by the A. D. Little Co. cryodyne, was achieved. The rapid cool-down was due to the excellent refrigeration capacity of the machine, coupled with the action of the thermal switch (SPS 37-31, Vol. III, p. 40) between the 4.2 and 15°K stations as shown in Fig. 23. The radiation shield has been removed in this figure.

The refrigeration capacity was at least 500 mw in addition to the thermal load because of the microwave transmission lines. This represents a very adequate reserve capacity for good stability.

The refrigerator was made approximately 4 in. shorter than the cryodyne in order to improve the mechanical rigidity of the 4.2°K station. The pyramidal disposition of the coaxial and waveguide transmission lines provides sufficient mechanical stability to the structure so that no auxiliary supports for the TWM will be necessary. Gain fluctuations in the maser due to mechanical vibration were found to be negligible.

Fig. 24 is a top view of the operational CCR. The same techniques used in the DSIF S-band maser system were retained in the design of the microwave connections. The crosshead assembly which synchronizes the motion of the displacer pistons and gas valves consists of an electric motor (shown centrally located in Fig. 24) driving a single self-lubricating disk valve. This represents a considerable simplification over the existing

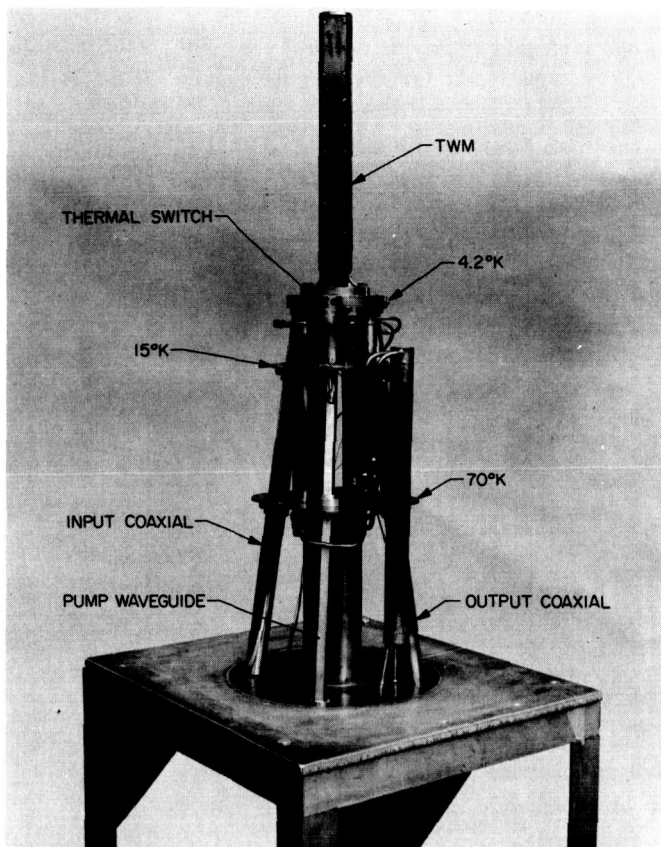


Fig. 23. Internal view of CCR/TWM

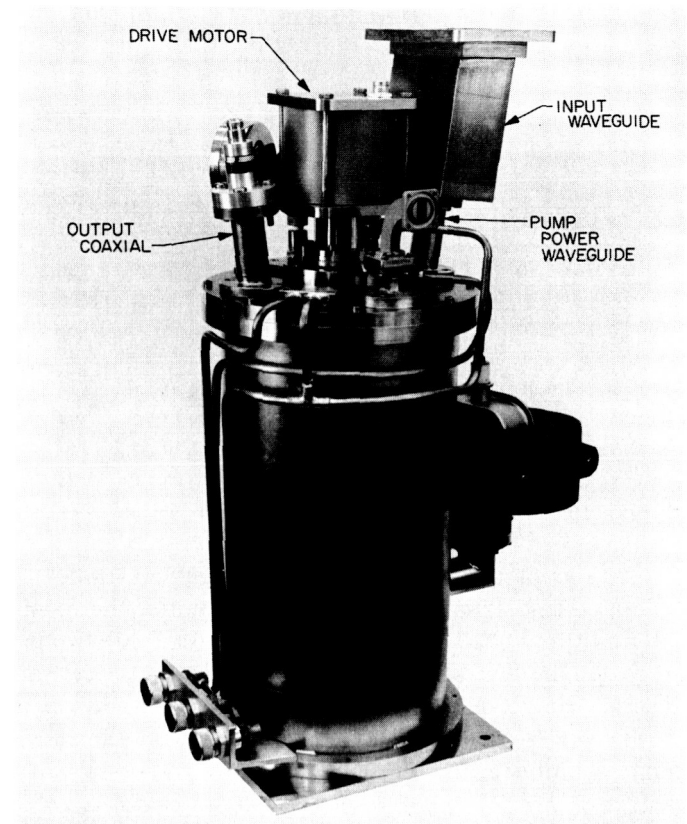


Fig. 24. External view of CCR/TWM

systems and should contribute significantly to the system reliability.

The machine is compatible with the A. D. Little Co. compressor and currently is operated with the spare unit. The investigation of suitable compressors is continuing.

C. Venus Station Operations

1. Experimental Activities

a. Summary. During the past 2 mo, the planetary radar on the 85-ft antenna continued to perform spectrum analysis experiments on Mars and Venus. Additionally, spectrum analysis and ranging experiments were performed on Mercury, and radiometer measurements of the thermal temperature of Mars have been made.

In support of the Venus Station's commitment to support the *Mariner* Mars 1964 spacecraft on demand, an

initial test of the ground-to-spacecraft link was successfully conducted February 26, 1965. Doppler data, with Pioneer Station receiving, were taken, and the feasibility of obtaining coherent doppler over the microwave link was tested. After evaluation of data obtained during this test, a second test was performed March 16, 1965; additional doppler data were obtained as well as comparisons between the antenna gains of Stations 11, 13, and 42. Finally, on April 8, 1965, a third test was conducted during which the Venus Station locked up the command link to the spacecraft and demonstrated readiness to send commands whenever required.

Table 11 is a summary of activities at the Venus Station during this period.

The reasons for transmitter outage are discussed further in Section 3 of this article. The servo system outages were, primarily, the result of a circuit breaker which failed in service; the maser-receiver outages were, primarily, the result of the maser being slow to cool down after the *Mariner* test of April 8, 1965. Failures in the Mod III-data system are under investigation and

Table 11. Summary of Venus Station experimental activity (February 16–April 12, 1965)

Activity	Hours	Percent
Primary experiments		
Planetary radar		
Mars	430	31.3
Venus	101	7.4
Mercury	57	4.2
Secondary experiments		
Star tracks	24	1.8
Black body (Mars)	36	2.6
Mariner Mars 1964, transmitters	136	10.0
Testing, calibration, construction, and maintenance (scheduled)	427	31.2
Down time ^a (equipment failure, includes unscheduled maintenance)	157	11.5
Total	1368	100.0

^aDown time is broken down and tabulated in Table 12

Table 12. Subsystems contributing to down time

Subsystem	Percent
Transmitter	54.0
Maser-receiver	10.9
MOD III-data	19.8
Servo	5.4
Other	9.9

the category "other" represents outages such as loose cables, power interruptions, operator error, etc., which cannot be placed easily into a system.

2. Preliminary Experiment Results

Experiments conducted at the Venus Station during this reporting period include planetary radar with Venus, Mars, and Mercury as targets, and a radiometer experiment with Mars.

The Venus experiment was concluded March 25, 1965 since, at that time, Mercury became a better target. The Venus experiment used a single channel of the nine-channel correlator to obtain a total spectrum of the returned signal. Venus is now near its maximum distance from Earth; therefore, the signal-to-noise ratio was low but confirmed expected values.

The Mars experiment continued until April 18, 1965. This experiment uses the single-channel correlator to obtain the total spectrum of the returned signal. As pre-

viously described, the spectra are separated according to the longitude of Mars in 10-deg intervals. At the conclusion of this experiment, all individual spectra from a particular longitude will be combined.

The Mercury experiment, started at the conclusion of the Venus experiment, used similar techniques with a single channel of the nine-channel correlator being used to obtain a total spectrum of the returned signal. A ranging experiment also was conducted using the 511 PN coders to phase-modulate the transmitter. Detection for the ranging experiment was in the nine-channel correlator. Good total spectra were obtained, showing a doppler offset of approximately 4 cycles. Results of the ranging experiment are not yet available.

A total power radiometer experiment is being carried out with Mars as the target. This experiment makes use of digital control to sample the signal and control the antenna. The new SDS 930 computer has been used for near real-time data reduction. Results are not yet available.

3. Subsystem Performance

a. 100-kw transmitter (operation). The transmitters for this reporting period were used in conjunction with the planetary experiments with Mars, Venus, Mercury, and the *Mariner IV* spacecraft trackings.

During this period, the transmitters and associated components have lost a total of 84.6 hr of tracking time. The reasons for failures and lost tracking time are:

Reasons	Hours lost
Replace high-voltage power supply water hoses	11.9
Replace high-voltage cable through antenna wrap up	16.0
Repair and clean oil leaks in solid-state rectifier	1.3
Repair water load waveguide switches	20.8
Clean water from waveguide and waveguide switches	28.3
Miscellaneous interlocks during operations	6.3

Water in the waveguide apparently was the result of the water load glass tube being broken (Fig. 25) by some foreign particle.

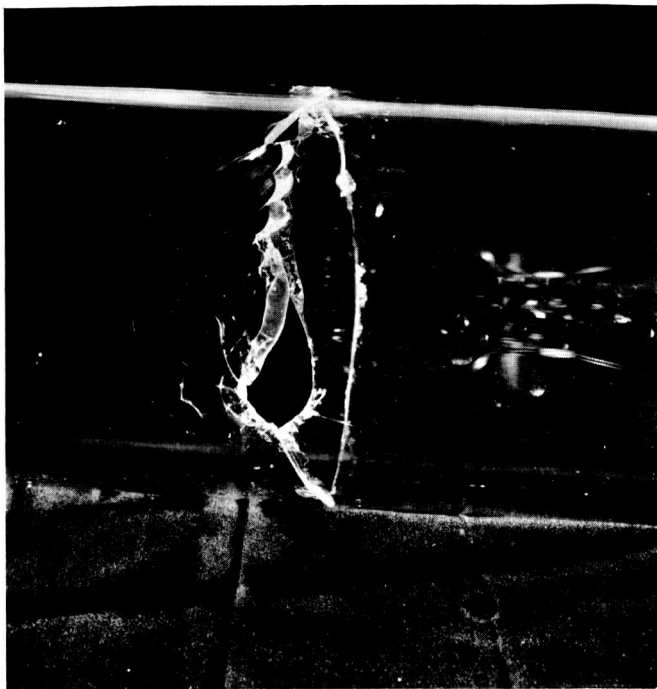


Fig. 25. RF water load glass

b. System improvements and modifications. New automatic drive attenuators have been constructed and installed in both the *Mariner* and R&D cones.

Transient suppressors have been installed across all switches in the system to prevent transient kickoffs by the switch action.

A new series limiter resistor box was installed on the antenna to eliminate the carrier modulation caused by noise from the filament transformers of the series limiter in the power supply room. This also puts the limiter closer to the klystron tube and reduces the effect of the capacitance of the high-voltage cable. This was noted in the operations with the read, write, and verify (RWV) and associated *Mariner* equipment tests.

The 1-mw solid-state rectifier is now in the system and is being used for all operations and tests. Since it was installed, it has operated satisfactorily with no trouble except for minor oil leaks which were repaired.

The eight-channel Sanborn recorder has been installed in the tracking system for recording of operational parameters of the transmitters required by the committed *Mariner* mission.

c. Testing. The *Mariner* 100-kw transmitters have been tested on the antenna and in the cone storage area, with a total of 234.1 filament hr and 118.6 beam hr on Amplifier 1, and 163.3 filament hr and 71.7 beam hr on Amplifier 2. Other tests have been run with the *Mariner* transmitters on the antenna for compatibility of the system with the spacecraft.

d. Digital equipment. The only new digital equipment installed during this reporting period was an SDS 930 computer system. This is a high-speed, solid-state computer with 8,192 words of core storage. The word length is 24 bits, and the machine has a 1.75- μ sec cycle time. The computer has a typewriter, paper tape reader, and punch for input-output. Auxiliary equipment includes 16 channels of priority interrupt and 2 digital-to-analog converters. Software supplied with the machine includes: HELP, POP, SYMBOL 4, and FORTRAN II. It is planned to use this equipment in real-time spectrum analysis for a low-speed telemetry system.

A program has been written for the Mod III stored program controller (SPC) to allow the automatic measurement of receiving system temperature. Relays in the SPC are pulsed to turn the noise tube on and off. The signal is supplied to the analog-to-digital converter of the SPC through the ranging channel of the Mod IV receiver with a 40-kc low-pass filter installed. The signal is sampled every 20 msec for 10 sec with the noise tube off, and then the noise tube is turned on for a similar period. The preliminary results indicate this may be a useful method for obtaining system temperature while an experiment is being conducted, although it is not presently as accurate as the normal procedure of using a precision attenuator. The automatic method does, however, have the advantage of checking the operation of the receiver completely through the IF amplifiers.

A comparison was made of ephemeris tapes generated directly (on-Lab) and those reconstructed from polynomials (on-site). The polynomial tapes were found to have much smoother second differences, which is to be expected because of the filtering action of the polynomial. The roughness in the original data is due to truncation error and soon will be corrected by a double precision ephemeris.

e. S-band receiver. During this period, the S-band receiver became inoperable on four different occasions because of water damage to the receiver cone interconnecting cables and connectors. Once, the damage was caused by rain water leaking into the cone. All other

failures were caused by leaks from the water-cooling system. To prevent a reoccurrence of such failures, new receiver cables with watertight jackets and connectors have been installed in the R&D cone.

Evaluation of the new digital phase modulator is continuing and all test results are being forwarded to the JPL project engineer.

A faulty crystal oven in the Resdel signal generator was repaired, and the generator was remounted in the R&D cone. Operation of the generator was normal for approximately 4 wk before it failed again.

f. X-band receiver. All the X-band receiving equipment, X-band to 30-Mc converter, power supply and waveguide, has been removed from the 30-foot antenna. This was done to facilitate the use of the antenna in other experiments. In preparation for future X-band experiments, new receiver cables for the antenna have been ordered.

g. Programmed local oscillator (PLO).

Digital control subsystem. Operation of the digital portion of the local oscillator, using the modified doppler tapes (SPS 37-29, Vol. III), has been satisfactory throughout the entire period.

However, two failures did occur, one in the tape reader unit and one in the timing logic. Both failures have been repaired, and the equipment is now operating properly. Total operating time on the equipment is now 10,700 hr.

RF portions. Several modifications were made to this equipment in a continuing program to simplify operation, increase dependability, and improve system performance.

All test instruments (frequency counter, VTVM, oscilloscope) have been removed since they are no longer required to set up the PLO for proper operation. All associated switching equipment and cabling were removed also.

The acquisition voltage supply for the receiver main VCO (31.44 Mc) and the down-loop VCO (475 kc) bias supply were replaced with units having improved DC voltage standards.

The system also was modified for use in Mercury planetary experiments. This change involved the addition of a 36-Mc distribution amplifier to the output of the Montronics synthesizer, and elimination of a relatively narrow band X75 frequency multiplier in the S-band doppler chain.

An H-P 5100A frequency synthesizer is being used temporarily to replace the Montronics synthesizer. This will allow a comparison of both synthesizers and also releases the Montronics for rework or modification.

h. Central frequency synthesizer (CFS). No failures occurred in the CFS during this period.

The standby rubidium frequency standard was returned to JPL, Pasadena, for modification to update its circuitry.

An evaluation of the present standby battery system is under way. Tests will be made to determine the charging capabilities of the present battery charger.

i. Collimation tower. Repeated wind damage to the collimation tower waveguide run has impaired the use of the collimation tower in making receiver sensitivity measurements. To correct this situation, a low-loss coaxial cable, supported in such a manner as to prevent vibration due to wind, is being installed in place of the waveguide.

j. Maser. The maser performed satisfactorily during this period, successfully surviving three changes of Cassegrain feed cones and the associated "warm up" and "cool down." The gain continues to be a nominal 46 db.

Routine pre- and post-calibration measurements on the receiving system (2388 Mc) at Venus include measurement of the system temperature on a variety of input terminations with the antenna stopped at the zenith position. These measurements are made by the Y-factor method using a noise source with a nominal excess noise temperature of 51°K. This value of excess noise temperature has been measured several times (SPS 37-31, Vol. III, pp. 82-84) and the resulting values used to calculate system temperature from the Y-factor measurements.

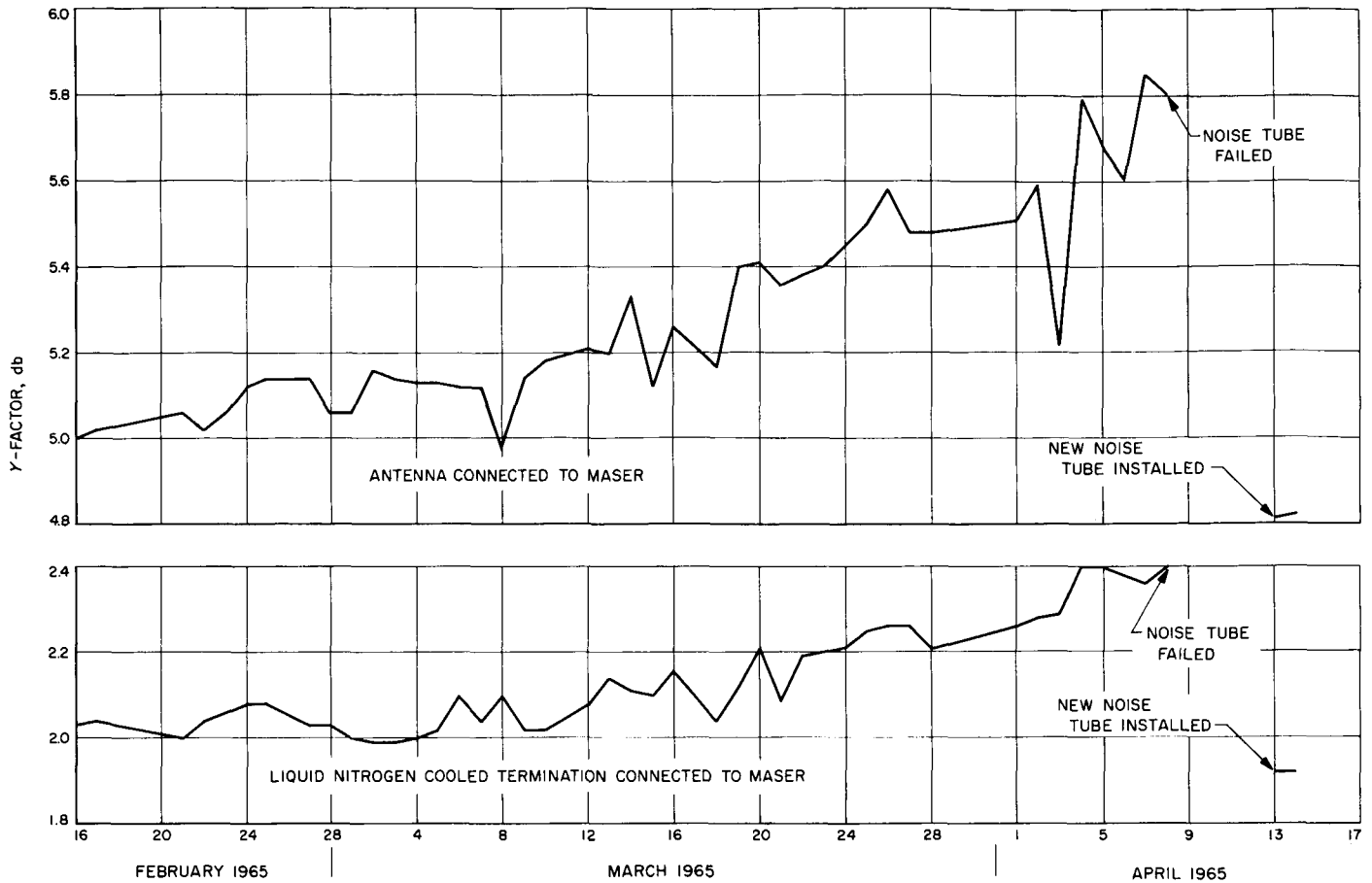


Fig. 26. Measured Y-factor on Venus receiving system (2388 Mc)

Fig. 26 illustrates the values measured on the antenna and liquid nitrogen load from February 16 to April 14, 1965. Observation of the plotted values indicated that either the excess noise temperature of the noise source was increasing or the temperature of the terminations was decreasing, inasmuch as the measured Y-factors were increasing steadily. The excess noise temperature of the source was remeasured during the week ending March 27, and was discovered to be 60.6°K, an increase of approximately 20% since the previous measurement. During the week ending April 3, it was noticed that the current in the noise source no longer could be maintained at a nominal 50 ma and had dropped to a maximum of 40 ma. Finally, on April 9, the noise tube failed completely and was replaced with a new one April 13. The excess noise temperature of the new tube has been measured, and a nominal value of 47.8°K has been established. Further measurements will be made to substantiate this number.

D. High-Power 100-kw S-Band Transmitter

1. 100-kw S-Band Klystrons

The final amplifier in the Venus S-band transmitter is a 100-kw klystron. The system was first placed in operation in January 1963, using one klystron and one spare—both prototypes. The operating history of these tubes was reported in *SPS 37-29, Vol. III*. The Planetary Radar Experiment was resumed in November 1964, with only one klystron, Serial No. 3; the other unit, Serial No. 1, was found to have a cracked collector and was retired from service.

Procurement has been initiated for new klystrons of an improved design which should result in a substantially longer operating life. The new tubes will have

larger collectors and will not have an ion pump magnet; collector failure accounted for a large portion of the malfunctions on the prototypes, and the ion pump magnet is suspected of distorting the magnetic fields and creating hot spots in the collector. The klystron focus magnet will provide the magnetic field for the ion pump in the new tube.

A modulating anode, to be incorporated in the klystrons, will permit electronic switching of the beam current at rates up to 10 kc, minimum, when used with a floating deck modulator. This technique reduces the interpulse noise.

Salient features of the specification are:

Power output	100 kw, minimum
Service	Continuous wave (CW) or pulsed; types of modulation include frequency, phase, amplitude, single and double sideband suppressed carrier
Frequency	Tunable from 2.1 to 2.4 Gc
Gain-bandwidth	65-db minimum at 4-Mc bandwidth at 3-db points; 55-db minimum at 6-Mc bandwidth (high efficiency) at 3-db points; 35-db minimum at 15-Mc bandwidth at 3-db points
Efficiency	35% minimum
DC beam voltage	40 kv dc or less
Linearity	Within $\pm 10\%$ for outputs from 0 to 70 kw
Incidental phase modulation ¹	Less than 1 ± 0.5 deg peak-to-peak
Incidental amplitude modulation ¹	At least 60 db below the carrier

Delivery of the first tube is expected in August 1965; the 100-kw transmitter will be modified to accommodate the new tube, and extensive testing is scheduled prior to commitment of the system to a program.

¹ Using the existing Venus power supply.

E. X-Band Lunar Radar Transmitter

1. Introduction

The X-band transmitter (SPS 37-31, Vol. III, pp. 45-49), used during the October-November 1964 Lunar Radar Experiment, and the beam voltage keyer (SPS 37-29, Vol. III, pp. 85-86) have been installed temporarily in the 30-ft antenna power supply building at the Venus Station. The beam voltage keyer uses two solenoid-operated high-voltage relays to switch the power supply output from the klystron to a dummy load (a power triode) during the receiver mode; this eliminates the klystron noise that otherwise would degrade the receiver system temperature. The transmitter and beam voltage keyer presently are undergoing testing and modification for the May-June 1965 Lunar Radar Experiment. Transmitter tests and improvements and the principal problems which have been encountered are discussed in this report.

2. Beam Voltage Drop-Out Time

The high-voltage beam power supply incorporates a contactor in the primary side of the high-voltage transformer-rectifier and a high-voltage vacuum switch in the DC output to remove beam voltage in case of a fault or open interlock. Although the energizing coils of both devices are connected in parallel, their reaction times are different. With the vacuum switch bypassed, the measured time for decay of the beam voltage to 10% of its original value was 200 msec. With the vacuum switch in the circuit (the normal operating condition), the time delay was reduced to 32 msec. The power supply was operated at 2 kv and no load for the time delay measurements.

3. Focus Power Supply Time Delay

The cavities and drift tubes of klystrons can be damaged through loss of focus magnet current while the beam voltage is on. To prevent such damage to the VA849G klystron, a capacitor, diode, and resistor time-delay network were added to the focus power supply *on-off* contactor to delay shutoff of the focus supply for 100 msec after the beam voltage is off. This provides protection from shutoffs caused by low water flow through the focus magnet or through accidental focus power supply turnoff by the transmitter operator.

4. VA849G Klystron Testing

A VA849G (Serial No. 28) klystron was used on the October–November 1964 Lunar Radar Experiment. During the present testing period, the spare VA849G (Serial No. 26) klystron was installed in the transmitter and developed an output of 9 kw at 8,448 Gc. The limitation on output power was established by the DC power supply which originally was designed for other use and which had a maximum output of 17.5 kv under load, while the klystron is designed to operate at 26 kv to deliver a rated output of 25 kw. The klystrons are more than 3 yr old and still appear to conform to the manufacturer's data.

5. Power Supply Ripples

The ripple content of the high-voltage beam power supply, focus power supply, and filament power supply was measured while connected to their normal loads. The results are:

Power supply	Test voltage	Test current, amp	Ripple, RMS
Filament	11 v	5.5	3.8 %
Focus	130 v	6.0	0.17 %
Beam	18 kv	2.0	14 V

6. Heat Exchanger Water Heaters

To prevent heat exchanger damage from coolant water freezing during cold weather, the heat exchanger was modified to permit automatic water heater and water pump turn on when the ambient temperature drops below a preset value (usually 35°F). The modification also prevents the heat exchanger fan from operating at low temperatures. Previously, the heat exchanger and water heaters had to be turned on manually during cold weather.

7. Klystron Phase Modulation

The klystron output phase modulation resulting from power supply ripple can be calculated by using the formula

$$\Delta\theta = \frac{\theta}{2} \frac{\Delta V}{V}$$

where

θ = electrical length of klystron, rad

$\Delta\theta$ = RF phase modulation, rad

V = DC beam voltage

ΔV = beam voltage ripple

The operating parameters of the system are

$\theta = 30$ rad for the VA849G klystrons

$V = 18$ kv

$\Delta V = 14$ v, RMS

Therefore,

$$\begin{aligned} \Delta\theta &= \frac{1}{2} \times 30 \times \frac{14}{18,000} \\ &= 0.0117 \text{ rad, RMS} \\ &= 0.67 \text{ deg, RMS} \end{aligned}$$

8. Beam Voltage Keyer

After installation of the beam voltage keyer the vacuum switches were run for approximately 5,000 cycles without applying beam voltage. During this time three out of the four switches ceased operating because of solenoid malfunction and were returned to the manufacturer for adjustment and rebuilding. One solenoid was found to be defective, and three required adjustment. After the rework, each switch was run 10,000 cycles at the manufacturer's plant, using JPL's control circuitry. Since then, two of the switches have been run an additional 10,000 cycles without failure. The two remaining spare switches have not been tested.

9. Beam Keying Transients

The primary problem area in testing the beam keyer has been the transients caused by the high-voltage beam keying. Transients first were noticed when the transmitter's arc detector was triggered falsely during beam keying at 4 kv. Subsequently, the interconnecting cable between the light amplifier, reflected power amplifier, and monitor cabinet was shielded. Beam keying arc detector transients then ceased to be a problem. After eliminating the arc detector problem, false triggering of the beam keyer control chassis became evident above 13 kv. The present theory is that a ground loop exists between the cabinet containing the control chassis and the high-voltage rectifier-transformer and/or the 400-cps motor generator supplying the high-voltage rectifier.

Attempts will be made to eliminate the transient problem by powering the control chassis with batteries instead of line-operated power supplies, and by changing the method of triggering the control chassis from a pulse trigger to an integrated square wave trigger system that is less susceptible to noise.

10. Conclusion

The X-band transmitter is undergoing testing and modification and is scheduled to be installed in the 30-ft antenna at the Venus Station for the May-June 1965 Lunar Radar Experiment. Pending solution of the transient problem, the beam keyer also is scheduled for operational testing during that experiment.

F. Lunar—Planetary Radar

1. Programmed Exciter

a. Introduction. The work and schedule plans for the programmed exciter (PE) have been completed, and work has been initiated on schedule in each of the planning areas.

b. Planning and procurement. To facilitate assignment of responsibility, the work has been divided into four areas. Area 1 encompasses all phases of the design effort from circuit design and power distribution to hardware design for the cabinet. Area 2 constitutes the module development and fabrication; a portion of the fabrication work is being done by outside vendors. Area 3 includes DC power distribution and monitoring, switching and cabling. Area 4 involves modifications to the cabinet and installation of hardware in the cabinet.

While major procurements for the PE have been initiated, some minor procurements still must be made, such as coaxial relays, limit detectors for monitoring, cold plates and distribution amplifiers. Ample time remains for the latter procurements.

Work in these areas should be completed by mid-August, so that system tests can be initiated. The completed system should be shipped to the Venus Station in September in order to be operational at the beginning of October.

c. Construction of the system. As reported in SPS 37-32, Vol. III, pp. 36-38, the PE system design has been simplified considerably, making it possible to house two

programmed exciters in one standard JPL cabinet. This plan has been adopted since it provides an even greater flexibility of operation. The total unit will be capable of programming two exciters or two receivers, or one exciter and one receiver.

Since the PE is to be computer-controlled, any indicators will be in parallel with the computer and will, primarily, indicate component failure. The indicators will be for maintenance only as all operation will be through the computer.

Test points will be internal to the system whenever practicable. A minimum of maintenance is to be done in the field so that the test points should be used infrequently. In addition, the cabling will be simplified considerably. The test points will be indicated on the block diagram and clearly labeled to facilitate their location.

There will be a dual test option for the PE. A computer test program will be used to test the over-all system operation. In addition, manual modes will be available but they will be monitored by the computer during operation to avoid interference by a manual input. This test procedure will separate a hardware failure from a software (program) failure in order to locate a source of trouble more easily.

2. S- and X-Band Central Frequency Synthesizer

The central frequency synthesizer has been modified to meet the new demands of the programmed exciter (SPS 37-32, Vol. III, pp. 36-38). This report contains evaluation data on 9 procured balanced mixers and 15 distribution amplifiers.

Fig. 27 is the new block diagram for the central frequency synthesizer. Five frequencies have been eliminated: 800 and 925 kc; 4.16, 4.56, and 36.0 Mc. This change involves the removal of three balanced mixers, five distribution amplifiers, the 4.16-Mc synthesizer, a $\times 2$ multiplier, the $\times 36$ multiplier, and the entire 36-Mc phase-lock loop (SPS 37-30, Vol. III, p. 87). This represents a total of 15 modules removed, of which 8 can be reused by retuning; they are the 800- and 925-kc distribution amplifiers retuned to 455 and 500 kc, respectively. The 3.635-Mc balanced mixer inputs are to be retuned to 31.44 and 35.075 Mc. The entire 36-Mc loop will be transferred to the 35.2-Mc loop and retuned. A $\times 2$ multiplier (0.4 to 0.8 Mc) and a $\times 36$ multiplier (1 to 36 Mc) have not been constructed. The five modules at 4.16 and 4.56 Mc will not be used at this time.

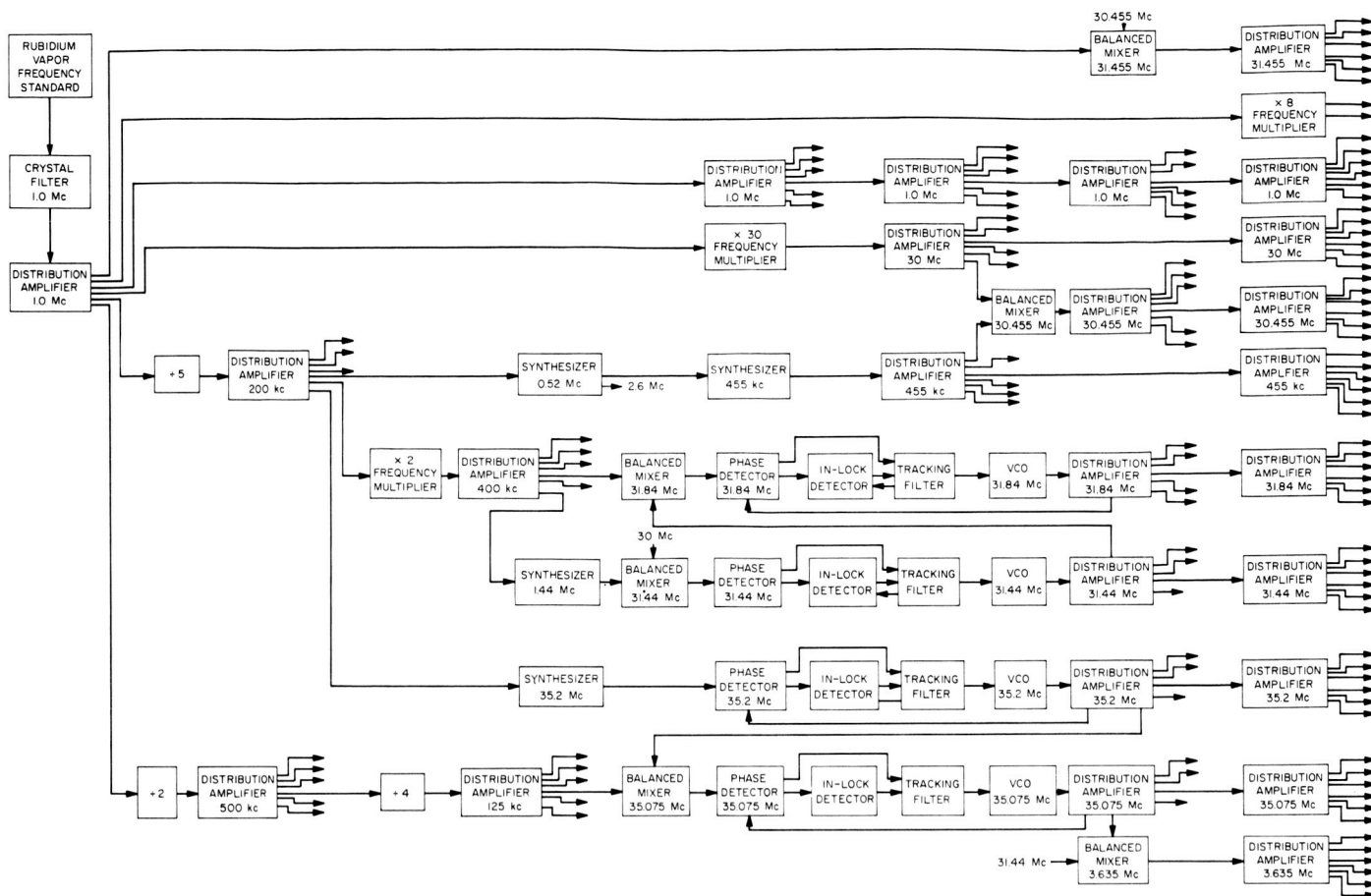


Fig. 27. Central frequency synthesizer

a. **Balanced mixer.** Twelve balanced mixers were fabricated by a vendor, nine of which will be used at this time. Performance data appear in Table 13. The balanced mixers have proved to be a reproducible module that has met stringent performance tests. (SPS 37-27, Vol. III, p. 92).

b. **Distribution amplifiers.** A new distribution amplifier was designed and 15 were fabricated by a vendor. The amplifiers consist of solid-state circuitry on printed circuit boards housed in a machined and gold-plated cavity-type chassis having six outputs (Fig. 28). Other performance features are output levels of +13 dbm, -0 db, + 3 db into 51 Ω , 10% bandwidth, 1.3-w power drain from a +30-v dc system, input impedance of 51 $\Omega \pm 10\%$, and limiting level at 0.05 v RMS. Three modules, at 455 kc, 4.56 and 31.455 Mc, were subjected to a temperature environment from 0 to 50°C. Output

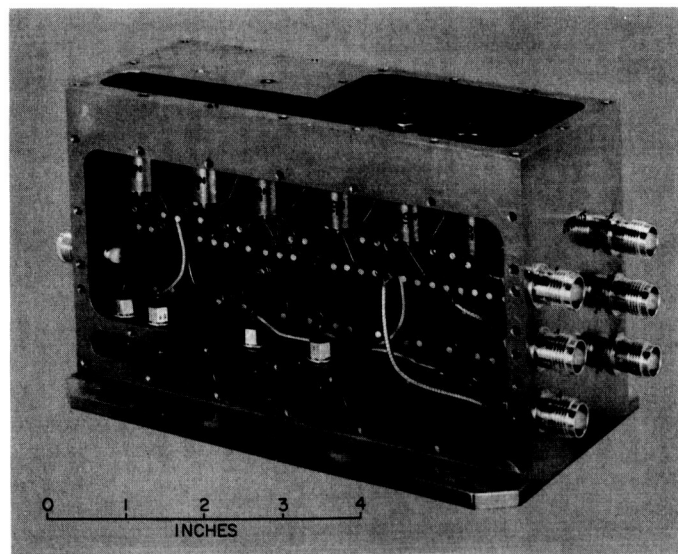


Fig. 28. Distribution amplifier

Table 13. Balanced mixer performance data

Balanced mixer	Balanced mixer output frequency, Mc	Spurious signal, μv	RF leakage (all frequencies), μv	Dynamic range, both inputs for constant output, db	Input impedance, VSWR	Variation of output with power supply variation of 20 %	Bandwidth at 6-db points, kc
1	31.44	2.7	0.1	10	≤ 1.10	20	43.7
2	31.44	3.0	0.0	20	≤ 1.10	20	55.4
3	31.84	0.0	0.0	20	≤ 1.10	20	44.3
4	31.84	28.0	0.5	20	≤ 1.10	11	52.4
5	31.455	90.0	0.2	20	≤ 1.10	18	51.5
6	35.075	2.0	0.0	20	≤ 1.10	15	47.6
7	35.075	0.0	0.2	20	≤ 1.10	17	54.8
8	35.2	11.0	0.2	20	≤ 1.10	17	52.4
9	35.2	1.2	0.1	20	≤ 1.10	19	48.6

Table 14. Performance data for distribution amplifiers

Amplifier, Mc	Isolation		Output noise (input terminated), μv	Dynamic range on input for constant output, db	RF leakage (all frequencies), μv	Bandwidth at 3-db points, Mc	Power supply variation of 10 % versus output, -db	Power drain, w
	Output to input, db	Output to output, db						
0.455	112	32	60	27	0.0	0.95	1.0	1.20
0.800	>60	36	40	30	0.0	0.14	1.0	1.11
0.925	120	36	230	23	0.0	0.14	0.7	1.11
1.0	102	38	28	23	0.0	0.14	0.7	1.11
3.635	86	35	20	25	0.0	0.55	0.7	1.05
4.16	84	36	15	24	0.0	0.55	0.7	1.05
4.56	84	35	10	28	0.0	0.52	0.7	1.08
30.0	88	30	8	23	1.0	3.0	0.7	1.17
30.455	74	31	8	20	1.0	3.0	0.7	1.23
31.44	67	31	8	20	0.1	5.0	0.7	1.26
31.455	74	32	12	27	0.0	3.0	0.7	1.32
35.075	76	30	5.0	26	0.2	3.0	0.7	1.20
35.2	74	30	1.4	26	0.0	3.0	0.7	1.20
36.0	74	32	1.0	19	0.1	3.2	0.7	1.23

level varied no greater than 4% on any of the 18 outputs. Additional performance data (worst case) are presented in Table 14.

Two separate circuit designs were adapted. Amplifiers that range in frequency from 455 kc to 4.56 Mc employ seven transistors (Fig. 29), whereas amplifiers above 4.56

Mc have the conventional nine transistors (Fig. 30). Excessive gain at the lower frequencies resulted in removal of the two transistors.

Consistent performance data that are within the required specifications for distribution amplifiers insures a reliable, long-life, and maintenance-free module.

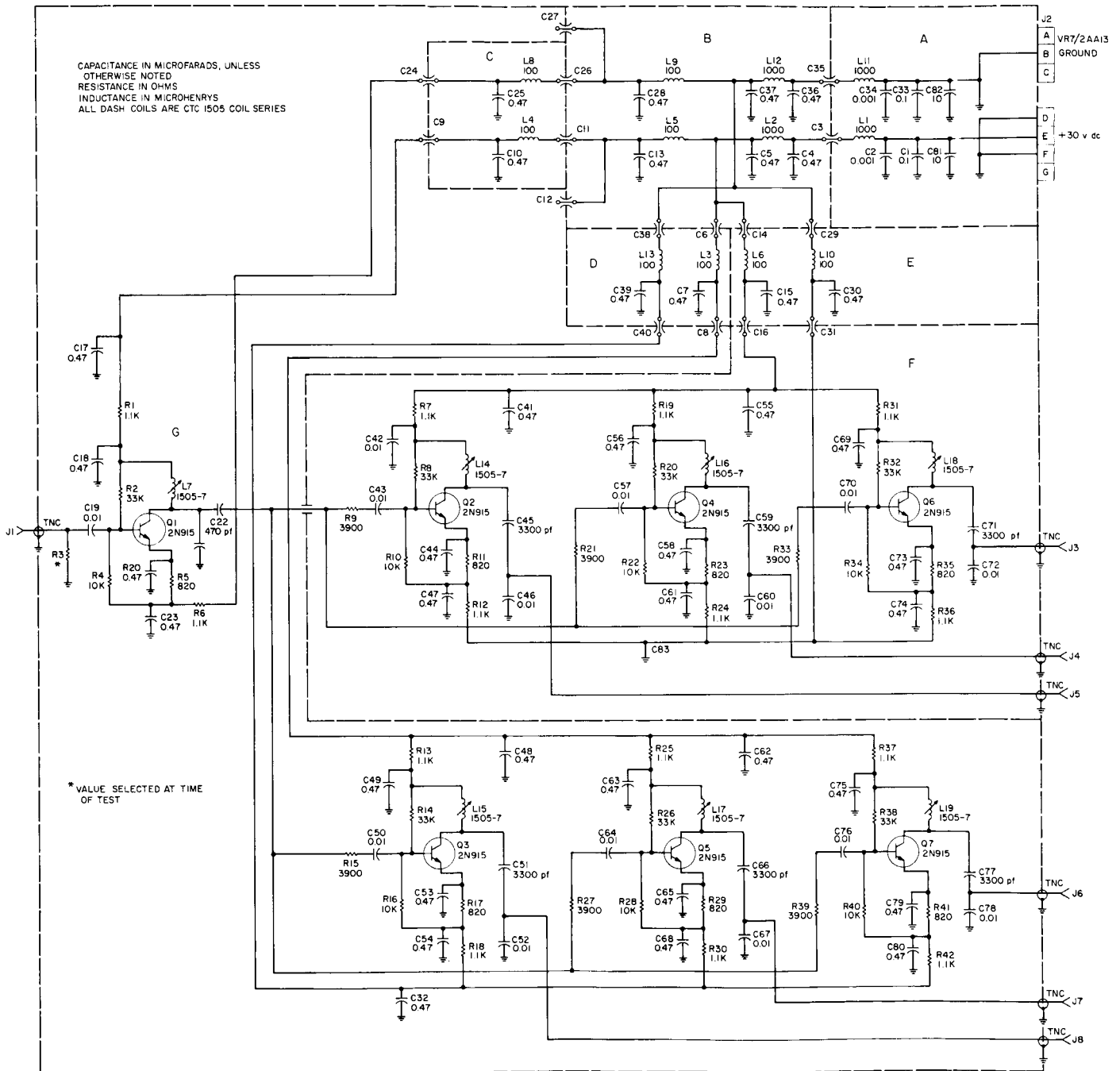


Fig. 29. Low-frequency distribution amplifier schematic

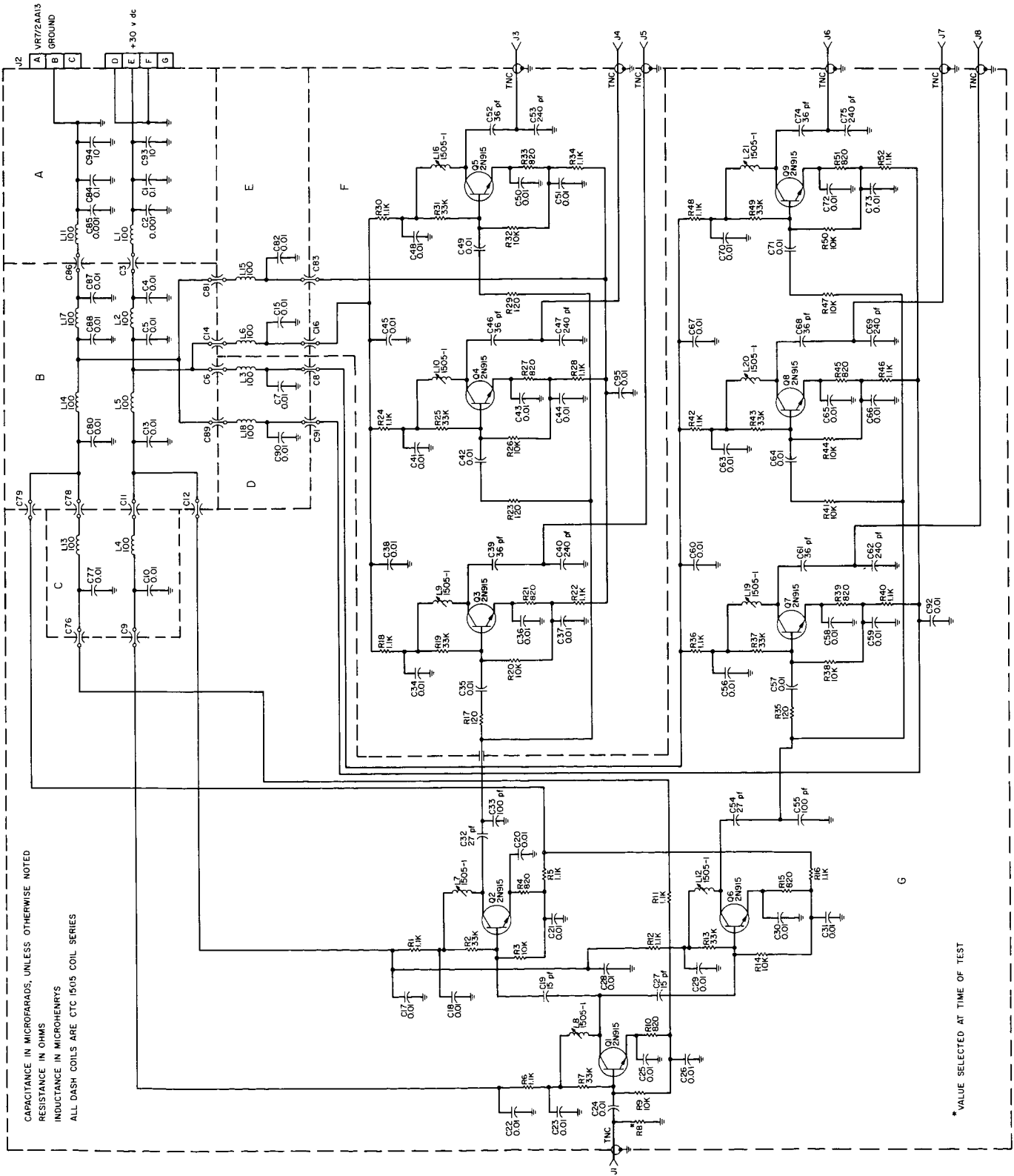


Fig. 30. High-frequency distribution amplifier schematic

G. Communication Systems

1. Wide-Band Receiver System

a. Introduction. The wide-band receiver system (WBRS) is an S-band system suitable for use in the Deep Space Network (DSN). The WBRS frequency range covers both the DSN and Manned Space Flight Net (MSFN) frequency bands. The system has two different names which distinguish its immediate application from its ultimate capability. The system name for the immediate application is Prototype DSIF/MSFN Receiver System. This application implies operation on one of the 29 DSN or 4 MSFN channels. The WBRS which is the ultimate capability of the system, is capable of changing the S-band frequency in 1-cps increments over the entire DSN and MSFN frequency bands.

The WBRS preliminary diagram shown in a previous report (SPS 37-30, Vol. III, pp. 86-92) has been modified. The modification consists of replacement of the *a priori* S-band offset doppler frequency synthesizer with a RF frequency synthesizer. The following advantages were achieved by this modification:

- (1) The system conforms with the proposed acquisition mode for the *Apollo* mission and the acquisition mode for the DSN.
- (2) The system's versatility is increased since the transmitter and receiver can be programmed independently in increments of 1 cps at S-band over the entire DSN and MSFN frequency bands.

- (3) The system is simpler for two reasons: the synthesis operation necessary to translate the preset down-link doppler frequency to the required receiver frequency is no longer required, and the number of required synthesized reference frequencies is reduced.

Another modification was incorporated in the ranging clock receiver and the code clock sections. This modification incorporates a switched frequency synthesis scheme which eliminates the requirement for the VCO's in the two sections to shift the entire clock doppler frequency when the system is changed from synchronizing to operating mode. The system modes and frequency synthesis scheme will be discussed in the ranging receiver section.

2. System Configuration

The functional system performance for the WBRS was described in SPS 37-30, Vol. III, pp. 86-92. A functional description follows for each section of the system.

a. Transmitter section. The transmitter section is divided into two parts, exciter (Fig. 31) and doppler extractor (Fig. 32). The exciter part determines the S-band frequency to be transmitted. The output of the frequency synthesizer is mixed with a multiplied-by-3 fixed center frequency from the transmitter VCO. The mixed frequency is multiplied by 32 to S-band. The S-band signal is amplified to approximately 10 w of S-band power at the antenna terminals. The exciter is phase-modulated

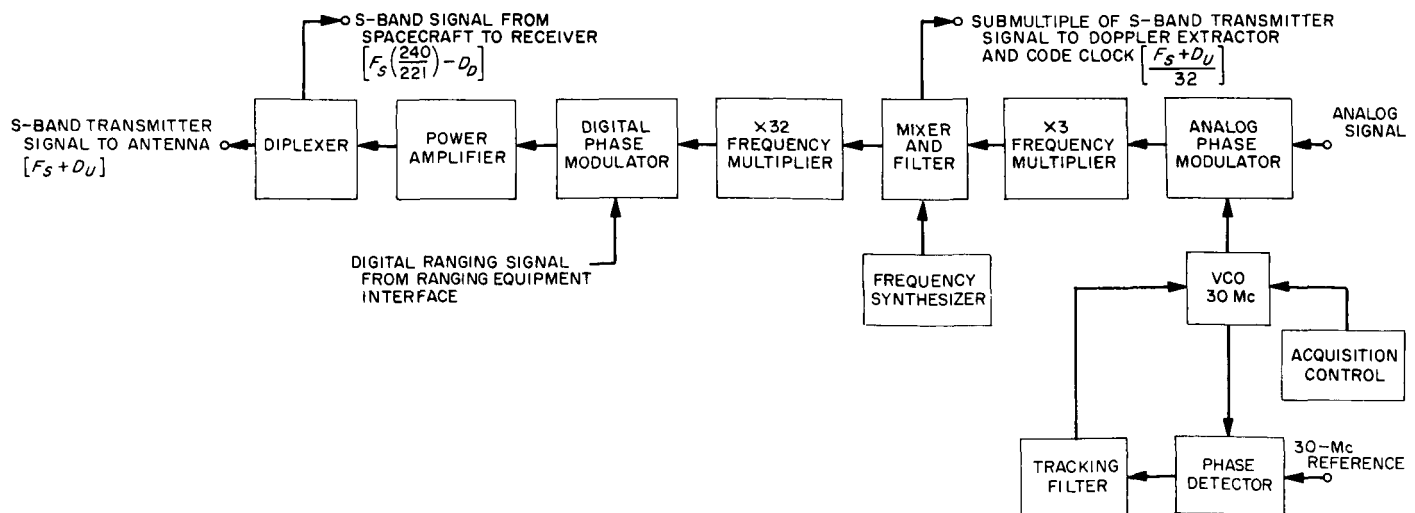


Fig. 31. Exciter

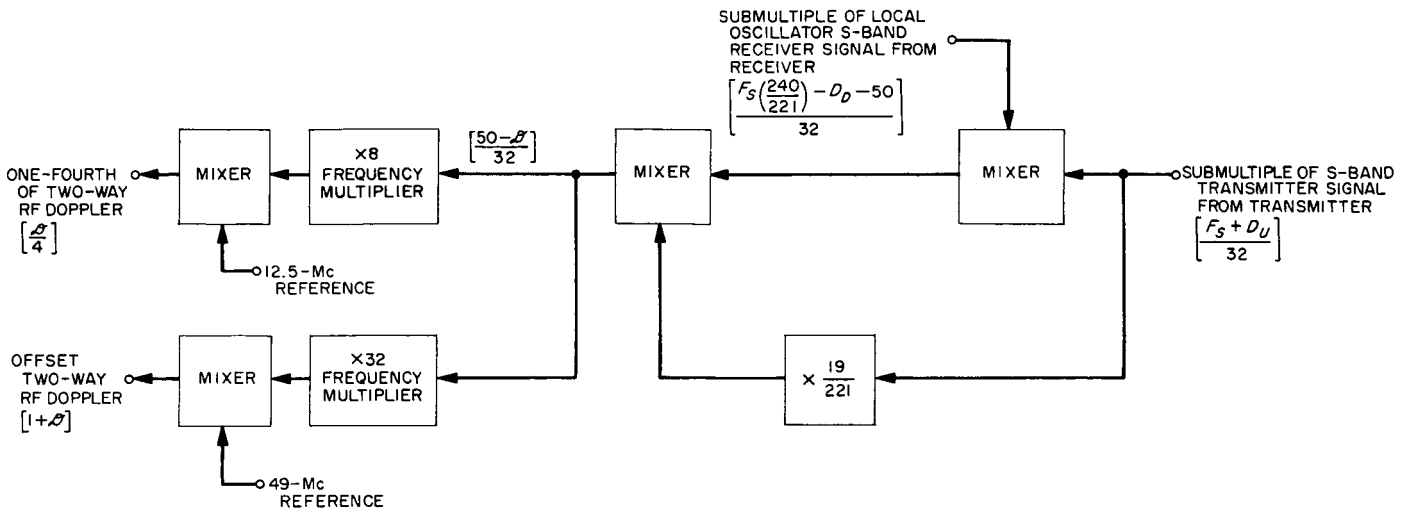


Fig. 32. Doppler extractor

with a digital ranging signal or an analog signal. The wide-swing 30-Mc VCO is capable of swinging the transmitted S-band frequency to acquire the spacecraft (uplink) initially. This is an acquisition requirement in the *Apollo* configuration.

The doppler extractor derives the RF doppler from the transmitted and received signals. A submultiple of the S-band transmitted signal is mixed with a submultiple of the local oscillator S-band received signal. The

output of this mixer is mixed with 19/221 of the input submultiple of the S-band transmitted signal to produce $(50 - \mathcal{D})/32$, where \mathcal{D} is the two-way RF doppler. The submultiple offset doppler signal is multiplied (1) by 8 and mixed with 12.5 Mc producing one-fourth of the two-way RF doppler ($\mathcal{D}/4$), and (2) by 32 and mixed with 49 Mc producing an offset two-way RF doppler $(1 + \mathcal{D})$.

b. Receiver section. The receiver functionally shown in Fig. 33 is variable narrow band, phase coherent, double

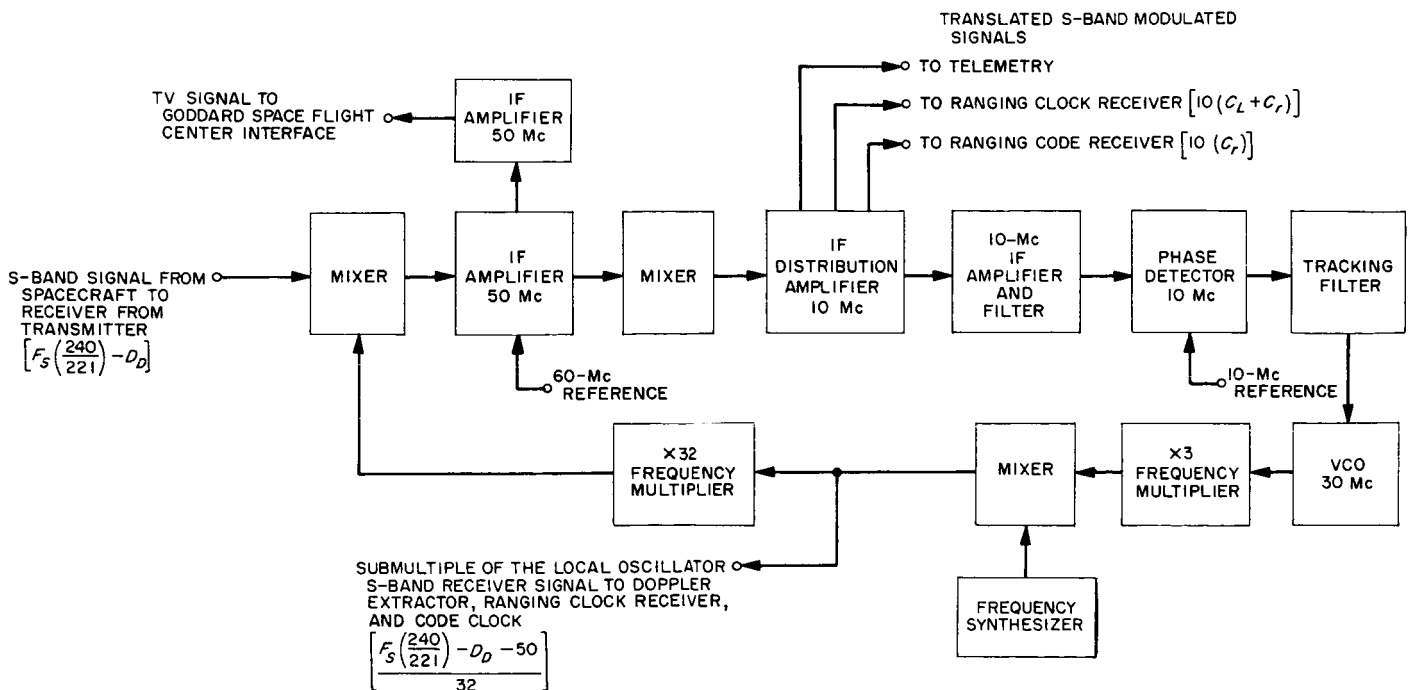


Fig. 33. Receiver

conversion superheterodyne. The received S-band signal from the spacecraft is mixed with the local oscillator S-band signal to produce a 50-Mc IF frequency. The local oscillator S-band frequency of the receiver is produced by multiplying a generated frequency by 32. The generated frequency is produced by mixing the output of the frequency synthesizer with a multiplied-by-3 fixed center frequency from the receiver VCO. The 50-Mc IF frequency is mixed with a 60-Mc reference signal to generate the 10-Mc second IF frequency. The 10-Mc IF distribution amplifier supplies signals to four separate receiver channels. The receivers are: coherent, ranging clock, ranging code, and telemetry. (The coherent receiver is the RF carrier tracking loop being described in this section. The other receivers are described in their respective sections.) The crystal filter at the input of the 10-Mc IF amplifier following the 10-Mc IF distribution amplifier, determines the predetection noise bandwidth of the receiver. The 10-Mc phase detector and tracking filter complete the RF carrier tracking loop.

For the *Apollo* mission, the receiver section supplies a TV channel signal to an interface with equipment to be supplied by the Goddard Space Flight Center. The TV signal is taken from the 50-Mc IF amplifier and amplified.

c. Ranging receiver section. This section has two ranging receivers. The ranging clock receiver requires the modulation on the 10-Mc carrier from the 10-Mc IF distribution amplifier in the receiver to be clock plus code. The ranging code receiver requires the modulation to be the only code.

The ranging clock receiver (Fig. 34), requiring clock plus code modulation, receives a 10-Mc carrier with modulation from the receiver. This incoming signal is mixed with a 10-Mc reference signal which has been phase-switched by the receiver pseudonoise (PN) coder. The derived signal is the received clock signal. A phase-locked loop which has a constant IF frequency is locked to this signal. A frequency synthesis scheme designed to provide a fixed center frequency in the phase-lock loop consists of mixing a signal with the ranging clock receiver VCO to produce the ranging clock receiver local oscillator signal. Another function of the frequency synthesis scheme is the ability to change from the synchronizing mode¹ to the operating mode with only a

¹The synchronizing mode establishes the synchronous operation of both the receiver and transmitter PN coders. This is accomplished by driving the receiver PN coder with the transmitted clock signal. The operating mode differs from the synchronizing mode by using the coherent receiver clock signal to drive the receiver PN coder. The transmitter clock signal drives the transmitter PN coder.

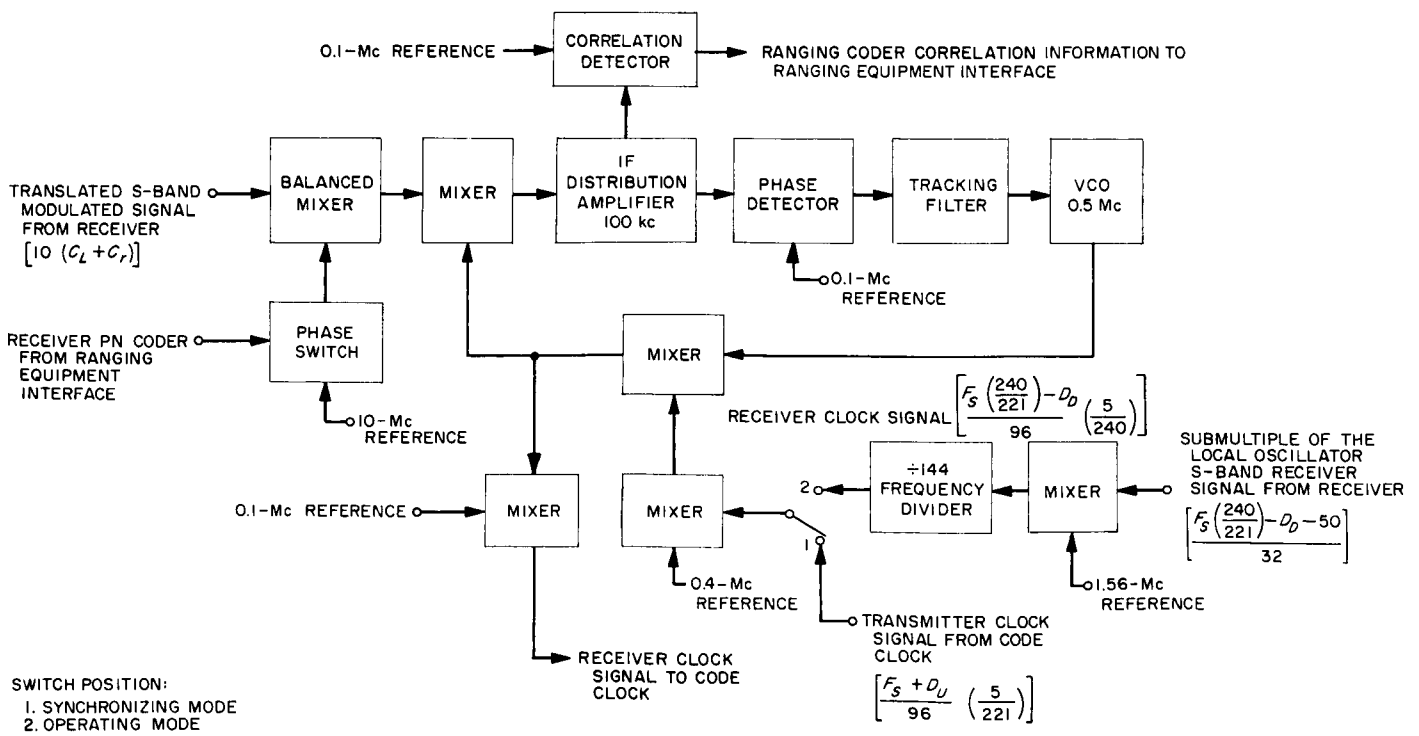


Fig. 34. Ranging clock receiver

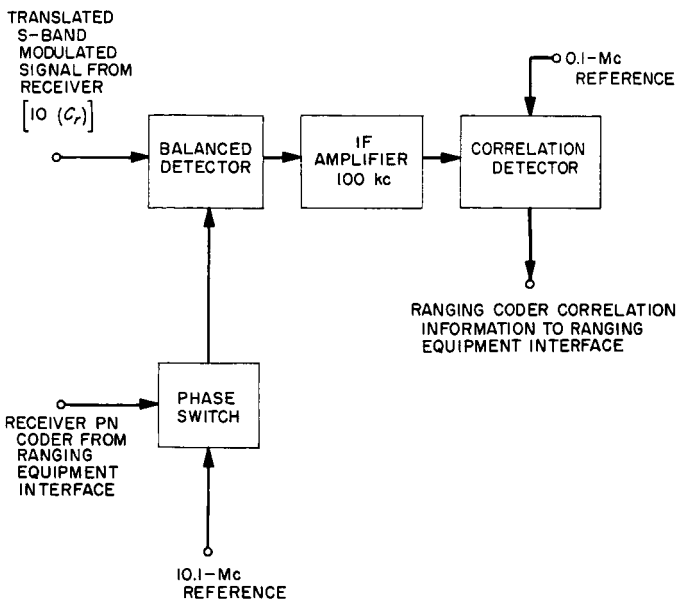
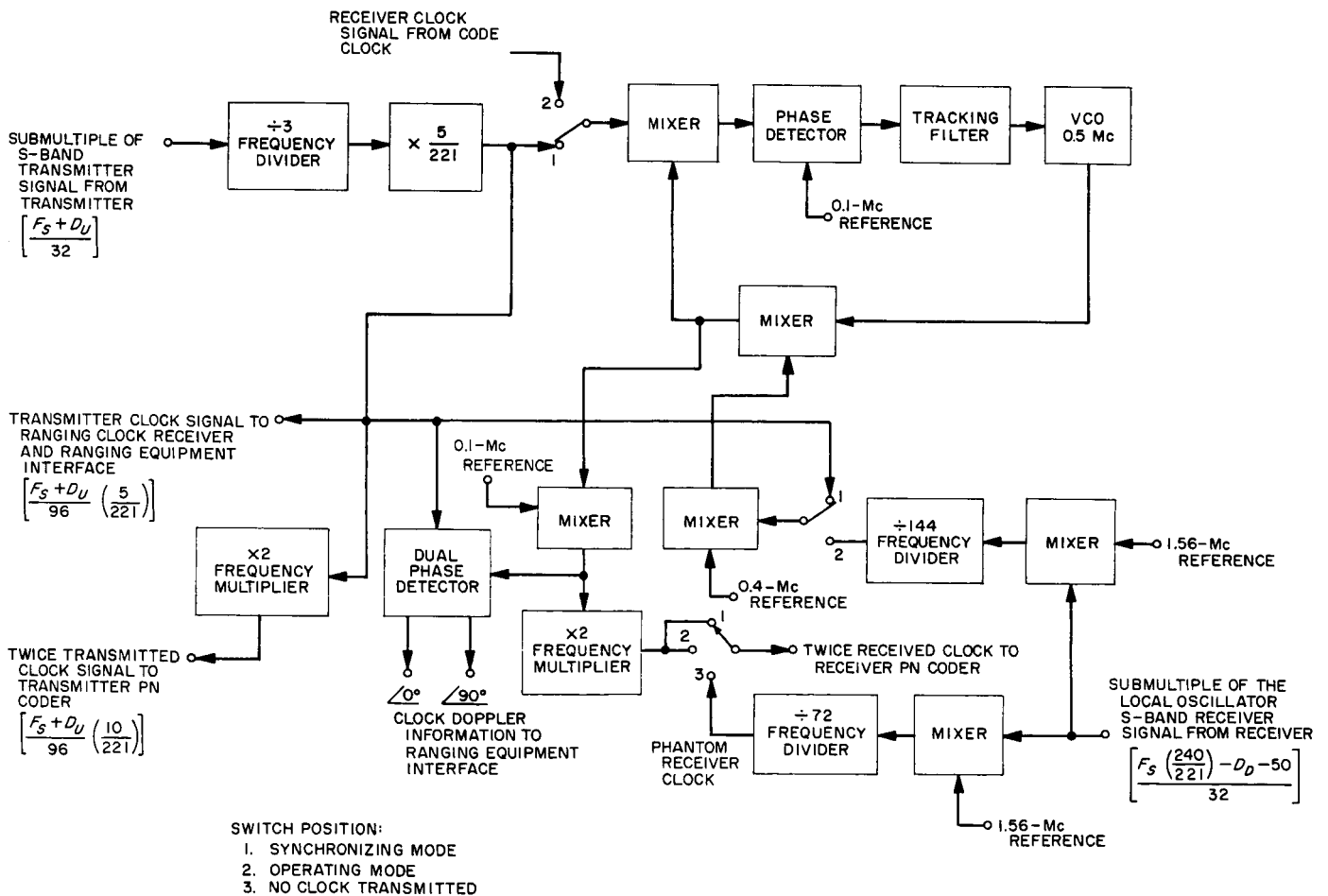


Fig. 35. Ranging code receiver

phase transient introduced in the closed loop. With this scheme, the ranging clock receiver VCO is not required to change the full clock doppler frequency when switching modes. This provides a faster reacquisition time for the loop. The ranging clock correlation detector produces a maximum output indication to the ranging equipment interface when the receiver PN coder is coherent with the incoming signal. A coherent receiver clock signal is derived from the phase-lock loop and supplied to the code clock section.

The ranging code receiver (Fig. 35) requiring only code modulation, receives a 10-Mc carrier with modulation from the receiver. This incoming signal is mixed with a 10.1-Mc reference signal which has been phase-switched by the receiver PN coder. The derived signal is a fixed offset (100-kc) signal. The signal is amplified and coherently detected. The ranging code correlation detector produces a maximum output indication to the



SWITCH POSITION:
 1. SYNCHRONIZING MODE
 2. OPERATING MODE
 3. NO CLOCK TRANSMITTED

Fig. 36. Code clock

ranging equipment interface when the receiver PN coder is exactly coherent with the incoming coded signal.

d. Code clock section. The code clock is functionally shown in Fig. 36. The transmitter and receiver clocks which drive the respective PN coders are supplied by the code clock section. The transmitter clock is derived by dividing the submultiple of the S-band transmitted signal by 3 and then multiplying by 5/221. In the synchronizing mode the code clock phase-lock loop locks to the transmitter clock signal. The output from the closed loop drives the receiver PN coder. When the mode is switched to the operating position, the coherent receiver clock signal is supplied by the ranging clock receiver. The frequency synthesis scheme used in the phase-lock loop of the ranging clock receiver also is used in the phase-lock loop of the code clock. Again only a phase transient is introduced in the closed loop during the switching operation. After changing to the operating mode, the receiver PN coder is driven by the receiver clock instead of the transmitter clock. When only code modulation is transmitted and the ranging code receiver is used, the code clock must derive a coherent receiver clock signal for the receiver PN coder. For this condition a phantom coherent receiver clock signal is derived from the submultiple of the local oscillator S-band signal.

When the transmitter and receiver PN coders are running coherently, clock doppler information may be obtained from the dual phase detector. This information is supplied to a ranging equipment interface.

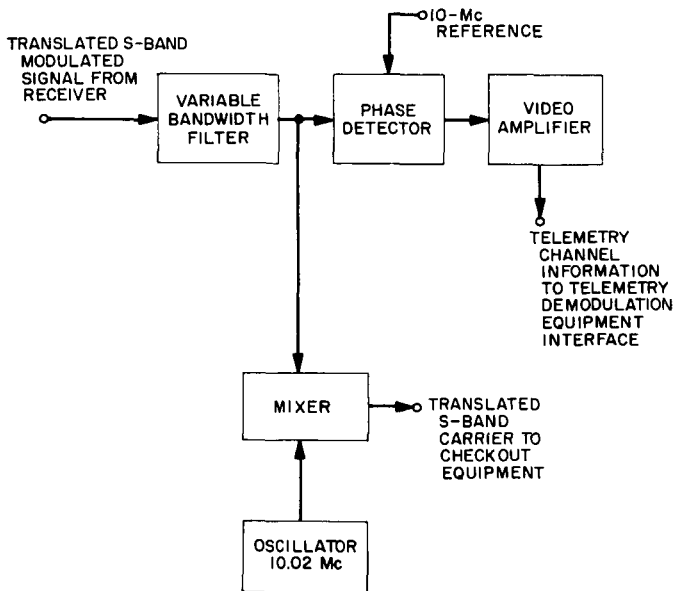


Fig. 37. Telemetry

e. Telemetry section. The telemetry section (Fig. 37) demodulates the telemetry channel signals to the RF carrier baseband. The input signal to this section is filtered by a filter whose bandwidth can be varied to eliminate some of the noise outside the received telemetry channel bands. Another function performed in this section is the translation of the S-band carrier to 20 kc for checking carrier suppression.

f. Synthesizer section. The synthesizer section (Fig. 38) provides the stable reference frequency signals used in all the other sections. A stable frequency is divided, multiplied, translated, or a combination of these processes, to synthesize all the required reference signals. The stability of the reference signals is determined by the stability of the rubidium frequency standard.

The modified preliminary system block diagram of the WBRS is shown in Fig. 39 which is derived by combining the functional block diagrams. The functional

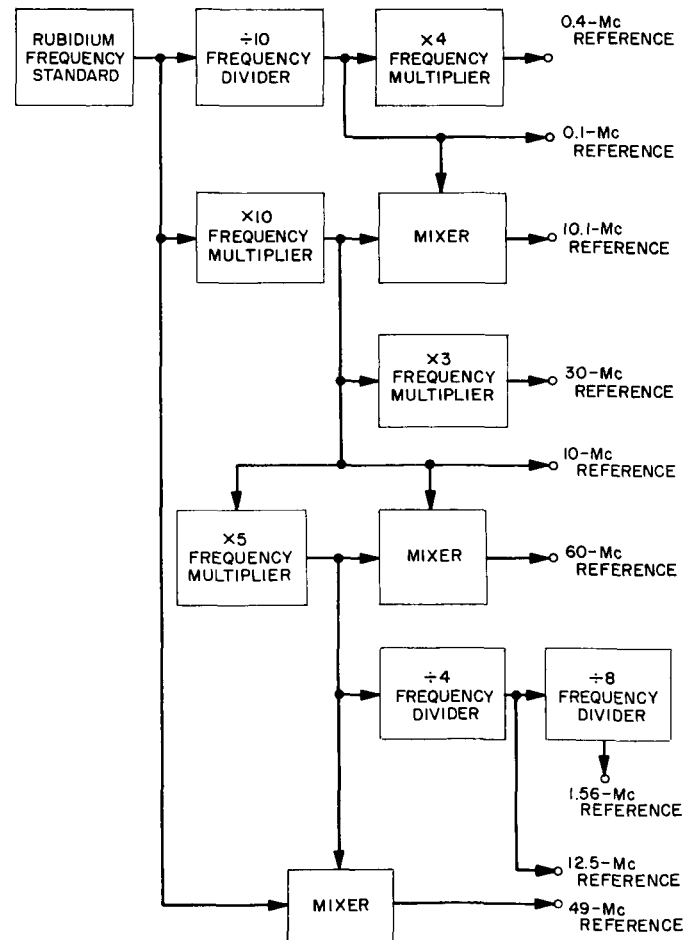


Fig. 38. Synthesizer

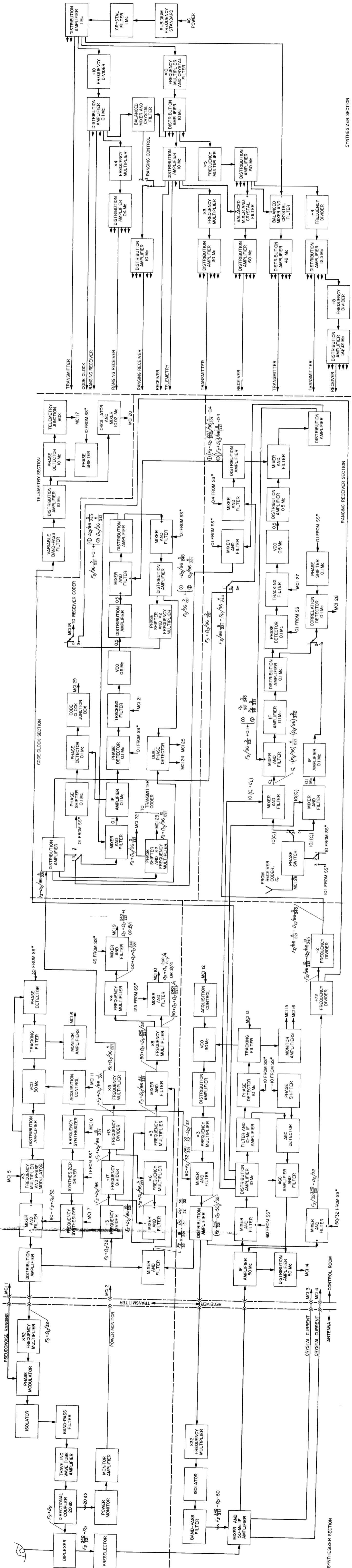


Fig. 39. Wide-band receiver system

blocks have been expanded in the modified preliminary system block diagram to show a detailed (module level) diagram.

2. Low Data-Rate Telemetry

a. Introduction. In spite of the enormous lifting capabilities of today's largest rocket boosters, there are still many space exploration tasks which require a simple, lightweight spacecraft. For example, consider the task of mapping some function of space (such as the magnetic field) throughout the solar system. In this case, the volume to be mapped is so large that a complete mapping would require a great many spacecraft, so it would be essential that they be not too complicated, too heavy, nor too expensive. Another example is the hard landing of a simple experimental package on a planet. If such a package were expected to survive ejection from, say, an orbiting planetary probe, and hard landing on the planetary surface, then it could not be too complicated.

Since the main contributor to a simple package's weight and complexity is usually its transmitter and power supply, the requirement that it be light and simple dictates the use of a low-power communication system. Such a system will be discussed here. This system's transmitted power will be only 1 w and its spacecraft antenna will be omnidirectional. However, this system will be useful for a low data-rate communication over distances in excess of an astronomical unit (1 AU = 149,000,000 km), and at 1 AU it could maintain a data rate of 0.5 bits/sec, which is adequate for many simple experiments.

b. Antenna and transmitter power. Before a high-gain, directional antenna can be used on a spacecraft, it is necessary for the spacecraft to be attitude stabilized so that the antenna can be pointed toward the Earth. However, an attitude stabilization system would unduly complicate the spacecraft being discussed here, so in what follows it will be assumed that the spacecraft is not stabilized. For this reason the spacecraft antenna must be nearly omnidirectional, so it will be assumed that it has a gain of unity.

Though this low antenna gain is certainly a disadvantage as far as the communication system is concerned, the spacecraft motion which makes it necessary can, in some cases, be used to simplify other parts of the system. For example, tumbling of a spacecraft which maps the magnetic field can allow a single magnetometer to measure two orthogonal components of the field.

The weight of a spacecraft's transmitter (including its primary power supply) depends primarily on its output power and the efficiency of its final amplifier. Since the primary power supply contributes significantly to the weight of these two elements, any increase in output power which is obtained at a sacrifice in efficiency causes a disproportionate increase in weight. For this reason it will be assumed for this simple system that the spacecraft transmitter's output power is limited to the 1 w or so available from relatively efficient solid-state devices.

c. Signal-to-noise ratio at ground receiving station. The (predetection) SNR at a ground receiving station can be expressed as

$$SNR = \frac{S}{N_0 W} = \frac{P_{sc} G_{sc} D^2}{4.9 R_{AU}^2 Temp W}$$

where

- S = received signal power, w
- N_0 = system noise power spectral density, w/cps
- W = system bandwidth, cps
- P_{sc} = spacecraft transmitted power, w
- G_{sc} = spacecraft antenna gain
- D = effective diameter of receiving antenna, m
- R_{AU} = distance to spacecraft in astronomical units
- $Temp$ = system effective noise temperature, °K

If we assume a receiving station similar to the one being built for the DSN at Goldstone, D is approximately 64 m (210 ft) and $Temp$ is about 25°K, and since we have already assumed $P_{sc} = 1$ w and $G_{sc} = 1$, the SNR can be expressed as

$$\frac{S}{N_0 W} = \frac{33}{R_{AU}^2 W}$$

This is sufficient to determine an upper bound on the rate at which information can be transmitted. This bound is given by the channel capacity which is (Ref. 12)

$$C = W \log \left(1 + \frac{S}{N_0 W} \right)$$

and which is bounded by

$$C \leq \frac{S/N_0}{\ln 2} = \frac{47.5}{R_{AU}^2} \text{ bits/sec.}$$

In practice it is possible to attain information rates of from one-half to one-tenth of this bound, but in order to do so it is necessary to have phase coherence in the received signal and to use rather involved coding and

decoding of the information transmitted. The most common way of maintaining phase coherence at the receiver is to use a phase-locked loop to track the RF phase of the received signal. The variance in the phase error of such a loop is approximately (Ref. 13)

$$\sigma_{\phi}^2 = \frac{N_0 W_L}{S_c}$$

where

W_L = bandwidth of the phase-locked loop
 S_c = power in the received carrier

This variance should be less than about 0.2 rad² for coherent reception, so the fraction of the total transmitted power which would have to be put into the carrier satisfies

$$\left(\frac{S_c}{S}\right) \left(\frac{S}{N_0 W_L}\right) \geq 5$$

or

$$\frac{S_c}{S} \geq \frac{5 R_{AV}^2 W_L}{33}$$

But the bandwidth of practical phase-locked loops is at least 5 cps, so this implies

$$\frac{S_c}{S} \geq 0.76 R_{AV}^2$$

which in turn implies that for coherent communication at distances greater than 1 AU, practically all of the available power would have to be carrier power, with little left over to transmit information.² For this reason, consideration will be restricted to a noncoherent system, and an information rate which is much less than the bound represented by the channel capacity will be realized.

d. Modulation and reception. Since the data to be transmitted from the spacecraft either is in digital form, or can be converted to this form, the choice of a modulation technique reduces to simply choosing a set of waveforms to represent a set of discrete symbols. It is well known that in a noncoherent communication system the best choice for such a set of waveforms is a set of orthogonal functions of time, and for the system considered here a set of orthogonal sinewaves will be used, since these functions can be generated easily in a simple spacecraft. The resulting modulation technique is what is called "multiple frequency shift" (MFS) modulation.

²A more rigorous discussion of this problem is reported in SPS 37-25, Vol. IV, pp. 176-181.

This is implemented by assigning a different signaling frequency to each of the N discrete symbols which must be sent. Then a symbol is sent by transmitting its corresponding frequency for a time duration T . In order for these N signals to be mutually orthogonal, they must differ in frequency by multiples of $1/(2T)$ cps.

The function of the receiver in an MFS communication system is simply to determine for each time interval which of the N signaling frequencies was transmitted. The optimum device for doing this is the envelope detector which determines the quantity

$$\hat{S}(f) = \left[\int_0^T x(t) \cos 2\pi ft \, dt \right]^2 + \left[\int_0^T x(t) \sin 2\pi ft \, dt \right]^2$$

[where $x(t)$ is the received waveform] for each value of frequency f which possibly could be received. Then the value of f for which $\hat{S}(f)$ is a maximum is decided to be the frequency which was received. It can be shown readily that $\hat{S}(f)$ can also be expressed as

$$\hat{S}(f) = 2 \int_0^T \hat{R}_x(\tau) \cos 2\pi f\tau \, d\tau$$

where

$$\hat{R}_x(\tau) = \int_0^{T-\tau} x(t) x(t + \tau) \, dt \quad 0 \leq \tau \leq T$$

which shows that $\hat{S}(f)$ can be considered to be an estimate of the power spectral density of the received waveform, and that the value of frequency f for which this estimated power spectral density is a maximum is the best estimate of the received frequency.

If the maximum in the power spectral density estimate is to serve as an estimate of the received frequency, then it is necessary that the received frequency be constant to within a small fraction of $1/(2T)$ cps during the observation interval $(0, T)$. For values of T in excess of 10 sec, which are the values of interest here, this implies an RF frequency stability of better than 0.05 cps, which is far better than can be expected from a simple spacecraft. To alleviate this problem we will simply truncate $\hat{R}_x(\tau)$ at τ_{max} and base our decision on the f which maximizes (Ref. 14)

$$\begin{aligned} \hat{S}_T(f) &= 2 \int_0^{\tau_{max}} \hat{R}_x(\tau) \cos 2\pi f\tau \, d\tau \\ &= 2\tau_{max} \int_{-\infty}^{\infty} \hat{S}(\phi) \operatorname{sinc}[2\tau_{max}(f - \phi)] \, d\phi \end{aligned}$$

where

$$\text{sinc}(x) = \frac{\sin \pi x}{\pi x}$$

In other words, we will simply observe the original estimated spectrum $\hat{S}(f)$ through a "spectral window" $\text{sinc}(2\tau_{max}f)$ of width $1/\tau_{max}$ cps. When this is done, it is necessary for the signaling frequencies to be separated by multiples of $1/2\tau_{max}$ cps, and for their stability to be a small fraction of this. Thus, the quantity τ_{max} will be chosen to accommodate the frequency jitter which occurs at the output of the receiver's mixer.

e. Digital implementation. In practice, the operations which are to be performed on the received waveform can be conveniently done digitally. In this case the received signal is heterodyned down to a low-frequency band, low-pass filtered to a bandwidth W , and sampled at a rate of one sample every $1/2W$ sec. (It is assumed that the signal duration T and the bandwidth W are such that the number $2TW$ of samples is large, so that the sampling does not destroy a significant amount of the information contained in the received waveform.) If the samples are denoted by $x_i = x(i/2W)$, $i = 1, 2, \dots, 2TW$, use can be made of the approximations (Ref. 15)

$$\hat{S}(f) \propto 1 + 2 \sum_{k=1}^{2W\tau_{max}} \hat{R}_r \left(\frac{k}{2W} \right) \cos \left[\frac{\pi k}{W} f \right]$$

and

$$\hat{R}_r \left(\frac{k}{2W} \right) = \left[\sum_{i=1}^{2WT-k} x_i x_{i+k} \right] / \left[\sum_{i=1}^{2WT} x_i^2 \right]$$

These calculations can be carried out quite simply if one further simplification is made; this is the association of a hard limiter with the sampler. If we let

$$y_i = \text{sgn}(x_i)$$

where

$$\text{sgn}(x) = \begin{cases} 1 & 0 < x \\ -1 & 0 > x \end{cases}$$

then the function

$$\hat{R}_y \left(\frac{k}{2W} \right) = \frac{1}{2WT} \sum_{i=1}^{2TW-k} y_i y_{i+k}$$

can be determined by a digital correlator that need only keep track of the relative number of coincidences of sign of the y_i and y_{i+k} . Now, if we assume that, due to the low SNR at which this system operates, the x_i represent an

approximately Gaussian process, then we can make use of the relation

$$R_x(\tau) = \sin \left[\frac{\pi}{2} R_y(\tau) \right]$$

(where we assume normalization such that $R_y(0) = 1$), which relates the correlation functions of the output and a Gaussian input of a hard limiter, to write

$$\hat{R}_x \left(\frac{k}{2W} \right) = \sin \left[\frac{\pi}{2} \hat{R}_y \left(\frac{k}{2W} \right) \right]$$

which yields

$$\hat{S}(f) \propto 1 + 2 \sum_{k=1}^{2W\tau_{max}} \sin \left[\frac{\pi}{2} \hat{R}_y \left(\frac{k}{2W} \right) \right] \cos \left[\frac{\pi k}{W} f \right]$$

It can be shown that the use of the hard limiter reduces the effective SNR by a factor of $2/\pi = 0.636 = -2$ db.

The correlation estimates $\hat{R}_y(k/2W)$, $k = 1, 2, \dots, 2W\tau_{max}$ can be calculated by a special-purpose digital correlator, and then the determination of $\hat{S}(f)$ can be determined by a small general-purpose digital machine. These operations are carried out easily in real time. Fig. 40 is the block diagram for this system.

f. Theoretical performance. The RMS variation in $\hat{S}(f)$ divided by its expected value when f differs from the frequency of the received signal by a multiple of $1/2\tau_{max}$ cps is [Ref. 15, Eq. (21)] $\pi(\tau_{max}/2T)^{1/2}$, and when f equals the frequency of the received signal, the RMS variation is very nearly the same, but the expected value is increased by a factor of $(1 + 2S\tau_{max}/N_0)$. As long as

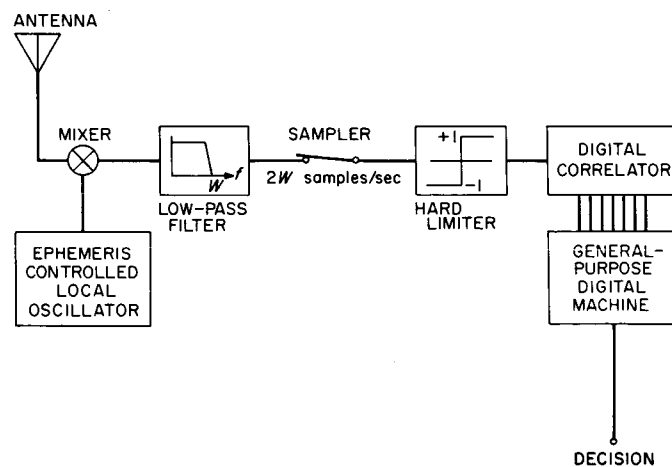


Fig. 40. Low data-rate telemetry system block diagram

$\tau_{max} \ll T$ the central limit theorem will apply to the probability distribution of $\hat{S}(f)$, and this probability distribution will be nearly Gaussian. Then the probability P_C that $\hat{S}(f)$ has its maximum at the correct value of f can be expressed as

$$P_C \approx (2\pi)^{-N/2} \int_{-\infty}^{\infty} \exp(-u^2/2) \times \left[\int_{-\infty}^{u+b} \exp(-z^2/2) dz \right]^{N-1} du$$

where

$$b = \frac{ST}{N_0} \frac{2(2)^{1/2}}{\pi} \left(\frac{\tau_{max}}{T} \right)^{1/2}$$

and where $\hat{S}(f)$ is checked for a maximum over a band of frequencies of width $N/2\tau_{max}$. For a small probability of error P_E this can be simplified to

$$P_E = 1 - P_C \approx \frac{N-1}{2} \left[1 - \Theta \left\{ \frac{ST}{\pi N_0} (2\tau_{max}/T)^{1/2} \right\} \right]$$

where $\Theta(x)$ is the error integral (Ref. 16)

$$\Theta(x) = 2/(\pi)^{1/2} \int_0^x \exp(-t^2) dt$$

For values of the argument $x \gg 1/4$, the error integral can be approximated by the first term of its asymptotic series, which is (Ref. 16)

$$1 - \Theta(x) \approx \frac{e^{-x^2}}{x(\pi)^{1/2}}$$

This latter expression will be useful for the low values of P_E in which we will ordinarily be interested.

g. Example. The main factors which influence the design of a communication system of the type being considered here are: (1) the frequency instability at the mixer output, (2) the number N of different signaling frequencies which are to be used, and (3) the error probability which can be tolerated.

First of all, we must insure that the frequency separation $1/2\tau_{max}$ considerably exceeds the frequency instability at the mixer output. For this example we will assume that the signaling frequencies are separated by multiples of 100 cps from each other, so that

$$\tau_{max} = 0.005 \text{ sec.}$$

Next we will assume that

$$N = 32 = 2^5$$

so that 5 bits of information is received each T sec. Then the bandwidth W will be about $N/2\tau_{max} = 3.2 \text{ kc}$,

and the incoming waveform will be sampled every $1/2W = 150 \mu\text{sec}$. Clearly, samples taken at this rate can be processed easily in real time.

Finally, for a reliable communication system we will want the error probability P_E to be on the order of 10^{-4} or less, which requires that

$$\frac{ST}{\pi N_0} (2\tau_{max}/T)^{1/2} = \left[\frac{S(T)^{1/2}}{N_0} \right] \frac{(2\tau_{max})^{1/2}}{\pi} \geq 3.1$$

or

$$(T)^{1/2} \geq \left(\frac{3.1}{S/N_0} \right) \left(\frac{\pi}{(2\tau_{max})^{1/2}} \right) = 3.0 R_{AU}^2$$

$$T \geq 9 R_{AU}^4$$

which in turn means that we are interested in signal durations in the range of 10 sec to 2.5 min for the spacecraft at a distance of 1 to 2 AU.

h. Synchronization. In the preceding discussion it has been assumed that it is known when the beginning and end of each transmitted signal will arrive at the receiver, so that it is known when to begin and end the summations which yield the estimates $\hat{S}(f)$. However, since the spacecraft occasionally will be out of view from the tracking station, it will ordinarily be necessary to reacquire this signal timing at least once every 24 hr. This operation will be referred to as symbol synchronization. To see how this can be accomplished, it is first noted that the maximum value of k for which the estimated correlation function $\hat{R}_y(k/2W)$ is calculated is $2W\tau_{max} = N = 32$, and that $2W\tau_{max} \ll 2WT$, so that practically no error results when $\hat{R}_y(k/2W)$ is calculated by

$$\hat{R}_y \left(\frac{k}{2W} \right) = \frac{1}{2WT} \sum_{i=1}^{2WT} y_i y_{i+k} \quad k = 1, 2, \dots, N$$

rather than by letting the upper limit of the summation be $2WT - k$, as was done above. This means that now the functions $\hat{R}_y(k/2W)$, $k = 1, 2, \dots, N$ can be easily updated as each new sample is received, so that they will always represent the summation over the last $2WT$ samples. Now it is possible to arbitrarily divide the received data into consecutive T sec segments, and to simultaneously divide it into another set of consecutive T sec segments which are "180 deg out of phase" with the first set, i.e., such that the divisions between the segments of the second set occur exactly at the centers of the segments of the first set. In general, the divisions between the signals actually received will not coincide with those of either of these sets, and so during each

segment a portion of two different signals will be received. As a result, the function $\hat{S}_v(f)$, which can be calculated for each T sec segment, will exhibit two distinct peaks, and the relative magnitude of these peaks will indicate the fraction of T sec by which the timing of the corresponding segment is off. The analogous information obtained from the "180 deg out of phase" segments allows one to determine whether the timing should be advanced or retarded. Of course, this could be determined by trial and error also.

Due to residual errors in the estimated doppler shift which the signals undergo, it sometimes will be necessary to acquire the received signals in frequency as well as in time. In principle this best can be done by simply increasing the frequency range over which $\hat{S}(f)$ is examined for its peak (i.e., by effectively increasing N) so that the entire range of frequency uncertainty is included in $W = N/2\tau_{max}$ cps. However, practically this requires increasing both the sampling rate and the number of values of k for which $\hat{R}_v(k/2W)$ is determined, and both of these changes increase the complexity of the receiver. For this reason it will usually be better to simply search the frequency uncertainty region for the received signals. If the received signal does not lie in the W -cps range for which $\hat{S}(f)$ is calculated, then $\hat{S}(f)$ will, with high probability, be relatively independent of frequency, and when this occurs the receiver local oscillator can be programmed to change so that a different frequency band can be examined during the next T sec.

Finally, another type of synchronization must be performed. In most cases it will not be possible to assign a separate signaling frequency to every possible value of the variable which is being telemetered back to the receiving station, e.g., in this example it usually will not be possible to quantize the telemetered quantity to only 32 levels. In order to increase the number of distinct levels (or "messages") which can be transmitted, it is necessary to use sequences of symbols to form "words" for transmission. If each such word consists of a sequence of k symbols, then N^k different words can be formed. For our example this means that 1024 two-symbol words can be formed, 32,768 three-symbol words can be formed, etc. With this scheme, however, word synchronization must be accomplished at the receiver before the received data can be used, i.e., the divisions between the symbols of consecutive words must be located. This can be done in several different ways, e.g., by transmitting only words which form a comma-free code (Ref. 17). However, in this example it will probably be possible to maintain word synchronization a

long time once it has been accomplished, so a more efficient method is to program the spacecraft data processor to transmit a known synchronizing word every so often, say once every 100 words. It can be shown (SPS 37-29, Vol. IV, pp. 293-296) that the best choice for such a k -symbol synchronizing word is one of the N symbols followed by $k-1$ repetitions of one of the $N-1$ other symbols. Then, in order to insure that this word is uniquely identifiable in an unsynchronized string of symbols, the words which begin with the last half of the synchronizing word, or end with the first half or more of the synchronizing word, are not used. Then any k consecutive received symbols which are identical to the synchronizing word must, in fact, be the synchronizing word, and once this is received the divisions between all other words can be found by simply marking off k symbols at a time, starting at the synchronizing word.

i. Conclusion. It has been seen how a very simple and lightweight communication system could be constructed for low data-rate space telemetry. The transmission system consists of an omnidirectional antenna, a 1-w transmitter, and a multiple frequency shift (MFS) modulator using 32 frequencies and a transmission time of from 10 sec to 2.5 min. The ground receiving station consists of a very large (210 ft) dish antenna and a low-noise (25°K) receiver feeding a mixer, low-pass filter, sampler, and hard limiter. This is followed by a digital data processor which consists of a special correlator and a small general-purpose digital machine. With this system a probability of error of 10^{-4} can be maintained at a data rate given by $0.56/R_{AT}$ bits/sec, where R_{AT} is the distance to the spacecraft in astronomical units. Acquisition of the signal is accomplished automatically in real time by the digital processor. Word synchronization is accomplished by the use of a special periodically-transmitted synchronizing word.

H. Information Systems

1. Quantile System

a. Summary. The quantile system of data compression as described in Refs. 18 and 19, SPS 37-27, Vol. III, pp. 103-112, and SPS 37-32, Vol. III, pp. 50-51, is based upon the statistical fact that a complete histogram of data can be compressed effectively into four *sample quantiles*. The quantiles also are called *percentage points*

of the distribution, i.e., the quantile of order p is the sample point below which $100p\%$ of the data lies. The four quantiles allow the mean and variance of the partial histogram to be computed with high efficiency, and allow further statistical tests to be made. Furthermore, the implementation is simple, being nonarithmetic.

The quantile system that has been built and described in the previous issues of SPS uses four quantiles to compress a histogram of 1024 sample values. The random events being observed are thought of as particle counts/unit time and a spread of 0-255 counts/unit time is provided. For distributions with larger or smaller spreads, a time base control has been provided, and is described. Due to the unary system of storing the histogram where the number of zeroes between address markers (ones) in a circulating delay line represents the number of samples of the size given by that address, the calculation of the quantiles is reduced to a counting and coincidence detection, resulting in an extremely compact and yet flexible data compression system.

b. Automatic time base requirement. The original system design included a time base control to multiply or divide the time base by successive factors of two, based on the criterion of an excess of overflows or underflows of the data counter. Specifically, if 16 overflows of the data counter were recorded during the time needed to take the 1024 samples, a reload signal would cause this data to be discarded and new data taken with a time base of one-half the previous base. On the other hand, if 16 zeroes were recorded a new sample would start with a time base twice as long as the previous.

Upon completion and testing of the quantile system however, it was noticed that the underflow criterion used to increase the time base did not always produce the most desirable histogram. For example, if there is a decrease in the data rate while the quantiler is in some relatively high sample rate, the complete histogram may well be contained in the first few slots of storage but yet not have 16 zero samples. This is because we are sampling from a nonnegative population which does not have a low-order "tail." Similarly, no quantitative check on the number of low-value readings observed will guarantee to produce a histogram with a maximum spread of values.

It has been decided instead, to check the highest value recorded during the 1024 samples and to lower the sample rate if this value is less than one-half the permissible spread, i.e., 127 or less. This criterion detects

a situation in which the time base can be doubled and still have the next histogram contained within the spread of 0-255. This check is made after a complete histogram has been stored so that no data is lost, but it may take as many as seven histograms to produce the optimum base (the maximum time base spread at present is 2^6 slower than the fastest rate of one sample every 1280 μsec). An added data compression feature is obtained: as soon as the data rate decreases, the time between histograms increases, which is exactly the desired effect.

c. Implementation. Fig. 41 is a block diagram of the implementation of the new time base control. The input ripple counter has its last bit connected to another four-bit counter which records data overflow. If 16 overflows occur before the histogram is compiled, a count-up signal is delivered to the 3-bit up-down counter; this counter controls the selection of the time base. Seven of the counter positions are used, and control a division of the timing pulses from 1 to 2^6 . The basic timing pulses occur every 1280 μsec as derived from the delay line storage element of this length operating at 1 Mc. A lockup is included if overflows continue during the highest sampling rate.

The lowering of the sample rate, if necessary, is accomplished during the quantile calculation mode of the machine. Previous articles have reported that, during this mode, an address counter is used to count the ones on the line and a cumulator counter is used to count the zeroes (that is, the number of samples). The correlation of these two counters allows the computation of the quantiles by detecting coincidence of the cumulator with the desired quantile values, and the storing of the value of the address register at this time.

It is an easy matter also to detect if the largest value recorded was less than 128. This is accomplished by a simple *and* function, i.e., examining the most significant bit of the address counter for zero when the cumulator is at full scale (a signal already used for another purpose) during the quantile calculation mode. A lockup is provided to prevent count-down signals while in the lowest sample rate.

d. Conclusion. The new time base control has been implemented and observed to search out an optimum time base. The control not only provides for the widest spread of data in the available storage, but does so using less hardware than the original design. An added

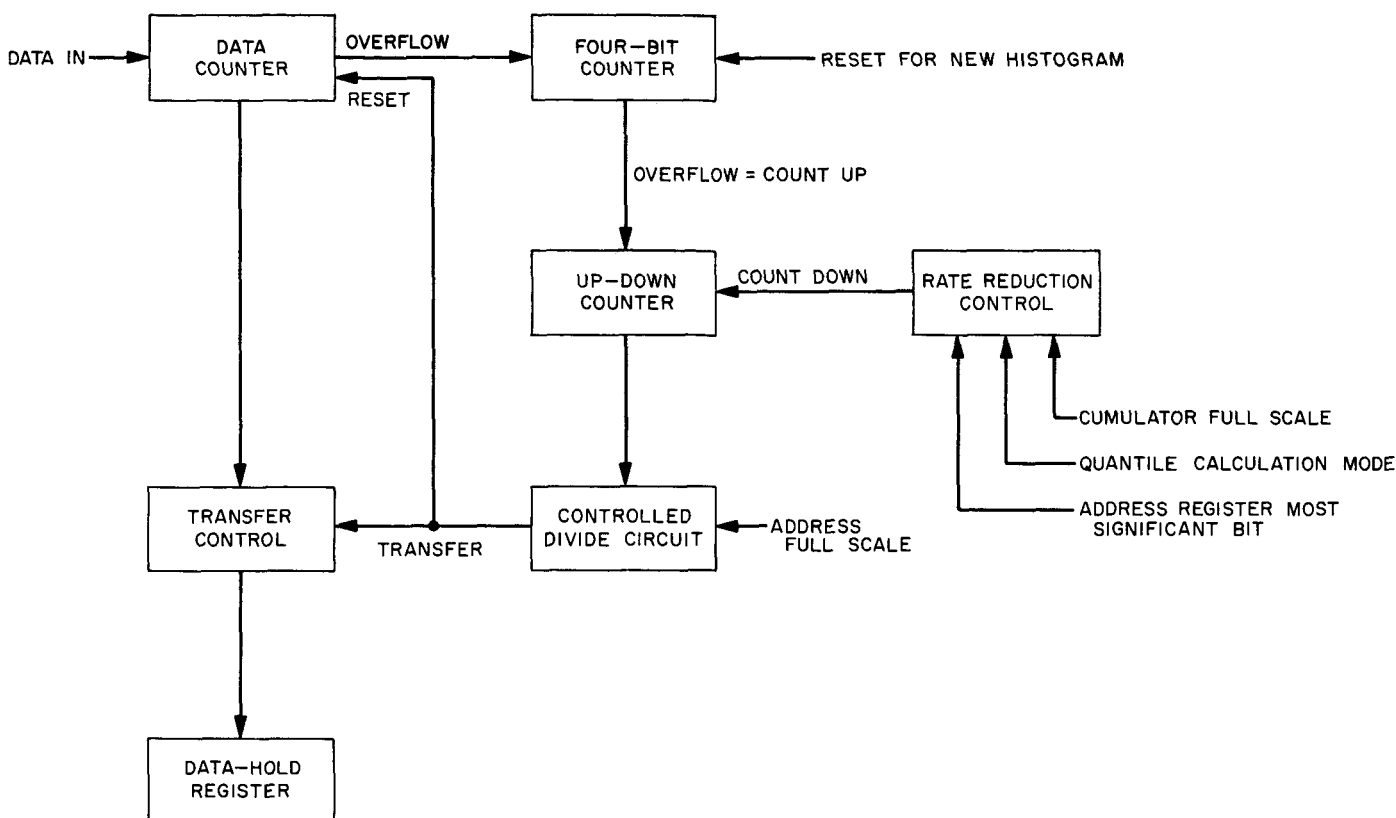


Fig. 41. Automatic time base control block diagram

feature of this control is that data during the more inactive periods of the data source are more efficiently compressed since the time base control will lengthen the time to collect a histogram during these periods.

2. A New Look at the Inter-DSN Teletype Channel

a. Introduction. In order to determine a method for correcting errors in a transmitted message, it is imperative to know the medium through which the message is to travel. When the channel is unknown, the system might turn out to be much too weak to correct the errors which could occur. For this reason, there has been undertaken the investigation of the channel in which teletype messages are transmitted between JPL-Goldstone and the tracking sites operated in Australia and Africa.

In the initial investigations of the channel, a 16,000-bit message was formed from the output of a shift register using the recursion relation $x^{23} = x^5 \oplus 1$. This test message was sent on a one-way and two-way basis throughout the DSIF, received tapes were compared

with the original message and any discrepancies noted. This part of the investigation was carried out by a computer program written for the SDS 910 and reported in *SPS 37-31*, Vol. III, pp. 76-78. When a sufficient number of tests had been performed, an analysis was begun to determine the characteristics of the teletype channel. In *SPS 37-32*, Vol. III, pp. 51-54, results of the investigation are reported and specific suggestions for improvement of the channel are made.

When the channel was known, a code could be chosen for transmission of messages. In particular, the Reed-Solomon (15, 9) code over the field of 2^4 elements was chosen. This code corrects 3 symbol errors in a block of 15 symbols. Since the teletype format assigns five levels to each symbol and the code chosen uses only four levels, the fifth level was utilized as an odd parity check on the previous four levels. This odd parity also prevents the occurrence of certain configurations incompatible with the communications processor at Goddard Space Flight Center (GSFC).

Since the message format was changed, it was decided to create a new test message which would have the same format as the encoded message in order to determine

how the new message format would work out. Also, a new program was written to test the accuracy of messages transmitted with the new format.

b. New message. For the new message, the shift register with the same recursion formula $x^{2^3} = x^5 \oplus 1$ was used. However, only four information bits were included in each teletype symbol and the fifth level was used to form an odd parity check with the four information bits. The message length was set at 16,000 bits and the test message formed for transmission throughout the DSIF. The message data is to be collected only on one-way messages.

Because spacecraft messages are routed through the communications processor at GSFC, the most meaningful results of this experiment would require that the test message also go through the communications processor. The problems of "blank suppression" and "figures-H-letters," which was discussed in SPS 37-32, would be avoided in this experiment by the odd parity condition.

c. New error-checking program. The new error-checking program follows along the line of the old one, discussed in SPS 37-31, with a few exceptions. The changes are of a minor type, speaking from a programming point of view, but the effect they could have is quite important.

Single errors (errors in exactly one level of a symbol) can occur in two ways in a teletype message. There can

be either a 0→1 transition or a 1→0 transition. It was noticed while running a hand comparison of several message tapes that quite often the preponderance of single-error transition was of one type, either 0→1 or 1→0, and in many cases these were the only single errors that occurred. It was decided to check three kinds of error patterns: just 0→1 transitions, just 1→0 transitions, and both types. The third category will serve as a check on the first two and it also will spot a double error (2 levels changing), where one level is a 0→1 transition and the second is a 1→0 transition, which the first two categories would denote as single errors. If it turns out that whole messages have errors of only one type, it may be possible to encode information in such a way as to make use of this fact. It is results of this nature that show the folly of not checking the characteristics of the channel.

Another feature of the first error-checking program which will not be included in the new program is the burst error counter. This counter recorded the length of a string of symbols, all of which were in error. Since the channel was found to be nonbursty on the symbol level, this set of counters is not necessary. The program will, however, continue to count the number of binary errors in each of the five levels and the total number of binary errors as a check on the level error counters. The number of errors in a symbol also will still be counted.

d. Conclusion. The work is now complete on these programs and the test messages will be sent soon.

References

1. Beatty, R. W., "Insertion Loss Concepts," *Proceedings of the IEEE*, pp. 633-671, June 1964.
2. Stelzried, C. T., "Temperature Calibration of Microwave Thermal Noise Sources," *Correspondence IEEE Transactions on Microwave Theory and Techniques*, Vol. MTT-13, No. 1, p. 128, January 1965.
3. White, G. K., "Experimental Techniques in Low-Temperature Physics," p. 104, Oxford University Press, 1959.
4. Stelzried, C. T., and Petty, S. M., "Microwave Insertion Loss Test," *IEEE Transactions on Microwave Theory and Techniques (Correspondence)*, Vol. MTT-12, pp. 475-477, July 1964.

References (Cont'd)

5. Ruze, J., Research Laboratory of Electronics, Technical Report 248, Massachusetts Institute of Technology, Cambridge, Massachusetts, October 1952.
6. Silver, S., "Microwave Antenna Theory and Design," Radiation Laboratory Series No. 12, p. 199, McGraw-Hill Book Co., Inc., New York, 1949.
7. Slayton, W. T., "Design of Microwave Antenna Gain Standards 0.77 cm to 31.5 cm," Naval Research Laboratory Report 4433, Washington, D. C., November 9, 1954.
8. Operating and Service Manual "8402A Power Meter Calibration," pp. 3-6, Hewlett-Packard Co., Palo Alto, California, November 1962.
9. Kerr, D. E., "Propagation of Short Radio Waves," Massachusetts Institute of Technology Radiation Laboratory Series No. 13, First edition, p. 641, McGraw-Hill Book Co., New York.
10. Barratt, A. H., and Chung, V. K., "A Method for the Determination of High Altitude Water Vapor Abundance from Ground Based Microwave Observatories," *Journal of Geophysical Research*, Vol. 67, No. 11, p. 4259, October 1962.
11. Potter, P. D., "Antennas," Space Communications, McGraw-Hill Book Co., New York, 1963.
12. Shannon, C. E., and Weaver, W., *The Mathematical Theory of Communication*, University of Illinois Press, Urbana, Illinois, 1959.
13. Viterbi, A. J., "Phase-Locked Loop Dynamics in the Presence of Noise by Fokker-Planck Techniques," *Proceedings of the IEEE*, Vol. 51, No. 12, pp. 1737-1753, Eqs. (35) and (37), December 1963.
14. Woodward, P. M., *Probability and Information Theory, with Application to Radar*, Chapter 2, McGraw-Hill Book Co., New York, 1953.
15. Goldstein, R. M., *Radar Exploration of Venus*, Technical Report No. 33-280, Jet Propulsion Laboratory, Pasadena, California, May 25, 1962.
16. Jahnke, E., and Emde, F., *Tables of Functions*, p. 24, Dover Publications, Inc., New York, 1945.
17. Golomb, S. W., Gordon, B., and Welch, L. R., "Comma-Free Codes," *Canadian Journal of Mathematics*, Vol. 10, No. 2, pp. 202-209, 1958.
18. Eisenberger, I., and Posner, E. C., "Systematic Statistics Used for Data Compression in Space Telemetry," *Journal of the American Statistical Association*, Vol. 60, pp. 97-133, March 1965, and Technical Report No. 32-510, Jet Propulsion Laboratory, Pasadena, California, October 1, 1963.
19. Posner, E. C., "The Use of Quantiles for Space Telemetry Data Compression," *Proceedings of the National Telemetry Conference*, Section 1-3, pp. 1-6, 1964.